Singularities in a BEC in a double well potential

Singularities in a BEC in a double well potential

JESSE D. MUMFORD, M.Sc.

A Thesis Submitted to the School of Graduate Studies in Partial Fulfilment of the Requirements for the Degree of
Doctor of Philosophy

June 7, 2017

DOCTOR OF PHILOSOPHY (2017) McMaster University
(Physics) Hamilton, Ontario

TITLE: Singularities in a BEC in a double well potential
AUTHOR: Jesse D. Mumford, M.Sc.
SUPERVISOR: Professor D. H. J. O'Dell
NUMBER OF PAGES: viii, 121

Abstract

This thesis explores the effects singularities have on stationary and dynamical properties of many-body quantum systems. In papers I and II we find that the ground state suffers a $\mathbb{Z}_2$ symmetry breaking phase transition (PT) when a single impurity is added to a Bose-Einstein condensate (BEC) in a double well (bosonic Josephson junction). The PT occurs for a certain value of the BEC-impurity interaction energy, Λ_c. A result of the PT is the mean-field dynamics undergo chaotic motion in phase space once the symmetry is broken. We determine the critical scaling exponents that characterize the divergence of the correlation length and fidelity susceptibility at the PT, finding that the BEC-impurity system belongs to the same universality class as the Dicke and Lipkin-Meshkov-Glick models (which also describe symmetry breaking PTs in systems of bosons).

In paper III we study the dynamics of a generic two-mode quantum field following a quench where one of the terms in the Hamiltonian is flashed on and off. This model is relevant to BECs in double wells as well as other simple many-particle systems found in quantum optics and optomechanics. We find that when plotted in Fock-space plus time, the semiclassical wave function develops prominent cusp-shaped structures after the quench. These structures are singular in the classical limit and we identify them as catastrophes (as described by the Thom-Arnold catastrophe theory) and show that they arise from the coalescence of classical (mean-field) trajectories in a path integral description. Furthermore, close to the cusp the wave function obeys a remarkable set of scaling relations signifying these structures as examples of universality in quantum dynamics. Within the cusp we find a network of vortex-antivortex pairs which are phase singularities caused by interference. When the mean-field Hamiltonian displays a $\mathbb{Z}_2$ symmetry breaking PT modelled by the Landau theory of PTs we calculate scaling exponents describing how the separation distance between the members of each pair diverges as the PT is approached. We also find that the cusp becomes infinitely stretched out at the PT due to critical slowing down.

In paper IV we investigate in greater detail the morphology of the vortex network found within cusp catastrophes in many-body wave functions following a quench. In contrast to the cusp catastrophes studied so far in the literature, these structures live in Fock space which is fundamentally granular. As such, these cusps represent a new

type of catastrophe, which we term a 'quantum catastrophe'. The granularity of Fock space introduces a new length scale, the quantum length $l_q = N^{-1}$ which effectively removes the vortex cores. Nevertheless, a subset of the vortices persist as phase singularities as can be shown by integrating the phase of the wave function around circuits in Fock-space plus time. Whether or not the vortices survive in a quantum catastrophe is governed by the separation of the vortex-antivortex pairs $l_v \propto N^{-3/4}$ in comparison to l_q, i.e. they survive if $l_v \gg l_q$. When particle numbers are reached such that $l_q \approx l_v$ the vortices annihilate in pairs.

Acknowledgments

I would like to thank the following people for helping me complete this work:

- Duncan O'Dell for being a great supervisor and always being available to discuss my research or to chat.
- Sung-Sik Lee for being a fantastic teacher and for answering questions I had any time of the day.
- Jonas Larson at Stockholm University for the collaborations.

Contents

List of Figures

Chapter 1

Introduction

Quantum mechanics is one of the pillars of modern physics and leads to the idea that massive particles can behave as waves. The notion of matter waves first came from de Broglie in 1924 [1] and ever since physicists have been studying them intensely in a wide range of systems. One of the most dramatic displays of matter waves is in a Bose-Einstein condensate (BEC) where a macroscopic number of massive bosonic particles are condensed into a single quantum state. Such a state of matter was first predicted by Einstein [2] in 1924 using Bose statistics [3] and was first experimentally observed in 1995 [4, 5, 6]. The generation of two independent matter waves can be achieved by splitting a BEC [7, 8, 9] and their merger leads to interference effects like lasers for light.

When two BECs are weakly coupled, like in a system of a BEC in a double well potential separated by a finite barrier, the energy difference between the single particle ground state and first excited state is much less than the energy difference between the ground state and all other single particle states. This leads to interesting coherent behaviour like the tunneling of massive bosons between two macroscopically occupied states localized in the left and right wells. This type of tunneling was first postulated by Josephson [10] in the context of current tunneling between two superconductors through an insulator, so the BEC in a double well potential is often called a bosonic Josephson junction (BJJ).

The reduction of the single particle Hilbert space to just two states in a BJJ means the size of the Hilbert space of the many-body states is equal to the number of bosons plus one. This allows for exact numerical calculations to be done of system sizes of up to 10^4 bosons using modest computational resources. On the experimental side of things, through Feshbach resonances [11] and precise trapping potentials [11] the interactions between bosons as well as their tunneling rate, respectively, can be precisely controlled. This allows for the BJJ to be tuned over a wide range of regimes making it an ideal system to do experiments with.

Theoretical and experimental work has focused on both steady-state and dynami-

cal aspects of the BJJ. Some theoretical work includes spatial fragmentation [12, 13], finite temperature effects [14, 15], low energy excitations [16] and phase diffusion [17]. While some experimental work has focused on controlling number and phase difference fluctuations [18, 19], fundamental quantum effects like continuous measurements producing the Zeno effect [20] and using the BJJ as a thermometer [21].

Recently, research into coupling the BJJ to other quantum systems has also been undertaken. Early research into coupled quantum systems focused on the interactions between laser light and atoms resulting in the cooling of atomic motion in the 1980s [22, 23, 24]. This lead to many applications from atomic clocks and precision measurements to the BJJ itself [25]. Optomechanics is another example and is an extremely active field which aims at understanding and manipulating the interactions between light in optical cavities and mechanical oscillators [26]. Both of these examples focus on the coupling of light and some other system and although the coupling can lead to nonlinear behaviour, light by itself cannot. The BJJ, on the other hand, is nonlinear because of the boson-boson interactions, so its coupling to other systems should lead to new phenomena. On top of that, the BJJ has high controllability and is macroscopically large making it an excellent candidate and perhaps a canonical example of a system to couple to in order to observe nonlinear behaviour. Indeed, the coupling of two species of BECs in a double well has helped in the study of transitions from independent to synchronous quantum dynamics [27]. Even the coupling of a BJJ to a small quantum system like a single atom has produced dramatic effects. Some examples include a quantum dot inducing coherent shuttling of bosons from one well to the other resulting in Josephson oscillations [28] and a fermionic impurity doing the same [29]. In this thesis we show that impurity induced coherent tunneling in the BJJ is the result of a second order $\mathbb{Z}_2$ symmetry breaking phase transition (PT) of the ground state as the BEC-impurity interaction energy approaches some critical value. In general, equilibrium PTs are associated with drastic changes in macroscopic properties of the system as a parameter is tuned through some critical value. We show the critical exponents which characterize this PT put it in the same universality class as the Lipkin-Meshkov-Glick [30] and Dicke [31] models (among others) both of which describe systems of two-state atoms coupling to themselves and light, respectively. We emphasize the equivalence to the PT in the Dicke model, which results in the coherent emission of light, because of its recent experimental confirmation in 2010 [32].

Non-equilibrium processes in many-body systems have also gained much interest over the past decade as a result of developments in experimental technology involving BECs [26]. There are two main protocols used to produce non-equilibrium behaviour: (1) a sudden quench [33] where some parameter is flashed and kept on at $t = 0$ or (2) a periodic perturbation [34] where a parameter is flashed on and off periodically. In our simulations we use a combination of the two resulting in flashing on, then off

(a kick) either the tunneling energy or interaction energy of the BJJ ground state at $t = 0$.

In recent research it has been shown that after a sudden quench, dynamical properties of a system can change drastically depending on the strength of the quench, perhaps signalling the existence of non-equilibrium PTs. In the one-dimensional XXZ spin model critical speeding up was observed at a critical value of the quenched anisotropy energy [35] and in the one-dimensional Bose-Hubbard model a quasistationary state was separated from a rapidly thermalized state by a critical value of the quenched interaction energy [36].

In general, the act of applying an external force on an otherwise isolated quantum system produces excitations. The evolution of these excitations is determined by the Schrödinger equation or equivalently the Feynman path integral [37] which weights each path by an exponential whose (imaginary) phase is the inverse of Planck's constant, $\hbar$, multiplied by the classical action. A well known semiclassical approximation to the path integral is the method of stationary phase [38] which uses the fact that as $\hbar \to 0$ the terms which contribute most to the integral are those which extremize the action. Thus, one can get a good picture of the dynamics under most situations by finding the critical points of the classical action. There are many mathematical techniques used to analyze such situations with varying degrees of success, but one which covers a broad range of phenomena is called Catastrophe Theory (CT). Developed by René Thom in 1975 in his book *Stabilité Structurelle et Morphogènése* [39], CT applies primarily to systems where the extremized value of some function is sought making it ideal for analyzing quantum dynamics. The main results of CT are that in the parameter space near the region where the extrema of the action coalesce the action takes certain universal forms based on its number of parameters and dimensionality and that these forms are stable to perturbations. These forms are called elementary catastrophes (catastrophes for short).

The universal aspects of CT have been investigated in quantum systems by mapping the potential of a Hamiltonian to one of the catastrophes near an equilibrium PT [40, 41, 42, 43, 44, 45], but very little has been done in the way of dynamics. In fact, this author can only find two instances where CT was used directly to analyze dynamics after a quench: a kicked quantum rotor [46] and plasma oscillations of a quenched BJJ [47], both displaying cusp catastrophes. Neither paper analyzes the effects of a PT on the resulting cusp, so the application of CT to dynamical PTs represents a new field with as of yet untapped potential. The universal aspects of CT give a possible path to making connections between seemingly very different systems through their dynamical PTs. In this thesis we take the first step towards using CT to analyze the semiclassical behaviour of a cusp produced by the dynamics of a kicked BJJ as it approaches a critical point of an excited state PT.

Optics is the subfield of physics in which CT is featured most prominently [48,

49]. It turns out that any reflecting, refracting or diffracting surface which is not perfectly parabolic in shape will produce caustics (regions of high light intensity) forming catastrophes. Common examples include the bright reflections of light on the surface of water and the cusp shape of light reflecting from the inside of a coffee cup onto the surface of the coffee inside it. It was Huygens who originally discovered that the cusp was stable and was produced by light wavefronts [50], but did not realize it was part of a hierarchy of catastrophes. The next progress came from Pearcey who discovered the diffraction integral of the cusp [51] which takes the form of a Feynman path integral, but he also did not know about the catastrophe hierarchy. After Thom elucidated the universal forms of the catastrophes Arnol'd derived universal scaling exponents for their intensities [52] and Berry derived a set of exponents describing the dependence of the fringe spacings on the wavenumber for each one [53]. Within the cusp the interference of the light waves produce a network of vortex-antivortex pairs. The Berry exponents determine how the density of vortex-antivortex pairs change with wavenumber. With light the vortices cannot be seen with the naked eye, but are visible when magnified.

The vortices are *points* of undefined phase and zero intensity of the wave and occur in the wave theory of light due to interference effects and the fact that the waves are continuous. The second condition is subtle and only becomes important when continuity of the wave breaks down. This happens when one needs to take into account that light is composed of photons. This happens in other many-body quantum systems like the BJJ for the same reason. We can ask the question, what happens to vortices when the waves producing the cusp are discrete? This question was partially answered by Berry and Dennis when they considered the particular nature of light and found the vortices were smoothed out over a radius proportional to $\sqrt{\hbar}$ [54]. However, effects relating to the phase of the wave remained uninvestigated. In this thesis, we look at the effects of granularity on the phase of the many-body wavefunction in the BJJ and find some remnants of the vortices persist, but they too vanish when a condition on the number of bosons in the BEC is met.

Thesis Outline

The first part of this work (Ch. 2) outlines the basic theories that are used in the papers and is broken up into four major sections. Section 2.1 discusses general properties of both classical and quantum equilibrium PTs and how PTs produce singularities in some quantities. Section 2.2 discusses many-body quantum mechanics in general, then focuses on the BJJ. Afterwards, Sec. 2.3 focuses on the addition of an impurity to the BJJ and the resulting equilibrium PT. Finally, Sec. 2.4 discusses the basic ideas of elementary CT and connects them to the three previous sections.

The second part (Ch. 3) presents four publications along with their summaries

which represent the contributions of the author. The papers can be broken up into two parts. Papers I and II both describe the second order PT resulting from the interaction of the BJJ with an impurity; paper I taking a mean-field approach and paper II taking a quantum approach. Papers III and IV describe how catastrophes emerge in the dynamics of many-body quantum systems, but mainly focus on the BJJ (without an impurity). Paper III focuses on the effects of an excited state PT on the cusp and the vortices within it while paper IV focuses on the effects of discreteness on the vortices.

In the third part (Ch. 4) a summary is given of the work presented as well as a look forward to what other interesting questions the BJJ-impurity system can explore and what CT can tell us about the connections between dynamics of different systems.

Finally, the last part (Appendix A) consists of a description of how catastrophes emerge in the dynamics of single particle excitations in the transverse field Ising model. A brief discussion is also given on the effects of the PT within the model on the catastrophes. The results constitute new, but as of yet unpublished work.

Chapter 2

Basic background theory of phase transitions, quantum field theory and catastrophe theory

2.1 Phase transitions

Phase transitions (PTs) are transitions between two or more phases of a system. The PTs most people are familiar with are ones between the solid, liquid and gas phases of water. During a PT certain properties of the system change, some times discontinuously, as a set of parameters called driving parameters are tuned through a set of critical values. For the case of water, it transitions from a solid to a liquid as the temperature is increased through the PT at $T = T_c \approx 273\text{K}$ resulting in a sudden decrease in density. PTs are often described as being non-analytic because certain quantities which characterize the PT become discontinuous or singular. By discontinuous we mean they take sudden jumps and by singular we mean they diverge. The non-analyticity in the water example comes from the solid and liquid phases having the same free energy at T_c resulting in a divergence of the compressibility.

PTs can be further characterized by the lowest order derivative of the free energy (with respect to the driving parameter) which becomes discontinuous at the PT. For instance, first order PTs happen when the first derivative of the free energy is discontinuous. This quantity is called the order parameter and measures the order of the phases. Usually the order parameter is zero in one phase and nonzero in the other. For water $\rho_s - \rho(T)$ can act as the order parameter for the solid-liquid transition where ρ_s is the density of ice and $\rho(T)$ is the density of the system at temperature T. Other examples are magnetic systems where the total magnetization, $M(T)$, is the order parameter for the transition between the paramagnetic and ferromagnetic phases. A discontinuity in the second derivative of the free energy characterizes a second order

PT which is the type we will focus on in this thesis. This quantity determines how susceptible the order parameter is to changes in the driving parameter and is usually called the susceptibility. Common susceptibilities are the specific heat, $C \propto -\frac{\partial^2 f_s}{\partial T^2}$ for PTs involving temperature and the magnetic susceptibility, $\chi_h \propto -\frac{\partial^2 f_s}{\partial h^2}$ for PTs involving applied fields, where h is the applied magnetic field and f_s, which we will discuss later, is the singular part of the free energy.

The majority of PTs, and the ones we will look at, involve the breaking of some symmetry. Indeed, symmetry breaking can be viewed as the cause of the change in the order parameter between the two phases. In second order PTs some symmetry is spontaneously broken via uncontrollable fluctuations. This is in contrast to first order PTs where symmetry is broken manually by an applied field. Using magnetic systems as an example, in the paramagnetic phase the magnetic spins point in random directions, so rotating the system causes no change in the direction of total magnetization. However, as the temperature decreases the spins align in the same direction and we enter the ferromagnetic phase where rotating the system causes a change in the direction of magnetization. The direction of magnetization that is 'chosen' in the ferromagnetic phase is random because the thermal fluctuations that cause it are random. In general, for PTs involving temperature the higher temperature phase has more symmetry than the lower one.

What is shocking is that the scaling of physical quantities like correlations and the susceptibilities given above are universal near the PT where the scaling forms are independent of the microscopic details of the system and instead depend on the symmetries and dimensionality of the free energy [55, 56]. This introduces the concept of universality where systems differing wildly on the microscopic level can share certain scaling properties on a macroscopic level near a PT if they have the same symmetries and dimensionality. Both classical and quantum PTs exhibit universal behaviour in some way and even though this thesis focuses on quantum PTs we will be purposefully vague about the type of PTs discussed in the coming three sections. However, in the section focusing on quantum PTs clear distinctions will be made.

2.1.1 Landau theory of phase transitions

It was Landau [57] who in the late 1930s argued that for a second order PT an order parameter, m, must exist and that in the vicinity of the PT $m \ll 1$. He also argued that the most important features of a PT are determined by expanding the free energy in terms of m. In general m can be a vector, complex, or something even more exotic, however we can go a long way toward describing second order PTs by keeping m a scalar. Thus, the free energy takes the form

$$f(m;\Lambda) = f_0(\Lambda) + b(\Lambda)m + c(\Lambda)m^2 + \mathcal{O}(m^3) \tag{2.1}$$

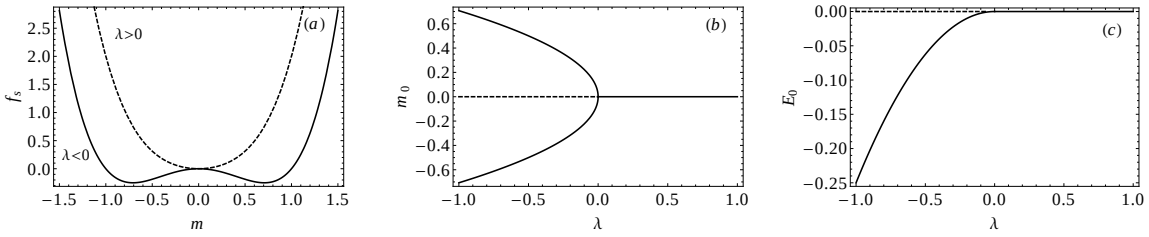

Figure 2.1: Mean-field properties of the energy and order parameter for different values of the reduced driving parameter λ. (a) The free energy as a function of the order parameter m for $\lambda > 0$ showing a single well and $\lambda < 0$ showing a double well. (b) The ground state value of the order parameter as a function of λ where it becomes nonzero for $\lambda < 0$. (c) The ground state energy as a function of λ where it also becomes nonzero for $\lambda < 0$. In both (b) and (c) the dashed line marks energetically unstable values of both m_0 and E_0.

where the coefficients $b, c, ...$ are some functions of the driving parameter, Λ, and f_0 is the part of the free energy independent of m, but not necessarily Λ, although, it is a smooth function of it. Equation (2.1) is a simplified version of the Landau approach to PTs provided m is uniform over the system. We make a further simplification by noting near the PT we can define a critical value of Λ, Λ_c, and expand the coefficients in terms of a reduced driving parameter, $\lambda = |\frac{\Lambda - \Lambda_c}{\Lambda_c}| \ll 1$. We can also apply some symmetry constraints to f. For instance, for second order PTs (m changes continuously across the PT) $f(m) = f(-m)$, so we only keep even orders of the order parameter. Keeping only up to quartic terms, the free energy becomes

$$f(m; \lambda) \approx a_1 \lambda m^2 + a_2 m^4 \tag{2.2}$$

where f_0 has been removed and a_1 and a_2 are some constants that we will set to unity without loss of generality. Also, we have kept up to first order in λ for the quadratic term and zeroth order for the quartic term. The shape of Eq. (2.2) can be seen in Fig. 2.1a for different values of λ. For $\lambda > 0$ there is a single minimum at $m = 0$, while for $\lambda < 0$ there are two minima an equal distance away from $m = 0$ on either side. The locations of the minima are found by extremizing Eq. (2.2), so we have

$$m_0 = \begin{cases} 0 & , \ \lambda \geq 0 \\ \pm\sqrt{\frac{|\lambda|}{2}} & , \ \lambda < 0 \end{cases} \tag{2.3}$$

and plugging this into the free energy gives the ground state energy in the two phases

$$E_0 = \begin{cases} 0 & , \ \lambda \geq 0 \\ -\frac{\lambda^2}{4} & , \ \lambda < 0 \, . \end{cases} \tag{2.4}$$

where for Eqns. (2.3) and (2.4) the parameters a_1 and a_2 have been set to unity without loss of generality. Both equations are plotted in Fig. 2.1 where we see the m_0 image shows a pitchfork bifurcation for $\lambda < 0$. The dashed line shows the unstable stationary point at $m_0 = 0$ while the two symmetric curves are new stable solutions representing the minima of the double well in image (a). We also see that for $\lambda < 0$ $m_0 \propto |\lambda|^\beta$ where $\beta = 1/2$. This is an example of a critical scaling exponent and describes the behaviour of the order parameter near the PT. It is independent of the microscopic details of the system and is therefore universal. Equation (2.4) shows why the PT is of second order since the susceptibility, $\chi_\lambda = -\frac{\partial^2 E_0}{\partial \lambda^2}$, is discontinuous at $\lambda = 0$: $\chi_\lambda \sim 0$ as $\lambda \to 0^+$ and $\chi_\lambda \sim 1/2$ as $\lambda \to 0^-$.

The one glaring problem with what we have done so far is we have neglected fluctuations. We can see from Fig. 2.1 if we started with $\lambda > 0$ with the system in its ground state and changed λ so it was negative, the system would still be in the state $m = 0$ where the tiniest nudge one way or the other would evolve the system to one of the new minima. Thus, the system is extremely sensitive to fluctuations of m near the PT. m can also be allowed to vary in space i.e. $m \to m(\vec{x})$ where $\vec{x}$ usually represents real space, but can represent more abstract spaces. To account for the energy cost of spatial variations of m we modify the free energy once again by adding the lowest order correction

$$f(m, \lambda) \to f(m(\vec{x}), \lambda) = \frac{s}{2} \left(\nabla m(\vec{x})\right)^2 + \lambda m(\vec{x})^2 + m(\vec{x})^4 \tag{2.5}$$

where the free energy is now an energy density and must be integrated over all of space to get the total energy of the system. We are allowed to truncate f at the lowest order of spatial fluctuations because near the PT the system is most sensitive to fluctuations involving many particles [55] which corresponds to long wavelength deviations of m. To quantify the degree of correlation of the fluctuations we introduce the correlation length, ξ, which is singular at the PT, $\xi \propto |\lambda|^{-\nu}$, where $\nu > 0$ is the correlation length critical exponent. In mean-field theory $\xi \propto |\lambda|^{-1/2}$ [56].

2.1.2 Singular part of the free energy

The two mean-field critical exponents β and ν are a part of a set which describes the singular nature of various quantities at a PT in the thermodynamic limit, $N \to \infty$. Since many quantities are related through the free energy it is important to determine the singular part of it. We go back to a uniform m starting with Eq. (2.2), however we include an applied field, h, to make things more general, and simplify so that the only parameters are h and λ

$$f(m; \lambda, h) = \lambda m^2 + m^4 - hm\,. \tag{2.6}$$

By minimizing f we can find h in terms of m and λ

$$h(m,\lambda) = 2\lambda m + 4m^3 \tag{2.7}$$

and scaling m by its nonzero ground state value for $h = 0$, given in Eq. (2.3) gives

$$h(m,\lambda) = |\lambda|^{3/2}\left[2\left(\frac{m}{|\lambda|^{1/2}}\right) + 4\left(\frac{m}{|\lambda|^{1/2}}\right)^3\right], \tag{2.8}$$

thus m as a function of λ and h must take the form

$$m = |\lambda|^{1/2} g_h(h/|\lambda|^{3/2}) \tag{2.9}$$

where g_h is some function. In the Landau theory Eq. (2.8) gives the universal form of the scaling of m and h with respect to λ, so applying these scalings to the free energy allows us to write it in its universal form as well

$$f(m;\lambda,h) = \lambda^2\left[2\left(\frac{m}{|\lambda|^{1/2}}\right)^2 + 4\left(\frac{m}{|\lambda|^{1/2}}\right)^4 - \left(\frac{h}{|\lambda|^{3/2}}\right)\left(\frac{m}{|\lambda|^{1/2}}\right)\right]. \tag{2.10}$$

Finally, substituting Eq. (2.9) into Eq. (2.10) gives the singular part of f

$$f_s(\lambda,h) = \lambda^2 g_f(h/|\lambda|^{3/2}) \tag{2.11}$$

where g_f is some function. What we have done is focused on the minima of the free energy which is the singular part and through rescaling were able to reduce the dependence of the free energy to two variables from three by eliminating the order parameter.

The derivation of Eq. (2.11) was done using the uniform field Landau theory which is the lowest order description of PTs. The major assumption going forward is that beyond the Landau theory f_s keeps the same form [56], but in general has different exponents, so

$$f_s(\lambda,h) = \lambda^{2-\alpha} g_f(h/|\lambda|^{\Delta}). \tag{2.12}$$

The exponents α and Δ are the susceptibility and gap critical exponents and are the same among systems in the same universality class. The reason for the exponent $(2-\alpha)$ is because once again the susceptibility is defined $\chi_\lambda \equiv -\frac{\partial^2 f_s}{\partial \lambda^2} \sim \lambda^{-\alpha}$ as $h \to 0$. The form of Eq. (2.11) allows us to compute relations among different scaling exponents, but we will do that in the following sections. For now, we go back to spatially dependent fields and derive Eq. (2.11) in a more subtle, but general way with a process called renormalization.

2.1.3 Rescaling and renormalization

Now, we build on what we have done to find useful relations between the exponents we have derived. First, we note that at the critical point $\lambda = h = 0$ we have scale invariance because the correlation length diverges implying fluctuations take place at all length scales. To explain scale invariance further we use a technique called renormalization which allows us to look at the system at different length scales and consists of three steps [55]:

1. There exists a short length cut off distance, a, which is usually a lattice spacing or mean separation distance between atoms. If we use a different length scale we must coarse-grain the order parameter by averaging over regions of size ba where $b > 1$ is the scaling parameter,

$$\tilde{m}(\vec{x}) = \frac{1}{b^d} \int \mathrm{d}^d y \, m(\vec{x} + \vec{y}) \tag{2.13}$$

   where the integration is over a cell around $\vec{x}$.

2. Since the system looks grainier after the averaging we rescale our lengths, $\vec{x}' = \vec{x}/b$, so the minimum length scale is again unity.

3. The result of the previous two steps is that the fluctuations of $\tilde{m}(\vec{x}')$ may appear larger than the original $m(\vec{x})$, so we tune the contrast by some factor, ζ, which gives the final rescaled and renormalized field

$$m'(\vec{x}') = \frac{1}{\zeta b^d} \int \mathrm{d}^d y \, m(b\vec{x}' + \vec{y}) \, . \tag{2.14}$$

Now the system can be compared to the original before the rescaling process took place. Under the renormalization procedure the parameters of the system also change and in general are functions of every parameter from the unscaled system, $\mathcal{R}\{\lambda\} = \lambda'(\lambda, h)$ and $\mathcal{R}\{h\} = h'(\lambda, h)$, where $\mathcal{R}$ is the renormalization procedure described above. However, at the PT we have scale invariance, so we expect $\lambda' \to 0$ as $\lambda \to 0$ and $h' \to 0$ as $h \to 0$. This means near the PT the leading order behaviour is

$$\begin{aligned} \lambda' &\approx b^{y_\lambda} \lambda \\ h' &\approx b^{y_h} h \, , \end{aligned} \tag{2.15}$$

where $b^{y_\lambda} = \frac{\partial \lambda'}{\partial \lambda}\big|_{\lambda=h=0}$ and $b^{y_h} = \frac{\partial h'}{\partial h}\big|_{\lambda=h=0}$, so $\mathcal{R}$ is a linear transformation of the parameters. Also, the free energy does not change under this procedure [55, 56], so $V f(\lambda, h) = V' f(\lambda', h')$ and since $V' = V/b^d$, plugging in Eq. (2.15) gives the singular part

$$\begin{aligned} f_s(\lambda, h) &= b^{-d} f_s(b^{y_\lambda}\lambda, b^{y_h} h) \\ \xi(\lambda, h) &= b\,\xi(b^{y_\lambda}\lambda, b^{y_h} h)\,. \end{aligned} \tag{2.16}$$

where we have also assumed the correlation length takes the same form and used $\xi' = \xi/b$. Using Eqns. (2.15) and (2.16) it is easy to see what the generalization to an arbitrary number of parameters looks like. Since $\mathcal{R}$ is a linear transformation, then the general form is

$$f_s(x_1, x_2, ...) = b^r f_s(b^{r_1} x_1, b^{r_2} x_2, ...) \tag{2.17}$$

as long as f_s is a homogeneous function.

We are free to choose any value of b we want however some values are more useful than others. For instance, having $b = \lambda^{-1/y_\lambda}$ changes Eq. (2.16) to

$$\begin{aligned} f_s(\lambda, h) &= \lambda^{\frac{d}{y_\lambda}} g_f(1, \lambda^{-\frac{y_h}{y_\lambda}} h) = \lambda^{\frac{d}{y_\lambda}} g_f(\lambda^{-\frac{y_h}{y_\lambda}} h) \\ \xi(\lambda, h) &= \lambda^{-\frac{1}{y_\lambda}}\, g_\xi(1, \lambda^{-\frac{y_h}{y_\lambda}} h) = \lambda^{-\frac{1}{y_\lambda}}\, g_\xi(\lambda^{-\frac{y_h}{y_\lambda}} h) \end{aligned} \tag{2.18}$$

where g_f and g_ξ are some functions. From these equations we can see $\nu = 1/y_\lambda$ and since $\frac{\partial^2 f_s}{\partial \lambda^2}|_{h=0} \propto |\lambda|^{-\alpha}$, this means

$$\alpha = 2 - \nu d \tag{2.19}$$

which is known as the Josephson hyperscaling relation. Comparing the free energy in Eq. (2.18) to Eq. (2.12) we also see $y_h = \Delta/\nu$. Other relations can be found between other exponents by using Eq. (2.16), but we will be focusing on the above relation.

2.1.4 Finite Size Scaling

Strictly speaking there are no PTs in finite systems. However, experiments and numerical simulations all use finite systems. Indeed, some quantum phenomena depend on the finiteness of the the system since N^{-1}, where N is the number of particles, usually plays the role of $\hbar$ in many-body systems. The question we look to examine here is how does the finiteness of a system affect its scaling properties.

For a system with volume L^d, where L is a length and d is the dimension, the scaling of the singular part of the free energy is changed to [58]

$$f_s(\lambda, L^{-1}) = b^{-d} f_s(b^{1/\nu}\lambda, bL^{-1}) \tag{2.20}$$

where we have left out the scaling of h for simplicity. We see the inverse size of the system is just another parameter that we scale. It is easy to see in the infinite

size limit, $L \to \infty$, we return to our previous expression of the scaling of the free energy given in Eq. (2.18). The factor of b in front of L^{-1} comes from the fact that in the renormalization procedure length scales are scaled by b^{-1}. Performing the same rescaling we did earlier, i.e. having $\lambda b^{1/\nu} = 1$ or $b = \lambda^{-\nu} \propto \xi_\infty$ where ξ_∞ is the correlation length for $L \to \infty$, gives

$$f_s(\lambda, L^{-1}) = |\lambda|^{2-\alpha} g_f(L^{-1}\xi_\infty) \tag{2.21}$$

where the Josephson relation from Eq. (2.19) was used. We can see the critical behaviour of $g_f(x)$ is governed by the ratio $x = \xi_\infty/L$. Looking at the two possible limits, when $L \gg \xi_\infty$ we get back the scaling of Eq. (2.18) (for $h = 0$) while the limit $L \ll \xi_\infty$ we should expect $g_f(x)$ to play some role in the critical behaviour. Putting this in another way, we should only expect finite size effects when $L \ll \xi_\infty$ because the correlation length cannot extend beyond the size of the system. What we end up with is the relation

$$\xi(\lambda = \lambda_{\max}) = L^\mu \,, \tag{2.22}$$

so where the correlation length in the thermodynamic limit diverges at $\lambda = 0$, for finite systems there is a maximum value at a potentially shifted critical point given by $\lambda_{\max}$. We can look at the shift in the critical point by examining the susceptibility when $b = L$

$$\chi_\lambda(\lambda, L^{-1}) \equiv -\frac{\partial^2 f_s}{\partial \lambda^2} = L^{-d} L^{2/\nu} G_f(L^{1/\nu}\lambda) \tag{2.23}$$

where $G_f(x) = -\frac{d^2 g_f(x)}{dx^2}$. This shows that if the new maximum is located at x_0, then its position scales as

$$\lambda_{\max} = x_0/L^{1/\nu} \propto L^{-1/\nu} \tag{2.24}$$

with respect to L. We also see the maximum value of χ_λ scales as

$$\chi_\lambda(0, L^{-1}) = L^{-d} L^{2/\nu} G_f(x_0) \propto L^{-d} L^{2/\nu} \quad \text{or} \quad \propto L^{\alpha/\nu} \,, \tag{2.25}$$

thus even in finite systems thermodynamic limit critical scaling exponents can be calculated. What is even more remarkable is we can also calculate the thermodynamic limit critical value of the driving parameter, Λ_c, by examining the correlation length when $b = L$

$$\begin{aligned} \xi(\lambda, L^{-1}) &= b\xi(b^{1/\nu}\lambda, bL^{-1}) \\ &= L g_\xi(L^{1/\nu}\lambda) \,. \end{aligned} \tag{2.26}$$

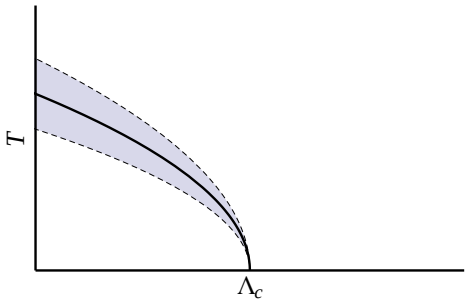

Figure 2.2: Temperature as a function of the parameter Λ. The black line marks T_c and the shaded region highlights the region where thermal fluctuations dominate over quantum fluctuations.

We know in the limiting case $L \to \infty$ and finite λ, $\xi(\lambda, 0) \propto |\lambda|^{-\nu}$, so $g_\xi(x) \to x^{-\nu}$ as $x \to \infty$, where $x = L^{1/\nu}\lambda$. In the other limiting case of finite L, but $\lambda \to 0$, $g_\xi(x) \to A$ where A is some constant, so in this limit the inverse of the scaled correlation length can be expanded around $\lambda = 0$ giving

$$\frac{L}{\xi(\lambda, L^{-1})} = A + B\lambda L^{1/\nu} \tag{2.27}$$

where B is also a constant. This shows that at the true critical point of $\lambda = 0$ the value of L/ξ for different system sizes is the same, namely A. This same technique can be used for other parameters we know less about.

2.1.5 Quantum phase transitions

In general, both classical and quantum PTs are characterized by the vanishing of an energy scale, ΔE, usually associated with the energy needed to cause excitations from the ground state. The vanishing of ΔE is accompanied by a divergence of the correlation length meaning there are fluctuations over all wavelengths of the system. In classical PTs the fluctuations are thermal because $\Delta E \to 0$ as $T \to T_c$. In quantum PTs $T = 0$, so thermal fluctuations are frozen out, however due to competition between non-commuting terms in a Hamiltonian which describe interactions between degrees of freedom there are still quantum fluctuations. The interactions give rise to interesting collective behaviour around a singularity at $\lambda = 0$, which, like in classical PTs, can be mathematically expressed in terms of scaling functions and scaling exponents.

In Fig. 2.2 the temperature is plotted as a function of Λ where Λ_c is marked on the $T = 0$ axis. The solid line is where the free energy is singular, i.e. where fluctuations cause divergences in correlations and susceptibilities, and so marks T_c for a given Λ. For $T > 0$ in the vicinity of the line the shaded region highlights where thermal

fluctuations are dominant over quantum fluctuations and the temperature is such that it satisfies the condition

$$k_B T \gg \hbar\omega_\star \tag{2.28}$$

where $\omega_\star$ is some typical frequency at which the important degrees of freedom oscillate. Essentially, this condition says that we only need to worry about thermal effects when the average thermal energy is much larger than the average energy spacing in the quantum spectrum. Although in reality there is always some nonzero temperature, experimentalists are able to achieve very low temperatures on the order of hundreds of picoKelvin (10^{-10}K), so it is safe to assume in many experiments quantum fluctuations dominate.

In this section we will make the switch from discussing singularities in the free energy to discussing singularities in the ground state of the Hamiltonian because as $T \to 0$ $f_s \to E_0$ where E_0 is the ground state energy. We will use what we have learned from the previous section, especially finite size scaling, and apply it to quantum PTs.

The quantum object we will mainly focus on is the fidelity susceptibility (FS), but before that we will discuss the concept of fidelity in quantum systems. The quantum fidelity is simply the overlap of an eigenstate of two Hamiltonians differing only by a small perturbation. The standard approach to fidelity assumes the Hamiltonian takes the form

$$H = H_0 + \lambda H_1 \tag{2.29}$$

where once again λ is the parameter tuned to drive the system through its PT. Usually the fidelity is taken with respect to the ground state and is generally written as

$$\mathcal{F}^2 = |\langle\psi_0(\lambda - \delta\lambda/2)|\psi_0(\lambda + \delta\lambda/2)\rangle|^2 \tag{2.30}$$

where $\delta\lambda \ll 1$ is the perturbation. Before diving into the details we can already make some qualitative judgements about how we expect $\mathcal{F}$ to behave near a PT. If both $\lambda - \delta\lambda/2$ and $\lambda + \delta\lambda/2$ are on the same side of the critical point (either above or below), then we expect $\mathcal{F} \approx 1$ because there is almost no difference between the two ground states. However, when both ground states straddle the critical point we expect a relatively large drop because both states have different symmetries and therefore are quite different.

The simplicity of Eq. (2.30) allows for its use without any previous knowledge of the system or the PT. However, there are some limitations in the effectiveness of $\mathcal{F}$, namely the parameter $\delta\lambda$ is supposed to be small, but beyond that its actual value in calculations is subjective. Also, Eq. (2.30) does not give information on the number or types of phases divided by the critical point; the only information it provides is that there is a critical point.

Next, we switch our focus to the FS and see how it overcomes the shortcomings of the fidelity. The FS emerges naturally from an expansion of the fidelity in $\delta\lambda$

$$\begin{aligned}\mathcal{F}^2 &= \langle\psi_0(\lambda-\delta\lambda/2)|\psi_0(\lambda+\delta\lambda/2)\rangle\langle\psi_0(\lambda+\delta\lambda/2)|\psi_0(\lambda-\delta\lambda/2)\rangle \\ &= 1+\frac{1}{2}\Bigg[\langle\psi_0(\lambda)|\frac{\partial^2\psi_0(\lambda)}{\partial\lambda^2}\rangle+\langle\frac{\partial^2\psi_0(\lambda)}{\partial\lambda^2}|\psi_0(\lambda)\rangle \\ &\quad +2\langle\psi_0(\lambda)|\frac{\partial\psi_0(\lambda)}{\partial\lambda}\rangle\langle\frac{\partial\psi_0(\lambda)}{\partial\lambda}|\psi_0(\lambda)\rangle\Bigg]\delta\lambda^2+\mathcal{O}(\delta\lambda^3)\,, \end{aligned} \tag{2.31}$$

where the linear term is zero, so the lowest order dependence on $\delta\lambda$ is captured by the quadratic term. This allows us to write

$$\mathcal{F}^2 \approx 1-\frac{\chi_F}{2}\delta\lambda^2 \tag{2.32}$$

where we have defined

$$\chi_F = -\left[\langle\psi_0(\lambda)|\frac{\partial^2\psi_0(\lambda)}{\partial\lambda^2}\rangle+\langle\frac{\partial^2\psi_0(\lambda)}{\partial\lambda^2}|\psi_0(\lambda)\rangle+2\langle\psi_0(\lambda)|\frac{\partial\psi_o(\lambda)}{\partial\lambda}\rangle\langle\frac{\partial\psi_o(\lambda)}{\partial\lambda}|\psi_0(\lambda)\rangle\right] \tag{2.33}$$

as the FS. For numerical analysis a more useful way to express χ_F is by expanding the shifted ground state using perturbation theory which allows us to write the fidelity to leading order as

$$\mathcal{F}^2 = 1-\delta\lambda^2\sum_{n\neq 0}\frac{|\langle\psi_n(\lambda)|H_1|\psi_0(\lambda)\rangle|^2}{\left[E_n(\lambda)-E_0(\lambda)\right]^2} \tag{2.34}$$

thus the FS takes the new form [59]

$$\chi_F = 2\sum_{n\neq 0}\frac{|\langle\psi_n(\lambda)|H_1|\psi_0(\lambda)\rangle|^2}{\left[E_n(\lambda)-E_0(\lambda)\right]^2} \tag{2.35}$$

which is useful when the eigenstates and eigenenergies can be calculated exactly numerically.

We can gain some intuition about how χ_F behaves near a PT by knowing the gap between the ground and excited states closes as $\Delta E = E_1 - E_0 \propto |\lambda|^{-\Delta}$ where Δ is once again the gap exponent [55]. Therefore, we should expect the FS to diverge at the critical point if the matrix element $\langle\psi_1(\lambda)|H_1|\psi_0(\lambda)\rangle \neq 0$. It will also help to compare the FS to other forms of susceptibility we have encountered. In classical PTs we have seen susceptibilities come from the second derivatives of the free energy with respect to the driving parameter. The quantum version of the second derivative with respect to some parameter is given in perturbation theory as

$$\frac{\partial^2 E_k(\lambda)}{\partial \lambda^2} = 2 \sum_{n \neq k} \frac{|\langle \psi_n(\lambda)|H_1|\psi_k(\lambda)\rangle|^2}{E_n(\lambda) - E_k(\lambda)} \,. \tag{2.36}$$

It is important to remember that in the above expression the states and energies are for the full Hamiltonian in Eq. (2.29), i.e. we are not expanding for small λ, but for small $\delta\lambda$. Setting $k = 0$ in Eq. (2.36) and comparing it with Eq. (2.35) we see the FS is more sensitive to the critical point due to the extra factor of $\frac{1}{E_n(\lambda)-E_0(\lambda)}$.

Using finite size scaling theory it has been shown that away from the critical point the FS scales as [59, 60]

$$\chi_F(\lambda) \propto L|\lambda|^{-2+d\nu} \tag{2.37}$$

and at the critical point it scales as

$$\chi_F(0) \propto L^{2/\nu} \,. \tag{2.38}$$

Both scalings we could have guessed from our previous calculations as Eqns. (2.37) and (2.38) can be calculated from Eqns. (2.23) and (2.25), respectively, using the Josephson scaling relation. Something not discussed yet is the fact that χ_F can scale differently on either side of the PT

$$\chi_F \propto |\lambda|^{-\alpha_\pm} \tag{2.39}$$

where $\alpha_\pm$ corresponds to the scaling exponent as $\lambda \to 0^\pm$. From Eq. (2.19) the different scalings can be achieved by having different ν and/or different d. What is more common, and what is the case in this thesis in paper II, is d changes. This doesn't mean the dimension of the system changes, but that some length scale or time scale changes its dependence on d.

2.2 Many-body quantum theory

Quantum many-body theory (QMBT) follows the regular quantum treatment of elevating classical objects to operators. In quantum mechanics (first quantization) *variables* like the energy and momentum are turned into operators

$$E \;\to\; \hat{H} = i\hbar\partial_t \tag{2.40}$$

$$p \;\to\; \hat{p} = -i\hbar\partial_x \tag{2.41}$$

and the Poisson bracket is replaced by the commutation relation between operators

$$[\hat{x}, \hat{p}] = i\hbar \,. \tag{2.42}$$

In QMBT (second quantization) fields, which are *functions*, are turned into operators

$$\Psi(x) \to \hat{\Psi}(x)\,. \tag{2.43}$$

Physically, the field operator acts on a many-body state to add a particle at or remove a particle from position x. QMBT gives us the tools to deal with a macroscopic number of particles and therefore allows us to look at collective behaviour like phase transitions. Because the field is now a quantum object it undergoes quantum fluctuations and so obeys a new commutation relation

$$\left[\hat{\Psi}(x), \hat{\Psi}(y)\right] = \delta(x-y) \tag{2.44}$$

which states that the order of field operators does not matter unless they are acting on the same location in space. However, the field operators need not only act on states described by spatial position. Like states in the first quantized theory, field operators can be represented in different bases

$$\text{first quantization}: \qquad \Psi(x) = \sum_n c_n \psi_n(x) \tag{2.45}$$

$$\text{second quantization}: \qquad \hat{\Psi}(x) = \sum_n \psi_n(x)\hat{a}_n \tag{2.46}$$

where the new operator, $\hat{a}_n$, now annihilates a particle in state n. Finally, where the normalization condition in first quantization, $\int \mathrm{d}x\,|\Psi(x)|^2 = 1$, leads to the conservation of probability, the equivalent quantity in QMBT leads to the number operator, $\int \mathrm{d}x\,\hat{\Psi}^\dagger(x)\hat{\Psi}(x) = \sum_n \hat{a}_n^\dagger \hat{a}_n = \hat{N}$.

In QMBT the Hamiltonian takes the general form

$$\hat{H} = \int \mathrm{d}x\,\hat{\Psi}^\dagger(x)\left[-\frac{\hbar^2}{2m}\nabla^2 + U(x)\right]\hat{\Psi}(x) + \frac{1}{2}\int \mathrm{d}x\mathrm{d}y\,\hat{\Psi}^\dagger(x)\hat{\Psi}^\dagger(y)V(x-y)\hat{\Psi}(x)\hat{\Psi}(y) \tag{2.47}$$

where $U(x)$ is an external potential and $V(x-y)$ is an interaction potential depending on the distance between particles. It should be noted we have kept only pairwise interactions where in general there could be interactions involving higher numbers of particles, but for our purposes it will suffice. Equation (2.47) highlights a major, but subtle difference between first and second quantization: in first quantized theory physical quantities are represented in terms of single particle wave functions, but now they have become operators acting on many-body states. This shift of focus from wave functions to operators makes the analysis of macroscopically large systems more accessible.

2.2.1 Bose-Einstein condensate

A system of N identical bosons (integer spin particles) confined to a trap at temperature T obeys Bose-Einstein statistics which means the expected number of particles in each state at thermal equilibrium is given by the Bose-Einstein distribution

$$\langle \hat{n}_i \rangle \equiv n_i(T) = f(E_i, T) = \left(\mathrm{e}^{\frac{E_i - \mu}{k_B T}} - 1 \right)^{-1} \tag{2.48}$$

where E_i is the energy of the i^{th} state, μ is the chemical potential and k_B is the Boltzmann constant. The chemical potential is defined by the conservation of the total number of particles $N = \sum_i n_i(\mu)$ where for a large enough particle number and low enough temperature it can be comparable to the ground state energy. This means it becomes increasingly less likely to populate states above the ground state as the temperature is lowered or more bosons are added. Therefore, there can be a critical temperature, T_c, based on the physical details of the system where any additional bosons can only be added to the ground state. The result is a macroscopic occupation of the ground state called a Bose-Einstein condensate (BEC).

To get an idea of the physics behind T_c one can think of each boson being a little wave. From de Broglie [1] we know the wavelength of each wave can be given in terms of its momentum $\lambda = \hbar/p$. For a very weakly interacting gas of bosons the energy can be approximated as being only kinetic and can be obtained using the equipartition theorem which states for each degree of freedom the average energy is $k_B T/2$. For a three-dimensional gas we have $E = \frac{p^2}{2m} = \frac{3}{2} k_B T$ which means $p = \sqrt{3 m k_B T}$ and putting this together with the wavelength gives $\lambda(T) = \sqrt{\frac{\hbar^2}{3 m k_B T}}$. Now, we expect the BEC to form when the wavelength becomes comparable to the particle separation distance and since the average distance between particles is $n^{-1/3}$, where n is the number density, the critical temperature is

$$T_c = \frac{\hbar^2 n^{2/3}}{3 m k_B} \,. \tag{2.49}$$

Although Eq. (2.49) isn't exact it is only off by an overall factor, so its derivation is a good way to illuminate some of the physics behind the formation of a BEC.

2.2.2 Bosonic Josephson junction

At sufficiently low temperatures a BEC can be utilized as a bosonic Josephson junction by confining it in a double well potential. The barrier between the two wells must be prepared in such a way as to provide a weak link between each well to allow tunneling. This is accomplished when the energy associated with the barrier height is below the chemical potential of the bosons in each well resulting in an exponentially

small energy difference between the ground and first excited states [61]. The bosons also interact and at temperatures where the interaction range is much smaller than the average distance between bosons it can be approximated by two-body contact collisions represented by the pseudopotential $V(x-y) = g\delta(x-y)$ where $g = \frac{4\pi\hbar^2 a}{m}$, where a is the s-wave scattering length and m is the mass of the boson. The scattering length can be tuned to produce attractive ($a < 0$) and repulsive ($a > 0$) interactions. In this thesis only repulsive interactions will be dealt with as attractive BECs tend to be unstable [62]. Also, symmetries in the Hamiltonian, which we will go over near the end of this section, show the many-body ground state for $a < 0$ depends on the parameters of the system in the same way the many-body highest state does for $a > 0$, so we can also get an idea of the attractive case from the repulsive one. In order to maintain the two-mode approximation the boson interactions must not be able to excite particles out of these modes. Under these conditions Eq. (2.47) becomes

$$\hat{H}_{\mathrm{B}} = \overbrace{\int \mathrm{d}x\, \hat{\Psi}^\dagger(x) \left[-\frac{\hbar^2}{2m}\nabla^2 + U(x)\right] \hat{\Psi}(x)}^{\hat{H}_0} + \overbrace{\frac{g}{2}\int \mathrm{d}x\, \hat{\Psi}^\dagger(x)\hat{\Psi}^\dagger(x)\hat{\Psi}(x)\hat{\Psi}(x)}^{\hat{H}_I} \tag{2.50}$$

where $\hat{\Psi}(x) = \psi_g(x)\hat{b}_g^\dagger + \psi_e(x)\hat{b}_e^\dagger$. The new many-body operators $\hat{b}_g^\dagger$ and $\hat{b}_e^\dagger$ ($\hat{b}_g$ and $\hat{b}_e$) create (annihilate) a boson in the ground and excited states, respectively, and obey the usual bosonic commutation relation $\left[\hat{b}_i, \hat{b}_j^\dagger\right] = \delta_{i,j}$. The wave functions ψ_g and ψ_e are the first quantized versions of the field operators. When the ground or excited states are macroscopically occupied their temporal evolution can be defined in terms of the nonlinear Schrödinger equation otherwise known as the Gross-Pitaevskii equation [63] (GPE)

$$i\hbar\frac{\partial\psi_i(x)}{\partial t} = \left[-\frac{\hbar^2}{2m}\nabla^2 + U(x) + gN_i|\psi_i(x)|^2\right]\psi_i(x) \tag{2.51}$$

where $i = g, e$ and N_i is the number of bosons in the i^{th} mode. We can see the interactions manifest themselves as an energy cost dependent on the density of bosons $n_i(x) = N_i|\psi_i(x)|^2$ where $\int_{-\infty}^{\infty}\mathrm{d}x\,|\psi_i(x)|^2 = 1$. The GPE is a mean-field description of the field operators.

Sometimes a more useful basis of operators is the left/right (l/r) basis which is given by symmetric and antisymmetric superpositions of the ground/excited basis

$$\hat{b}_r = (\hat{b}_g + \hat{b}_e)/\sqrt{2} \quad \hat{b}_l = (\hat{b}_g - \hat{b}_e)/\sqrt{2}\,. \tag{2.52}$$

Now the field operator is $\hat{\Psi}(x) = \psi_r(x)\hat{b}_r + \psi_l(x)\hat{b}_l$ where $\psi_r(x) = [\psi_g(x) + \psi_e(x)]/\sqrt{2}$ and $\psi_l(x) = [\psi_g(x) - \psi_e(x)]/\sqrt{2}$. Plugging in the field operator in the new basis into Eq. (2.50) gives

$$\hat{H}_0 = \epsilon_r \hat{N}_r + \epsilon_l \hat{N}_l - J(\hat{b}_r^\dagger \hat{b}_l + \hat{b}_l^\dagger \hat{b}_r) \tag{2.53}$$

for the first term where $\hat{N}_r = \hat{b}_r^\dagger \hat{b}_r$, $\hat{N}_l = \hat{b}_l^\dagger \hat{b}_l$ and

$$\epsilon_{l/r} = \int \mathrm{d}x\, \psi_{l/r}(x)^* \left[-\frac{\hbar^2}{2m}\nabla^2 + U(x) \right] \psi_{l/r}(x) \tag{2.54}$$

$$J = -\int \mathrm{d}x\, \psi_{l/r}(x)^* \left[-\frac{\hbar^2}{2m}\nabla^2 + U(x) \right] \psi_{r/l}(x)\,. \tag{2.55}$$

The interaction term is more complicated, so to make things simpler the fact that the single particle wave functions overlap very weakly inside the barrier is used [64]. Under this approximations only bosons in the same well can feel the interaction potential eliminating cross integrals, e.g. $\int \mathrm{d}x\, |\psi_l(x)|^2 |\psi_r(x)|^2$ and $\int \mathrm{d}x\, |\psi_l(x)|^2 \psi_l(x)^* \psi_r(x)$ and we end up with

$$\hat{H}_I = \frac{U_r}{2} \hat{b}_r^\dagger \hat{b}_r^\dagger \hat{b}_r \hat{b}_r + \frac{U_l}{2} \hat{b}_l^\dagger \hat{b}_l^\dagger \hat{b}_l \hat{b}_l \tag{2.56}$$

where

$$U_{l/r} = g \int \mathrm{d}x\, |\psi_{l/r}(x)|^4\,. \tag{2.57}$$

Using the definitions $\hat{n} \equiv (\hat{N}_r - \hat{N}_l)/2$ and $\hat{N} \equiv \hat{N}_r + \hat{N}_l$ and for equal intra-well interactions, $U = U_l = U_r$ (not to be confused with the external potential $U(x)$ in Eq. (2.50)) the Hamiltonian becomes

$$\hat{H}_\mathrm{B} = (\epsilon_r - \epsilon_l)\hat{n} - J(\hat{b}_r^\dagger \hat{b}_l + \hat{b}_l^\dagger \hat{b}_r) + U\hat{n}^2 + \frac{(\epsilon_r + \epsilon_l)}{2}\hat{N} + \frac{U}{2}\left(\frac{\hat{N}^2}{2} - \hat{N} \right). \tag{2.58}$$

Finally, defining $\Delta\epsilon \equiv \epsilon_r - \epsilon_l$ and $\hat{\alpha} \equiv (\hat{b}_r^\dagger \hat{b}_l + \hat{b}_l^\dagger \hat{b}_r)$ and neglecting the constant $\hat{N}$ terms we get [61, 64]

$$\hat{H}_\mathrm{B} = \Delta\epsilon \hat{n} - J\hat{\alpha} + U\hat{n}^2\,. \tag{2.59}$$

Physically, $\Delta\epsilon$ can be thought of as any bias in energy between the two wells and is referred to as the tilt. The parameter J gives the strength of tunneling between the two wells and is controlled by the height of the barrier between the two wells. U contains g, so it gives the interaction energy between bosons in the same well and is controlled by Feshbach resonance [11]. For the remainder of the thesis $\Delta\epsilon$ will be set to zero.

Due to the two-mode approximation if we assume the number of bosons is conserved in an experiment the Hilbert space is spanned by $N + 1$ states. This is a slow scaling

with N for a many-body system, especially when compared to lattice systems like the one-dimensional transverse field Ising model whose Hilbert space scales as 2^N. This means one can do exact numerical simulations of experimentally accessible regimes of $N = 10^3 - 10^4$ bosons on average desktop computers. Thus, we should take some time to examine the many-body states and operators in the l/r basis. Particle conservation, $[\hat{N}, \hat{H}_{\rm B}] = 0$, means the many-body states can be characterized by a single number $n = (N_r - N_l)/2$ where $N_{l/r}$ is the number of particles in the l/r wells. The states range from $|n = -N/2\rangle$ for all the bosons in the left well to $|n = N/2\rangle$ for all the bosons in the right well. In this basis the matrix elements of the $\hat{n}$ and $\hat{\alpha}$ operators are

$$\langle n'|\hat{n}|n\rangle = n\,\delta_{n',n} \tag{2.60}$$

$$\langle n'|\hat{\alpha}|n\rangle = \sqrt{\left(\frac{N}{2}-n\right)\left(\frac{N}{2}+n+1\right)}\,\delta_{n',n+1} + \sqrt{\left(\frac{N}{2}+n\right)\left(\frac{N}{2}-n+1\right)}\,\delta_{n',n-1}\,, \tag{2.61}$$

so $\hat{n}$ is diagonal as expected and $\hat{\alpha}$ is off-diagonal. Combining these into Eq. (2.59) gives the tri-diagonal Hamiltonian matrix

$$\begin{aligned}\hat{H}_{n',n} = {} & \left(Un^2 + \Delta\epsilon n\right)\delta_{n',n} \\ & -J\left[\sqrt{\left(\frac{N}{2}-n\right)\left(\frac{N}{2}+n+1\right)}\,\delta_{n',n+1} + \sqrt{\left(\frac{N}{2}+n\right)\left(\frac{N}{2}-n+1\right)}\delta_{n',n-1}\right]\end{aligned} \tag{2.62}$$

which allows for the computation of the energies of the system. In Fig. 2.3 the spectrum for $N = 100$ is plotted where it shows the spectrum can be broken up into three regions. The bottom third is roughly linear and corresponds to states of the Hamiltonian dominated by the $\hat{\alpha}$ term. The eigenstates of $\hat{\alpha}$ are coherent superpositions of the $|n\rangle$ states and closely resemble those of an harmonic oscillator where the agreement gets better for larger N. The top third is roughly quadratic and corresponds to states dominated by the $\hat{n}^2$ term. Due to this term being quadratic the states in this region come in nearly degenerate pairs which are symmetric and antisymmetric superpositions of the $|n\rangle$ states, i.e. $((|n\rangle + |-n\rangle)/\sqrt{2}$ and $(|n\rangle - |-n\rangle)\sqrt{2})$. In the middle region neither term dominates and its most notable feature is the energy boundary at JN called the separatrix. The spectrum around the separatrix is narrowly spaced resulting in a peak in the density of states.

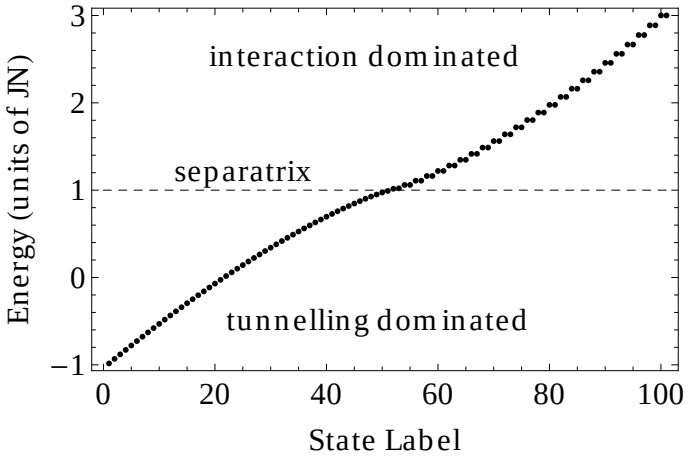

Figure 2.3: The energy spectrum of a BEC in a double well. The spectrum can be broken up into three regions: interaction dominated where the states come in nearly degenerate pairs, tunneling dominated where the states resemble those of an harmonic oscillator and a region where neither dominates which contains the separatrix which is the boundary between the other two regions at $E = JN$. The plot is for $N = 100$, $\Delta\epsilon = 0$ and $\Lambda = \frac{UN}{2J} \approx 5.8$.

2.2.3 Mean-field theory

Mean-field theory is the first step in further understanding the physics behind the three regions in Fig. 2.3. We have already seen mean-field theory in real space in the GPE, however we can have analogous equations in Fock space when we demote the creation/annihilation operators to complex numbers

$$\hat{b}_{l/r} \to \sqrt{N_{l/r}}\, \mathrm{e}^{i\phi_{l/r}}\,, \qquad \hat{b}^\dagger_{l/r} \to \sqrt{N_{l/r}}\, \mathrm{e}^{-i\phi_{l/r}}\,. \tag{2.63}$$

Substituting these into Eq. (2.59) gives [65]

$$H_{MF} \equiv \lim_{N\to\infty} \frac{\hat{H}_{\mathrm{B}}}{JN} = \Lambda \frac{z^2}{2} - \sqrt{1-z^2}\cos\phi \tag{2.64}$$

where $\phi = \phi_r - \phi_l$, $z = (N_r - N_l)/N$. We have also divided through by JN and defined a new parameter $\Lambda \equiv \frac{UN}{2J}$. If we identity z with the angular momentum and ϕ with the angular displacement, then H_{MF} is the Hamiltonian of a pendulum of mass Λ^{-1} with an angular momentum dependent length due to the square root factor. The mean-field theory reduces the many-body system to a nonlinear single particle and is therefore most accurate when all of the bosons are in a state which minimizes fluctuations of $\hat{n}$ and $\hat{\alpha}$. This occurs for the lowest (highest) energy many-body state where all of the bosons are in the single particle ground (excited) state. To calculate the energies we realize they correspond to stationary states of the pendulum where it is either pointing straight down or straight up. Therefore, using Hamilton's equations

$$\dot{z} = -\frac{\partial H_{MF}}{\partial \phi}\,, \qquad \dot{\phi} = \frac{\partial H_{MF}}{\partial z} \tag{2.65}$$

for $\dot{z} = \dot{\phi} = 0$ gives

$$\Lambda z + \frac{z\cos\phi}{\sqrt{1-z^2}} = 0\,, \qquad -\sqrt{1-z^2}\,\sin\phi = 0 \tag{2.66}$$

From the second equation we find $\phi = n\pi$ (ignoring the trivial $z = 1$ solution) where $n = 0, 1, 2, ...$ which for the first equation gives $z = 0$ for $\Lambda \leq 1$ and $z = 0$, $z_\pm = \pm\sqrt{1-\Lambda^{-2}}$ for $\Lambda > 1$. Plugging these into H_{MF} gives

$$\frac{E_\pm}{JN} = \begin{cases} \pm 1 & ,\ \Lambda \leq 1 \\ -1\,,\, \frac{\Lambda}{2}\left(1 + \frac{1}{\Lambda^2}\right) & ,\ \Lambda > 1 \end{cases} \tag{2.67}$$

where $\pm$ signifies the highest and lowest many-body energies, respectively. With the value of Λ from Fig. 2.3 we get $E_-/JN = -1$ and $E_+/JN \approx 3$ matching the minimum and maximum energies in the figure.

The mean-field theory can also be used to describe interesting phenomena in the dynamics of the BEC. For instance, self-trapping occurs for certain values of initial number difference where the BEC does not oscillate back and forth between the two wells when initially placed into one well, but gets trapped in that one well. In the pendulum analogy this behaviour is analogous to oscillations about the downward vertical position and the self-trapping is analogous to the pendulum having a large enough angular momentum to make a full rotation. Barring any friction the pendulum will keep swinging around indefinitely with some nonzero angular momentum. The critical value of the number difference, z_c can be calculated from the condition that the total energy must be greater than the separatrix

$$\Lambda\frac{z_0^2}{2} - \sqrt{1-z_0^2}\,\cos\phi_0 > 1 \tag{2.68}$$

where z_0 and ϕ_0 are the initial number and phase difference between the two wells. For $\phi_0 = 0$ the critical number difference is $|z_c| = \frac{2\sqrt{\Lambda-1}}{\Lambda}$, so it can only occur for $\Lambda > 1$.

As previously mentioned the mean-field theory is accurate when the phase and number difference between two wells are well defined. However, since they are conjugate variables this puts constraints on what values of Λ accomplish this because of the uncertainty principle. To help define the region of validity we look at the ground state many-body number difference fluctuations and the coherence, α [61], given by

$$\Delta n^2 = \langle \hat{n}^2 \rangle - \langle \hat{n} \rangle^2\,, \qquad \alpha = \langle \hat{\alpha} \rangle\,. \tag{2.69}$$

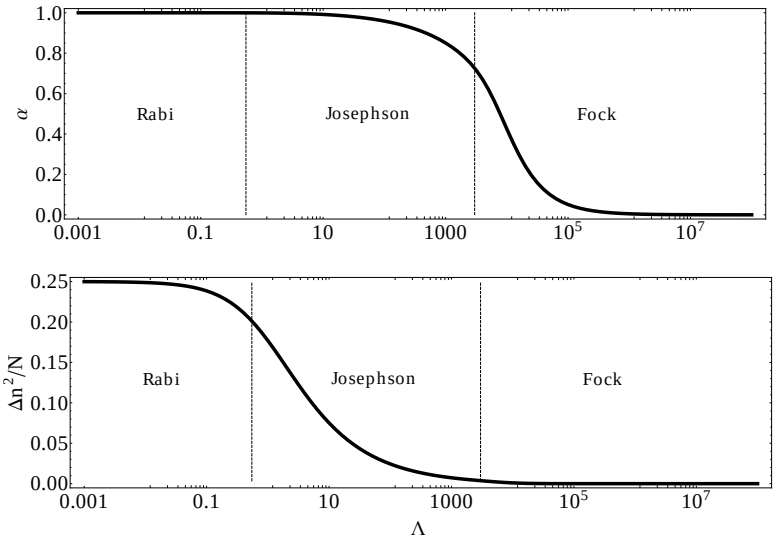

Figure 2.4: Coherence, α, and boson number difference fluctuations, Δn^2 as a function of Λ. In each image three regimes are highlighted: (1) Rabi regime where the coherence is high and the number difference fluctuations are large, (2) Josephson regime where the coherence is high and the number difference fluctuations are small and (3) Fock regime where the coherence is low and the number difference fluctuations are small. Each image is for $N = 100$.

Low Δn^2 means there is a well defined number difference while high α means there is a well defined phase difference. Figure 2.4 shows these quantities for different values of Λ for $N = 100$. It is clear that increasing Λ decreases both the coherence and number difference fluctuations, however they begin to decrease substantially at different values. For Δn^2 the decrease starts at $\Lambda \approx 1/4$ and for α it starts at $\Lambda \approx N^2/4$. From this result three regimes can be identified [66]: (1) the coherence is high and the number difference fluctuations are large, (2) coherence is high and the number difference fluctuations are small and (3) the coherence is low and the number difference fluctuations are small. These regimes are defined by their range of Λ

- Rabi regime: $\Lambda \ll 1/4$,
- Josephson regime: $1/4 \ll \Lambda \ll N^2/4$,
- Fock regime: $\Lambda \gg N^2/4$.

The Rabi regime is dominated by the tunnelling term and so the eigenstates of $\hat{H}$ are close to being coherent superpositions of Fock states. The Josephson regime is the ideal regime for mean-field theory and corresponds to neither term dominating. The Fock regime is dominated by the interactions term and therefore the Fock states $|n\rangle$ are close to the eigenstates of $\hat{H}$. Throughout this thesis the value of Λ is in the range $10^{-1} \leq \Lambda \leq 10^{1}$, so mean-field theory is often used as a starting point for analysis.

2.2.4 Beyond mean-field theory

Beyond the mean-field theory the energies and wave functions of the lowest lying states can be approximated by re-quantizing the mean-field Hamiltonian. This is done by promoting z and ϕ to operators obeying the commutation relation $[\hat{\phi}, \hat{z}] = 2i/N$, so $1/N$ plays the role of $\hbar$. These steps represent a semiclassical description of the system where aspects of both the mean-field (continuous z and ϕ) and first quantized (z and ϕ are operators) theories are taken into account. For $\Lambda < 1$ the low-lying states can be approximated as harmonic oscillator states by expanding the semiclassical Hamiltonian about $z = \phi = 0$

$$\hat{H}_{\mathrm{SC}} \approx (\Lambda + 1)\frac{\hat{z}^2}{2} + \frac{\hat{\phi}^2}{2} \tag{2.70}$$

which gives the low lying energy spacing seen in Fig. 2.3 as

$$\omega_{\mathrm{pl}} = 2J\sqrt{\Lambda + 1} \tag{2.71}$$

also known as the plasma frequency. Equation (2.70) also gives the variances in z and ϕ

$$\Delta z^2 = \frac{1}{N\sqrt{\Lambda + 1}}, \qquad \Delta\phi^2 = \frac{\sqrt{\Lambda + 1}}{N} \tag{2.72}$$

which shows the mean field approximation gets better as N increases since the uncertainty relation is $\Delta z \Delta\phi \geq N^{-1}$ which we could have gotten from the Robertson relation $\Delta z \Delta\phi \geq \frac{1}{2}|\langle[\hat{\phi}, \hat{z}]\rangle|$ and the commutation relation.

2.3 Adding an impurity

In this section we explore the new phenomena which arise from the addition of a single impurity boson into the bosonic Josephson junction. In general, the impurity can be a different atomic species than the bosons in the BEC or it can be the same species, but in a different internal state. The same two-mode approximation as the BEC applies to the impurity, so its field operator is $\hat{\Phi}(x) = \phi_r(x)\hat{a}_r + \phi_l(x)\hat{a}_l$ where $\hat{a}^\dagger_{l/r}$ ($\hat{a}_{l/r}$) create (annihilate) the impurity in the left/right well and obey the usual boson commutation relation $[\hat{a}_i, \hat{a}^\dagger_j] = \delta_{i,j}$. The impurity interacts with the bosons the same way the bosons interact amongst themselves, that is through direct contact s-wave scattering, so $V_{\mathrm{B,i}}(x - y) = g_{\mathrm{B,i}}\delta(x - y)$ where $g_{\mathrm{B,i}} = \frac{4\pi\hbar^2 a_{\mathrm{B,i}}}{m}$. However, the impurity has no self-interaction. The subscript 'B,i' has been used to show the BEC-impurity interactions can be tuned separately from the boson-boson interactions. The impurity can also tunnel through the barrier and experiences a tilt and we assume

these energies can be tuned independently as well. Therefore, the Hamiltonian for the impurity plus BEC-impurity interactions takes the form

$$\hat{H}_{\rm i} + \hat{H}_{\rm B,i} = \Delta\epsilon^a \hat{m} - J^a \hat{\beta} + 2W\hat{n}\hat{m} \tag{2.73}$$

where the constant terms have been neglected. The operators $\hat{m} = (\hat{a}_r^\dagger \hat{a}_r - \hat{a}_l^\dagger \hat{a}_l)/2$ and $\hat{\beta} = \hat{a}_r^\dagger \hat{a}_l + \hat{a}_l^\dagger \hat{a}_r$ have been introduced analogously to the BEC operators $\hat{n}$ and $\hat{\alpha}$, respectively. Also, the three new energies are

$$\begin{aligned} W &= \frac{g_{\rm B,i}}{2} \int {\rm d}x |\psi_{l/r}(x)|^2 |\phi_{l/r}(x)|^2 & (2.74)\\ J^a &= \int {\rm d}x \phi_{l/r}(x)^* \left[-\frac{\hbar^2}{2m}\nabla^2 + U(x) \right] \phi_{r/l}(x) & (2.75)\\ \Delta\epsilon^a &= \epsilon_r^a - \epsilon_l^a & (2.76) \end{aligned}$$

where

$$\epsilon_{l/r}^a = \int {\rm d}x \phi_{l/r}(x)^* \left[-\frac{\hbar^2}{2m}\nabla^2 + U(x) \right] \phi_{l/r}(x)\,. \tag{2.77}$$

Here, $W > 0$ is the impurity-BEC intrawell interaction energy, $J^a > 0$ is the impurity tunnelling energy and $\Delta\epsilon^a$ is the impurity tilt. The full BEC-impurity Hamiltonian is

$$\begin{aligned} \hat{H}_{\rm tot} &= \hat{H}_{\rm B} + \hat{H}_{\rm i} + \hat{H}_{\rm B,i} \\ &= U\hat{n}^2 - J\hat{\alpha} - J^a\hat{\beta} + 2W\hat{n}\hat{m} + \Delta\epsilon\hat{n} + \Delta\epsilon^a\hat{m} & (2.78) \end{aligned}$$

where the reader is reminded $\Delta\epsilon = \Delta\epsilon^a = 0$ for the remainder of the thesis unless specified otherwise.

With the addition of the impurity the Hilbert space of the entire system is enlarged. Since the impurity is distinguishable from the bosons in the BEC the Hilbert space doubles in size because it becomes a product of the two Hilbert spaces $(1+1)\times(N+1) = 2(N+1)$. Thus, even with the addition of the impurity simulations can be done of experimentally large BECs. The Fock states of the system are now product states of the impurity and BEC bases, $|n\rangle|m\rangle = |n,m\rangle$. This changes the matrix elements slightly from the form of Eq. (2.62) to

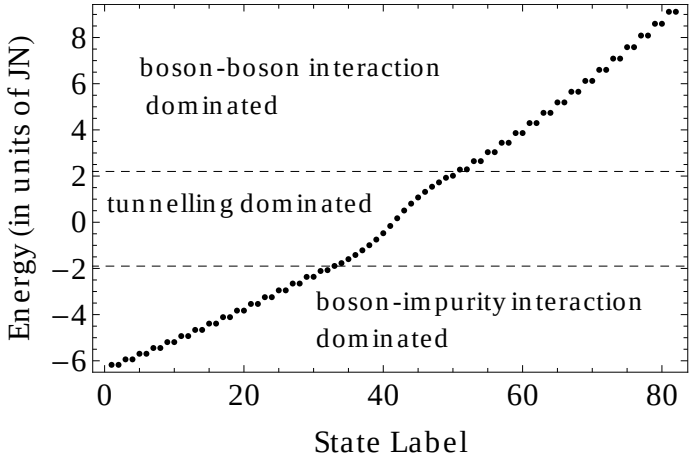

Figure 2.5: The energy spectrum of an impurity in a BEC in a double well. The top two regions are similar to those of the same system without the impurity shown in Fig. 2.3, but the bottom region is different and is dominated by boson-impurity interactions. The quasidegenerate pairs in this region are due to the $(n, -m) \to (-n, m)$ in the $2W\hat{n}\hat{m}$ term in the Hamiltonian. The parameters used are $N = 40$, $U/J = 6$, $J^a/J = 1$ and $W/J = 15$. These parameters were specifically chosen to highlight the effect of the boson-impurity interaction term.

$$\begin{aligned}
&\langle m', n'|\hat{H}_{\rm tot}|n, m\rangle = \left(Un^2 + 2Wmn\right)\delta_{n',n}\delta_{m',m} \\
&-J\left[\sqrt{\left(\frac{N}{2}-n\right)\left(\frac{N}{2}+n+1\right)}\,\delta_{n',n+1} + \sqrt{\left(\frac{N}{2}+n\right)\left(\frac{N}{2}-n+1\right)}\,\delta_{n',n-1}\right]\delta_{m',m} \\
&-J^a\left[\sqrt{\left(\frac{1}{2}-m\right)\left(\frac{1}{2}+m+1\right)}\,\delta_{m',m+1} + \sqrt{\left(\frac{1}{2}+m\right)\left(\frac{1}{2}-m+1\right)}\,\delta_{m',m-1}\right]\delta_{n',n}
\end{aligned} \tag{2.79}$$

.

The spectrum for $N = 40$ is shown in Fig. 2.5, but should not be regarded too seriously as it can look quite different depending on the parameter choice. Specific parameters were chosen to highlight the three major regions where as was the case without the impurity we have the boson-boson interaction dominated and tunnelling dominated regions. The bottom region is different as the states come in quasidegenerate pairs. The degeneracy can be explained by looking at the boson-impurity interaction term, $2W\hat{n}\hat{m}$, where the pairs are due to the symmetry $(n, -m) \to (-n, m)$. This symmetry is important because it is what will be broken in the PT we will be discussing starting in Sec. 2.3.3. The linearity comes from the fact that the term is linear in $\hat{n}$.

2.3.1 Mean-field theory with impurity

Since the mean-field approximation treats a many-body system like a single particle it is exact for a single impurity. This is made clear by looking at a general quantum state for the impurity, $|\text{imp}\rangle = a_r|r\rangle + a_l|l\rangle$, where a_r and a_l are the probability amplitudes for the impurity being in the right and left wells, respectively. The constraints that we only can measure phase differences between the two states and probability conservation, $|a_r|^2 + |a_l|^2 = 1$, means that any impurity state is specified by only two numbers. The transformation from creation and annihilation operators to complex numbers

$$\hat{a}_{l/r} \to \sqrt{M_{l/r}}\mathrm{e}^{i\alpha_{l/r}} \qquad \hat{a}^\dagger_{l/r} \to \sqrt{M_{l/r}}\mathrm{e}^{-i\alpha_{l/r}} \tag{2.80}$$

together with the fact we can only measure $\alpha = \alpha_r - \alpha_l$ and particle conservation means the mean-field theory specifies the impurity state with two numbers. With Eq. (2.63) the mean-field Hamiltonian is

$$H_{MF} = \lim_{N\to\infty} \frac{\hat{H}_{\text{tot}}}{JN} = \Lambda\frac{z^2}{2} - \sqrt{1-z^2}\cos\phi - \Gamma^a\sqrt{1-y^2}\cos\alpha + \gamma yz/2 \tag{2.81}$$

where the new parameters are $\Gamma^a = J^a/JN$ and $\gamma = W/J$ and the new variables are $y = M_r - M_l$ and α. It should be noted that the assumption $\Gamma^a \neq 0$ as $N \to \infty$ is an important one, but it must be the case if the impurity hopping is to have any affect on the system as a whole; something we will find is important for the criticality of the system near a PT. We could find the mean-field ground and excited state energies by finding the stationary solutions to the equations of motion with the additional Hamilton's equations $\dot{\alpha} = \frac{\partial H_{MF}}{\partial y}$ and $\dot{y} = -\frac{\partial H_{MF}}{\partial \alpha}$ and the main result would be that there is a critical value of γ, γ_c, that marks the location of a second order phase transition. Instead, the semiclassical route will be taken to get this result because the derivation is simpler and it will supplement results in papers I and II in chapter 3.

2.3.2 Beyond mean-field: Schwinger representation, Holstein-Primakoff transformation

Schwinger representation

In this section we wish to find the ground state energy and critical value of the BEC-impurity interaction energy. To do this we use the fact that since there are two single particle modes this means the bosons in the BEC to be represented as a single particle with spin using the Schwinger's oscillator model of angular momentum [67]. For N bosons the total spin is $j = N/2$ with z-component $m_z = n$. Thus, in the spin operator representation we have

$$\hat{S}_z = \frac{1}{2}(\hat{b}_r^\dagger \hat{b}_r - \hat{b}_l^\dagger \hat{b}_l)\,, \qquad \hat{S}_x = \frac{1}{2}(\hat{b}_r^\dagger \hat{b}_l + \hat{b}_l^\dagger \hat{b}_r)\,, \qquad \hat{S}_y = \frac{i}{2}(\hat{b}_l^\dagger \hat{b}_r - \hat{b}_r^\dagger \hat{b}_l) \tag{2.82}$$

with the commutation relation $[\hat{S}_i, \hat{S}_j] = i\epsilon_{ijk}\hat{S}_k$. This means the number difference Fock states can be mapped to spin-j states, $|N/2, n\rangle \leftrightarrow |j, m_z\rangle$. The impurity can similarly be represented as a spin-1/2 particle with $\hat{S}_i \to \hat{\sigma}_i^a$ ($\hat{\sigma}_i^a$ is a Pauli spin matrix) giving the Hamiltonian

$$\hat{H}_{\rm tot} = U\hat{S}_z^2 - 2J\hat{S}_x - 2J^a\hat{\sigma}_x^a + 2W\hat{S}_z\hat{\sigma}_z^a\,. \tag{2.83}$$

Since the ground state of Eq. (2.83) has all of the bosons and the impurity in their single particle ground states it is better to work in the ground/excited state basis. In the spin representation the rotation of $\hat{H}$ by $\pi/2$ about the $\hat{S}_y$ axis is the same as the transformations given in Eq. (2.52). Under the rotation the spin operators transform as $\hat{S}_z \to \hat{S}_x$, $\hat{S}_x \to -\hat{S}_z$ and the impurity Pauli matrices transform in the same way giving

$$\hat{H}_{\rm tot} \to e^{i\pi\hat{S}_y/2}\hat{H}_{\rm tot}e^{-i\pi\hat{S}_y/2} = U\hat{S}_x^2 + 2J\hat{S}_z + 2J^a\hat{\sigma}_z^a + 2W\hat{S}_x\hat{\sigma}_x^a\,. \tag{2.84}$$

Holstein-Primakoff transformation

In the Holstein-Primakoff transformation (HPT) the ground state of $\hat{H}_{\rm tot}$ is taken to be the vacuum state for a set of boson operators where each subsequent excitation is the addition of one of these bosons to the vacuum. In the ground/excited state basis the ground state is $|GS\rangle = |-N/2\rangle$, so in the HPT we have

$$|-N/2+n\rangle \to \frac{1}{\sqrt{n!}}\left(\hat{f}^\dagger\right)^n|0\rangle\,. \tag{2.85}$$

Each additional boson increases the spin by unity, so to maintain the commutation relation amongst the spin operators the spin raising and lowering operators are

$$\hat{S}_- = \sqrt{N}\sqrt{1-\frac{\hat{f}^\dagger\hat{f}}{N}}\,\hat{f}\,, \qquad \hat{S}_+ = \sqrt{N}\hat{f}^\dagger\sqrt{1-\frac{\hat{f}^\dagger\hat{f}}{N}} \tag{2.86}$$

where $\hat{S}_x = \frac{1}{2}(\hat{S}_+ + \hat{S}_-)$ and $\hat{S}_y = \frac{i}{2}(\hat{S}_- - \hat{S}_+)$ and $\hat{S}_z = \hat{f}^\dagger\hat{f} - N/2$. To proceed one realizes that the low lying states the square root in Eq. (2.86) can be set to unity, so $\hat{S}_- \approx \sqrt{N}\hat{f}$ and $\hat{S}_+ \approx \sqrt{N}\hat{f}^\dagger$. The approximations made to the BEC spin operators are exact for the impurity spin operators, so $\hat{\sigma}_+^a = \hat{g}^\dagger$ and $\hat{\sigma}_-^a = \hat{g}$. Substituting these into Eq. (2.84) gives

$$\hat{H}_{\rm tot} \approx \hat{H}_{\rm SC} = \frac{UN}{4}\left(\hat{f}^\dagger + \hat{f}\right)^2 + 2J\left(\hat{f}^\dagger\hat{f} - \frac{N}{2}\right) + 2J^a\left(\hat{g}^\dagger\hat{g} - \frac{1}{2}\right) + \frac{W\sqrt{N}}{2}\left(\hat{f}^\dagger + \hat{f}\right)\left(\hat{g}^\dagger + \hat{g}\right) \tag{2.87}$$

which is a Hamiltonian for two coupled harmonic oscillators. To make this comparison clearer the transformation $\hat{f} \to \sqrt{N}\hat{f}$ is made, then $\hat{f} \equiv \frac{1}{2}(2\hat{x} - i\hat{p}_x)$ and $\hat{g} \equiv \frac{1}{2\sqrt{\Gamma^a}}(2\Gamma^a\hat{y} - i\hat{p}_y)$ giving

$$\frac{\hat{H}_{\rm SC}}{JN} \approx \frac{\hat{p}_x^2}{2} + \frac{\hat{p}_y^2}{2} + 2\Gamma^{a^2}\hat{y}^2 + 2(1+\Lambda)\hat{x}^2 + 2\gamma\sqrt{\Gamma^a}\,\hat{x}\hat{y} + E_0 \tag{2.88}$$

where $E_0 = -(\Gamma^a + 1)$ and the definitions of the new parameters are given in Sec. 2.3.1. To uncouple the harmonic oscillators we make another transformation

$$\hat{x} = \hat{q}_1\cos\theta^* + \hat{q}_2\sin\theta^*\,, \qquad \hat{y} = \hat{q}_2\cos\theta^* - \hat{q}_1\sin\theta^* \tag{2.89}$$

where the angle satisfies the relation

$$\tan 2\theta^* = \left(\frac{\gamma\sqrt{\Gamma^a}}{\Gamma^{a^2} - 1 - \Lambda}\right)\,. \tag{2.90}$$

The resulting Hamiltonian is two uncoupled harmonic oscillators

$$\hat{H}_{\rm SC} = \frac{1}{2}\left(\hat{p}_1^2 + \hat{p}_2^2 + \epsilon_+^2\hat{q}_1^2 + \epsilon_-^2\hat{q}_2^2\right) + E_0 \tag{2.91}$$

with frequencies $\epsilon_\pm$ given by

$$\epsilon_\pm = \sqrt{(1 + \Gamma^{a^2} + \Lambda) \pm \sqrt{(1 - \Gamma^{a^2})^2 + \Gamma^a\gamma^2 + 2\Lambda(1 - \Gamma^{a^2} + \Lambda/2)}}\,. \tag{2.92}$$

2.3.3 Hints of a quantum phase transition

At the beginning of Sec. 2.1.5 we mentioned the vanishing of some gap energy as some parameter approaches its critical value signalled the occurrence of a quantum PT. In Eq. (2.92) ϵ_- vanishes as

$$\epsilon_- \sim \sqrt{\frac{\gamma_c\Gamma^a}{1 + \Gamma^{a^2} + \Lambda}}\,(\gamma_c - \gamma)^{1/2}\,, \qquad \text{as} \quad \gamma \to \gamma_c^- \tag{2.93}$$

where

$$\gamma_c = 2\sqrt{\Gamma^a}\sqrt{\Lambda + 1}\,. \tag{2.94}$$

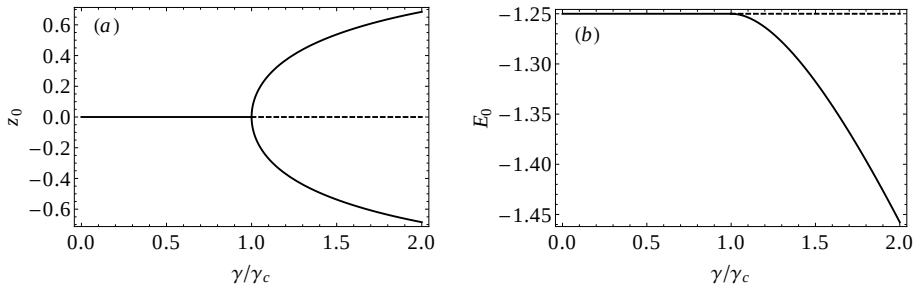

Figure 2.6: Image (a) shows the order parameter z_0, which is the ground state number difference between the right and left wells, vs. the scaled BEC-impurity interaction energy. A pitchfork bifurcation occurs at $\gamma = \gamma_c$ signalling a PT. Due to fluctuations the system will evolve to one of the two new states spontaneously breaking $\mathbb{Z}_2$ symmetry. Image (b) shows the ground state energy vs. the scaled BEC-impurity interaction energy. Both images should be compared to the corresponding images in Fig. 2.1 for the general Landau theory.

We can see in Eq. (2.94) that the closing of the gap does not depend on the boson-boson interactions, so to simplify the analysis we can set $\Lambda = 0$ leaving only the boson-impurity interactions. This lets us move ahead with finding the stationary solutions to the mean-field equations of motion from the Hamiltonian in Eq. (2.81). What we find is

$$\{y_0, z_0\} = \begin{cases} \{0, 0\} & , \ \gamma \leq \gamma_c \\ \left\{ \pm\frac{1}{\gamma}\sqrt{\frac{\gamma^4-\gamma_c^4}{\gamma^2+\gamma_c^4/4}}, \mp\frac{1}{\gamma}\sqrt{\frac{\gamma^4-\gamma_c^4}{\gamma^2+4}} \right\} & , \ \gamma > \gamma_c \end{cases}, \tag{2.95}$$

so when $\gamma \leq \gamma_c$ (normal phase) there are equal amounts of the BEC and impurity in each well. However, when $\gamma > \gamma_c$ (symmetry broken phase) the impurity expels some of the BEC particles from the well it has chosen due to the repulsive interaction energy. The impurity will expel more and more bosons as γ increases further. The well the impurity chooses is determined randomly by quantum fluctuations and results in the breaking of the $\mathbb{Z}_2$ symmetry of the normal phase. Equation (2.95) for z is plotted in Fig. 2.6 along with the ground state energy for different values of the boson-impurity interaction γ.

2.3.4 $T > 0$ phase transition

Given that every experiment takes place at finite temperatures it is necessary to confirm the quantum PT found in the previous section survives. The boson-boson interactions will once again be set to zero, so in the unscaled parameters the critical BEC-impurity interaction energy is $\gamma_c = 2\sqrt{\Gamma^a}$. The partition function is given by the trace over the degrees of freedom of the Boltzmann factor

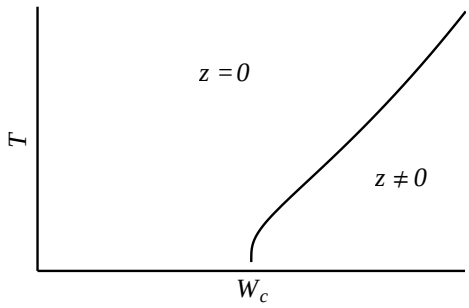

Figure 2.7: The critical temperature, T_c, given in Eq. (2.106) as a function of W. Above T_c the phase has an equal number of bosons in each well. Below T_c there is a build-up of bosons in one well over the other.

$$Z = \mathrm{Tr} e^{-\beta \hat{H}}, \qquad \beta = \frac{1}{k_B T} \tag{2.96}$$

where k_B is the Boltzmann constant. To evaluate the trace, Eq. (2.83) is written in terms of the elementary Pauli spin matrices

$$\frac{\hat{H}}{J} = -\sum_i^N \left(\hat{\sigma}_x^i + \Gamma^a \hat{\sigma}_x^a - \frac{\gamma}{2} \hat{\sigma}_z^i \hat{\sigma}_z^a \right) \tag{2.97}$$

where $\hat{S}_z = \sum_i^N \hat{\sigma}_z^i$ and $\hat{S}_x = \sum_i^N \hat{\sigma}_x^i$ and we have used the scaled parameters defined in 2.3.1. Before continuing we make an approximation to Eq. (2.97) by replacing the impurity operators with their coherent state expectation values [68]

$$\begin{aligned} \langle \theta, \phi | \hat{\sigma}_z^a | \phi, \theta \rangle &= -\cos\theta \\ \langle \theta, \phi | \hat{\sigma}_x^a | \phi, \theta \rangle &= \sin\theta \cos\phi \,. \end{aligned} \tag{2.98}$$

where the the minus sign in front of the cosine is a convention, so $m = -1$ corresponds to $\theta = 0$ on the Bloch sphere. The approximation does not have much justification and is mainly used so some analytic results can be computed. However, the approximation is expected to become more accurate as the number of particles and/or the temperature increases, so thermal fluctuations dominate over the quantum fluctuations. Since the bosons in the BEC don't interact we can calculate the partition function for a single boson and use the fact that $Z_N = (Z_1)^N$. The Hamiltonian for a single boson is

$$\begin{aligned} \hat{h} &= -\hat{\sigma}_x - \Gamma^a \sin\theta\cos\phi - \frac{\gamma}{2}\hat{\sigma}_z \cos\theta \\ &= \begin{pmatrix} -\Gamma^a \sin\theta\cos\phi - \frac{\gamma}{2}\cos\theta & -1 \\ -1 & -\Gamma^a \sin\theta\cos\phi + \frac{\gamma}{2}\cos\theta \end{pmatrix} \end{aligned} \tag{2.99}$$

which has eigenvalues

$$\mu_{\pm} = -\Gamma^a \sin\theta\cos\phi \pm \sqrt{1+\left(\frac{\gamma\cos\theta}{2}\right)^2}. \tag{2.100}$$

Thus, for the BEC the partition function is

$$\begin{aligned} Z_N = \left(\mathrm{Tr} e^{-\beta\hat{h}}\right)^N &= \left(\sum_{s=\pm1}\langle s|e^{-\beta\hat{h}}|s\rangle\right)^N = \left(e^{-\beta\mu_+}+e^{-\beta\mu_-}\right)^N \\ &= 2^N e^{\beta N\Gamma^a\sin\theta\cos\phi}\cosh^N\left[\beta\sqrt{1+\left(\frac{\gamma\cos\theta}{2}\right)^2}\right] \end{aligned} \tag{2.101}$$

The trace over the impurity degrees of freedom now becomes the integral over a sphere $\mathrm{Tr}_a \to \int_{-1}^{1}\int_0^{2\pi} \mathrm{d}(\cos\theta)d\phi$ [69, 70], so the full partition function becomes

$$Z = \frac{2^N}{2\pi}\int_{-1}^{1}\int_0^{2\pi} \mathrm{d}\cos\theta d\phi e^{\beta N\Gamma^a\sin\theta\cos\phi}\cosh^N\left[\beta\sqrt{1+\left(\frac{\gamma}{2}\cos\theta\right)^2}\right]. \tag{2.102}$$

Using the identity $\int_0^{2\pi}\mathrm{d}\phi e^{x\cos\phi} = 2\pi I_0(x)$, where I_0 is the Bessel function of the first kind, and substituting in $x = \cos\theta$ gives the final form of the partition function

$$Z = 2^N\int_{-1}^{1}\mathrm{d}x e^{\Omega(x)} \tag{2.103}$$

where

$$\Omega(x) = \ln\left\{I_0(\beta N\Gamma^a\sqrt{1-x^2})\cosh^N\left[\beta\sqrt{1+\left(\frac{\gamma}{2}x\right)^2}\right]\right\}. \tag{2.104}$$

For $N \gg 1$ the major contributor to the integral is at x_* which satisfies $\Omega'(x_*) = 0$. This condition gives the transcendental equation

$$\left(\frac{\gamma_c}{\gamma}\right)^2\eta(x_*) = \sqrt{1-x_*^2}\tanh\left[\beta\eta(x_*)\right] \tag{2.105}$$

where $\eta(x) = \sqrt{1+\left(\frac{\gamma}{2}x\right)^2}$ and we have replaced the Bessel function with its asymptotic approximation, $I_i(x) \sim \frac{e^x}{2\pi x}$ as $x \to \infty$. Looking at Eq. (2.105) we see the maximum the RHS can be is unity, while the minimum of the LHS is $(\gamma_c/\gamma)^2$. Therefore, we expect the number of solutions to change at $\gamma = \gamma_c$ which confirms the $T = 0$ result from the previous section. When $\gamma > \gamma_c$ the number of solutions to Eq. (2.105)

also depends on the temperature. The critical temperature at which the number of solutions changes can be found by setting $x_* = 0$ giving

$$\frac{k_B T_c}{J} = \operatorname{arctanh}\left[\left(\frac{\gamma_c}{\gamma}\right)^2\right]^{-1} . \tag{2.106}$$

Here, T_c marks the point which separates the $z = 0$ ($T \geq T_c$) and $z \neq 0$ ($T < T_c$) phases discussed in the previous section, thus the PT does survive. Note that the broken symmetry phase occurs at a lower temperature than the normal phase agreeing with the general statement made at the beginning of Sec. 2.1 regarding the more ordered phase occurring at lower temperature. Equation (2.106) is plotted in Fig. 2.7 which should be compared to Fig. 2.2 showing the general crossover behaviour between thermal and quantum PTs. Equation (2.106) is of the same form as the Dicke model [70] which means we may find differences between the two systems if we don't take the asymptotic limit of the Bessel functions.

2.4 Catastrophe theory

2.4.1 Splitting lemma

The mathematics behind derivations in CT is beyond the scope of this thesis, however the beauty of CT is the simplicity of its results. To gain an idea about the basis of the results as well as when they are useful it is important to give them some context with respect to similar theories. CT can be viewed as the third and latest major step in the identification of local forms of functions. The first step is the implicit function theorem which depends on first derivatives of the function; the second is the Morse lemma which depends on second derivatives of functions; and the third is the Thom's splitting lemma which depends on higher than second order derivatives. A basic outline of the three steps is given below [45]

Implicit Function Theorem. Given a function $f(\mathbf{x})$, of a set of state variables, $\mathbf{x} = (\mathbf{s}, \mathbf{y})$ where $\mathbf{s} = (s_1, s_2, ...s_p)$ and $\mathbf{y} = (y_1, y_2, ...y_q)$, the equation

$$f(\mathbf{x}) = 0 \tag{2.107}$$

is a graph of a function $\mathbf{y} = \mathbf{y}(\mathbf{s})$ provided locally at some point, $\mathbf{s}_\star$, $\mathbf{y}$ can be linearized around that point.

Morse Lemma. For simplicity we will take $q = 1$, so $\mathbf{y} = y$ is a scalar. If the linear approximation does not work, i.e. $\nabla y|_{\mathbf{s}_\star} = 0$, then at $\mathbf{s}_\star$ y is an extreme (either a minimum, maximum, or saddle point). If the stability matrix is nonsingular,

$$\det\left|\frac{\partial^2 y}{\partial s_i \partial s_j}\right| \neq 0 , \tag{2.108}$$

Table 2.1: Universal forms of $y_{\rm NM}$ for co-dimension $K \leq 3$. Co-dimension is defined as the dimensionality of the control space minus the dimensionality of singularity. The state variables are given by $\mathbf{s} = \{s_1, s_2, ...\}$ and the control parameters are given be $\mathbf{C} = \{c_1, c_2, ...\}$.

name	K	germ $G(\mathbf{s})$	perturbation $P(\mathbf{s};\mathbf{C})$
fold	1	s_1^3	$c_1 s_1$
cusp	2	s_1^4	$c_2 s_1^2 + c_1 s_1$
swallowtail	3	s_1^5	$c_3 s_1^3 + c_2 s_1^2 + c_1 s_1$
elliptic umbilic	3	$s_1^3 - 3 s_1 s_2^2$	$c_3(s_1^2 + s_2^2) + c_2 s_2 + c_1 s_1$
hyperbolic umbilic	3	$s_1^3 + s_2^3$	$c_3 s_1 s_2 + c_2 s_2 + c_1 s_1$

then in the vicinity of $\mathbf{s}_*$ y can be approximated as being quadratic

$$y = \sum_i \lambda_i s_i^2 \tag{2.109}$$

where λ_i is an eigenvalue of the stability matrix. The condition in Eq. (2.108) means any eigenvalue of the stability matrix being equal to zero causes it to be singular, so it is a stringent constraint.

Splitting Lemma. The splitting lemma becomes useful when the stability matrix is singular at some point which happens because one (or more) eigenvalue are equal to zero. The splitting lemma says that there exists a smooth change of variables, $\mathbf{s} \to \mathbf{s}'$, such that f can be put in the following form

$$y = y_{\rm NM}(s'_1, ..., s'_m) + y_{\rm M}(s'_{m+1}, ...s'_d) \tag{2.110}$$

for d dimensions. Here $y_{\rm M}$ is a function of $d - m$ variables tangent to eigenvectors of the stability matrix whose eigenvalues don't vanish, so it is a Morse function and can therefore be written in quadratic form. The function $y_{\rm NM}$ is the non-Morse function and so has a form beyond quadratic in the m variables.

2.4.2 Functional form of catastrophes

The splitting lemma is one of Thom's key results because it breaks any function up into interesting (non-Morse) and uninteresting (Morse) parts. The question then is what determines the form of $y_{\rm NM}$? A typical function will not have a singular stability matrix, however, in general y will also be a function of some control parameters, $\mathbf{C}$ (physical examples include applied fields and driving parameters discussed in Sec. 2.1), such that $\lambda_i = \lambda_i(\mathbf{C})$. This means there could be some value of the control parameters which causes one or more eigenvalues to be zero. Thom showed that if the non-Morse function is a function of m state variables and k control parameters, $y_{\rm NM}(\mathbf{s};\mathbf{C}) = y_{\rm NM}(s_1, ..., s_m; c_1, ..., c_k)$, then it can be split into two parts

$$y_{\mathrm{NM}}(\mathbf{s};\mathbf{C}) = G(\mathbf{s}) + P(\mathbf{s};\mathbf{C}) \tag{2.111}$$

where $G(\mathbf{s})$ is referred to as the catastrophe germ and is the source of the singularity of y_{NM}. The function $P(\mathbf{s};\mathbf{C})$ is the perturbation function of the germ and is linear in the control parameters. Thom showed the number of state variables and control parameters uniquely determines the form of y_{NM} where the first five are given in Table 2.1. The functions are ranked in terms of their co-dimension, K. The co-dimension is defined as the dimensionality of the control space minus the dimensionality of the singularity, or in other words it is defined as the dimensionality of the space one needs to explore the singularity.

The catastrophe functions in Table 2.1 are structurally stable in that they will take the same form when perturbed further. To illustrate this we examine the cusp germ $G_2(s) = s^4$ where the subscript is the co-dimension of the cusp catastrophe. This function has a degenerate critical point at $s = 0$ that is a minimum. If we add the perturbing function $p_\epsilon = \epsilon s^2$ to it where $|\epsilon| \ll 1$, then $s = 0$ either becomes a Morse minimum (non-degenerate minimum) or a maximum straddled by two minima for positive and negative ϵ, respectively. In either case $G_2 + p_\epsilon$ is drastically different from G_2. More specifically it is more stable than G_2, but still unstable because adding $p_\delta = \delta s$ where $|\delta| \ll 1$ changes things drastically again. However, $\Phi = G_2 + p_\epsilon + p_\delta$ is stable since there always exists a transformation to remove s^3 terms and put it back into the form of Φ. Adding higher order terms also does not affect the stability since if we have $s^4 + \epsilon s^n$ where $n \in \mathbb{Z} : n > 4$, then for $\epsilon < 0$ the critical points are at $s = 0$ and $s = \left(\frac{4}{|\epsilon| n}\right)^{\frac{1}{n-4}}$ and since ϵ is very small the extra critical point that comes about from adding the s^n term is far away from the neighbourhood around $s = 0$ which we are interested in. In general, the higher the order of the germ the more sensitive it is to perturbations. The process of perturbing the germ until it is stable to further perturbation is called *unfolding*.

2.4.3 Cusp catastrophe

Basic properties

The focus of this thesis in regard to catastrophes is the cusp catastrophe, so we provide a dedicated discussion of it here. The cusp generating function is $\Phi_2 = s^4 + c_2 s^2 + c_1 s$ where the subscript once again stands for the co-dimension of the cusp. The critical points of Φ_2 are given by

$$\frac{\partial \Phi_2}{\partial s} = 4s^3 + 2c_2 s + c_1 = 0\,. \tag{2.112}$$

Due to the fact that Eq. (2.112) is cubic it can have one to three real roots. The number of real roots depends on the values of the two control parameters. In the

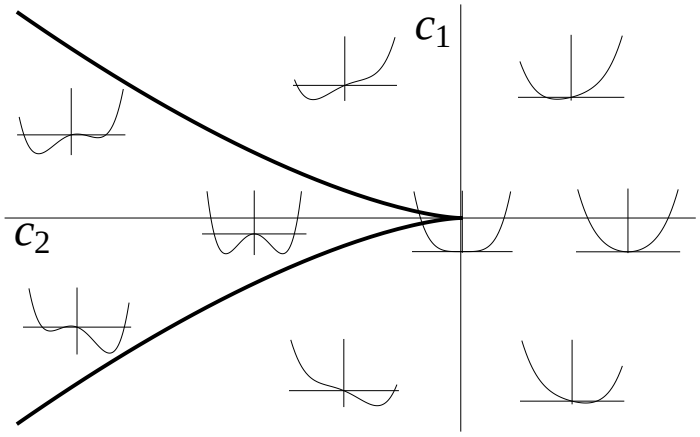

Figure 2.8: The thick, black curves mark the values of the control parameters c_1 and c_2 which satisfy the conditions $\frac{\partial \Phi_2}{\partial s} = \frac{\partial^2 \Phi_2}{\partial s^2} = 0$ and are given by Eq. (2.114). The insets show Φ_2 as a function of the state variable, s, for the different regions of the cusp.

control parameter plane seen in Fig. 2.8 regions depending on the number of real roots are separated by two symmetric curves forming a cusp. The additional condition

$$\frac{\partial^2 \Phi_2}{\partial s^2} = 12s^2 + 2c_2 = 0 \tag{2.113}$$

along with Eq. (2.112) gives the equation for the cusp

$$c_{1,\pm} = \pm\sqrt{\frac{8}{27}}(-c_2)^{3/2} \tag{2.114}$$

where $c_{1,\pm}$ is the value of c_1 on the cusp curve.

Figure 2.8 can be broken up into four regions

1. outside the cusp there is one real root
2. inside the cusp there are three real roots
3. on the fold curves emanating from the cusp point there are three real roots, but two of them coalesce
4. at the cusp point at the origin all three real roots coalesce and this is the most singular part of the cusp

The insets in Fig. 2.8 give Φ_2 for different control parameter values where the real roots are the extrema. If we take the cusp generating function as a potential for some system the insets along the $c_1 = 0$ axis represent a potential with no applied field undergoing a second order PT where the cusp point $(c_1, c_2) = (0, 0)$ is the critical point. For a given value of $c_2 < 0$ a first order PT occurs on the fold curve given in Eq. (2.114).

Subcatastrophes

Equation (2.114) can be explicitly shown to contain the fold catastrophe by first realizing that solving for s in Eq. (2.113) gives $s_\pm = \pm\sqrt{\frac{|c_2|}{6}}$ which are the values of s where the two roots coalesce. Expanding Φ_2 around $s_\pm$ and around the fold curve, $c_{1,\pm}$, gives

$$\tilde{\Phi}_2 \approx A + By + y^3 \tag{2.115}$$

where $\tilde{\Phi}_2$ is the form of the fold generating function near the cusp curve. Also, we have chosen to expand around the $c_{1,+}$ fold curve, A is an unimportant constant, $B = \left(\frac{3}{8a}\right)^{1/6}(c_1 - c_{1,+})$ and $y = s - s_+$. It is easy to see that the two real roots of $\frac{\partial\tilde{\Phi}_2}{\partial y} = 0$ coalesce when $B = 0$ or on the fold curve when $c_1 = c_{1,+}$.

Equation (2.115) for the cusp is a general result for all catastrophes, that is the higher catastrophes contain the lower ones. In Fig. 2.9 we go in the other direction and show that the elliptic umbilic catastrophe, whose generating function is shown in Table 2.1, contains cusps. In (a) we show how the regions with different numbers of real roots of $\frac{\partial\Phi_{3,\text{eu}}}{\partial s_1} = \frac{\partial\Phi_{3,\text{eu}}}{\partial s_2} = 0$ are separated in control parameter space, where $\Phi_{3,\text{eu}}$ is the elliptic umbilic catastrophe generating function. The image is three dimensional as opposed to Fig. 2.8 due to there being one more control parameter for the elliptic umbilic than the cusp. Image (b) shows a cross-section of image (a) for constant c_1 (not to be confused with the cusp catastrophe c_1) where three inward opening cusps can clearly be seen. This shape is well known to be a three-cusped hypocycloid [71].

2.4.4 Physical meaning of structural stability

In science we depend on the repeatability of experiments, i.e. an experiment should produce the same results when under the same conditions. This is of course an idealized notion of repeatability and in actual experiments, despite having a large degree of control, unpreventable external influences have an effect on each run of the experiment. Thus, the experimenter must decide what sort of outside influences they want their experiment to be insensitive to. Likewise, in mathematical models, theorists must account for all perturbations that have a large impact on the system. The structural stability of catastrophes partially addresses this by giving the most general function under the constraints of dimensionality and number of control parameters. As an example, the Hamiltonian of the transverse field Ising model takes the form of Φ_2 in the mean-field theory where s is the total magnetization, c_1 is the applied magnetic field and c_2 is the interaction energy between neighbouring sites. Any experiment performed on this system will be done in the presence of Earth's fluctuating magnetic field causing different results for each run of the experiment. However, due to the structural stability of Φ_2 the Earth's magnetic field only causes a shift of the

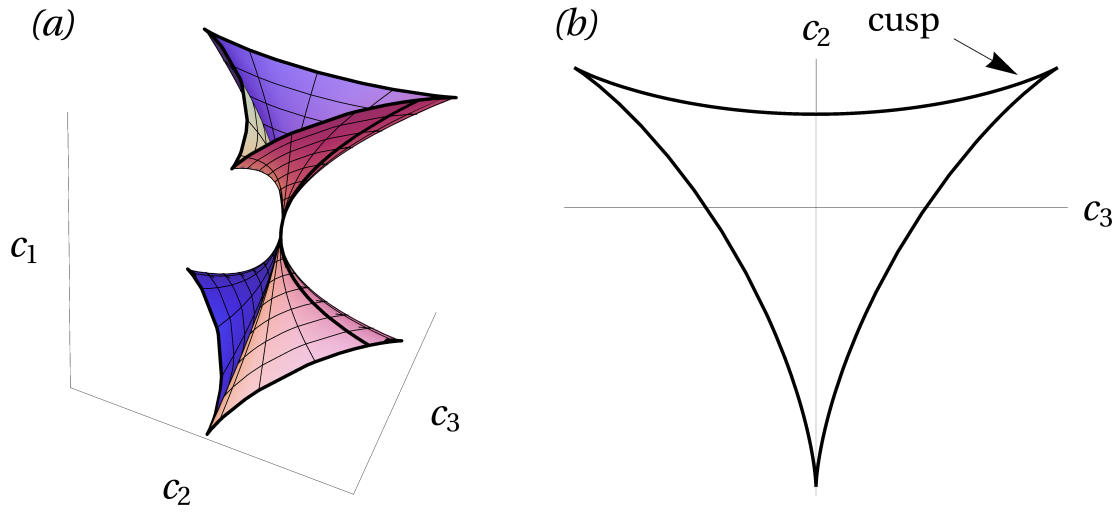

Figure 2.9: Image (a) shows the boundary in control parameter space of the elliptic umbilic catastrophe which separates regions with different real roots of $\frac{\partial \Phi_{3,\mathrm{eu}}}{\partial s_1} = \frac{\partial \Phi_{3,\mathrm{eu}}}{\partial s_2} = 0$. Image (b) shows a cross section of (a) for constant c_1 which clearly displays three inward facing cusps also known as a three-cusped hypocycloid.

cusp along the c_1 axis. The form of the critical point remains unchanged where only its position has changed.

In practice there can be some difficulty in knowing which catastrophe generating function best captures the physics of a particular system. The transverse field Ising model was stable to perturbations of Earth's magnetic field, but what if there was a perturbation involving a coupling between the spins and an additional degree of freedom? Terms like this take the form cs_1s_2 where we see in Table 2.1 they are accounted for in higher order catastrophes, namely the hyperbolic umbilic catastrophe. Usually the structural stability of catastrophes can be taken as equivalent to repeatability of experiments, but only under perturbations of a certain type, so we cannot blindly associate the two.

One may ask if second order PTs occur at all in nature because the free energy given in Eq. (2.2) is unstable to perturbations linear in the state variable. The answer is yes they do occur as a result of either artificially or naturally imposed symmetries. Typically, in the lab experimentalists will not succeed entirely in imposing the desired symmetry resulting in PTs in systems being weakly first order, however, as techniques are refined the closer they can get to their goals in both eliminating the asymmetry and accounting for its presence. An extremely relevant and recent example of this is the experiment mapping the full phase diagram of a parity-symmetry breaking PT in an ultracold atomic gas in a double well potential [72]. In that experiment the ground

state energy takes the form of Eq. (2.2), but with a linear term from an energy bias between the two wells. They were not able to remove the linear term, but were able to account for its presence in the classification of the second order quantum PT.

2.4.5 Catastrophes in mean-field dynamics

Caustics

Mean-field dynamics takes place in the short wavelength limit where wave effects governed by the Schrödinger equation are too small to be detected. In the mean-field theory a system evolves along a definite path called a trajectory. It is unclear where singularities might occur, and certainly there are none when speaking of a single trajectory because a system evolves deterministically and uniquely. However, what if identical copies of the system are made, each one starting in a different initial state and they are allowed to evolve? One can easily imagine that if the system is complicated enough some trajectories might overlap at some point. This overlapping is the source of singularities in mean-field dynamics because the different paths are no longer unique at those points. The general term for the region of focusing of the trajectories comes from optics and is called a *caustic* coming from the Latin word causticus meaning burnt. In optics caustics are the brightest features of light patterns after reflection or refraction, and appear everywhere in our everyday lives from the twinkling of starlight caused by the atmosphere to rainbows. This means we should expect them to be the most noticeable features in the mean-field dynamics involving many trajectories.

The singularities described above may seem artificial since on a macroscopic level we only ever observe a single trajectory at a time. However, often semiclassical approximations are used to describe full quantum dynamics where a Wigner distribution [73] of initial states are chosen to mimic an initial quantum state, but each trajectory evolves classically. This type of approach is used in many semi-classical theories [74], so there is justification for taking these singularities seriously.

The simplest example of a system which generates a caustic is the 1D simple harmonic oscillator (SHO) which is described by the Hamiltonian

$$H_{\mathrm{SHO}} = \frac{p^2}{2} + \frac{x^2}{2} \tag{2.116}$$

where p is the momentum and x is the position. Also, all constants have been set to unity because they play no role in the proceeding analysis. For zero initial momentum and initial position x_0 the dynamics of x is given by $x(t) = x_0 \cos t$ where we see each trajectory is determined uniquely by the initial position. More importantly, each trajectory has the same period, $T_{\mathrm{SHO}} = 2\pi$, so a caustic forms precisely at the point $(x, t) = (0, \pi/2)$ where every trajectory overlaps as seen in image (a) of Fig. 2.10.

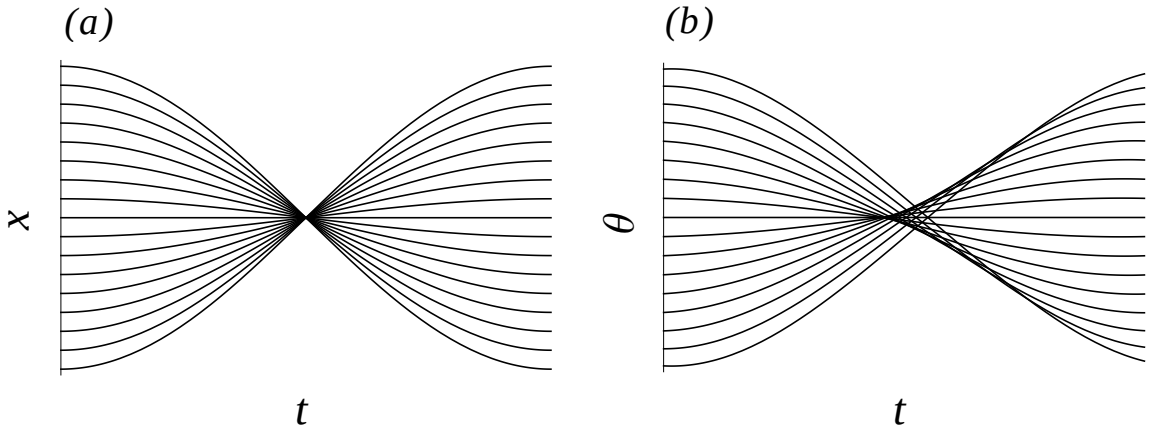

Figure 2.10: Dynamics for a distribution of initial states: (a) a simple harmonic oscillator and (b) a pendulum. The trajectories of the harmonic oscillator come to a single point because they oscillate at the same frequency, but when the system is slightly more complicated like the pendulum they smear out into a cusp shape.

Although the SHO is one of the simplest systems displaying a caustic it does not properly represent nature because it is idealized, and in terms of CT it is unstable to perturbations. Any deviation in the curvature of the potential term from the parabolic shape will result in a smearing of the focus point so it becomes an extended region in space. In optics a great effort is directed toward the creation of perfect lenses able to focus light rays to a single point, but it is impossible and the term used for the inevitable smearing of the focus is 'aberration'. In order to see the effects of the smearing we look at another simple 1D system, the rigid pendulum, which is described by the Hamiltonian

$$H_{\text{pend}} = \frac{L_z^2}{2} - \cos\theta \tag{2.117}$$

where L_z is the angular momentum in the z-direction (the direction is arbitrary) and θ is the angular displacement from the downward position. For similar initial states as the SHO, that is zero initial angular momentum, the angular displacement dynamics is given by $\theta(t) = \sin(\theta_0/2)\,\text{cn}[t|\sin^2(\theta_0/2)]$ where θ_0 is the initial angular displacement and $\text{cn}[u|m]$ is the Jacobi Elliptic cosine function. We can see once again each trajectory is determined by the initial displacement, however, due to the departure of the cosine potential from the parabolic shape in the SHO, each trajectory has a different period, $T_{\text{pend}} = 4K[\sin(\theta_0/2)]$ where $K[x]$ is the elliptic integral of the

first kind. This results in the caustics forming the now familiar cusp-shape seen in image (b) of Fig. 2.10.

Connections to catastrophe theory

A natural question to ask is what exactly is the connection of the dynamics in Fig. 2.10 to CT? The first hint comes from the fact that the cusp exists in spacetime signalling that space and time are related to the control parameters of the cusp generating function, c_1 and c_2. Second, we know from the Lagrange formalism of classical mechanics any trajectory is determined from the principle of stationary action. This means $\frac{\partial S}{\partial \theta_0} = 0$, where S is the action. When θ and t are such that they lie on the caustic the action is stationary to higher order, so we have $\frac{\partial^2 S}{\partial \theta_0^2} = 0$. These two conditions are the same as those for the cusp when θ_0 is the state variable and S is the cusp generating function. In general, S will look nothing like any catastrophe generating function, however, near the caustics it can be Taylor expanded to look like them. For the pendulum case near the cusp point CT tells us that the action must take the form $S \approx c_1(\theta, t)\theta_0 + c_2(\theta, t)\theta_0^2 + \theta_0^4$ where c_1 and c_2, now referred to as the *canonical* control parameters are functions of the spacetime coordinates, now referred to as the *physical* control parameters. CT tells us the form of S is universal for systems displaying a cusp, but the dependence of the canonical parameters on the physical parameters is not. However, near the cusp point they too can be expanded to leading order. For the pendulum near the first cusp we have $c_1 \propto \theta$ and $c_2 \propto (\pi/2 - t)$ [75] where applying the stationary conditions of the action gives the usual cusp equation $\theta \propto (t - \pi/2)^{3/2}$. Lastly, in Sec. 2.4.3 we discussed how the cusp is the boundary separating regions with different numbers of real roots. When the generating function is the action the number of real roots to $\frac{\partial S}{\partial \theta_0} = 0$ is the number of paths allowed at any (θ, t) coordinate. This can be seen in (b) of Fig. 2.10 where outside the cusp only one trajectory is allowed at any point and inside, close to the cusp point, three can overlap. Although hard to see, on the fold caustic two trajectories overlap.

It should come as no surprise to us that the cusp appears in 1D dynamics because it is the highest order catastrophe that can exist purely in two dimensions. This means we already know the form of the action near the cusp itself, which is that of the fold. Likewise, if we increase the spatial dimension by one we should expect dynamics which resembles one or both of the umbilic catastrophes. CT has been used by us to predict umbilic catastrophes in quantum dynamics in Fock space after a quench of a BEC in a triple well when a cusp was seen in the dynamics after a similar quench of a BEC in a double well [76].

2.4.6 Catastrophes in waves

In quantum dynamics the evolution of a state is determined by the Feynman propagator [37]

$$K(x,t;x_0,t_0) = \sum_{\text{all paths}} \mathrm{e}^{iS/\hbar} \tag{2.118}$$

where S is the action and the sum is over all paths originating at position x_0 at time t_0 and ending at position x at time t. Also, $\hbar$ is Planck's constant, although, in many-body systems N can play the role of the inverse of Planck's constant. In either case the short wavelength limit discussed in the previous section corresponds to the limits $\hbar \to 0$ (continuum) or $N \to \infty$ (thermodynamic). When this happens the only paths that contribute to the propagator are those given by the stationary action, $\partial S/\partial x_0 = 0$, and the rest cancel due to destructive interference. If we move away from the $\hbar \to 0$ limit, but still have $\hbar \ll 1$, then the classical paths are still good and can be used in various semiclassical wave approximations like the Wentzel-Kramers-Brillouin (WKB) [77] method. However, these approximations also breakdown when the roots of $\partial S/\partial x_0 = 0$ are degenerate. CT is exactly what is needed as it gives us universal wave function forms around these critical regions. These forms were originally studied in wave optics, so at first we will use focus on examples with light, then switch to quantum wavefunctions.

Universal diffraction catastrophes

In the wave theory of optics it has been shown that a general wave function near a singularity can be transformed into one of a finite set of diffraction integrals [78, 79, 80] called 'diffraction catastrophes' of the form

$$\Psi(\mathbf{C};k) = \left(\frac{k}{2\pi}\right)^{n/2} \int_{-\infty}^{\infty} \cdots \int_{-\infty}^{\infty} \mathrm{d}^n\mathbf{s}\, \mathrm{e}^{ik\Phi(\mathbf{s};\mathbf{C})} \tag{2.119}$$

where Φ is the catastrophe generating function and n is the corank of Φ, or the number of directions in state space which are singular. Thus, the study of wavefunctions near caustics boils down to the study of integrals given in Eq. (2.119), i.e. path integrals with coalescing saddles. What is surprising is that the majority of the catastrophe integrals are unknown to physicists. It should be noted that the bulk of the study of these integrals was done in the context of optics, but we will find they describe quantum wavefunctions near caustics as well. For now we look at the basic properties of the cusp diffraction integral.

For the cusp Eq. (2.119) takes the form

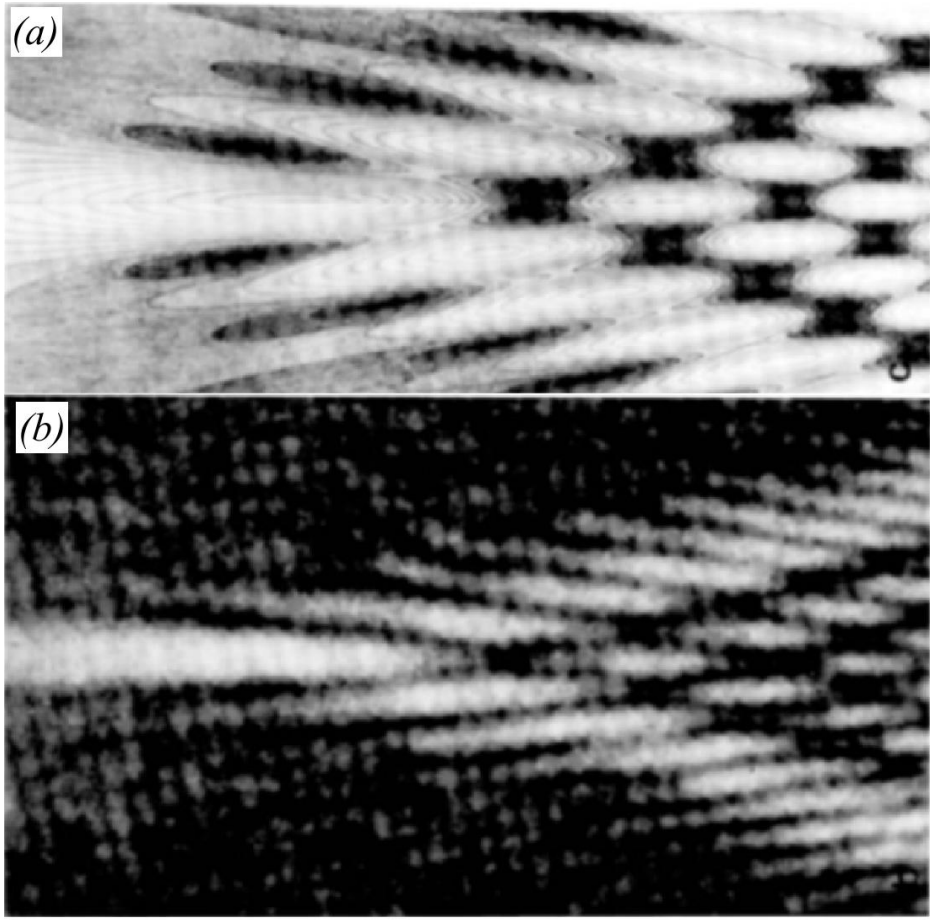

Figure 2.11: Images of the cusp catastrophe: (a) computer generated image of the amplitude $|\mathrm{Pe}(c_1, c_2, 1)|$ and (b) an image of laser light focused onto a spatial plane after being focused by a water-droplet lens. Dark and light colour signify regions of low and high intensity, respectively. Both images are courtesy of Berry [48].

$$\mathrm{Pe}(c_1, c_2; k) = \sqrt{\frac{k}{2\pi}} \int_{-\infty}^{\infty} \mathrm{d}s_1 \, \mathrm{e}^{ik\left(c_1 s_1 + c_2 s_1^2 + s_1^4\right)} \, . \tag{2.120}$$

This function (with $k = 1$) was first studied by Pearcey [51] and is therefore called the Pearcey function and given the special notation Pe. From the mean-field theory we know caustics form a cusp where outside of it no trajectories intersect and inside it three trajectories intersect. Therefore, we should expect there to be a more intricate interference pattern within the cusp. Looking at image (a) Fig. 2.11, which shows the amplitude $|\mathrm{Pe}(c_1, c_2; k)|$ this is exactly what is found. Image (b) shows a photograph of laser light focused by a water-droplet lens onto a spatial plane. The agreement between the two images is very impressive as the Pearcey function is able to capture

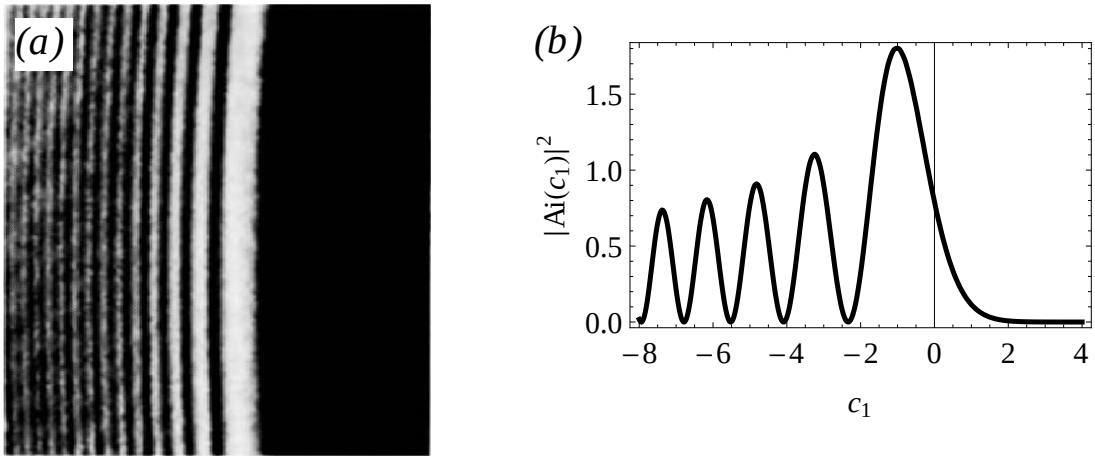

Figure 2.12: Images of the fold catastrophe: (a) a photograph of the fold catastrophe produced by light focused through a water-droplet lens and (b) a computer generated image of the intensity of the Airy function which is the diffraction integral of the fold catastrophe. Image (a) is courtesy of Berry [48].

even the finest details of the interference pattern in the cusp.

Before we go further discussing the interference pattern within the cusp we examine the wavefunction form near the caustics, but away from the cusp point. We know from the mean-field theory the caustics are described by the fold generating function. This means the wavefunction takes the form

$$\mathrm{Ai}(c_1;k) = \frac{k^{1/2}}{2\pi}\int_{-\infty}^{\infty} \mathrm{d}s_1\, \mathrm{e}^{ik\left(c_1 s_1 + s_1^3\right)} \tag{2.121}$$

which has been given the special notation Ai because it is a version of the Airy function (when $k = 1$) [81]. In image (a) of Fig. 2.12 we show the caustic region away from the cusp point of the same water-droplet focused light as in Fig. (2.11. Comparing image (a) with the intensity of the Airy function in image (b) we see the Airy function properly describes the qualitative features of the spacing of the fringes as well as the decrease in intensity as one goes further inward from the dark side of the caustic.

Phase singularities: vortices

We can see within the cusp there is a regular pattern of dark (low intensity) and light (high intensity) spots and at the centres of the darkest spots the intensity of the wavefunction goes to zero. To have the amplitude of the wavefunction go precisely to zero at any point may seem like it requires special conditions because it means all contributing waves at that point exactly cancel out. However, Berry was able to show that these zero intensity points are general features of wave interference patterns

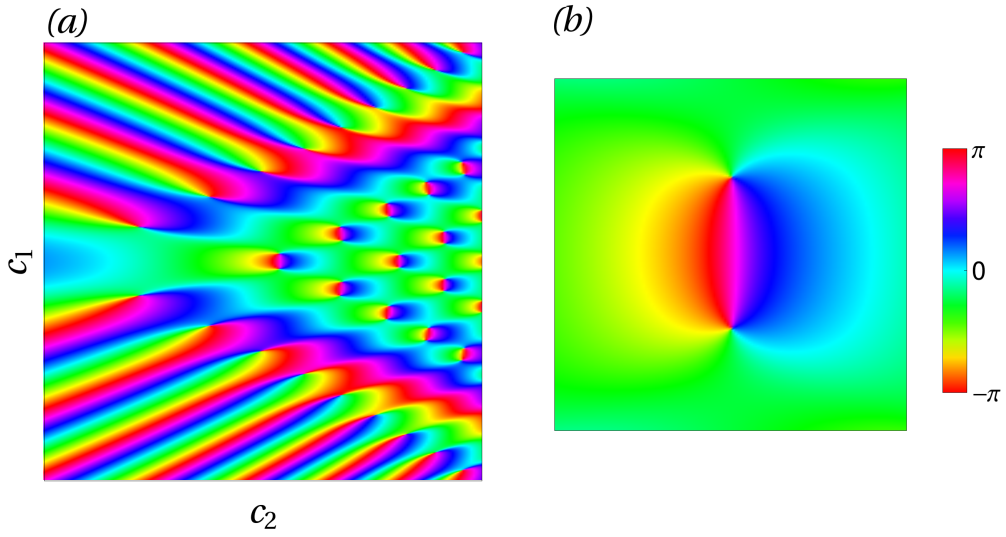

Figure 2.13: Image (a) shows the phase of the Pearcey function given in Eq. (2.120) in the control parameter space. Image (b) shows a closeup of a vortex-antivortex pair where we can see the vortex cores are points where curves of constant phase terminate.

[48]. The consequence of this is that a wavefunction of the form $\psi = \rho e^{i\chi}$ where ρ is the amplitude and χ is the phase, has $|\rho| = 0$ at some point, then the phase is undefined at that point and therefore takes all possible values. These points are phase singularities and called 'wavefront dislocations' by Nye and Berry [82] because of their close similarity to dislocations in crystal structures. The fact that ψ is single-valued means that around any circuit, C, enclosing a phase singularity, χ changes by $\pm 2\pi n$ where $n = 0, 1, 2, \ldots$ and determines the strength of the singularity. Mathematically, this means

$$\oint_C \mathrm{d}\chi = \oint_C \nabla\chi \mathrm{d}r = \pm 2\pi n \,. \tag{2.122}$$

Because the singularities are general features of interference patterns they come in a wide variety both isolated and in groups. The ones within the cusp come in vortex-antivortex pairs as shown in Fig. 2.13. Image (a) shows the phase of image (a) in Fig. 2.11 and image (b) shows a magnified view of a particular vortex pair. The colours represent the values of the phase from 0 to 2π where we can clearly see they terminate at the dislocation points. For all pairs within the cusp the phase changes by $\pm 2\pi$ where it is $+2\pi$ for one member of each pair and -2π for the other. These sort of pairs appear in materials displaying the Kosterlitz-Thouless PT [83]. The difference between the vortices found in those materials and the cusp vortices is the cusp vortices never vanish and remain paired for finite k. In the limit $k \to \infty$ all

Table 2.2: Universal scaling exponents for the the catastrophe integrals with co-dimension $K \leq 3$. Here, β determines how the intensity scales, σ_j determines how the interference fringes scale and γ determines how the volume in the control parameter space scales. β should not be confused with the scaling exponent discussed in Sec. 2.1.

name	β	σ_j	γ
fold	1/6	$\sigma_1 = 2/3$	2/3
cusp	1/4	$\sigma_1 = 3/4$, $\sigma_2 = 1/2$	5/4
swallowtail	3/10	$\sigma_1 = 4/5$, $\sigma_2 = 3/5$, $\sigma_3 = 2/5$	9/5
elliptic umbilic	1/3	$\sigma_1 = 2/3$, $\sigma_2 = 2/3$, $\sigma_3 = 1/3$	5/3
hyperbolic umbilic	1/3	$\sigma_1 = 2/3$, $\sigma_2 = 2/3$, $\sigma_3 = 1/3$	5/3

vortices get scrunched up into the cusp point, but then the mean-field theory takes over because the wave theory no longer applies.

It is also interesting to consider the resemblance of the constant phase curves around each pair to the curves of constant electric field around a pair of equally but oppositely charged particles. Each vortex acts as a charged particle with constant phase lines originating at one vortex and terminating at the other.

Universal scaling

As $k \to \infty$ the spacing of the interference fringes goes to zero. We can ask the question, how exactly do the spacings go to zero? It turns out the effects of k on the spacings can be determined by rescaling s_1 in $\mathrm{Pe}(c_1, c_2; k)$. If we define a new variable of integration, $s = k^{1/4} s_1$, then the Pearcey function becomes

$$\mathrm{Pe}(c_1, c_2, ; k) = \frac{k^{1/4}}{\sqrt{2\pi}} \int_{-\infty}^{\infty} \mathrm{d}s \, \mathrm{e}^{i\left(k^{3/4}s + k^{1/2}s^2 + s^4\right)}, \tag{2.123}$$

thus $\mathrm{Pe}(c_1, c_2, k) = k^{1/4}\mathrm{Pe}(k^{3/4}c_1, k^{1/2}c_2; 1)$ which shows the k dependence of the fringe spacing in the c_1 and c_2 directions is $k^{-3/4}$ and $k^{-1/2}$, respectively. This means as $k \to \infty$ distances change anisotropically and the fine structure within the cusp becomes elongated.

It turns out that every catastrophe integral has a set of exponents associated with it describing the $k \to \infty$ behaviour. The general scaling equation is

$$\Psi(\mathbf{C}; k) = k^{\beta} \Psi(k^{\sigma_j} c_j; 1) \tag{2.124}$$

where $1 \leq j \leq K$ and where K is the number of control parameters describing the caustic singularity. The exponent β is the "singularity index" as it is the singular part of the wavefunction as $k \to \infty$ and was first introduced by Arnol'd [52]. The fringe spacing exponents, σ_j, were first introduced by Berry [53] along with the exponent

$$\gamma = \sum_{j}^{K} \sigma_j \tag{2.125}$$

describing how the volume in control parameter space scales. The values of these exponents for the catastrophes given in Table 2.1 is given in Table 2.2 [48].

In paper III we study the dynamics of semiclassical many-body wave functions after a term in the Hamiltonian is flashed on and off at $t = 0$. Furthermore, when a symmetry of the Hamiltonian is broken by a second order PT we show $k \propto \lambda^q$ where $q \in \mathbb{Z}$ and λ is the reduced driving parameter of the PT defined in Sec. 2.1.1. This allows us to relate the scaling discussed in this section to scaling near a PT discussed throughout Sec. 2.1. Relating the driving parameter to the wavenumber is demonstrated explicitly when the action, S, in Eq. (2.118) is a homogeneous function of space (can be abstract spaces like Fock space) and time. This means with proper scaling of space and time the action becomes

$$S(\lambda^{u_1} x, \lambda^{u_2} t) = \lambda^u S(x, t) \tag{2.126}$$

where the RHS is what we are after. This allows us to identify universal features of quantum dynamics. This is novel because universality is usually discussed in the context of equilibrium states.

2.4.7 Catastrophes in many-body quantum dynamics

The evolution in time of many-body quantum systems is smooth, but there is an innate granularity in the dynamics due to the excitations being quantized. This raises many questions regarding CT: (1) do catastrophes exist in many-body wave functions? (2) if so, does the quantization destroy the fine details of the catastrophes like vortices? (3) if they survive are they altered in any way?

The first of these questions has been answered recently by O'Dell [47] by analyzing the dynamics of a BEC in a double well potential after a quench. Equation (2.59) gives the Hamiltonian which generates the system's dynamics. The procedure consists of preparing the system with two independent BECs by having an infinite barrier height, then at $t = 0$ suddenly dropping the barrier to some value and letting the system evolve. Figure 2.14 shows the result of such a scheme for $N = 100$ bosons. Here, we plot the intensity of the wave function in the number difference basis, $z = (N_r - N_l)/N$, defined in Sec. 2.2.3 as a function of time. We can see cusps periodically form along the $z = 0$ axis, but lose their shape near $z = \pm 1$ due to energy constraints. The first cusp is not a true cusp because the initial state is $|z = 0\rangle$ which is a point, but the second cusp is. Looking closer at the interference pattern near the cusp point of the middle cusp we see a pattern similar to that of the Pearcey function in Fig. 2.11, but it is in fact discretized by a new length scale, $1/N$, introduced by

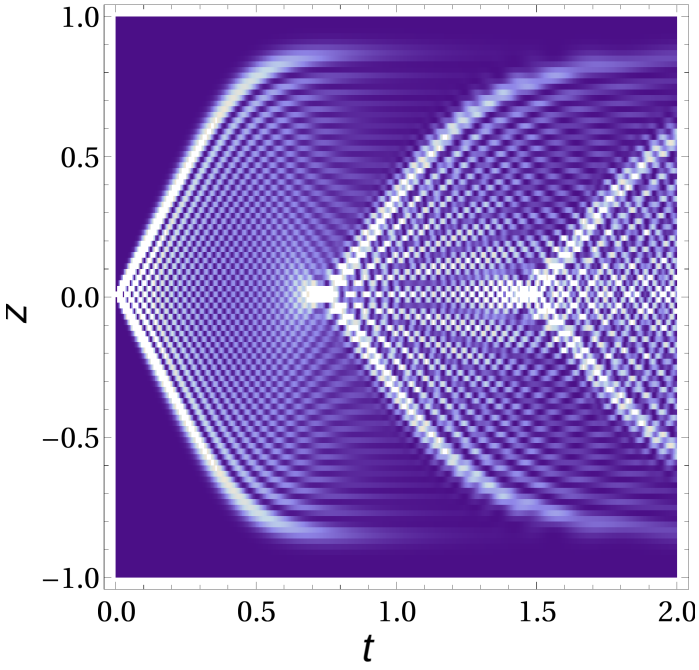

Figure 2.14: Many-body dynamics after a quench of a BJJ. The initial state is $|z = 0\rangle$ which is two independent BECs, then their coupling is flashed on at $t = 0$. Cusps form periodically around the $z = 0$ axis as a result of the quench, however the cusp at $t = 0$ is not a true cusp because the wave function is focused to a point there and cusps are extended objects. The image is for $N = 100$

the discreteness of the Fock space. This means details of the wave function cannot be discerned past the length $1/N$ and the vortex cores are removed making their exact locations unknowable. Remarkably, however, the vortices still exist as phase singularities as can be shown by integrating the phase around square circuits in Fock-space plus time. Thus, we get a partial answer to question number two, yes, the vortex cores are destroyed, by the phase dislocations persist.

A full investigation of these questions is the subject of paper IV where we look at the dynamics of the same system, but with a different quench scheme. We examine the dynamics of an initial Gaussian distribution of Fock states after the interactions between bosons of the BEC are flashed on and off at $t = 0$. Specifically, we look at the competition between the vortex-antivortex separation distance in Fock space and $1/N$.

Chapter 3

Publications

3.1 Paper I: Impurity in a bosonic Josephson junction: Swallowtail loops, chaos, self-trapping, and Dicke model

Jesse Mumford, Jonas Larson, and D. H. J. O'Dell
Impurity in a bosonic Josephson junction: Swallowtail loops, chaos, self-trapping, and Dicke model
Phys. Rev. A **89**, 023620 (2014);
DOI: https://doi.org/10.1103/PhysRevA.90.063617

Summary: This paper explores the effects of the inclusion of a single impurity in a BEC in a double well potential. Specifically, we show at the mean-field level the impurity is responsible for a $\mathbb{Z}_2$ symmetry breaking PT where at the critical BEC-impurity interaction energy, W_c, the ground state changes from having equal amounts of the BEC in each well to a build-up in one well over the other (the 'choosing' of one well over the other is what breaks the $\mathbb{Z}_2$ symmetry). We show as a result of the PT the mean-field dynamics become chaotic by examining Poincaré sections in the BEC-impurity phase space.

On the quantum side we show the ground state expectation value of the number difference operator, $\hat{S}_z$, is zero for $W < W_c$ and nonzero for $W > W_c$. This confirms the mean-field theory prediction of the existence of a PT where $\langle \hat{S}_z \rangle$ is the order parameter. Finally, we show the impurity induces dynamical trapping of the BEC where the time average of $\langle \hat{S}_z(t) \rangle$ is nonzero.

Content: All calculations with the exception of those done in Sec. VI, which were done by Jonas Larson, were done by the author. The majority of the article was written by the author with the following notable exceptions: most of the introduction,

Sec. VII and conclusion were written by Duncan O'Dell, and Sec. VI was written by Duncan O'Dell and Jonas Larson.

PHYSICAL REVIEW A **89**, 023620 (2014)

Impurity in a bosonic Josephson junction: Swallowtail loops, chaos, self-trapping, and Dicke model

Jesse Mumford,[1] Jonas Larson,[2,3] and D. H. J. O'Dell[1]

[1]*Department of Physics and Astronomy, McMaster University, 1280 Main St. W., Hamilton, Ontario, Canada L8S 4M1*

[2]*Department of Physics, Stockholm University, AlbaNova University Center, Se-106 91 Stockholm, Sweden*

[3]*Institut für Theoretische Physik, Universität zu Köln, Köln, De-50937, Germany*

(Received 13 November 2013; published 14 February 2014)

We study a model describing N identical bosonic atoms trapped in a double-well potential together with a single-impurity atom, comparing and contrasting it throughout with the Dicke model. As the boson-impurity coupling strength is varied, there is a symmetry-breaking pitchfork bifurcation which is analogous to the quantum phase transition occurring in the Dicke model. Through stability analysis around the bifurcation point, we show that the critical value of the coupling strength has the same dependence on the parameters as the critical coupling value in the Dicke model. We also show that, like the Dicke model, the mean-field dynamics goes from being regular to chaotic above the bifurcation and macroscopic excitations of the bosons are observed. Although the boson-impurity system behaves like a poor man's version of the Dicke model, we demonstrate a self-trapping phenomenon which thus far has not been discussed in the realm of the Dicke model.

DOI: 10.1103/PhysRevA.89.023620 PACS number(s): 03.75.Lm, 05.45.Mt, 03.75.Gg, 67.85.Pq

I. INTRODUCTION

The system comprising of a single quantum particle tunneling in the presence of a many-particle environment is of fundamental interest in the study of decoherence and is relevant to certain well-known models such as the spin-boson model and the Kondo problem [1,2]. In this paper, we consider a trapped ultracold-atom version: a single distinguishable "impurity" atom and N indistinguishable bosons all trapped together in a double-well potential. Within the single-band two-site Bose-Hubbard model, both the impurity and the bosons become two level systems, i.e., pseudospins. This model has previously been studied by Rinck and Bruder [3], by us [4], and by Lu and co-workers [5]. Closely related but distinct models that have been studied recently include the cases of an impurity atom trapped in a double well and coupled to a uniform Bose-Einstein condensate (BEC) [6], an atomic quantum dot acting as a coherent single-atom or photon shuttle between two BECs [7] or two optical resonator modes [8], respectively, and of two impurities immersed in a BEC [9]. Also related are studies of double wells containing atoms of two different species [10], a system suited to investigating the quantum aspects of phase separation [11–13]. Away from the immediate arena of cold atoms, essentially the same Hamiltonian as we shall use here occurs in the Mermin central-spin model (also known as the spin star model) which can be pictured as a central distinguished spin coupled equally to N surrounding spins located on the points of a star [14–16].

Various elements of our proposed system are already well established in the laboratory, although combining them may of course prove challenging. For example, tunnel-coupled atomic BECs (bosonic Josephson junctions) have been realized in a variety of different ways including the case where the double well might be an actual external potential [17–26], or be formed from two hyperfine states whose coupling is controlled by microwave or radiofrequency fields (internal Josephson effect) [27,28]. Although binary mixtures of BECs in the same trap were first made in the early days of atomic BEC [29], placing a precise number of atoms in a trap is a more recently achieved feat [30]. One setup which comes close to the one we have in mind here was created in an experiment where an optical lattice containing a Bose-Fermi mixture was suddenly ramped up to a large depth [31]. This resulted in an array of traps, each containing either one or zero fermions together with a small number of coherent bosons. The depth of the lattice effectively shut off tunnel coupling between the wells in that experiment, but ramping to smaller lattice depths would leave tunneling switched on. We also note in this context that optical lattices are versatile enough that they can be manipulated to produce a lattice of double wells [32]. Yet another relevant experiment has studied the fate of a superposition of two motional states of fermionic atoms immersed in a BEC [33].

In our previous paper [4], we studied the symmetry-breaking bifurcation that occurs in the ground state above a critical value of the boson-impurity interaction strength. The symmetry that is broken is a Z_2 parity symmetry whose physical order parameter is the expectation value of the difference in the number of bosons between the left and right wells (or the corresponding quantity for the impurity) which spontaneously develops a nonzero value at the bifurcation. From the energetic point of view, above the critical interaction strength it becomes preferable for the impurity to localize in one well and for the bosons to favor the other (assuming a repulsive boson-impurity interaction) leading to a number imbalance. Related symmetry-breaking bifurcations have been studied experimentally in purely bosonic Josephson junctions (no impurity) [28], in spin-orbit-coupled BECs [34], and in BECs in cavities [35]. In the case of [28], the bifurcation arises from the nonlinearity due to boson-boson interactions [36–45] and is thought to become a full blown quantum phase transition (QPT) in the limit that $N \to \infty$ [36,42–45]. When the net interaction energy is negative, this bifurcation occurs in the ground state, spontaneously breaking the symmetry of the Hamiltonian so that the bosons clump together in either the left or right well (in the case of the internal Josephson effect, a spontaneous polarization develops [40]). When the interaction energy is positive, the bifurcation breaks the symmetry of excited states and manifests itself physically as the transition from oscillations to macroscopic self-trapping, i.e., a dynamical phase transition [45]. In contrast to the purely

bosonic Josephson junction, in our system it is the nonlinearity due to the boson-impurity interaction that leads to symmetry breaking, and this can occur in the ground state for either repulsive or attractive interactions. Self-trapping due to the boson-impurity interaction can also occur as we shall see.

For a perfectly balanced double well, the number-difference symmetry is only broken in the mean-field theory: in the fully quantum treatment, the many-body wave function in Fock space (number-difference space), which has Gaussian fluctuations in the Bogoliubov approximation [46], develops non-Gaussian number fluctuations in the critical regime and eventually separates into two macroscopically distinguishable pieces, i.e., a Schrödinger cat state. This state is notoriously delicate and tiny external perturbations not included in the Hamiltonian are liable to break the symmetry by effectively introducing a tilt between the two wells. This collapses the cat state and thereby restores the validity of the mean-field result. Another difference between the full quantum theory and the mean-field theory is that the latter is nonlinear and this is the origin of the bifurcation which takes the form of a three-pronged pitchfork when the number difference is plotted as a function of the boson-impurity interaction strength and appears as a swallowtail loop [4] (see Fig. 2) when the energy is plotted versus an externally imposed tilt (which plays a role analogous to quasimomentum [47]). These characteristic loop structures also occur in many other bifurcating systems including bosonic Josephson junctions [39], the band structure of BECs in optical lattices [48–50] including at the Dirac point for a honeycomb lattice [51], the band structure of noninteracting atoms in cavity-QED [52], and the equivalent of band structure for BECs in toroidal traps [53,54]. Their presence has also been inferred experimentally due to a sudden breakdown in adiabaticity during a parametric sweep of the tilt between wells in a bosonic Josephson junction [55].

In this paper, we shall show that at the same time the bifurcation appears, the mean-field dynamics goes from regular to chaotic. Chaos in our system requires the presence of the impurity and does not occur in the ordinary bosonic Josephson junction which is classically integrable in the two-mode regime. Indeed, by adding an additional degree of freedom such as spin chaos has been previously predicted to appear in both mean-field BECs [56] and bosonic Josephson junctions [57]. Alternatively, chaos may also occur by removing energy conservation [58–61]. Chaos is a classical phenomenon that is usually defined as exponential sensitivity to initial conditions, that is, two arbitrarily close points in phase space will diverge exponentially over time. In quantum mechanics, precise trajectories do not exist and positions in phase space can not be defined than better to an area of size $\approx \hbar$ precluding the possibility of exponential sensitivity. Nevertheless, quantum systems whose classical limit is chaotic do display tell-tale behavior such as level repulsion leading to the idea of quantum chaos [62–65]. Here, we demonstrate chaos via Poincaré plots giving stroboscopic sections through classical (mean-field) phase space and we also monitor the statistics of the quantum energy levels.

Similar regular-to-chaotic behavior as we observe has been predicted [66–68] in the celebrated Dicke model. Indeed, in this paper we make the claim that our model is a poor man's version of the Dicke model, behaving identically if one is close to the bifurcation. The original Dicke model [69] described N two-level atoms coupled to a single mode of the electromagnetic field and undergoes a quantum phase transition to a superradiant phase corresponding to the collective emission of photons at a critical value of the atom-light coupling strength [70,71]. Alternatively stated, the Dicke model consists of N spins coupled to a harmonic oscillator. The physical basis of our claim of the equivalence of the two models is that very near the critical point, the harmonic oscillator is barely excited and can be truncated to just two states, and therefore behaves like the two-state impurity atom in our model. The fact that at a phase transition quantum fluctuations become important, but that this point also coincides with the onset of chaos, which is a classical phenomenon, suggests intriguing connections between the quantum and classical worlds [72].

The layout of this paper is as follows: We introduce the boson-impurity and the Dicke Hamiltonians in Sec. II; Sec. III consists of an analysis of the stationary mean-field problem including loops and the stability of the solutions; Sec. IV discusses the critical properties of the quantum ground state using an analogy to magnetism; in Sec. V we show the emergence of classical chaos which is triggered by the bifurcation and hence the presence of the impurity; the following Sec. VI demonstrates self-trapping; and in Sec. VII we analyze the nearest-neighbor statistics of the quantum energy levels. We have also provided an appendix which explains how we ensure that the eigenstates produced by numerical diagonalization have well-defined parity.

II. MODEL

The simplest many-body description for bosons in a double-well potential is the single-band two-site Bose-Hubbard model. When an impurity atom is added, this takes the form [3,4]

$$\hat{H} = -J\hat{B} - J^a\hat{A} + \frac{W}{2}\Delta\hat{N}\Delta\hat{M} + \frac{\Delta\epsilon}{2}\Delta\hat{N} + \frac{\Delta\epsilon^a}{2}\Delta\hat{M}. \quad (1)$$

Here, $\Delta\hat{N} \equiv \hat{b}_R^\dagger\hat{b}_R - \hat{b}_L^\dagger\hat{b}_L$ is the number-difference operator between the two wells for the bosons, and $\hat{B} \equiv \hat{b}_L^\dagger\hat{b}_R + \hat{b}_R^\dagger\hat{b}_L$ is the boson hopping operator which also gives the coherence between the two wells [73]. Likewise, $\Delta\hat{M} \equiv \hat{a}_R^\dagger\hat{a}_R - \hat{a}_L^\dagger\hat{a}_L$ and $\hat{A} \equiv \hat{a}_L^\dagger\hat{a}_R + \hat{a}_R^\dagger\hat{a}_L$ are the equivalent operators for the impurity. We assume that both the boson and impurity creation and annihilation operators obey the standard bosonic commutation relations, i.e., $[\hat{b}_\alpha,\hat{b}_\alpha^\dagger] = [\hat{a}_\alpha,\hat{a}_\alpha^\dagger] = 1$ with $\alpha = L, R$ and ones like $[\hat{a}_\alpha,\hat{b}_\alpha^\dagger]$ are identically zero. However, because there is only one impurity, its statistics do not matter and it could be a boson or a fermion. W parametrizes the boson-impurity interaction, and J and J^a are the hopping amplitudes for the bosons and impurity, respectively. Using similar notation, $\Delta\epsilon$ and $\Delta\epsilon^a$ are the respective differences between the zero-point energies of the two wells, i.e., the tilt, for the bosons and the impurity. It is important to point out that we have chosen not to include direct boson-boson interactions, assuming that they can be removed by a Feshbach resonance if necessary [28]. In our previous paper [4], we did

include them, but for many of the effects we are interested in here, especially the bifurcation in the ground state, they are a distraction that does not make a qualitative difference to the behavior. One exception to this is the particular case of attractive boson-boson interactions above a certain threshold in which case they also cause a symmetry-breaking bifurcation in the ground state as discussed in the Introduction. Another point to note at this stage is that the Hubbard Hamiltonian is a tight-binding approximation that neglects the change in the mode wave functions due to interactions [74,75]. This means that strong coupling polaron effects [76] are beyond our treatment. Instead, the double-well system allows us to focus upon the rich many-body aspects of the impurity problem.

The Hamiltonian in Eq. (1) can be reexpressed in the basis of the symmetric and antisymmetric (S and AS) modes instead of the left and right (L and R) modes. The S and AS modes are the eigenmodes of the single-particle problem, i.e., in the absence of interactions. Therefore, in the limit that $W \to 0$, the ground state corresponds to all the particles in the S mode because it has lower energy. Using a simple Hadamard rotation of the L and R creation (annihilation) operators, we have

$$\hat{b}_L = \frac{1}{\sqrt{2}}(\hat{b}_S + \hat{b}_{AS}), \tag{2}$$

$$\hat{b}_R = \frac{1}{\sqrt{2}}(\hat{b}_S - \hat{b}_{AS}), \tag{3}$$

and similar expressions hold for the impurity operators. In the new basis, and for vanishing tilts $\Delta\epsilon = \Delta\epsilon^a = 0$, Eq. (1) takes the form

$$\hat{H}_{S,AS} = 2J\hat{S}_z + 2J^a\hat{S}_z^a + 2W\hat{S}_x\hat{S}_x^a, \tag{4}$$

where the Schwinger spin representation has been used [77], i.e., $\hat{S}_z \equiv (\hat{b}_{AS}^\dagger\hat{b}_{AS} - \hat{b}_S^\dagger\hat{b}_S)/2 = -\hat{B}/2$ and $\hat{S}_x \equiv (\hat{b}_{AS}^\dagger\hat{b}_S + \hat{b}_S^\dagger\hat{b}_{AS})/2 = -\Delta\hat{N}/2$. Apart from the trivial U(1) symmetry related to particle conservation, we note that the Hamiltonian supports a Z_2 parity symmetry under $\hat{S}_x \to -\hat{S}_x$, $\hat{S}_y \to -\hat{S}_y$, $\hat{S}_z \to \hat{S}_z$, and equivalently for the impurity spin operators. This spin rotation preserves the SU(2) angular momentum commutation relations. Note that in the original L and R bases, this symmetry is nothing but a reflection of the double well about the origin. It follows that a nonzero tilt $\Delta\epsilon \neq 0$ or $\Delta\epsilon^a \neq 0$ breaks this symmetry.

Our model Hamiltonian in the form of Eq. (4) shows some resemblance to the Dicke Hamiltonian [69,78]

$$\hat{H}_{\rm D} = \omega_B\hat{S}_z + \omega_A\hat{c}^\dagger\hat{c} + 2g(\hat{c} + \hat{c}^\dagger)\hat{S}_x. \tag{5}$$

Here, $\hat{c}^\dagger$ ($\hat{c}$) are photon, i.e., boson, creation (annihilation) operators and $\hat{S}_z$ and $\hat{S}_x$ are spin operators. Equation (5) describes a spin-$N/2$ system coupled to the position coordinate of a harmonic oscillator. The frequencies ω_B and ω_A are the spin precession and harmonic oscillator frequencies, respectively, and g is the coupling strength. This system experiences a QPT at a certain critical value g_c to be discussed further in the following [79]. By comparison, Eq. (4) can now be thought of as a system consisting of a spin-$N/2$ coupled to a spin-$\frac{1}{2}$ particle (impurity) instead of the harmonic oscillator in the Dicke mode. Here lies the most important distinction between the two Hamiltonians: in the Dicke model, the coupling is to the electromagnetic field which has infinitely many energy levels, whereas there are only two levels for the impurity. Despite this truncation of the Hilbert space of the Dicke model, the parity symmetry of the boson-impurity model has its analog in the Dicke model with $\hat{c} \to -\hat{c}$ and $\hat{c}^\dagger \to -\hat{c}^\dagger$, and $\hat{S}_x \to -\hat{S}_x$ and $\hat{S}_y \to -\hat{S}_y$. These similarities mean that the boson-impurity system behaves as a simplified, or poor man's, Dicke model that captures the crucial behavior near the QPT. We also note that the rotating-wave approximation has not been imposed in Eq. (4) or in Eq. (5).

In order to obtain many of the results presented in this paper, we numerically diagonalize the Hamiltonian given in Eq. (1). For N atoms this requires diagonalizing a $(2N+2)\times(2N+2)$ matrix which is tractable for $N \sim 1000$ on a small computer because of the linear scaling in N of the matrix dimension and thus we can obtain numerically exact results. There are, however, some subtleties involved which are reflected in the physics of the system: From the above discussion we see that in the absence of any tilt the eigenstates should all have well-defined parity in the two-dimensional Fock space (i.e., number-difference space) where the many-body quantum state lives. However, numerical diagonalization routines do not automatically respect this parity symmetry. The most severe test occurs in the critical region where the quantum state becomes non-Gaussian and eventually evolves into a Schrödinger cat state made of two almost separated pieces in Fock space connected only by exponentially small probability amplitudes in-between. This may be viewed as arising from the appearance of an effective double-well potential in Fock space: for each even-parity state there is an odd-parity one and their energies become almost degenerate except for an exponentially small tunnel splitting when they lie below the barrier top. Numerical routines find it hard to handle exponentially small numbers at the same time as numbers of order unity and tend to give eigenstates of broken parity above the critical value of W, i.e., the eigenstates choose one well or the other. It is amusing to reflect on the fact that numerical errors replicate the effects of a physical environment! As we explain in the Appendix A, we circumvent these problems by diagonalizing the Hamiltonian in a basis which has well-defined parity so that good parity in Fock space is enforced.

III. MEAN-FIELD ANALYSIS

We perform the mean-field approximation by replacing the operators $\hat{a}_{L/R}$ and $\hat{b}_{L/R}$ in Eq. (1) with complex numbers

$$\hat{a}_{L/R} \to a_{L/R} = \sqrt{M_{L/R}}\, e^{i\alpha_{L/R}(t)} \quad \text{[impurity]}, \tag{6}$$

$$\hat{b}_{L/R} \to b_{L/R} = \sqrt{N_{L/R}}\, e^{i\beta_{L/R}(t)} \quad \text{[bosons]}, \tag{7}$$

giving the mean-field Hamiltonian

$$H_{\rm MF} = -J\sqrt{N^2 - 4Z^2}\cos\beta - J^a\sqrt{1-4Y^2}\cos\alpha + 2WYZ + \Delta\epsilon Z + \Delta\epsilon^a Y. \tag{8}$$

In the above expression, we have introduced the classical variables giving the phase and population differences between the L and R sides: $\alpha \equiv \alpha_R - \alpha_L$, $Y \equiv \Delta M/2$, $\beta \equiv \beta_R - \beta_L$, and $Z \equiv \Delta N/2$. It should be noted that the mean-field

approximation is really only being applied to the boson field. The mean-field representation for the impurity is in fact exact because the quantum state of a spin-$\frac{1}{2}$ is fully characterized by the two real numbers α and Y which can be related to the two angles on the Bloch sphere. Here, we are essentially utilizing the boson-coherent-state ansatz to derive the semiclassical Hamiltonian (8), but an equally good approach would be to use spin-coherent states instead [68].

The equations of motion following from Eq. (8) can be obtained from Hamilton's equations [4]

$$\dot{\alpha} = \frac{\Delta\epsilon^a}{\hbar} + 2\frac{W}{\hbar}Z + \frac{4J^a}{\hbar}\frac{Y\cos\alpha}{\sqrt{1-4Y^2}}, \tag{9}$$

$$\dot{Y} = -\frac{J^a}{\hbar}\sqrt{1-4Y^2}\sin\alpha, \tag{10}$$

$$\dot{\beta} = \frac{\Delta\epsilon}{\hbar} + 2\frac{W}{\hbar}Y + \frac{4J}{\hbar}\frac{Z\cos\beta}{\sqrt{N^2-4Z^2}}, \tag{11}$$

$$\dot{Z} = -\frac{J}{\hbar}\sqrt{N^2-4Z^2}\sin\beta. \tag{12}$$

Setting the left-hand sides to zero gives the stationary solutions whose energies are plotted in Fig. 1 as a function of the tilt $\Delta\epsilon$. Ignoring the trivial solutions of $Z = \pm N/2$ and $Y = \pm\frac{1}{2}$, we consider the solutions $\alpha = \{0,\pi\}$ and $\beta = \{0,\pi\}$ to Eqs. (9)–(12) giving four different combinations of the phase differences. In terms of the double pendulum analogy advanced in [4], the combination ($\alpha = \beta = 0$) corresponds to both pendula pointing straight down, ($\alpha = \pi$, $\beta = 0$) corresponds to the impurity pendulum pointing straight up and the boson pendulum pointing straight down, and vice versa for ($\alpha = 0$, $\beta = \pi$). The combination ($\alpha = \pi$, $\beta = \pi$) corresponds to both pendula pointing straight up. In Fig. 1, each of these solutions is plotted with a different symbol. Each panel is for a different value of W and illustrates how swallowtail loops appear when W exceeds a certain critical value W_c.

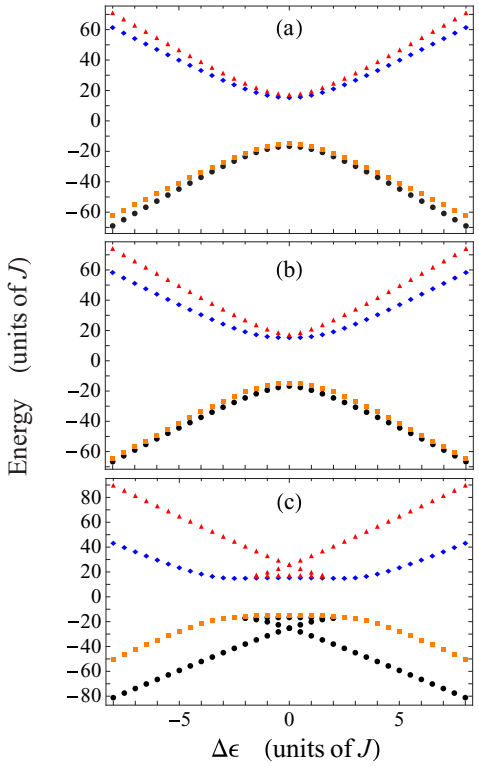

FIG. 1. (Color online) Energies of the static solutions to the mean-field equations (9)–(12) as a function of the tilt $\Delta\epsilon$. Each panel has a different value of the boson-impurity interaction energy: (a) $W = 0.1J$, (b) $W = 0.5J$, and (c) $W = 2.5J$. The various solutions within each panel are characterized by their phase difference. The four solutions are $\alpha = \beta = 0$ (black circles), $\alpha = \pi$ and $\beta = 0$ (orange squares), $\alpha = 0$ and $\beta = \pi$ (blue diamonds), and $\alpha = \beta = \pi$ (red triangles). All panels have $J^a = J$, $\Delta\epsilon^a = \Delta\epsilon$, and $N = 16$.

Let us focus upon Fig. 1(c) which is for $W > W_c$ and contains two swallowtail loops, one in the lowest- and one in the highest-energy band. The area of the loops depends on W, but their positions up the vertical energy axis are determined by J and J^a. At $\Delta\epsilon = \Delta\epsilon^a = 0$, the top of the $\alpha = \beta = 0$ band is fixed at $E = -NJ - J^a$ even when the loop is formed, i.e., in the presence of a loop $E = -NJ - J^a$ gives the energy of the upper branch of the lower loop. Meanwhile, the next band up, which has $\alpha = \pi$, $\beta = 0$, is fixed at $E = -NJ + J^a$. The energy gap between the two lowest bands is therefore $2J^a$ and the same goes for the energy gap between the two highest bands. The appearance of two loops is in contrast to the boson-only system where boson-boson interactions lead to a single loop, either in the highest band for the case of repulsive interactions or in the lowest band for the attractive case [48].

To investigate the appearance of loops further, we have plotted in Fig. 2 an enlargement of the lowest band. In Fig. 2(a) ($W < W_c$) we have a smooth curve. In Fig. 2(b) ($W = W_c$) a cusp forms at zero tilt heralding the emergence of the loop. In Fig. 2(c) ($W > W_c$) a loop forms where the number of solutions for ($\alpha = \beta = 0$) increases from one to three for a range of tilts. Each of these three solutions is distinguished by its number differences which form a pitchfork bifurcation when plotted as a function of W as illustrated in Fig. 3.

In order to see analytically how W causes the loop structure, we perform a stability analysis in the region where the loop first occurs. The lower band is characterized by $\alpha = \beta = 0$ and the loop begins to form at zero tilt. Therefore, solving the equations

$$2WZ + 4J^a\frac{Y}{\sqrt{1-4Y^2}} = 0, \tag{13}$$

$$2WY + 4J\frac{Z}{\sqrt{N^2-4Z^2}} = 0 \tag{14}$$

gives $\alpha = Y = \beta = Z = 0$ as the point at which the loop appears. If we define $\vec{x} = (\alpha, Y, \beta, Z)$ and linearize $\dot{\vec{x}}$ around $\vec{x}_0 = (0,0,0,0)$, we obtain

$$\dot{\vec{x}} = J(\vec{x}_0)\vec{x} + O(\vec{x}^2), \tag{15}$$

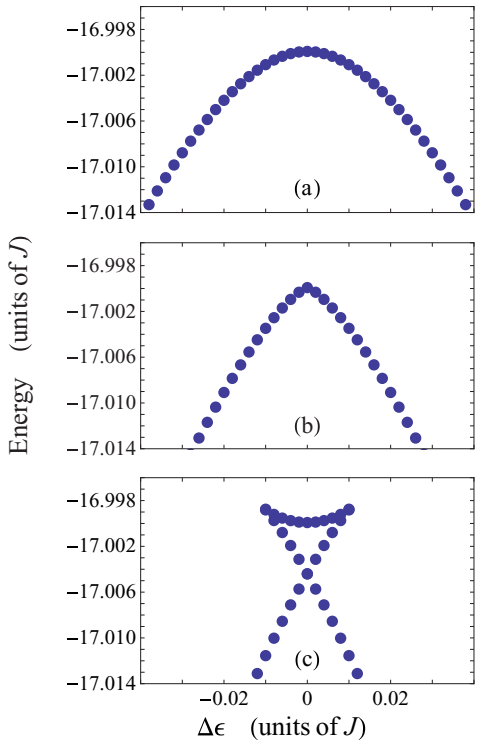

FIG. 2. (Color online) A closeup of the central region of the lowest band showing the emergence of the swallowtail loop as the boson-impurity interaction strength W is varied: (a) $W = 0.475J$, (b) $W = W_c = 0.5J$, and (c) $W = 0.525J$. The other parameters used in this plot are $J^a = J$, $\Delta\epsilon^a = \Delta\epsilon$, and $N = 16$. Of the three branches of the loop, the unstable one is the upper one, i.e., the curved part along the top.

where $J(\vec{x}_0)$ is the Jacobian matrix evaluated at $\vec{x}_0$:

$$J(\vec{x}_0) = \begin{bmatrix} 0 & 4J^a & 0 & 2W \\ -J^a & 0 & 0 & 0 \\ 0 & 2W & 0 & 4J/N \\ 0 & 0 & -JN & 0 \end{bmatrix}. \tag{16}$$

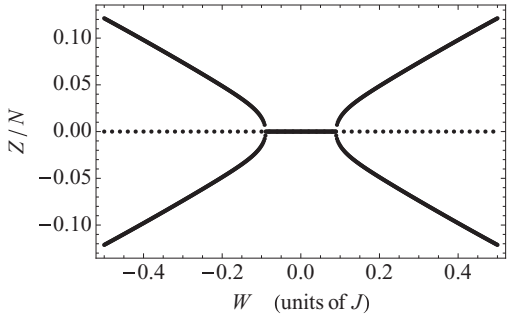

FIG. 3. Supercritical pitchfork bifurcation in the boson number difference Z between the right- and left-hand wells for the lowest band plotted as a function of the boson-impurity interaction strength W. The solid and dotted lines signify stable and unstable solutions, respectively. We see that the bifurcation occurs for both repulsive and attractive boson-impurity interactions. The values of the parameters are $N = 500$, $\Delta\epsilon = \Delta\epsilon^a = 0$, $J^a = J$.

The stability of the system at $\vec{x}_0$ depends on the eigenvalues of $J(\vec{x}_0)$. Every solution at $\vec{x}_0$ will be unstable if there is a positive real eigenvalue because there will be solutions such as $\vec{x}(t) = e^{\lambda t}$. The eigenvalues are

$$\lambda_{1,\pm} = -\sqrt{2\left(-J^2 - J^{a^2} \pm \sqrt{\left(J^2 - J^{a^2}\right)^2 + JJ^aW^2N}\right)}, \tag{17}$$

$$\lambda_{2,\pm} = \sqrt{2\left(-J^2 - J^{a^2} \pm \sqrt{\left(J^2 - J^{a^2}\right)^2 + JJ^aW^2N}\right)}. \tag{18}$$

Looking at $\lambda_{2,+}$ we find that the critical value of W when the loop emerges is

$$W_c = 2\sqrt{\frac{JJ^a}{N}}. \tag{19}$$

Comparing this with the critical coupling strength $g_c = \sqrt{\omega_A\omega_B/4N}$, at which a phase transition occurs in the Dicke model, we see that they have exactly the same dependence upon the associated parameters in the two Hamiltonians given in Eqs. (4) and (5) (the factor of 4 difference can be attributed to the definitions we use). Where the boson-impurity system experiences a bifurcation, the Dicke model experiences a QPT in the limit that $N \to \infty$ (see also Ref. [80]).

The preceding analysis also provides some information on the type of bifurcation shown in Fig. 3. Since the stationary point $\vec{x}_0 = (0,0,0,0)$ goes from being stable to unstable as W is increased through W_c, we have a supercritical pitchfork bifurcation. This type of bifurcation is common for systems with symmetry ($H_{\rm MF} \to H_{\rm MF}$ for zero tilt under $\vec{x} \to -\vec{x}$). When $W = W_c$, $\lambda_{1,\pm} = \lambda_{2,\pm} = 0$ and the solutions experience a process called "critical slowing down" where the decay and growth times are no longer exponential. A pitchfork bifurcation for Z has been observed experimentally in a bosonic Josephson junction [28], in a spin-orbit-coupled BEC [34], and at the onset of a density-wave instability in a BEC in an optical cavity [35]. In fact, this latter problem can be mapped onto the Dicke problem too [35,81–85]. If a nonzero tilt is applied then the pitchfork opens up, as shown in Figs. 5 and 6 in Ref. [4]. Considering Fig. 2, we can see that a finite tilt delays the onset of the bifurcation to a larger value of W because the loop is born at $\Delta\epsilon = 0$ and grows outwards.

The position in phase space of the new stable points can be found analytically by solving Eqs. (13) and (14) for $W > W_c$,

$$\vec{x}_\pm = \left(0, \pm\frac{1}{2W}\sqrt{\frac{N^2W^4 - 16J^2J^{a^2}}{N^2W^2 + 4J^{a^2}}}\,, \right.$$
$$\left. 0, \mp\frac{1}{2W}\sqrt{\frac{N^2W^4 - 16J^2J^{a^2}}{W^2 + 4J^2}}\right). \tag{20}$$

As $W \to \infty$, we have $\vec{x}_\pm \to (0, \pm\frac{1}{2}, 0, \mp N/2)$ corresponding to the complete localization of all the particles in one well or the other, as expected for a large interaction, attractive or repulsive, between the impurity and bosons. Figure 4 plots the mean-field energy in the $Y - Z$ plane for the lowest band for values of W close to W_c. As W passes through W_c, a

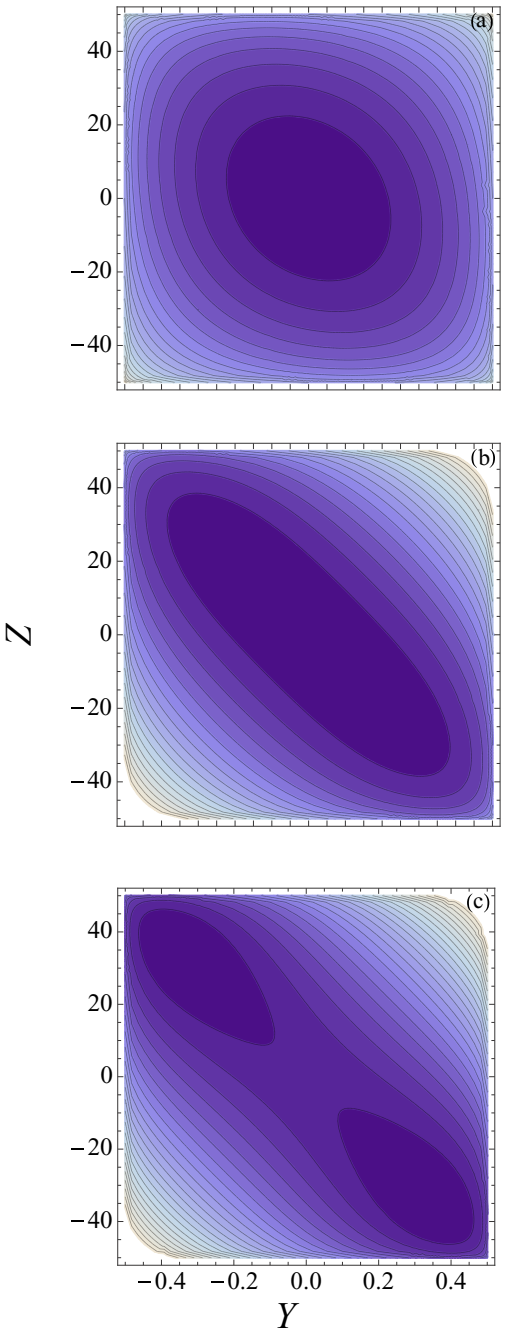

FIG. 4. (Color online) Contour plots of the mean-field energy $H_{\rm MF}$ evaluated for the lowest band in the number difference $(Y - Z)$ plane. This figure shows how a double well forms when $W > W_c$: (a) $W = 0.5\,W_c$, (b) $W = W_c$, and (c) $W = 1.5\,W_c$. The other parameter values are $J^a = NJ$, $N = 100$, and $\Delta\epsilon = \Delta\epsilon^a = 0$. Lighter colored regions are higher in energy.

double well forms in *Fock space* (number-difference space) in accordance with the Landau model for second-order phase transitions. In Fig. 4, this double well forms along the diagonal $Z = -Y$ because we have set $J^a = NJ$ which means that the hopping energies for the impurity and bosons contribute equally to the total energy of the system. In general, the axis of the double well can be at any angle in the $Y - Z$ plane depending on the parameters in $H_{\rm MF}$.

Defining $\chi = W/W_c$, the energies at the minima when $W > W_c$ and for zero tilt are

$$E_{|W|>W_c} = -2JN\left[\frac{\sqrt{(\eta+\chi^2)(1+\eta\chi^2)}}{2\eta\chi} - 1\right], \tag{21}$$

where $\eta = JN/J^a$. When $J^a = JN$, $\eta = 1$ giving

$$E_{|W|>W_c} = -JN[(\chi + \chi^{-1}) - 2]. \tag{22}$$

This corresponds to the case $\omega_A = \omega N$ and $\omega_B = \omega$ in the Dicke model where the ground-state energy in the superradiant phase becomes [86]

$$E_{|g|>g_c} = -\frac{\omega N}{4}[(\chi^2 + \chi^{-2}) - 2]. \tag{23}$$

We can see that Eqs. (22) and (23) differ slightly in their dependence on χ. However, in the vicinity of the critical coupling strengths we can set $\chi = 1 + \delta$ where $\delta \ll 1$ and expand to leading order to give $E_{|W|>W_c}/J = E_{|g|>g_c}/\omega = -N\delta^2$. Thus, near the critical point, the ground-state energies behave in exactly the same way.

IV. MAGNETIC PROPERTIES OF THE QUANTUM GROUND STATE

We now shift our focus from the number-difference representation of Eq. (1) to the spin representation of Eq. (4). Recall that $\hat{S}_x$ is half the number difference between left and right modes and $\hat{S}_z$ is half the number difference between the antisymmetric and symmetric modes. The spin representation allows us to interpret our system in terms of the familiar concept of magnetization. In particular, we will examine the dependence of $\langle \hat{S}_z \rangle$ evaluated in the ground state upon the control parameter W and we compare our results with those obtained from the Dicke model by Emary and Brandes [67] and Garraway [78]. In what follows, it is important to appreciate that our quantum ground state has unbroken symmetry (see the Appendix A) unless a tilt is added explicitly.

In this section only we use scaled versions of Eqs. (4) and (5):

$$\hat{H}_{S,AS} = 2J\hat{S}_z + 2J^a N\hat{S}_z^a + 2W\hat{S}_x\hat{S}_x^a - \Delta\epsilon\hat{S}_x - \Delta\epsilon^a N\hat{S}_x^a, \tag{24}$$

$$\hat{H}_{\rm D} = \omega_B\hat{S}_z + \omega_A\hat{c}^\dagger\hat{c} + \frac{2g}{\sqrt{N}}(\hat{c} + \hat{c}^\dagger)\hat{S}_x, \tag{25}$$

so that every term in each Hamiltonian is $O(N)$. This prevents the boson terms from dominating in the thermodynamic limit and ensures that the classical pitchfork bifurcation signals the presence of a QPT. With this scaling, the critical coupling parameters remain constant in the thermodynamic limit $N \to \infty$; $W_c = \sqrt{JJ^a}/2$ and $g_c = \sqrt{\omega_A\omega_B}/2$. Note that in Eq. (24) we have also included the tilt terms. Positive values of tilts correspond to external magnetic fields along the $+x$ direction. The tunneling parameters J and J^a also correspond to external magnetic fields, this time pointing along the $-z$ direction.

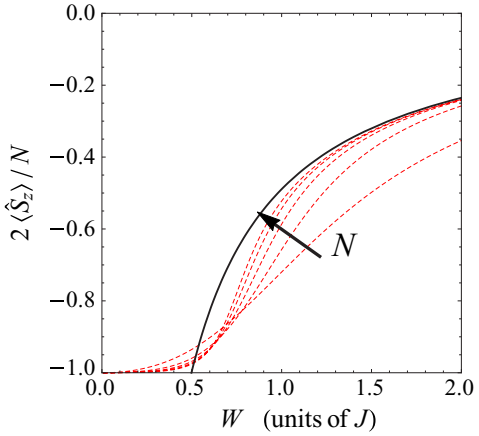

FIG. 5. (Color online) The "magnetization" $\langle\hat{S}_z\rangle$ along z, or in other words the degree of boson excitation in the S and AS bases (or, equivalently, the degree of coherence between the L and R wells) in the ground state and plotted as a function of W. Note the change in behavior at the critical point $W = W_c = 0.5J$. The solid black curve shows the $N \to \infty$ case and the red dashed curves represent different values of N: 2, 4, 6, 8, 10, where the arrow indicates the direction of increasing N. The values of the other parameters are $\Delta\epsilon = \Delta\epsilon^a = 0$, $J^a = J$. According to Eq. (26), $\langle\hat{S}_z\rangle \to 0$ as $W \to \infty$.

Figure 5 displays $\langle\hat{S}_z\rangle$ as a function of W. The dashed red curves are each for a different value of N and were calculated using the full quantum theory. The solid black curve gives the thermodynamic limit, and was calculated using the mean-field theory. According to the latter, when $W > W_c$, we have

$$\lim_{N\to+\infty}\frac{2\langle\hat{S}_z\rangle}{N} = -\frac{J}{2W}\sqrt{\frac{J^{a2}+4W^2}{J^2+4W^2}}. \tag{26}$$

It is perhaps surprising how small a number of bosons is needed in order to converge to the $N \to \infty$ limiting case, which agrees with the fact that the model becomes critical in the thermodynamic limit. Except when N is very small, all the curves in Fig. 5 agree that when $W < W_c$ the bulk of the bosons remain in the symmetric mode, and when $W > W_c$ there is a macroscopic excitation into the antisymmetric mode tending to an equal population so that the z magnetization vanishes as $W \to \infty$ in agreement with the prediction given by Eq. (26). In this limit, the external "fields" J and J^a are irrelevant in comparison to the magnitude of the boson-impurity spin-x coupling. If the L/R symmetry of the ground state was allowed to be broken, then the system would choose to be aligned along either x or $-x$. However, both cases correspond to an equal superposition along z and $-z$ and so the same $\langle\hat{S}_z\rangle \to 0$ result would be obtained as in the unbroken-symmetry case. Obviously, the symmetry breaking is visible if $\langle\hat{S}_x\rangle$ is plotted.

The Dicke model shows very similar qualitative dependence on g [67], the difference being the sensitivity: the Dicke model has more excitations for equal values of g and W. This is because the two-state nature of the impurity means that it can saturate, unlike a harmonic oscillator. Thus, when $W \to \infty$, the excitation of the impurity asymptotes to $\langle\hat{S}^a_z\rangle = 0$ (i.e., $Y = \pm\frac{1}{2}$), while the number of photons in the Dicke model

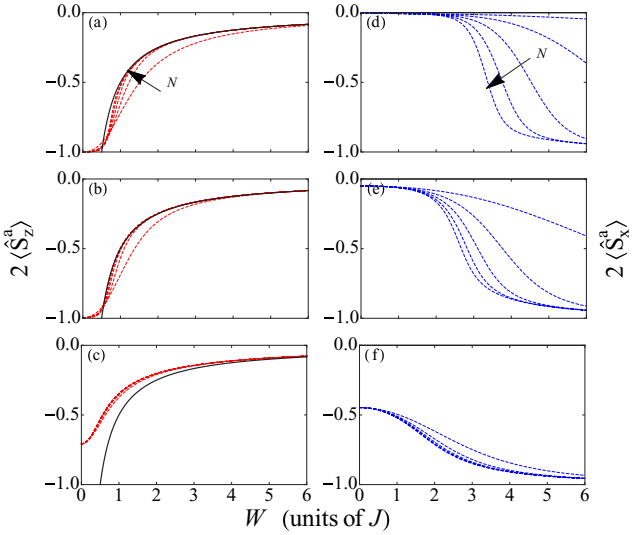

FIG. 6. (Color online) The effect of a finite-boson tilt upon the impurity magnetization. The left-hand column shows $\langle\hat{S}^a_z\rangle$ as a function of W for the ground state which measures the degree of excitation from the S mode into the AS mode (or, equivalently, the coherence between the L and R modes). The right-hand column shows $\langle\hat{S}^a_x\rangle$ which is the conjugate quantity to $\langle\hat{S}^a_z\rangle$. Each row is for a different value of the boson tilt: (a) $\Delta\epsilon = 0.01J$, (b) $\Delta\epsilon = 0.1J$, and (c) $\Delta\epsilon = J$. The dotted lines are each for a different N: 2, 4, 6, 8, 10, where the arrow indicates the direction of increasing N. The solid black curve plots the $N \to \infty$ limit for *zero tilt*, i.e., $\Delta\epsilon = 0$. The values of the other parameters are $J^a = J$, $W_c = 0.5J$, $\Delta\epsilon^a = 0$.

increases quadratically for large values of g:

$$\lim_{N\to+\infty}\frac{2\langle\hat{c}^\dagger\hat{c}\rangle}{N} = \frac{2g^2}{\omega_A^2}\left(1-\frac{\omega_A^2\omega_B^2}{16g^4}\right). \tag{27}$$

The degree of excitation of the impurity and the number of photons will only be of the same order near the critical value of g.

Let us now explicitly break the L/R symmetry of the double well. A nonzero tilt breaks the Z_2 parity symmetry and this prevents the system from being critical in the thermodynamic limit. The corresponding effect in the Dicke model is obtained by driving the boson mode and/or the spins [87]. In Fig. 6, we show the effect of different boson tilt values on the impurity by plotting $\langle\hat{S}^a_z\rangle$ and $\langle\hat{S}^a_x\rangle$ as functions of W. Analogously to the equivalent quantities for the bosons, the interpretation of $\langle\hat{S}^a_z\rangle$ is that it gives the degree of excitation (number difference) of the impurity from the S mode into the AS mode or, equivalently, the degree of coherence of the impurity between the L and R modes which vanishes when the impurity settles into just one well (which well is determined by the applied boson tilt). $\langle\hat{S}^a_x\rangle$ is the conjugate quantity and gives the coherence between the S and AS modes or, equivalently, the number difference between the L and R modes. We see that the tilt does not have a great effect in the vicinity of W_c until Fig. 6(c), where the tilt has the same magnitude as the tunneling energy and the system "realizes" it is tilted. To understand this better, we note that in the noninteracting limit $W = 0$, the Hamiltonian in the S and AS bases for the impurity is simply $\hat{H}_I = 2J^a\hat{S}^a_z - \Delta\epsilon^a\hat{S}^a_x$. Hence, for $W = 0$

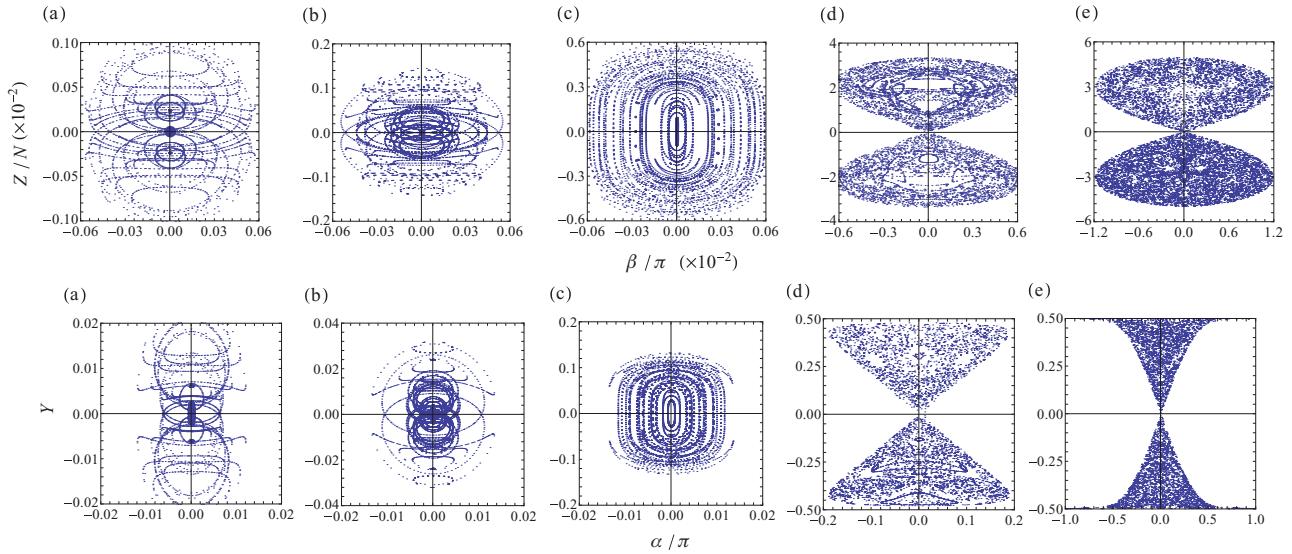

FIG. 7. (Color online) Poincaré sections showing the emergence of chaos as W increases through W_c. Top row: (β, Z) plane with each point corresponding to $\alpha = 0$. Bottom row: (α, Y) plane with each point corresponding to $\beta = 0$. From left to right, the plots increase in W: (a) $W = 0.5W_c$, (b) $W = 0.75W_c$, (c) $W = W_c$, (d) $W = 1.25W_c$, and (e) $W = 1.5W_c$. The values of the other parameters are $N = 500$, $\Delta\epsilon = \Delta\epsilon^a = 0$, $J^a = J$, and $E_{\text{shell}} = -501J$. For each plot, 30 random on-shell initial conditions are used and are evolved over a period $\tau = 150$ ($\tau = Jt/\hbar$). Please note the different ranges for each panel.

we have $\langle \hat{S}_z^a \rangle = -J^a/\sqrt{(4J^a)^2 + (\Delta\epsilon^a)^2}$. This finite degree of S and AS excitations, or equivalently, reduction in L and R coherences even in the noninteracting regime is yet another sign that for a nonvanishing tilt of the double well, the criticality appearing in the thermodynamic limit is lost. Indeed, the finite tilt restores the correspondence between the mean-field and quantum $\langle \hat{S}_x \rangle$ results: without a tilt, the quantum system does not choose a particular well and enters a Schrödinger cat state which has no classical correspondence. Only when fluctuations due to an external environment are included does the cat state collapse randomly to one or the other of the two wells. On the other hand, in the presence of tilt, the cat state never really forms.

V. MEAN-FIELD DYNAMICS

The main feature of classical (mean-field) dynamics in the Dicke model is global chaos when $g > g_c$ [68]. In this section, we employ Poincaré sections through phase space as a visual tool to investigate the emergence of chaos in the boson and impurity systems. Figure 7 shows Poincaré sections for the bosons (top row) and the impurity (bottom row) as W is increased at a fixed total energy. The dynamics takes place on an energy shell with energy equal to that of the unstable point located at $(\alpha, Y, \beta, Z) = (0,0,0,0)$, i.e., $E_{\text{shell}} = -NJ - J^a$. This corresponds to the center of the lowest band, and when the loop appears it becomes the unstable upper branch of the loop. We see that as W increases, chaos emerges and for $W > W_c$, chaos is dominant and ergodicity is observed.

In Fig. 8, we show Poincaré sections on different energy shells all with a fixed value of $W = 1.5W_c$ (so that we are always in the chaotic regime) in order to see how chaos depends on our position in the spectrum. The energy shell range is $-JN - J^a \leqslant E_{\text{shell}} \leqslant JN + J^a$ which covers the region between the two loops as shown in Fig. 1(c). The top two rows are for the bosons and the bottom two rows are for the impurity. Going from left to right, each plot shows an increase in the energy shell by $100J$ which is $\frac{1}{10}$ of the range for $J^a = 2J$ and $N = 498$. We see that the region of phase space accessible to the bosons is quite restricted, whereas the impurity can access its entire phase space. This is due to the small impurity hopping energy J^a relative to JN. The bosons can be thought of as a reservoir of energy, whose dynamic behavior on a global scale is scarcely affected by the impurity. However, locally the dynamics takes place in a band whose thickness depends on J^a; within the band, there is chaos.

In the bottom two rows of Fig. 8 we see that the dynamics of the impurity gets less chaotic as the energy shell is increased, and then becomes more chaotic again. To explain this, we note that the initial and final energy shells sit on the unstable branches of the lower and upper loops, respectively, and so are expected to be maximally chaotic. The symmetry of the classical stationary states about the point $E = 0$ [bottom plot Fig. 8(f)] gives this reduction and then increases in chaos as we move from one unstable branch to its symmetric twin. The location in phase space of the second unstable point is $(\pm\pi, 0, \pm\pi, 0)$. The top plot [Fig. 8(f)] shows the dynamics of the bosons when $E_{\text{shell}} = 0$. We see that when $\beta = 0$ or $\beta = \pm\pi$, $Z = \pm N/2$ and when $Z = 0$, $\beta = \pm\pi/2$, so the bosons are always at a maximal distance from the unstable points in phase space. When we increase E_{shell} further, we see the dynamics converges to regions around $(\beta, Z) = (\pm\pi, 0)$ which causes an increase in chaotic behavior of the impurity. The important point to make here is that for our parameters, the energy needed by the impurity to access all of its phase space is small compared to the energy of the entire system. This means that the impurity has access to the regions around $(\alpha, Y) = \{(0,0), (\pm\pi, 0)\}$. However, because the unstable points

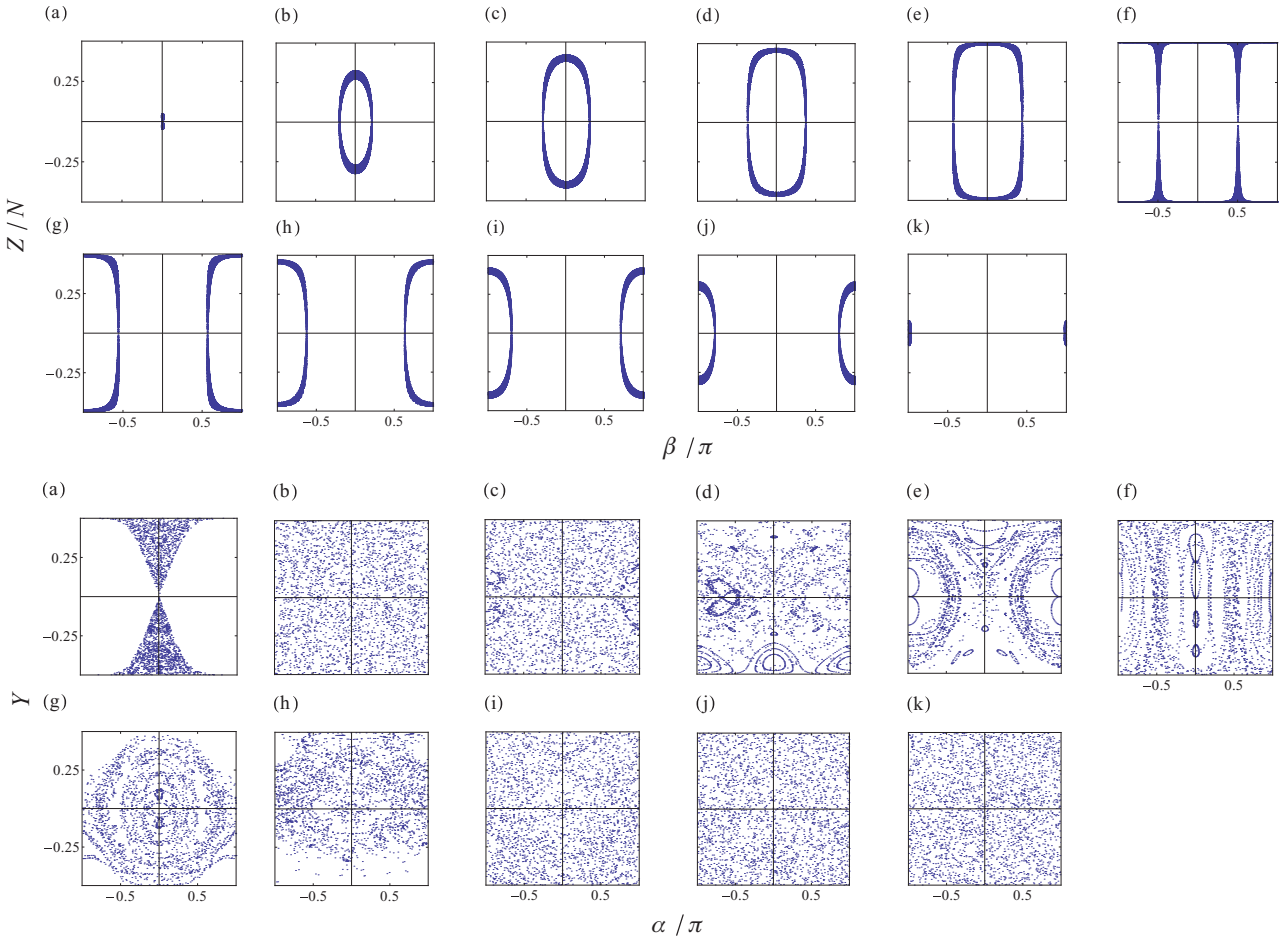

FIG. 8. (Color online) Variation of Poincaré sections with energy shell. The top two rows show the (β,Z) plane with each point corresponding to $\alpha = 0$ and the bottom two rows show the (α,Y) plane with each point corresponding to $\beta = 0$. From left to right, the plots increase in energy shell: (a) $E_{\text{shell}} = -500J$, (b) $E_{\text{shell}} = -400J$, (c) $E_{\text{shell}} = -300J$, (d) $E_{\text{shell}} = -200J$, (e) $E_{\text{shell}} = -100J$, (f) $E_{\text{shell}} = 0J$, (g) $E_{\text{shell}} = 100J$, (h) $E_{\text{shell}} = 200J$, (i) $E_{\text{shell}} = 300J$, (j) $E_{\text{shell}} = 400J$, and (k) $E_{\text{shell}} = 500J$. The values of the other parameters are $N = 498$, $\Delta\epsilon = \Delta\epsilon^a = 0$, $J^a = 2J$, and $W = 1.5W_c$. For each plot, 30 random on-shell initial conditions are used and are evolved over a period $\tau = 150$ ($\tau = Jt/\hbar$).

live in four-dimensional (4D) phase space, it is not enough for just the impurity to access this point in order to achieve maximum chaos: the bosons must at the same time access $(\beta,Z) = \{(0,0),(\pm\pi,0)\}$. Therefore, the degree of chaos of the impurity dynamics depends on how close the bosons are to $(\beta,Z) = \{(0,0),(\pm\pi,0)\}$.

In order to locate the precise value of W at which chaos emerges, we divide the impurity phase space into M subintervals defining a probability as $p_i = m_i/\mathrm{M}$ where m_i is the number of points in the ith subinterval (and we run the dynamics until $\sum m_i = M$). With this probability, we can define an entropy in the usual way as

$$S_{\text{MF}} = -\sum_i p_i \ln p_i. \tag{28}$$

Equation (28) can be thought of as a way to quantify the area of the phase space the impurity can explore. Even if the value of S_{MF} depends quantitatively on the partitioning of the phase space, we expect it to show some generic qualitative features. For example, looking at both extremes, if the points can be found entirely in one subinterval, then $S_{\text{MF}} = 0$ and if the points are maximally spread, then $p_i = 1/\mathrm{M}$, for all i, and $S_{\text{MF}} = \ln \mathrm{M}$. Since a system becomes ergodic when chaos is dominant, we expect higher values of S_{MF} as W increases. Looking at Fig. 9, this is exactly what we find. At $W = W_c$ there is a jump in S_{MF} signaling the onset of ergodicity.

Next, we look at another common aspect of classical chaos: sensitivity to initial conditions. Figure 10 shows the time dependence of Y and Z for $W < W_c$ (top row) and $W > W_c$ (bottom row). All dynamics takes place near $E_{\text{shell}} = -NJ - J^a$ with two trajectories initially separated by $\Delta Z/Z = \Delta Y/Y = 10^{-4}$. For $W < W_c$, we see that both trajectories remain close. However, for $W > W_c$ we see the trajectories begin to diverge at $\tau \approx 10$ signaling a loss of information about the initial state of the system.

VI. IMPURITY-INDUCED SELF-TRAPPING

Generally speaking, classical trajectories that set off in the vicinity of a stable fixed point remain close to the fixed point. Thus, the pitchfork structure of the fixed points, as

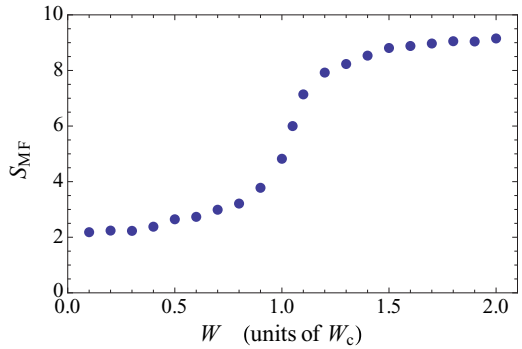

FIG. 9. (Color online) Mean-field entropy as a function of W showing a jump at W_c. Each point is calculated using Eq. (28) after dividing Poincaré sections for the impurity into subintervals 10^{-2} times the size of the αY plane. The other parameters of the plot are $J^a = J$, $N = 500$, $\Delta\epsilon = \Delta\epsilon^a = 0$, and $E_{\text{shell}} = -501J$. For each calculation, 100 random on-shell initial conditions were used and plotted until 20 000 intersections with the Poincaré plane were produced.

demonstrated in Fig. 3, implies that the classical system can become locked with a large population imbalance of the bosons: a large fraction of the bosons remains in one well and does not tunnel to the other well. This is the phenomenon of self-trapping [37,38]. Self-trapping in bosonic Josephson junctions derives from the self-interaction between the atoms and can maintain large differences in the populations of the two wells. Roughly speaking, the interaction effectively shifts the onsite energies in the two wells, and whenever there is a large population imbalance and strong shifts, the coherent tunneling becomes heavily detuned which therefore hinders the oscillations. While this effect is rather general, for atomic

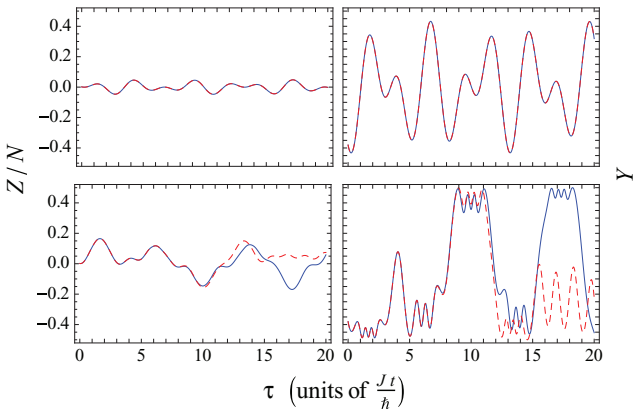

FIG. 10. (Color online) The atom number difference between the right and left wells as a function of the dimensionless time parameter τ ($\tau = Jt/\hbar$). Each row corresponds to a different value of W: $W = 0.5W_c$ (top row) and $W = 2W_c$ (bottom row). Each plot is generated using the same initial conditions for the number differences for the bosons and the impurity on the energy shell $E_{\text{shell}} = -100.5J$. The dashed red curves and solid blue curves differ by $\Delta Z/Z = \Delta Y/Y = 10^{-4}$. The other parameter values are $N = 100$, $J^a = J$, and $\Delta\epsilon = \Delta\epsilon^a = 0$.

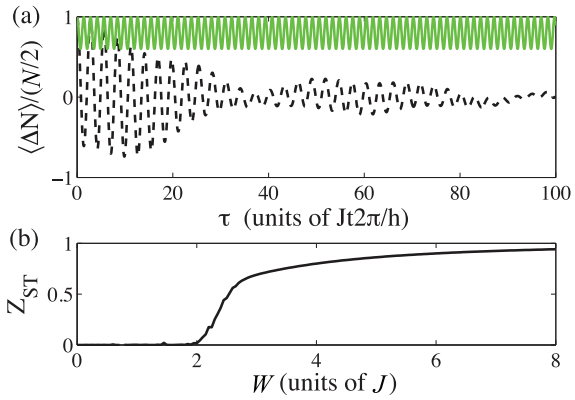

FIG. 11. (Color online) The evolution of the scaled boson population imbalance (a), and the long-time time average of the imbalance (b). In the upper plot, the dashed black curve displays the time evolution for an interaction strength $W = 1J$. For this interaction strength, no self-trapping occurs and the collapse of oscillations is due to the buildup of impurity-boson correlations. For $W = 4J$ (green solid curve), self-trapping is clearly apparent. Plot (b) demonstrates how the self-trapping sets in at around $W \approx 2J$ for the current parameters. The initial state has all the bosons in the right well and the impurity in the left well, and the rest of the parameters are $J^a = J$, $\Delta\epsilon = \Delta\epsilon^a = 0$, and $N = 100$.

condensates it was first demonstrated in a BEC double-well system [20].

The situation is different in the present setup where the bosons are noninteracting and so self-trapping can only stem from the boson-impurity interaction. A basic understanding of this case can be gained by fixing a value of $\Delta M \neq 0$ and setting $\Delta\epsilon = \Delta\epsilon^a = 0$. Referring to the Hamiltonian (1) expressed in the L and R bases we see that as far as the bosons are concerned, the impurity acts as an effective tilt which is the origin of the self-trapping. In this "adiabatic" picture, the motion of the bosons is free and can be solved exactly. In a complete description, the state of the impurity atom is itself also evolving and the coupled boson-impurity dynamics must be taken into account.

We demonstrate self-trapping by integrating the full quantum model of Eq. (1) for an initial state of N bosons in the right well and the impurity atom in the left well [88]. For small interactions W, both the impurity and the bosons display coherent oscillations between the two wells, as shown by the dashed black curve of Fig. 11(a). The mixing of time scales in this regime leads to a relaxation of the oscillations. During the decay period, a large entanglement is shared between the impurity and the bosons. Increasing W now leads to a rapid decrease of the amplitude of the Josephson oscillations in agreement with the expected trapping effect (green solid line). An estimate of the degree of the self-trapping can be obtained by calculating the long-time time average

$$Z_{\text{ST}} = \frac{1}{T_2 - T_1}\int_{T_1}^{T_2} dt\, \frac{\langle\Delta\hat{M}\rangle}{N/2}, \tag{29}$$

where $T_2 \gg T_1 \gg 0$ are two long times (as discussed below, there is another time scale for which the self-trapping is lost, and T_1 and T_2 should be long compared to the Josephson

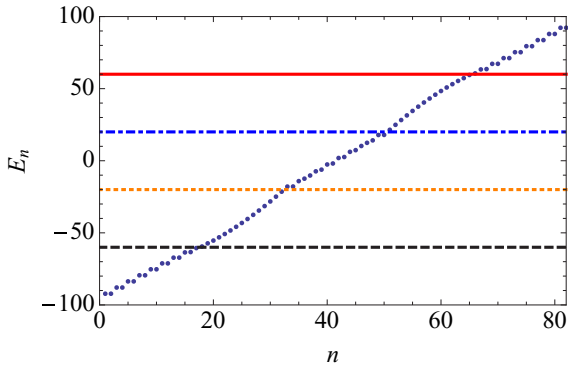

FIG. 12. (Color online) The quantum energy levels (blue dots) for $N = 40$, $J^a = 20J$, $W = 4J$, $W_c = \sqrt{2}J$, and $\Delta\epsilon = \Delta\epsilon^a = 0$. N is chosen relatively small so that the finer details of the spectrum are visible. The four horizontal lines give the positions of the mean-field stationary solutions as shown in Fig. 1 and we have maintained the same color scheme as there, namely, in ascending order: $E = -NJ - J^a$ ($\alpha = \beta = 0$, dashed black), $E = -NJ + J^a$ ($\alpha = \pi$, $\beta = 0$, dotted orange), $E = NJ - J^a$ ($\alpha = 0$, $\beta = \pi$, dotted-dashed blue), $E = NJ + J^a$ ($\alpha = \beta = \pi$, solid red). Note that because $W > W_c$, the lowest- and highest-energy classical solutions have loops and the positions given here correspond to the unstable branch, that is, the highest and lowest branches of the lower and upper loops, respectively.

oscillation period but short compared to the decay of the trapping effect). Figure 11(b) shows the W dependence of $Z_{\rm ST}$. There is a sudden onset of self-trapping at around $W \approx 2J$ for which the population imbalance increases rapidly and tends asymptotically to 1. We have numerically determined that the critical interaction $W_{\rm ST}$ for which self-trapping starts is only weakly dependent of atom number N and J^a, while it scales linearly with J, more precisely $W_{\rm ST} \approx 2J$.The critical coupling value here is $W_c = 0.2\,J$, so $W_{\rm ST} \approx 10\,W_c$.

As already mentioned, the Hamiltonian (1) supports a Z_2 parity symmetry. Each parity sector constitutes a separate spectrum and for nonzero W and in the large-N limit, the two spectra become identical. The energy gap δ between corresponding even- and odd-parity eigenstates is found to close exponentially fast with N, i.e., $\delta \sim \exp(-aN)$ for some N-independent constant a. In the self-trapping regime, the gap also closes exponentially with the interaction strength W, an effect that is associated with below-barrier tunneling in the double-well potentials that form in Fock space when $W > W_c$ and whose stationary points give the pitchfork bifurcation. To illustrate this, the full energy spectrum is plotted in Fig. 12 for different parameters than Fig. 11 to properly show the distinct regions of the spectrum. The most striking feature of Fig. 12 is that inside the lower and upper loops, *all* the energy levels are paired up in quasidegenerate pairs.

To see how self-trapping works schematically, consider a state initially localized in the L well. This state can be made by the superposition of an even-parity eigenstate and an odd-parity eigenstate $|{\rm L}\rangle = (|{\rm E}\rangle \exp[-i\omega_{\rm E}t] + |{\rm O}\rangle \exp[-i\omega_{\rm O}t])/\sqrt{2}$. If these states make up one of the quasidegenerate pairs, then the difference in the two energies is exponentially small $\delta = \hbar\omega_{\rm O} - \hbar\omega_{\rm E}$ and the time evolution of the superposition into the $|{\rm R}\rangle$ state is very slow. We have verified this numerically and also that the characteristic time for this collapse scales as $\tau_{\rm col} \sim K^N$ for some constant K. Since our initial state is not near the ground state, W must be increased past W_c until the loop envelops it and the effects of the quasidegenerate pairs can be felt. It is for this reason $W_{\rm ST} > W_c$, and $W_{\rm ST}$ will of course be different for different initial states. Naturally, this exponential growth of the collapse time means that the collapse will most likely be far beyond any realistic experimental observation. Of course, a general self-trapped state will be a projection over many eigenstates not just a single pair, but if the wave packet lies entirely within one of the loops it will be self-trapped because it will be solely made up of quasidegenerate even and odd pairs. However, the energy separation between different pairs introduces a different and larger energy scale than the tunnel-splitting effect and hence a faster oscillation about the mean value of ΔN as can be seen in the solid green curve in Fig. 11(a).

It has been argued that the mechanism behind self-trapping in a bosonic Josephson junction can be viewed as a quantum Zeno effect; the atom-atom interaction acts as an effective measurement in which the state of single atoms is measured by the remaining ones [89] (external measurement-induced Zeno effects on self-trapping have also been discussed [90]). The question then arises as to whether in the present self-trapping setup the bosons perform an effective measurement on the impurity (or vice versa)? During a standard quantum measurement, the meter (e.g., the bosons) becomes entangled with the system (e.g., the impurity) and in order for the measurement to distinguish between the two possible states they should be macroscopically distinguishable, i.e., a Schrödinger cat state should form. Finally, the cat state is collapsed by an environment and the state of the system can be read off from the state of the meter with which it is now perfectly classically correlated. The case of self-trapping is different because deep in the self-trapping regime, the bipartite state factorizes as the bosons and the impurity occupy *definite* positions due to our initial preparation of the system and are not in superpositions of both wells. In other words, they are classically anticorrelated but there is approximately no quantum entanglement shared between the two parties, i.e., the von Neumann entropy $S_{\rm vN} = -{\rm Tr}_{\rm im}[\hat{\rho}_{\rm im}\log(\hat{\rho}_{\rm im})]$ (where $\hat{\rho}_{\rm im}$ is the reduced density operator for the impurity atom, the trace is over the bosons, and the logarithm is to base two) approaches zero in the self-trapping regime, while the correlator $G_{\rm NM} = \langle\Delta\hat{N}\Delta\hat{M}\rangle/(N/2)$ goes towards -1. The above arguments are demonstrated in Fig. 13: (a) shows the time-averaged entropy and (b) the time-averaged correlator. It is noteworthy that the convergence of the correlator is slower than that of the entropy. We have not ruled out the quantum Zeno effect being at work here because that too begins with evolution from a known initial state. More discussion of the von Neumann entropy for this system and particularly the effect of tilt can be found in Sec. VIII of Ref. [4].

As a final remark, we note that the self-trapping effect described here is related to *population trapping* [91] and the locking of the atomic dipole to the quantized field predicted by the Jaynes-Cummings model [92]. More precisely, when the field possesses a defined phase (e.g., a large amplitude coherent state) and the atomic dipole is

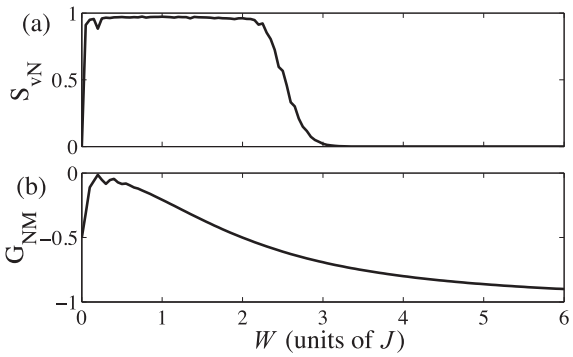

FIG. 13. The time-averaged von Neumann entropy S_{vN} (a) and scaled correlator $\langle \Delta\hat{N}\Delta\hat{M}\rangle/(N/2)$ (b). The two plots demonstrate the absence of entanglement and presence of classical anticorrelations deep in the self-trapping regime. The initial state and the parameters are the same as in Fig. 11.

aligned with the field (at zero detuning this implies that the spin of the two-level particle points in the σ_x direction), the atom and the field are phase locked. While the self-trapping phenomenon discussed above has not been directly studied in the Dicke model, we note that a direct outcome of this atom-field locking has been considered in terms of creation of Schrödinger cat states within the framework of the Tavis-Cummings model (Dicke model with the rotating-wave approximation applied) [93]. The same idea for preparation of cat states was recently also considered in the present impurity-boson model but again within the rotating-wave approximation [94].

VII. LEVEL-SPACING DISTRIBUTION

The idea that there is a connection between the properties of the energy levels of a quantum system and whether the classical limit of that system is integrable (regular) or chaotic goes back to Percival [62]. Berry and Tabor [63] first showed that the energy levels of "typical" or "generic" classically regular systems are, somewhat counterintuitively, distributed randomly so that the probability distribution for the spacings S between neighboring energy levels is Poissonian:

$$P_{\mathrm{P}}(S) = e^{-S}. \tag{30}$$

Conversely, they predicted that the energy levels of classically chaotic systems should display level repulsion because they are correlated with each other. More precisely, Bohigas, Giannoni, and Schmit [95] conjectured that classically chaotic systems which are time-reversal invariant (such as the real symmetric Hamiltonian matrices under study here) should obey level statistics which are the same as those of random matrices drawn from the Gaussian orthogonal ensemble (GOE), thus making a connection to the program initiated by Wigner [96], with important contributions by Dyson [97], of using random matrices to understand the properties of complicated Hamiltonians. The nearest-neighbor spacings of the GOE obey the Wigner-Dyson distribution which is given approximately by

$$P_{\mathrm{WD}}(S) \approx \frac{\pi S}{2} e^{-\frac{\pi S^2}{4}}. \tag{31}$$

Counter examples to this paradigm do exist: not all regular systems obey Poisson statistics as shown by the important case of coupled harmonic oscillators [63]. In fact, some regular systems display level repulsion and even have GOE statistics [98]. Similarly, chaotic systems are known which do not obey GOE [99]. Indeed, the elements of a GOE random matrix are chosen randomly from a Gaussian distribution, whereas most of the elements in our Hamiltonian are zero (in the Fock basis it is tridiagonal). Physically, this means that the GOE describes systems with infinite-range interactions [100], whereas the boson-impurity system has short-range ones. Therefore, we should not expect our system to necessarily conform to GOE statistics. Systems with a mixed classical phase space, some regions being regular and others chaotic, also defy classification purely in terms of either a Poisson or a Wigner-Dyson distribution. Nevertheless, the Dicke model does behave generically, obeying Poisson statistics when $g < g_c$ and Wigner-Dyson statistics when $g > g_c$ provided enough spins ($N \gtrsim 10$) are included in the calculation [66,67]. Interestingly, if the Dicke model is reduced to the Rabi model (a single spin coupled to a harmonic oscillator), then it does not behave generically any more, i.e., it displays neither Poisson nor Wigner-Dyson statistics [101,102]. The Rabi model is generally considered to be nonintegrable because the classical equations of motion obtained by averaging the Heisenberg equations of motion for the operators give chaotic motion [101], although recent progress on quantum integrability [103] has led to the claim that the Rabi model is in fact integrable (or quasi-integrable [104]) in a different, purely quantum, sense and the difference between the two designations is due to the lack of a quantum-classical correspondence for a spin-$\frac{1}{2}$ particle. In this section, we address the question as to whether the simplified version of the Dicke model discussed here has different spectral statistics below and above W_c and, if so, whether this change is from Poisson to Wigner-Dyson statistics?

The first step in obtaining the level-spacing distribution is to separate the eigenvalues based on their symmetry. Symmetries are in some sense special, or nongeneric, and lead to degeneracies that will skew the statistics away from universality. In particular, at zero tilt our Hamiltonian has a Z_2 parity symmetry that breaks it up into two independent blocks (one even and one odd), each of dimension $N+1$. We perform statistics on the two parity blocks separately and add the results together at the end [105].

The second step in obtaining the level-spacing distribution is to *unfold* the spectrum of each block. This is a standard procedure which rescales the local mean level spacing $\Delta E/\Delta N$, where $\Delta N(E)$ is the number of levels lying in the energy range ΔE, so that it is equal to unity, allowing spectral statistics from different systems or also different regions of the same spectrum to be compared despite originally having different mean level spacings. To explain unfolding, we start from the exact expression for the density of states

$$\rho(E) = \sum_{i=1}^{N+1} \delta(E - E_i), \tag{32}$$

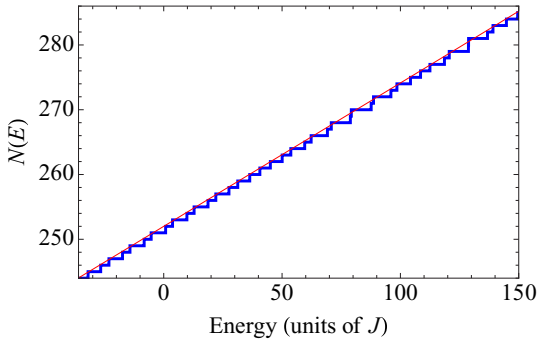

FIG. 14. (Color online) A part of the central section of the spectral staircase for the odd-parity block of the Hamiltonian. $N(E)$ counts the number of energy levels below energy E. The exact value of $N(E)$ is given by the blue steps and the local average $\bar{N}(E)$ is given by the smooth red line. The latter is calculated from the former by a polynomial fit. Parameter values are $N = 500$, $J^a = 0.68\,NJ$, $W = 4.1\,J \approx 2.47\,W_c$, and $\Delta\epsilon = \Delta\epsilon^a = 0$.

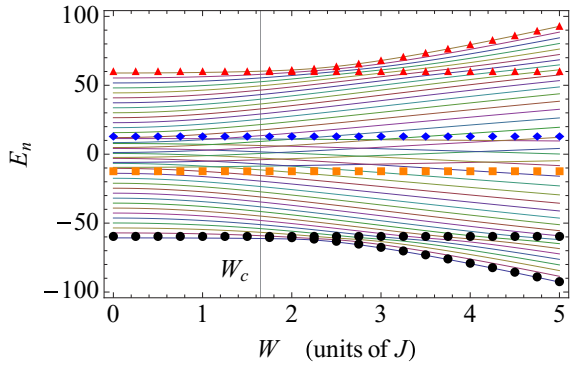

FIG. 15. (Color online) Quantum energy levels (solid curves) versus boson-impurity interaction W for $N = 40$ and $\Delta\epsilon = \Delta\epsilon^a = 0$. This plot only shows the energies of the even-parity eigenstates as the odd states behave similarly. The symbols mark the energies of the classical stationary points using the same scheme as Fig. 1. In particular, the four straight horizontal lines correspond to the energies $E = \{-NJ - J^a, -NJ + J^a, NJ - J^a, NJ + J^a\}$, with the formation of the loops at $W = W_c$ (marked by the solid vertical line) clearly visible. Other parameters: $J^a = 0.68\,NJ$.

where E_i is the energy of ith level, and define the spectral staircase as

$$N(E) \equiv \int_{-\infty}^{E} dE'\rho(E') = \sum_{i=1}^{N+1} \theta(E - E_i), \tag{33}$$

where θ is the Heaviside step function. This counts the number of levels up to energy E. The idea of unfolding hinges upon being able to separate the spectral staircase into an average, or smooth part $\bar{N}(E)$, and a fluctuating part $N_{\rm fl}(E)$:

$$N(E) = \bar{N}(E) + N_{\rm fl}(E). \tag{34}$$

The form of $N(E)$ is depicted in Fig. 14 with the full staircase in blue and the average $\bar{N}(E)$ given by the smooth red curve. $\bar{N}(E)$ is related to the average level density $\bar{\rho}(E) \equiv \Delta N/\Delta E$ as

$$\bar{N}(E) = \int_{-\infty}^{E} dE'\bar{\rho}(E'). \tag{35}$$

To unfold the original energy levels $\{E_1, E_2, \ldots, E_{N+1}\}$ to a new set $\{e_1, e_2, \ldots, e_{N+1}\}$, one can use $\bar{N}(E)$ as a map

$$e_i = \bar{N}(E_i); \quad i = 1,2,\ldots,N+1 \tag{36}$$

and this guarantees that $\bar{\rho}(e) = 1$ as explained in [107]. The final question is how to obtain $\bar{N}(E)$, and we choose a method where a low-order polynomial (maximum fourth order in our case) is numerically fitted to the spectral staircase [98,108–110]. The unfolded level spacings S are then given by

$$S_i = e_{i+1} - e_i; \quad i = 1,2,\ldots,N. \tag{37}$$

It is important to appreciate that the description of the spectral staircase in terms of an average part and a fluctuating part is somewhat arbitrary. Indeed, by fitting the energy levels to a high enough polynomial we could also capture the fluctuations. The distinction between $\bar{N}(E)$ and $N_{\rm fl}(E)$ only makes sense if there is a clear separation of scales between the two, with $\bar{N}(E)$ only varying very little over the mean level spacing $1/\bar{\rho}(E)$. Returning to Fig. 12, we already see a hint that the spectrum for boson-impurity model can undergo abrupt changes at the energies corresponding to the classical turning points where the assumption of separation of scales will break down (these kinks in the spectrum become more obvious as N is increased). The change in the nature of the spectrum at the energies of the classical stationary points can also be seen in Figs. 15 and 16. The most striking feature of Fig. 15, which plots energy levels as a function of W and only has $N = 40$ so that we an identify individual energy levels, is that the central portion of the spectrum (that lies in the range $-NJ + J^a < E < NJ - J^a$ and is bounded by the orange squares at the bottom and the blue diamonds at the top) is quite different from the other regions because it contains avoided crossings as a function of W. The other regions do not display any obvious avoided crossing structure as a function of W. The loops that appear at the very bottom and very top of the spectrum when $W > W_c$ are clearly visible in Fig. 15. The energy-level separations of states lying inside the loops are slightly smaller than those of the neighboring regions, and these are different again from those of the central region, and hence the kinks in the spectrum in Fig. 12 at the boundaries between the five different regions which exist when $W > W_c$. This behavior can also be seen in Fig. 16, which plots the nearest-neighbor energy separations when $N = 500$ for two different values of W, one with $W < W_c$ and the other with $W > W_c$. The central region is always distinctive due to the avoided crossings, but the spacings become seemingly irregular when $W > W_c$. The two downward-pointing cusps near $n = 100$ and 400 correspond to the unstable branches of the loops. It should be noted that in this section we have chosen J^a randomly so that it is incommensurate with J making the system more generic.

The sudden changes in the level statistics at the boundaries between the five regions oblige us to unfold each region separately. Once they are unfolded, they can then be combined although we choose not to combine the central region with the other four because we find it always displays unique statistics. The statistics are illustrated in Fig. 17 where the top row

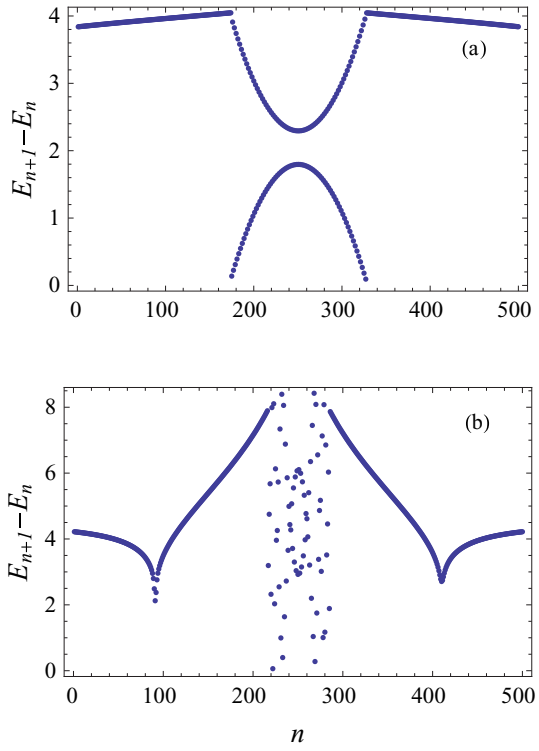

FIG. 16. (Color online) Nearest-neighbor energy-level spacings for $N = 500$ and $\Delta\epsilon = \Delta\epsilon^a = 0$. This plot only shows the spacings between the energies of the even-parity eigenstates: the odd-state spacings behave similarly. Each panel has a different value of the boson-impurity interaction energy: (a) $W = 0.45J$, (b) $W = 4.1J$. Here, $W_c = 1.66J$. The other parameters are the same as Fig. 15.

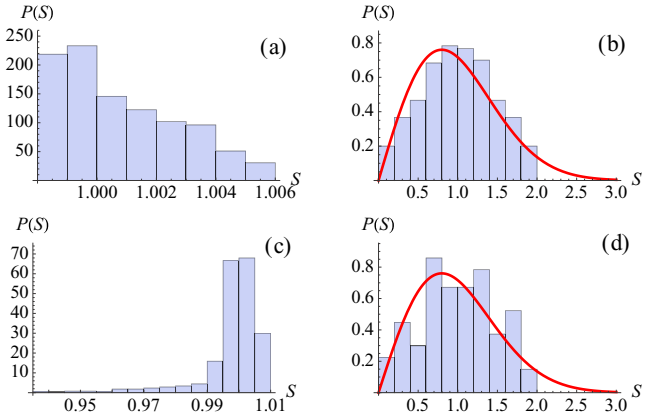

FIG. 17. (Color online) Probability distributions for nearest-neighbor level spacings illustrating the difference between $W < W_c$ (top row) and $W > W_c$ (bottom row). The left column is for the total spectrum excluding the central region between the ($\alpha = \pi$, $\beta = 0$) and ($\alpha = 0$, $\beta = \pi$) classical stationary points, i.e., $-NJ + J^a < E < NJ - J^a$, and the right column is for the central region of the spectrum only. For comparison, in the right column we have also plotted the Wigner-Dyson distribution (solid red curve) as given by Eq. (31). Parameters: $N = 500$, $J^a = 0.68\,NJ$, giving $W_c = 1.66J$. Top row: $W = 0.45J \approx 0.27\,W_c$; Bottom row: $W = 4.1J \approx 2.47\,W_c$. $\Delta\epsilon = \Delta\epsilon^a = 0$. In order to make these plots, the energy levels were unfolded as described in the text using a polynomial of the form $c_0 + c_1x + c_3x^3$ for panels (a) and (b) and a polynomial of the form $c_0 + c_1x + c_2x^2 + c_3x^3 + c_4x^4$ for panels (c) and (d).

corresponds to $W < W_c$ and the lower row to $W > W_c$, while the left column gives the combination of all the separately unfolded statistics, including even and odd blocks, for all the regions except the central one and the right column gives the same but for the central region. We see that none of the statistics correspond to either Poisson or Wigner-Dyson distributions. In fact, the distributions shown in Figs. 17(a) and 17(c) are reminiscent of those for the Rabi model given in Figs. 1 and 2 in [101]. We attribute this lack of genericity to having two oscillators which retain much of their oscillator structure despite the coupling. Indeed, when $W = 0$ (not shown), we have two uncoupled oscillators with frequencies J and J^a. The spectrum is then of the rigid "picket fence" type [67], familiar from the harmonic oscillator, and takes the form

$$E_{k,l} = J(2k - N) + J^a(2l - 1); \quad k = 0,1,2,\ldots,N \quad l = 0,1. \tag{38}$$

This structure is expected to be maintained as long as $W \ll J$. At the other end of the scale, when W becomes very large and dominates J and J^a, the eigenvectors of the Hamiltonian given in Eq. (1) tend to the number-difference eigenstates and are doubly degenerate. The degenerate pairs again form a rigid ladder with a spacing between the rungs of $W/2$.

Let us now consider intermediate values of W. When $W = 0.45J$ (which is less than W_c), we see from Fig. 17(a) that the statistics of the outer regions of the spectrum have evolved into a Poisson-type distribution, while from Fig. 17(b) the statistics of the central region is not of Poisson type but is instead very symmetrically distributed around the average value $S = 1$ (recall that unfolding sets $\bar{S} = 1$). Although we refer to the statistics in Fig. 17(a) as Poisson type, they are clearly not of the form given in Eq. (30) because they do not begin at $S = 0$ and are tightly compressed into the tiny range $0.998 \leqslant S \leqslant 1.006$. Nevertheless, their structural resemblance to a shifted, compressed, Poisson distribution suggests that they represent random fluctuations on the back of a very rigid oscillator spectrum. When $W = 4.1J$, which is here greater than W_c, we see from Fig. 17(c) that the fluctuations in the outer regions cover a much larger range of S (about one order of magnitude larger) than when $W = 0.45J$. They are also no longer Poisson type, with the peak shifting from the lower end to near the top end of the distribution. Comparing Figs. 17(a) and 17(c) shows that the statistics clearly do change with W, and from the reshaping of the distributions it seems reasonable to claim this effect as level repulsion (note again that the unfolding still always maintains $\bar{S} = 1$) arising from the chaotic behavior when $W > W_c$.

The central region of the spectrum, meanwhile, does not undergo any qualitative change in its level statistics as W passes through W_c as can be seen by comparing Figs. 17(b) and 17(d), although the statistics in 17(d) do seem a little more irregular than in 17(b). In contrast to the outer four regions of the spectrum, the nearest-neighbor level spacings in the central region are spread fairly evenly over a wide range

extending between $0 \leqslant S \leqslant 2$. Although the statistics for the central region are certainly not Poissonian, they do not really follow the Wigner-Dyson distribution either. Nevertheless, the fact that the peak occurs well away from $S = 0$ is perhaps a manifestation of level repulsion which occurs both below and above W_c.

In summary, we see that the single-impurity model discussed here does not reproduce the universal level statistics that are seen so unambiguously in the Dicke model [66,67] but instead gives nongeneric statistics with some similarities to those given by the Rabi model [101]. Certain regions of the impurity model spectrum seem to retain an oscillatorlike nature even when W is large. This lack of universality could be due to a number of factors, including the chaos being in some sense weak, as can be inferred from the persistence of integrable regions of phase space above W_c in our Poincaré plots in Figs. 7 and 8. When considered in light of the Kolmogorov-Arnold-Moser theorem [111–113], which states that integrable tori are not all immediately destroyed by a nonlinear perturbation (those with the most irrational frequencies survive to larger perturbations), this suggests that the nonlinearity in the single-impurity model is perturbative. By contrast, Poincaré plots for the Dicke model [67,68] display a mixed phase when $g < g_c$, but very rapidly become completely chaotic when $g > g_c$ providing N is large.

Of course, our system with a single impurity is only one step away from integrability (pure boson case) and so may not be irregular enough to see a clearer change from Poissonian to Wigner-Dyson distributions. A more complex Hamiltonian than Eq. (1) including, say, different intrawell interactions [110] or more impurities, might show more generic behavior.

VIII. DISCUSSION AND CONCLUSIONS

Placing the impurity system in a double-well potential allows many-body effects to be brought to the fore in the venerable impurity problem. Indeed, the quenching of kinetic energy down to tunnel coupling allows us to achieve a strong coupling regime such that there is a symmetry-breaking bifurcation in the ground state due to the boson-impurity interaction at the critical value W_c. This corresponds to a macroscopic reorganization of the bosons and coincides with the critical coupling for a similar symmetry-breaking QPT in the Dicke model.

Using a stability analysis of the mean-field solutions, we studied swallowtail loops that emerge in the energy spectrum when plotted as a function of either W or the tilt $\Delta\epsilon$. These loops play an important role in organizing the quantum spectrum and determining its nature. Notice that, except for the validity of the mean-field equations, there is no requirement in our treatment that the bosons should form a BEC. In the two-mode regime, a large fraction generally do form a BEC although at the bifurcation the depletion can become significant. However, the range of values of W where the system is critical, i.e., where the fluctuations in atom numbers between the two wells are non-Gaussian, is very narrow and on general grounds (e.g., the Bogoliubov theory) is expected to scale as $1/N^2$.

We used two different methods to show that classical (mean-field) chaos appears when $W > W_c$: Poincaré plots showed a fading of regular behavior and an increase in ergodicity, and trajectories with close initial conditions remained close for $W < W_c$, but diverged for $W > W_c$. Complementary to the mean-field calculations, a statistical analysis of the quantum energy levels revealed level repulsion sets in when $W > W_c$, albeit only for certain regions of the spectrum, level repulsion being one of the indicators of chaotic motion in the classical limit. Chaotic classical motion also occurs in the Dicke model above the QPT, but it is interesting to note that it is totally absent in the purely bosonic case (no impurity) due to the latter's integrability even though it can also display bifurcations and hence loops. The relationship between QPTs and mean-field chaos is therefore not an exclusive one.

We also found that self-trapping can occur in this system due purely to the boson-impurity interaction. We argued that the "impurity-induced" self-trapping states occur within the loops (as in the purely bosonic case) and have a lifetime scaling exponentially with the number N of bosons and so should be long lived for a moderate number of atoms. The self-trapping does not set in at $W = W_c$ because the loops are at that point only of infinitesimal size, but as W grows the loops grow and encompass a larger range of states.

We have claimed in this paper that the boson-impurity system can be regarded as a poor man's Dicke model. The same qualitative behavior occurs in both systems, and they appear to behave identically in the critical region with the exception of the energy-level statistics which are generic for the Dicke model (Poisson when $g < g_c$ and Wigner-Dyson when $g > g_c$) but nongeneric for the impurity model. It is remarkable that such a drastic reduction in the size of the Hilbert space preserves the critical features of the Dicke model. The lesson of this work is perhaps that all that is needed is a single additional state to simulate the presence of the harmonic oscillator.

At this point, we are led to wonder whether the bifurcation in the boson-impurity model is in fact a true second-order QPT like in the Dicke model (and whether the two are in the same universality class)? Studies of the purely bosonic case suggest that this is likely [36,42–45]. A modified version of the Dicke phase transition has recently been seen using cold atoms inside an optical cavity which is illuminated from the side by a laser [81]. Below the transition, most of the light passes through the cavity, but above it the atoms spontaneously form a matter-wave grating which efficiently scatters light into the cavity. The phase transition can be continuously observed by detecting the photons leaking through the end mirrors, but by the same token this means that the system is open and this modifies the critical behavior [82,85]. By contrast, our system is closed and so it may in fact give a better match to the quantum properties of the Dicke model.

In this paper, we have treated the many-body "environment", the bosons, exactly but they could also be integrated out to make connections to standard models of dissipative environments [1]. The conceptual and technical simplicity of a single impurity in a bosonic Josephson junction combined with the controllability of ultracold atoms make this an appealing toy model in which to study this type of problem and we hope to exploit this further in the future.

ACKNOWLEDGMENTS

We thank M. Olshanii and H. Pu for useful discussions. J.L. acknowledges support from the Swedish research council (VR) and D.O'D. acknowledges support from NSERC (Canada).

APPENDIX: A BASIS WITH WELL-DEFINED PARITY IN FOCK SPACE

Numerical diagonalization routines do not generally respect the parity of eigenstates that are nearly degenerate. This directly impacts the calculations of $\langle \hat{S}_z \rangle$ and the statistics of the level spacings since we separate the Hamiltonian into even- and odd-parity blocks. To overcome this obstacle, we force the eigenstates to have a well-defined or good parity (GP) by diagonalizing the Hamiltonian in a basis with given parity. Instead of using the "bare" Fock basis $|\Delta N, \Delta M\rangle$, we use a basis whose states are linear combinations of Fock states:

$$|\mathrm{GP}\rangle = \begin{cases} (|\Delta N, \Delta M\rangle + |-\Delta N, -\Delta M\rangle)/\sqrt{2}, \\ (|\Delta N, \Delta M\rangle - |-\Delta N, -\Delta M\rangle)/\sqrt{2}. \end{cases} \tag{A1}$$

After the diagonalization is complete, we still want to represent the eigenstates of the Hamiltonian in the Fock basis, so we rotate the parity states back with a unitary transformation

$$U^\dagger = \sum_{n=1}^{2N+2} |\mathrm{Fock}^{(n)}\rangle\langle \mathrm{GP}^{(n)}|. \tag{A2}$$

The Fock states now have good parity and can be used in our calculations.

[1] A. O. Caldeira and A. J. Leggett, Phys. Rev. Lett. **46**, 211 (1981); Ann. Phys. (NY) **149**, 374 (1983); **153**, 445(E) (1984).

[2] A. J. Leggett, S. Chakravarty, A. T. Dorsey, M. P. A. Fisher, A. Garg, and W. Zwerger, Rev. Mod. Phys. **59**, 1 (1987).

[3] M. Rinck and C. Bruder, Phys. Rev. A **83**, 023608 (2011).

[4] F. Mulansky, J. Mumford, and D. H. J. O'Dell, Phys. Rev. A **84**, 063602 (2011).

[5] P. Lu, Z.-H. Zhang, and S. Feng, and S.-J. Yang, Phys. Rev. B **86**, 104504 (2012).

[6] M. A. Cirone, G. De Chiara, G. M. Palma, and A. Recati, New J. Phys. **11**, 103055 (2009).

[7] I. Bausmerth, U. R. Fischer, and A. Posazhennikova, Phys. Rev. A **75**, 053605 (2007); U. R. Fischer, C. Iniotakis, and A. Posazhennikova, *ibid.* **77**, 031602(R) (2008).

[8] J. Larson, Phys. Rev. A **83**, 052103 (2011).

[9] S. McEndoo, P. Haikka, G. De Chiara, G. M. Palma, and S. Maniscalco, Europhys. Lett. **101**, 60005 (2013).

[10] Gh.-S. Paraoanu, M. Rodriguez, and P. Törmä, Phys. Rev. A **66**, 041603(R) (2002).

[11] H. T. Ng, C. K. Law, and P. T. Leung, Phys. Rev. A **68**, 013604 (2003).

[12] X. Q. Xu, L. H. Lu, and Y. Q. Li, Phys. Rev. A **78**, 043609 (2008).

[13] P. Ziń, B. Oleś, and K. Sacha, Phys. Rev. A **84**, 033614 (2011).

[14] H. P. Breuer, D. Burgarth, and F. Petruccione, Phys. Rev. B **70**, 045323 (2004).

[15] K. A. Al-Hassanieh, V. V. Dobrovitski, E. Dagotto, and B. N. Harmon, Phys. Rev. Lett. **97**, 037204 (2006).

[16] S. S. Garmon, P. Ribeiro, and R. Mosseri, Phys. Rev. E **83**, 041128 (2011).

[17] F. S. Cataliotti, S. Burger, C. Fort, P. Maddaloni, F. Minardi, A. Trombettoni, A. Smerzi, and M. Inguscio, Science **293**, 843 (2001).

[18] Y. Shin, M. Saba, T. A. Pasquini, W. Ketterle, D. E. Pritchard, and A. E. Leanhardt, Phys. Rev. Lett. **92**, 050405 (2004); Y. Shin, C. Sanner, G.-B. Jo, T. A. Pasquini, M. Saba, W. Ketterle, D. E. Pritchard, M. Vengalattore, and M. Prentiss, Phys. Rev. A **72**, 021604(R) (2005); G.-B. Jo, J.-H. Choi, C. A. Christensen, T. A. Pasquini, Y.-R. Lee, W. Ketterle, and D. E. Pritchard, Phys. Rev. Lett. **98**, 180401 (2007); G.-B. Jo, J.-H. Choi, C. A. Christensen, Y.-R. Lee, T. A. Pasquini, W. Ketterle, and D. E. Pritchard, *ibid.* **99**, 240406 (2007).

[19] Y.-J. Wang, D. Z. Anderson, V. M. Bright, E. A. Cornell, Q. Diot, T. Kishimoto, M. Prentiss, R. A. Saravanan, S. R. Segal, and S. Wu, Phys. Rev. Lett. **94**, 090405 (2005).

[20] M. Albiez, R. Gati, J. Fölling, S. Hunsmann, M. Cristiani, and M. K. Oberthaler, Phys. Rev. Lett. **95**, 010402 (2005).

[21] R. Gati, B. Hemmerling, J. Fölling, M. Albiez, and M. K. Oberthaler, Phys. Rev. Lett. **96**, 130404 (2006); J. Estève, C. Gross, A. Weller, S. Giovanazzi, and M. K. Oberthaler, Nature (London) **455**, 1216 (2008).

[22] T. Schumm, S. Hofferberth, L. M. Andersson, S. Wildermuth, S. Groth, I. Bar-Joseph, J. Schmiedmayer, and P. Krüger, Nat. Phys. **1**, 57 (2005); S. Hofferberth, I. Lesanovsky, B. Fischer, T. Schumm, and J. Schmiedmayer, Nature (London) **449**, 324 (2007); T. Betz, S. Manz, R. Bücker, T. Berrada, Ch. Koller, G. Kazakov, I. E. Mazets, H.-P. Stimming, A. Perrin, T. Schumm, and J. Schmiedmayer, Phys. Rev. Lett. **106**, 020407 (2011).

[23] S. Levy, E. Lahoud, L. Shomroni, and J. Steinhauer, Nature (London) **449**, 579 (2007).

[24] K. Maussang, G. E. Marti, T. Schneider, P. Treutlein, Y. Li, A. Sinatra, R. Long, J. Estève, and J. Reichel, Phys. Rev. Lett. **105**, 080403 (2010).

[25] F. Baumgärtner, R. J. Sewell, S. Eriksson, I. Llorente-Garcia, J. Dingjan, J. P. Cotter, and E. A. Hinds, Phys. Rev. Lett. **105**, 243003 (2010).

[26] L. J. LeBlanc, A. B. Bardon, J. McKeever, M. H. T. Extavour, D. Jervis, J. H. Thywissen, F. Piazza, and A. Smerzi, Phys. Rev. Lett. **106**, 025302 (2011).

[27] C. Gross, T. Zibold, E. Nicklas, J. Estève, and M. K. Oberthaler, Nature (London) **464**, 1165 (2010); E. Nicklas, H. Strobel, T. Zibold, C. Gross, B. A. Malomed, P. G. Kevrekidis, and M. K. Oberthaler, Phys. Rev. Lett. **107**, 193001 (2011).

[28] T. Zibold, E. Nicklas, C. Gross, and M. K. Oberthaler, Phys. Rev. Lett. **105**, 204101 (2010).

[29] D. S. Hall, M. R. Matthews, J. R. Ensher, C. E. Wieman, and E. A. Cornell, Phys. Rev. Lett. **81**, 1539 (1998).

[30] F. Serwane, G. Zürn, T. Lompe, T. B. Ottenstein, A. N. Wenz, and S. Jochim, Science **332**, 336 (2011).

[31] Sebastian Will, Thorsten Best, Simon Braun, Ulrich Schneider, and Immanuel Bloch, Phys. Rev. Lett. **106**, 115305 (2011).

[32] J. Sebby-Strabley, M. Anderlini, P. S. Jessen, and J. V. Porto, Phys. Rev. A **73**, 033605 (2006).

[33] R. Scelle, T. Rentrop, A. Trautmann, T. Schuster, and M. K. Oberthaler, Phys. Rev. Lett. **111**, 070401 (2013).

[34] Y.-J. Lin, K. Jimenez-Garcia, and I. B. Spielman, Nature (London) **471**, 83 (2011).

[35] K. Baumann, R. Mottl, F. Brennecke, and T. Esslinger, Phys. Rev. Lett. **107**, 140402 (2011).

[36] R. Botet and R. Jullien, Phys. Rev. B **28**, 3955 (1983).

[37] G. J. Milburn, J. Corney, E. M. Wright, and D. F. Walls, Phys. Rev. A **55**, 4318 (1997).

[38] A. Smerzi, S. Fantoni, S. Giovanazzi, and S. R. Shenoy, Phys. Rev. Lett. **79**, 4950 (1997).

[39] Z. P. Karkuszewski, K. Sacha, and A. Smerzi, Eur. Phys. J. D **21**, 251 (2002); B. Damski, Z. P. Karkuszewski, K. Sacha, and J. Zakrzewski, Phys. Rev. A **65**, 013604 (2001).

[40] C. Lee, W. Hai, L. Shi, and K. Gao, Phys. Rev. A **69**, 033611 (2004); C. Lee, Phys. Rev. Lett. **102**, 070401 (2009).

[41] R. Kanamoto, H. Saito, and M. Ueda, Phys. Rev. A **73**, 033611 (2006).

[42] V. S. Shchesnovich and V. V. Konotop, Phys. Rev. Lett. **102**, 055702 (2009).

[43] B. Oleś, P. Ziń, J. Chwedeńczukc, K. Sacha, and M. Trippenbach, Laser Phys. **20**, 671 (2010).

[44] P. Buonsante, V. Penna, and A. Vezzani, Phys. Rev. A **84**, 061601(R) (2011); P. Buonsante, R. Burioni, E. Vescovi, and A. Vezzani, *ibid.* **85**, 043625 (2012).

[45] B. Juliá-Díaz, D. Dagnino, M. Lewenstein, J. Martorell, and A. Polls, Phys. Rev. A **81**, 023615 (2010).

[46] G.-S. Paraoanu, S. Kohler, F. Sols, and A. J. Leggett, J. Phys. B: At., Mol. Opt. Phys. **34**, 4689 (2001).

[47] G. J. Krahn and D. H. J. O'Dell, J. Phys. B: At., Mol. Opt. Phys. **42**, 205501 (2009).

[48] B. Wu and Q. Niu, Phys. Rev. A **64**, 061603(R) (2001); B. Wu, R. B. Diener, and Q. Niu, *ibid.* **65**, 025601 (2002); B. Wu and Q. Niu, New J. Phys. **5**, 104 (2003).

[49] Dmitri Diakonov, L. M. Jensen, C. J. Pethick, and H. Smith, Phys. Rev. A **66**, 013604 (2002); M. Machholm, C. J. Pethick, and H. Smith, *ibid.* **67**, 053613 (2003); M. Machholm, A. Nicolin, C. J. Pethick, and H. Smith, *ibid.* **69**, 043604 (2004).

[50] E. J. Mueller, Phys. Rev. A **66**, 063603 (2002).

[51] Z. Chen and B. Wu, Phys. Rev. Lett. **107**, 065301 (2011).

[52] B. Prasanna Venkatesh, J. Larson, and D. H. J. O'Dell, Phys. Rev. A **83**, 063606 (2011).

[53] P. Mason and N. G. Berloff, Phys. Rev. A **79**, 043620 (2009).

[54] S. Baharian and G. Baym, Phys. Rev. A **87**, 013619 (2013).

[55] Y.-A. Chen, S. D. Huber, S. Trotzky, I. Bloch, and E. Altman, Nat. Phys. **7**, 61 (2011).

[56] S. Ghose, P. M. Alsing, and I. H. Deutsch, Phys. Rev. E **64**, 056119 (2001).

[57] J. Larson and M. Horsdal, Phys. Rev. A **84**, 021804(R) (2011).

[58] C. Weiss and N. Teichmann, Phys. Rev. Lett. **100**, 140408 (2008).

[59] C. Lee, W. Hai, L. Shi, X. Zhu, and K. Gao, Phys. Rev. A **64**, 053604 (2001).

[60] F. Kh. Abdullaev and R. A. Kraenkel, Phys. Rev. A **62**, 023613 (2000).

[61] K. W. Mahmud, H. Perry, and W. P. Reinhardt, Phys. Rev. A **71**, 023615 (2005).

[62] I. C. Percival, J. Phys. B: At., Mol. Opt. Phys. **6**, L229 (1973).

[63] M. V. Berry and M. Tabor, Proc. R. Soc. London, Ser. A **356**, 375 (1977).

[64] M. V. Berry, Proc. R. Soc. London, Ser. A **413**, 183 (1987).

[65] M. V. Berry, in *Classical Chaos and Quantum Eigenvalues* in *Order and Chaos in Nonlinear Physical Systems*, edited by Stig Lundqvist, Norman H. March, and Mario P. Tosi (Plenum, New York, 1988).

[66] R. Graham and M. Höhnerbach, in *Quantum Measurement and Chaos*, edited by E. R. Pike and S. Sarkar (Plenum, New York, 1987).

[67] C. Emary and T. Brandes, Phys. Rev. E **67**, 066203 (2003).

[68] A. Altland and F. Haake, Phys. Rev. Lett. **108**, 073601 (2012).

[69] R. H. Dicke, Phys. Rev. **93**, 99 (1954).

[70] Y. K. Wang and F. T. Hioe, Phys. Rev. A **7**, 831 (1973).

[71] K. Hepp and E. H. Lieb, Ann. Phys. (NY) **76**, 360 (1973).

[72] S. Ghose, P. M. Alsing, B. C. Sanders, and I. H. Deutsch, Phys. Rev. A **72**, 014102 (2005).

[73] R. Gati and M. K. Oberthaler, J. Phys. B: At., Mol. Opt. Phys. **40**, R61 (2007).

[74] J. Li, Y. Yu, A. M. Dudarev, and Q. Niu, New J. Phys. **8**, 154 (2006).

[75] O. Dutta, A. Eckardt, P. Hauke, B. Malomed, and M. Lewenstein, New J. Phys. **13**, 023019 (2011).

[76] F. M. Cucchietti and E. Timmermans, Phys. Rev. Lett. **96**, 210401 (2006).

[77] J. J. Sakurai, *Modern Quantum Mechanics* (Addison-Wesley, Boston, 1993).

[78] B. M. Garraway, Philos. Trans. R. Soc., A **369**, 1939 (2011).

[79] M. Hillery and L. D. Mlodinow, Phys. Rev. A **31**, 797 (1985).

[80] F. Dimer, B. Estienne, A. S. Parkins, and H. J. Carmichael, Phys. Rev. A **75**, 013804 (2007).

[81] K. Baumann, C. Guerlin, F. Brennecke, and T. Esslinger, Nature (London) **464**, 1301 (2010).

[82] D. Nagy, G. Konya, G. Szirmai, and P. Domokos, Phys. Rev. Lett. **104**, 130401 (2010); D. Nagy, G. Szirmai, and P. Domokos, Phys. Rev. A **84**, 043637 (2011).

[83] M. J. Bhaseen, J. Mayoh, B. D. Simons, and J. Keeling, Phys. Rev. A **85**, 013817 (2012).

[84] S. Gopalakrishnan, B. L. Lev, and P. M. Goldbart, Nat. Phys. **5**, 845 (2009).

[85] P. Strack and S. Sachdev, Phys. Rev. Lett. **107**, 277202 (2011); M. Buchhold, P. Strack, S. Sachdev, and S. Diehl, Phys. Rev. A **87**, 063622 (2013).

[86] E. Nahmad-Achar, O. Castaños, R. López-Peña, and J. G. Hirsch, Phys. Scr. **87**, 038114 (2013).

[87] J. Larson, Europhys. Lett. **90**, 54001 (2010).

[88] Starting with all particles in the same well, impurity plus bosons, does not change the conclusions of the impurity-induced self-trapping.

[89] B. Xiong, J. Gong, H. Pu, W. Bao, and B. Li, Phys. Rev. A **79**, 013626 (2009).

[90] W. D. Li and J. Liu, Phys. Rev. A **74**, 063613 (2006).

[91] K. Zaheer and M. S. Zubairy, Phys. Rev. A **39**, 2000 (1989); J. I. Cirac and L. L. Sanchez-Soto, *ibid.* **42**, 2851 (1990).
[92] J. Gea-Banacloche, Phys. Rev. A **44**, 5913 (1991); A. Auffeves, P. Maioli, T. Meunier, S. Gleyzes, G. Nogues, M. Brune, J. M. Raimond, and S. Haroche, Phys. Rev. Lett. **91**, 230405 (2003).
[93] C. E. A. Jarvis, D. A. Rodrigues, B. L. Györffy, T. P. Spiller, A. J. Short, and J. F. Annett, New J. Phys. **11**, 103047 (2009).
[94] S. Dooley, F. McCrossan, D. Harland, M. J. Everitt, and T. P. Spiller, Phys. Rev. A **87**, 052323 (2013).
[95] O. Bohigas, M. J. Giannoni, and C. Schmit, Phys. Rev. Lett. **52**, 1 (1984).
[96] E. P. Wigner, Ann. Math. **53**, 36 (1951); **62**, 548 (1955); **65**, 203 (1957); **67**, 325 (1958).
[97] F. J. Dyson, Commun. Math. Phys. **19**, 235 (1970).
[98] H. Wu, M. Vallières, D. H. Feng, and D. W. L. Sprung, Phys. Rev. A **42**, 1027 (1990).
[99] N. L. Balazs and A. Voros, Phys. Rep. **143**, 109 (1986); Europhys. Lett. **4**, 1089 (1987); N. L. Balazs, C. Schmit, and A. Voros, J. Stat. Phys. **46**, 1067 (1987).
[100] L. F. Santos and M. I. Dykman, New J. Phys. **14**, 095019 (2012).
[101] M. Kuś, Phys. Rev. Lett. **54**, 1343 (1985).
[102] J. Larson, J. Phys. B: At., Mol. Opt. Phys. **46**, 224016 (2013).
[103] D. Braak, Phys. Rev. Lett. **107**, 100401 (2011).
[104] A. Moroz, Ann. Phys. **338**, 319 (2013).
[105] Another symmetry which can play a role in lattices is number conservation. This breaks up the Hamiltonian into independent blocks each of dimension $2(L-1+N)!/[(L-1)!N!]$ where N is the total number of particles, and L is the number of wells [106]. We have also added a factor of 2 due to the impurity. Since we have a double well, the size of each block is $2N+2$ which is the whole Hamiltonian. Therefore, we can conclude that particle-number conservation does not affect the energy-level spacings.
[106] A. Gubin and L. F. Santos, Am. J. Phys. **80**, 246 (2012).
[107] F. Haake, *Quantum Signatures of Chaos* (Springer, New York, 2000), pp. 75–76.
[108] S. E. Ulloa and D. Pfannkuche, Superlattices Microstruct. **21**, 1 (1997).
[109] B. A. Berg, H. Markum, and R. Pullirsch, Phys. Rev. D **59**, 097504 (1999).
[110] C. Stone, Y. A. E. Aoud, V. A. Yurovsky, and M. Olshanii, New J. Phys. **12**, 055022 (2010).
[111] A. N. Kolmogorov, Dokl. Akad. Nauk. SSSR **98**, 527 (1954) [R. Abraham, *Foundations of Mechanics* (W. A. Benjamin, New York, 1967), Appendix D].
[112] V. I. Arnold, Uspekhi Mat. Nauk. **18**, 13 (1963) [Russian Math. Surveys. **18**, 9 (1963)].
[113] J. Moser, Nachr. Akad. Wiss. Göttingen, Math.-Phys. Kl. **II**, 1 (1962).

3.2 Paper II: Critical exponents for an impurity in a bosonic Josephson junction: Position measurement as a phase transition

Jesse Mumford and D. H. J. O'Dell
Critical exponents for an impurity in a bosonic Josephson junction: Position measurement as a phase transition
Phys. Rev. A **90**, 063617 (2014);
DOI: https://doi.org/10.1103/PhysRevA.89.023620

Summary: In this paper we go further in defining the quantum properties of the PT described in the previous paper. Using fidelity susceptibility (FS) and finite scaling analysis we derive critical exponents of the PT both numerically and analytically. We show the exponents associated with the FS are $\alpha_+ = 1/2$ and $\alpha_- = 2$ where the $\pm$ represent the exponents on the $W > W_c$ and $W < W_c$ sides of the PT, respectively. We also show the exponent associated with the correlation length is $\nu = 3/2$. These exponents match those of the Dicke model, so we make the claim that the BEC-impurity system is in the Dicke model universality class.

Content: The majority of the article was written by the author with the exception of the introduction which was mainly written by Duncan O'Dell. All numerical and analytic calculations were done by the author.

PHYSICAL REVIEW A **90**, 063617 (2014)

Critical exponents for an impurity in a bosonic Josephson junction: Position measurement as a phase transition

J. Mumford and D. H. J. O'Dell

Department of Physics and Astronomy, McMaster University, 1280 Main Street West, Hamilton, Ontario L8S 4M1, Canada

(Received 1 October 2014; published 9 December 2014)

We use fidelity susceptibility to calculate quantum critical scaling exponents for a system consisting of N identical bosons interacting with a single impurity atom in a double-well potential (bosonic Josephson junction). Above a critical value of the boson-impurity interaction energy there is a spontaneous breaking of $\mathbb{Z}_2$ symmetry corresponding to a second-order quantum phase transition from a balanced to an imbalanced number of particles in either the left- or the right-hand well. We show that the exponents match those in the Lipkin-Meshkov-Glick and Dicke models, suggesting that the impurity model is in the same universality class. The phase transition can be interpreted as a measurement of the position of the impurity by the bosons.

DOI: 10.1103/PhysRevA.90.063617 PACS number(s): 03.75.Lm, 03.65.Ta, 67.85.Pq, 05.30.Rt

I. INTRODUCTION

The fate of a single particle tunneling in a many-body environment is a subject of fundamental interest not least because of its connection to the decoherence problem in quantum mechanics [1,2]. In this paper we study a related system consisting of a single-impurity atom tunneling between the wells of a double-well potential in the presence of N indistinguishable bosonic atoms as illustrated schematically in Fig. 1. The bosons are also trapped in the double-well potential and thus form a bosonic Josephson junction in their own right. This setup can be considered to be an elementary example of a Bose-Fermi mixture, although, because the statistics of the impurity do not matter, in practice it can be a boson of the same species but in a different internal state. The prospects for realizing such a system in the laboratory are reasonably promising: a large number of experiments have studied ultracold bosons trapped in external double-well potentials [3–11], and others have realized the same effective system in a single trap but where two internal states of the atoms are coupled by microwave or radio frequency fields (internal Josephson effect) [12,13]. Adding a well-defined number of impurities is not easy but there has been some progress in this direction in optical lattices [14,15].

A theoretical analysis of a bosonic Josephson junction with an impurity has been given by Rinck and Bruder [16], who found that by applying a tilt to the double-well a multiparticle tunneling resonance could be induced towards a state where the impurity was expelled to the higher lying well. Subsequently, we undertook a study comparing the mean-field and many-body properties and described the appearance of a pitchfork bifurcation in the ground state of the mean-field theory above a certain critical value W_c of the boson-impurity interaction strength [17]. The mean-field bifurcation arises from the spontaneous localization of the impurity in one of the wells together with the localization of a majority of bosons in the opposite well (assuming repulsive interactions). In the fully quantum version W_c marks the onset of a splitting of the wave function into two coherent pieces in Fock space (the space spanned by the Fock states $|\Delta M,\Delta N\rangle$, corresponding to the number differences $\Delta M = M_R - M_L$ and $\Delta N = N_R - N_L$ between the left and the right wells for the impurity and bosons, respectively). As W is increased further the Fock-space splitting increases, and for large N it can develop into a fully blown Schrödinger cat state which is a superposition of two macroscopically distinguishable number differences of bosons. This state is associated with a saturation of the entanglement entropy between the impurity and the bosons at $S = k_B \ln 2$. The formation of a Schrödinger cat state in a macroscopic measurement device as a result of its coupling to a microscopic system is usually considered to be an essential element of quantum measurement [18,19]. One may therefore take the view that the bosons in the present system act as a quantum measurement device or meter which indicates the position of the microscopic impurity atom. This meter can be tuned between being microscopic (small N) and being macroscopic (large N). The formation and collapse of the Schrödinger cat state correspond here to a symmetry-breaking phase transition (PT) [20–24].

In another study [25], we argued that in many respects the impurity system behaves like the celebrated Dicke model [26–28] for N two-level atoms coupled to a single mode of the electromagnetic field whose Hamiltonian takes the form

$$\hat{H}_{\mathrm{Dicke}} = \hbar\omega\hat{a}^\dagger\hat{a} + \omega_0\hat{S}_z + \frac{2}{\sqrt{N}}\lambda(\hat{a}+\hat{a}^\dagger)\hat{S}_x. \qquad (1)$$

Here $\hat{a}$ and $\hat{a}^\dagger$ annihilate and create, respectively, a photon of energy $\hbar\omega$ in the electromagnetic field and $\hat{S}_x$ and $\hat{S}_z$ are collective spin operators that arise from treating the two-level atoms, whose levels are separated by energy $\hbar\omega_0$, as pseudospins. $\hat{S}_z$ measures half the difference between the number of atoms in the excited state and the number in the ground state and its eigenvalues lie in the range $-N/2 \ldots N/2$. $\hat{S}_x = (\hat{S}_+ + \hat{S}_-)/2$ measures the coherence between the excited and the ground states of the atoms and $\hat{a}+\hat{a}^\dagger$ is proportional to the position operator for the harmonic oscillator associated with the electromagnetic field. In a related pseudospin formulation the Hamiltonian for the bosonic Josephson junction plus impurity can be written (see Sec. II for details)

$$\hat{H} = 2NJ^a\hat{S}_z^a + 2J\hat{S}_z + 2W\hat{S}_x^a\hat{S}_x, \qquad (2)$$

where the superscript a denotes the impurity: J and J^a are the bare hopping frequencies between the two wells for the bosons and impurity, respectively, and W parameterizes the

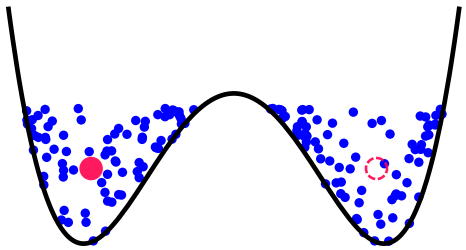

FIG. 1. (Color online) Schematic of the proposed setup. A bosonic Josephson junction consists of N identical bosons [represented by the small filled (blue) circles] which are able to tunnel between the two sides of a double-well potential. To this is added a single impurity atom [large filled (red) circle] which is also able to tunnel between the two wells.

boson-impurity coupling strength. In this form the impurity model is reminiscent of the Mermin central-spin model, where a distinguishable central spin is surrounded by N spins on a lattice which interact with the central spin with an effectively infinite-range interaction so that all pairwise interactions have the same magnitude [29–31]. In the impurity model $\hat{S}_z$ measures the coherence of the bosons between the two wells or, equivalently, half the difference in the number of bosons in the antisymmetric and symmetric modes formed, respectively, from the odd and even combinations of the modes associated with each well. $\hat{S}_x$ measures half the number difference between the two wells or, equivalently, the coherence between their symmetric and their antisymmetric combinations. S_x^a and S_z^a are the corresponding quantities for the impurity. In the thermodynamic limit where $N \to \infty$, the ground state of the Dicke model undergoes a second-order PT due to a spontaneous breaking of $\mathbb{Z}_2$ symmetry at the critical coupling strength $\lambda_c = \sqrt{\omega\omega_0}/2$ [32,33]. This PT bears a very close resemblance to the bifurcation that occurs in the impurity model at [17,25]

$$W_c = \sqrt{JJ^a}/2. \tag{3}$$

In the Dicke case the ground state below the transition ($\lambda < \lambda_c$) is known as the normal state and is characterized by $\langle \hat{S}_x \rangle = 0$ and $\langle \hat{a} + \hat{a}^\dagger \rangle = 0$, whereas the ground state above the transition is known as the super-radiant state because it corresponds to a spontaneous macroscopic excitation of the electromagnetic field with both $\langle \hat{S}_x \rangle \neq 0$ and $\langle \hat{a} + \hat{a}^\dagger \rangle \neq 0$. Analogous ground states occur for the impurity model: when $W < W_c$ both the boson and the impurity probability distributions are symmetric, $\langle \hat{S}_x \rangle = 0$ and $\langle \hat{S}_x^a \rangle = 0$, and both expectation values acquire finite values in the symmetry-broken state occurring when $W > W_c$. Furthermore, the dependence of the ground-state energy on the scaled parameters W/W_c and λ/λ_c is identical in the two models in the immediate vicinity of the transition [25]. It is also notable that the mean-field dynamics is, in both cases, regular below the transition and chaotic above it [25,27]. In this paper we further investigate the bifurcation in the impurity model by calculating the critical exponents in order to establish whether it is indeed a second-order PT in the same universality class as that in the Dicke model.

Although both the Dicke and the impurity models share many common features, there is one glaring difference: the Dicke model couples N spin-1/2 particles to a harmonic oscillator, whereas the impurity model couples N spin-1/2 particles to one other spin. In essence, the impurity model truncates the harmonic oscillator Hilbert space to just two states, the ground state and the first excited state. The spin-1/2 representing the impurity can never become macroscopically excited like the simple harmonic oscillator can. It is therefore quite remarkable that the impurity model behaves like the Dicke model, but the critical exponents we calculate here show that very close to the transition a two-state Hilbert space for the harmonic oscillator in the Dicke model suffices to describe its critical properties.

In order to investigate the critical behavior and obtain the critical scaling exponents we calculate the fidelity susceptibility (FS) of the ground state. Over the past decade the concept of fidelity, which originated in quantum information theory [34], has gained wide use in analyzing critical behavior and classifying the universality of systems. It is most commonly used to quantify changes in the ground state of a system over a PT. This is done by calculating the product between the ground state and itself at different points in parameter space,

$$F(W,\delta W) = |\langle \psi_0(W) | \psi_0(W + \delta W) \rangle|, \tag{4}$$

where W is the tunable parameter that drives the PT and ψ_0 is the ground state. It is expected that $F(W,\delta W)$ will tend to unity away from the critical region and reach a minimum when $W = W_c - \delta W/2$, where the scalar product will be between the ground state below and that above the critical point. One of the first PTs to be studied using the fidelity was the one-dimensional (1D) XY, model where it was shown to decrease to a minimum near the critical point [35]. Furthermore, the excited-state fidelity has been used to characterize quantum PTs where the ground-state fidelity has failed [36]. Since the fidelity is a quantity depending only on the geometry of the Hilbert space and requires no knowledge of the order parameter, it is useful in cases where the order parameter of a system is not obvious and has been studied in a variety of systems [37–39]. That being said, a more sensitive and natural quantity to study, where no *a priori* knowledge of the system is needed, is the FS [40,41]. The FS measures the response of the fidelity to infinitesimal changes in the driving parameter of the system. It is closely related to the second derivative of the ground-state energy with respect to the driving parameter, $\frac{\partial^2 E_0}{\partial W^2}$, so the FS is also similar to the magnetic susceptibility or specific heat when the driving parameters are the magnetic field and temperature, respectively. This means that the FS can be used to study the critical behavior of a system through calculations of scaling exponents.

In this paper we add to work done by others [42–44] regarding the scaling and criticality of bosons in a double-well potential. We follow standard steps [45,46] to show that the FS can be used to calculate scaling exponents for a general system. We then use the FS to focus on the critical behavior of the two-site boson-impurity Hubbard model. The paper is organized in the following way: In Sec. II we go into more detail about our model for the physical system under study. In Sec. III we show how critical scaling exponents can be extracted from the FS. In Sec. IV we apply the methods of Sec. III to our system as well as extrapolating data to find

numerical values for W_c. In Sec. V we find the FS critical exponents analytically and in Sec. VI we give a summary and outlook for further work. Some of the details of the analytic calculations are reported in the Appendix.

II. MODEL

We model the bosonic Josephson junction plus impurity system using the two-site Bose Hubbard Hamiltonian [16,17],

$$\hat{H} = -NJ^a\hat{A} - J\hat{B} + \frac{W}{2}\Delta\hat{N}\Delta\hat{M}. \tag{5}$$

Here, $\Delta\hat{N} \equiv \hat{b}_R^\dagger\hat{b}_R - \hat{b}_L^\dagger\hat{b}_L$ is the number difference operator between the two wells for the bosons and $\hat{B} \equiv \hat{b}_L^\dagger\hat{b}_R + \hat{b}_R^\dagger\hat{b}_L$ is the boson hopping operator. $\Delta\hat{M} \equiv \hat{a}_R^\dagger\hat{a}_R - \hat{a}_L^\dagger\hat{a}_L$ and $\hat{A} \equiv \hat{a}_L^\dagger\hat{a}_R + \hat{a}_R^\dagger\hat{a}_L$ are the equivalent operators for the impurity. The L and R subscripts denote the left and right modes and the creation and annihilation operators follow the usual bosonic commutation relations, i.e., $[\hat{b}_\alpha,\hat{b}_\alpha^\dagger] = [\hat{a}_\alpha,\hat{a}_\alpha^\dagger] = 1$, with $\alpha = L, R$, and all other combinations of the boson and impurity operators are 0. The scaling by N in the first term in Eq. (5) is applied so that every term is $\mathcal{O}(N)$ and therefore W_c takes a finite value in the thermodynamic limit. The pseudospin formulation of the Hamiltonian given in Eq. (2) is obtained from Eq. (5) by introducing the symmetric and antisymmetric combinations of the L and R modes, $\hat{b}_L \equiv \frac{1}{\sqrt{2}}(\hat{b}_S + \hat{b}_{AS})$ and $\hat{b}_R \equiv \frac{1}{\sqrt{2}}(\hat{b}_S - \hat{b}_{AS})$, and then applying Schwinger's oscillator model for angular momentum [47], $\hat{S}_z \equiv (\hat{b}_{AS}^\dagger\hat{b}_{AS} - \hat{b}_S^\dagger\hat{b}_S)/2 = -\hat{B}/2$ and $\hat{S}_x \equiv (\hat{b}_{AS}^\dagger\hat{b}_S + \hat{b}_S^\dagger\hat{b}_{AS})/2 = -\Delta\hat{N}/2$. An analogous set of transformations applies to the impurity.

We do not include direct boson-boson intrawell (or interwell) interactions in our calculations and assume that they can be removed (or the boson-impurity interaction enhanced) by a Feshbach resonance if necessary. We do this both to highlight the effect of the impurity and because it turns out not to change the results in a qualitative way. Indeed, the nonlinearity due to the boson-boson interactions can lead to results very similar to those resulting from the boson-impurity interaction (the impurity can be viewed as mediating an effective interaction between the bosons). In the case of repulsive boson-boson interactions, a purely bosonic system has no PT in the ground state but does experience a symmetry-breaking bifurcation in the excited states known as macroscopic self-trapping [48,49], which has been seen in experiments [5]. If, on the other hand, the boson-boson interactions are attractive, then there is a $\mathbb{Z}_2$ symmetry-breaking PT in the ground state above a critical interaction strength where the bosons clump together in a single well. This PT has been studied by Buonsante *et al.* [44] and we find that the PT in our system falls in the same universality class.

In previous work we found, through stability analysis around the mean-field stationary points [25], that a pitchfork bifurcation of ΔN occurs at a critical value of the boson-impurity interaction W_c given in Eq. (3). For $W < W_c$, $\Delta N = 0$ and the bosons occupy each well equally. Above W_c it becomes energetically favorable for the bosons to build up in one well and the impurity to be localized in the opposite well. This transition corresponds to the breaking of the $\mathbb{Z}_2$ symmetry, characterized by

$$(\Delta\hat{M},\Delta\hat{N},\hat{A},\hat{B}) \to (-\Delta\hat{M},-\Delta\hat{N},\hat{A},\hat{B}). \tag{6}$$

We consider W as the driving parameter and analyze the system's response to infinitesimal changes in it through the FS.

III. FIDELITY SUSCEPTIBILITY

As mentioned in Sec. I, a more sensitive quantity than the fidelity is the FS, which we denote χ_F. The two are related through the Taylor expansion of Eq. (4) to second order:

$$F(W,\delta W) \approx 1 - \frac{\chi_F(W)}{2}(\delta W)^2 + \cdots. \tag{7}$$

It can be viewed as the system's response to an infinitesimal change in the driving parameter. Equation (5) has the general form

$$\hat{H} = \hat{H}_0 + W\hat{H}_I, \tag{8}$$

where H_I is considered to be the driving term of the system. From perturbation theory [41] the FS is

$$\chi_F(W) = \sum_{n\neq 0}\frac{|\langle\psi_n(W)|\hat{H}_I|\psi_0(W)\rangle|^2}{(E_n - E_0)^2}, \tag{9}$$

where $\psi_n(W)$ and E_n are the nth eigenstate and eigenenergy of the entire Hamiltonian, respectively. It is expected that for finite N the FS scales as [45,46]

$$\frac{\chi_F}{N^d} \propto 1/|W - W_{\max}|^{\alpha_\pm}, \tag{10}$$

where $\alpha_\pm$ is the scaling exponent above and below the quantum critical point, respectively, $W_{\max}$ is the value of W at which χ_F is at a maximum, and χ_F/N^d is an intensive quantity. When $W = W_{\max}$, χ_F will be limited by the size of the system, so we have

$$\chi_{F\max} \propto N^\mu. \tag{11}$$

This quantity will diverge in the thermodynamic limit as $W_{\max} \to W_c$. In fact, when Eq. (5) is divided by N so that each term is $\mathcal{O}(1)$ rather than $\mathcal{O}(N)$, then the exponent μ also gives the scaling of the energy gap between the ground and the first excited states [50,51], as we have verified [52]. Figure 2 illustrates how $\chi_{F\max}$, which is given by the peak of each curve, depends on N. In order to capture the behavior of both Eqs. (10) and (11) we use the form [45]

$$\frac{\chi_F}{N^d} = \frac{c}{N^{-\mu+d} + g(W)|W - W_{\max}|^\alpha}, \tag{12}$$

where c is a constant and $g(W)$ is a nonzero function of W, both being intensive quantities. Since we are dealing with the susceptibility of the ground-state wave function in the Fock basis, N plays the role of the system size. With this in mind we can use the finite-size scaling hypothesis [53], giving

$$f = N^{-1}Y[N^a(W - W_{\max})], \tag{13}$$

where f is the free energy density and Y is some function. We expect Eq. (13) to vanish as $W \to W_{\max}$ and, at the same

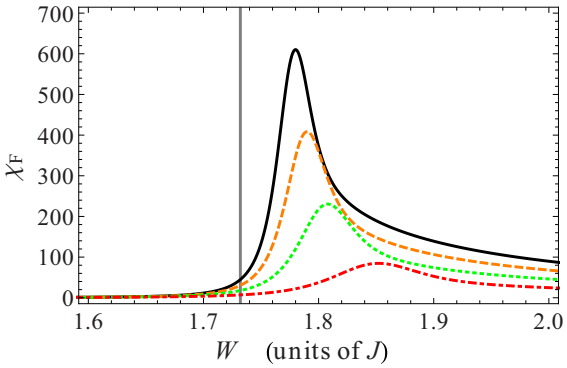

FIG. 2. (Color online) Fidelity susceptibility as a function of W for different system sizes: $N = 200$ [dot-dashed (red) curve], $N = 400$ [dotted (green) curve], $N = 600$ [dashed orange) curve], and $N = 800$ (solid black curve). Here $J^a = 0.75J$, so $W_c = \sqrt{3}J$, which is shown by the vertical black line. It is clear that χ_F is not symmetric about the transition, and hence the need for two indices $\pm\alpha$ as indicated in Eq. (10).

time, the domain of the correlations to diverge. In this limit it is natural to expect [54]

$$f \sim \xi^{-1} \sim (W - W_{\max})^{\nu}, \tag{14}$$

where ξ is the correlation length (in Fock space) and ν is the correlation length critical exponent. Combining Eqs. (13) and (14) gives the relation $a = 1/\nu$. Using the fact that, in general, the susceptibility due to W is $\chi = -\frac{\partial^2 f}{\partial W^2}$, we can show the reduced FS is a universal function of N and the driving parameter

$$\frac{\chi_{\text{Fmax}} - \chi_{\text{F}}}{\chi_{\text{F}}} = X[N^{1/\nu}(W - W_{\max})], \tag{15}$$

where X is some function. Finally, combining this equation with Eq. (12) gives us the important scaling relation

$$\alpha = \nu(\mu - d), \tag{16}$$

which we use to help classify the boson-impurity system. It should be noted that Eq. (15) has been defined by others [45,46] with the exponent of N being ν instead of $1/\nu$, which we have here. In the next section we numerically evaluate the FS and, guided by the above scaling hypotheses, find the critical exponents by collapsing the data onto universal curves.

IV. NUMERICAL RESULTS

Our results in this section are obtained by numerically diagonalizing the Hamiltonian given in Eq. (5). An N-boson system produces a $(2N + 2) \times (2N + 2)$ matrix, so a system size of $N \sim 1000$ can be easily accommodated, allowing us to obtain exact results. We note that, due to symmetry, parity is a conserved quantity, i.e., $[\hat{H}, \hat{P}] = 0$, and hence all the eigenvectors of our Hamiltonian are either even or odd in Fock space. Since we perform FS calculations on the ground state (which is of even parity), we can reduce the computation time by considering only even-parity states. However, above W_c the eigenstates typically come in even and odd pairs separated by an exponentially small energy difference and numerical

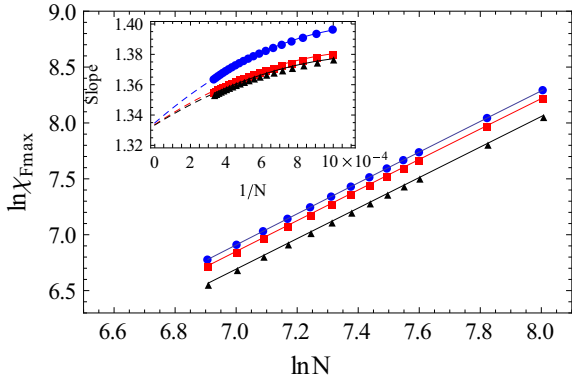

FIG. 3. (Color online) A log-log plot of χ_{Fmax} as a function of N for different values of J^a: $0.75J$ [(red) squares], $1J$ [(blue) circles], and $1.25J$ (black triangles). Inset: Slopes of the log-log plot as a function of $1/N$ extrapolated in the $1/N \to 0$ limit. The range of system sizes is $1000 \leqslant N \leqslant 3000$.

diagonalization routines find it very hard to identify the parity of such eigenvectors. Unless one is careful numerical errors lead to eigenvectors with broken symmetry [17], and this directly impacts our results since it is the critical region we are concerned with in our calculations. We have outlined the resolution to this problem in the Appendix of our previous work [25], where we force the eigenstates to have definite parity by diagonalizing the Hamiltonian in the parity basis.

Figure 2 shows the results of plugging the numerically calculated eigenstates and energies for different system sizes into Eq. (9). We observe a clear peak in the FS for each value of N, which increases in height and sharpness as N increases. This corresponds to the shrinking of the critical region and $W_{\max} \to W_c$ as $N \to \infty$. To find μ we first make a log-log plot of χ_{Fmax} as a function of N as shown in Fig. 3. We fit the curves to a second-degree polynomial and extrapolate their slopes in the limit $1/N \to 0$. In the inset we see that the slopes converge to a value of $\mu \simeq 4/3$. We calculate μ for different values of J^a to show that μ does not depend on J^a and therefore is universal. Next, we use Eq. (15) to

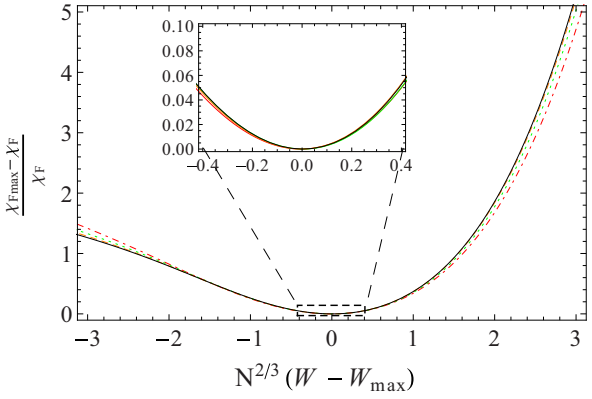

FIG. 4. (Color online) A plot of Eq. (15) for different system sizes. The parameters and values of N are the same as those used in Fig. 2. A value of $\nu \simeq 3/2$ results in the optimal overlay of the curves. Inset: Magnification of the region around the origin.

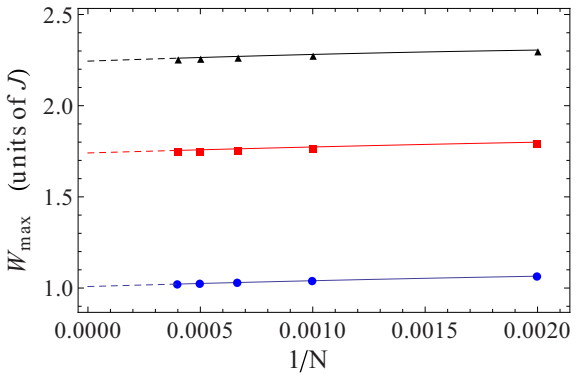

FIG. 5. (Color online) Extrapolated values of W_{max} for different values of J^a: $0.75J$ [(red) squares], $1J$ [(blue) circles), and $1.25J$ (black triangles). Dashed lines show quadratic fits for $1/N \to 0$ and the system size range is $500 \leqslant N \leqslant 2500$.

find ν by changing it in small increments until the average overlay of data points for different values of N is maximized. Figure 4 shows the scaled χ_F in the vicinity of W_{max}, where a maximum overlay is achieved for $\nu \simeq 3/2$. Figure 2 shows that, below W_{max}, χ_F is an intensive quantity, so we have $d = 0$ in Eq. (10). Above W_{max}, χ_F has a linear dependence on N, so χ_F/N is an intensive quantity and $d = 1$. Using Eq. (16) to calculate $\alpha_\pm$ we obtain $\alpha_- \simeq 2$ and $\alpha_+ \simeq 1/2$. These values of $\alpha_\pm$, μ, and ν (keeping in mind the different definitions of ν) are the same as those obtained for the Lipkin-Meshkov-Glick model numerically [46] and analytically [55], for the Dicke model obtained numerically [56], as well as for the system consisting of bosons in a double-well potential with attractive interactions obtained analytically [44]. This suggests that the boson-impurity system belongs in the same universality class as these models and that the quantum PT is second order.

We now shift our focus back to the convergence of W_{max} to W_c in the thermodynamic limit. Using the same steps used to determine μ we find the slope of a log-log plot of $|W_c - W_{max}|^\delta$ as a function of N, giving the convergence scaling exponent, δ, which we find to be the same as the inverse of the correlation length exponent, so $\delta = 1/\nu \simeq 2/3$. In Fig. 5 we show the effectiveness of the FS in predicting W_c with $1/N$ extrapolation. For three values of J^a, using Eq. (3), we have $W_c = 1$, $\sqrt{3}$, and $\sqrt{5}$, compared to the extrapolated values of $W_{max} = 1.0062$, 1.7387, and 2.2432 (all values are in units of J). With only five data points we find the two sets of values to be in good agreement. Thus, if we were unable to find W_c analytically, the FS would provide an excellent avenue for determining values numerically. We summarize our numerical results in Table I, where the uncertainties are standard errors using a least-squares fit to our data.

TABLE I. Critical scaling exponents and analytic and extrapolated values of the quantum critical point (QCP) for different values of J^a. Scaling exponents and QCP values are calculated with system size ranges of $1000 \leqslant N \leqslant 3000$ and $500 \leqslant N \leqslant 2500$, respectively. Circles, squares, and triangles refer to data in Figs. 3 and 5.

	J^a		
	0.25 (circles)	0.75 (squares)	1.25 (triangles)
μ	1.335(3)	1.334(2)	1.333(2)
ν	1.499(2)	1.504(5)	1.502(3)
W_c	1	$\sqrt{3}$	$\sqrt{5}$
W_{Extrap}	1.0062(2)	1.7387(3)	2.2432(3)

V. ANALYTIC CALCULATION OF $\alpha_\pm$

In the thermodynamic limit the critical region collapses to a point and fluctuations vanish away from this point. For large systems away from the critical region this property allows us to use a mean-field approximation to analyze the FS. In previous work [17] we have shown that the mean-field Hamiltonian corresponding to Eq. (5) is

$$\frac{H_{MF}}{N} = -J\sqrt{1-Z^2}\cos\beta - J^a\sqrt{1-Y^2}\cos\alpha + \frac{W}{2}ZY. \tag{17}$$

In H_{MF} we have defined $\beta \equiv \beta_R - \beta_L$ and $Z \equiv \Delta N/N$ as the boson phase and number difference between the two wells, respectively, and $\alpha \equiv \alpha_R - \alpha_L$ and $Y \equiv \Delta M$ are similarly defined for the impurity. The conjugate nature of the number and phase variables means that Hamilton's equations take the form

$$\dot{\alpha} = \frac{1}{\hbar}\frac{\partial H}{\partial Y}, \quad \dot{Y} = -\frac{1}{\hbar}\frac{\partial H}{\partial \alpha}, \tag{18}$$

$$\dot{\beta} = \frac{1}{\hbar}\frac{\partial H}{\partial Z}, \quad \dot{Z} = -\frac{1}{\hbar}\frac{\partial H}{\partial \beta}, \tag{19}$$

and the stable stationary solutions (which includes the ground state) of the system are

$$(\alpha, Y, \beta, Z) = \begin{cases} (0,0,0,0), & W \leqslant W_c; \\ \left(0, \pm\frac{1}{W}\sqrt{\frac{W^4-16J^2J^{a2}}{W^2+4J^{a2}}}\right. & \\ \quad \left. 0, \mp\frac{1}{W}\sqrt{\frac{W^4-16J^2J^{a2}}{W^2+4J^2}}\right), & W > W_c. \end{cases} \tag{20}$$

Note that for simplicity we have only displayed the solutions for the case when $W > 0$, corresponding to a repulsive boson-impurity interaction. An intuitive understanding of the role of the impurity can be gained if we use the solutions in Eq. (20) to simplify Eq. (17) by adiabatically eliminating the impurity with the relation

$$Y = -Z\sqrt{\frac{W^2+4J^2}{W^2+4J^{a2}}}, \tag{21}$$

giving us an effective Hamiltonian for the bosons alone,

$$\frac{H_{eff}}{N} = -J\sqrt{1-Z^2} - J^a\sqrt{1-Z^2\gamma^2} - \frac{W\gamma}{2}Z^2, \tag{22}$$

where $\gamma = \sqrt{\frac{W^2+4J^2}{W^2+4J^{a2}}}$. Setting $J^a = J$ for further simplification and scaling Eq. (22) by $2J$ gives an effective Hamiltonian dependent on a single parameter, $\Sigma = W/J$,

$$\frac{H_{eff}}{2NJ} = -\frac{|\Sigma|}{4}Z^2 - \sqrt{1-Z^2}. \tag{23}$$

A mean-field Hamiltonian of the same form occurs in the case of a purely bosonic Josephson junction where the microscopic origin of Σ is direct boson-boson interactions [48,49]. Specifically, the minus sign in front of the first term indicates effectively attractive boson-boson interactions. Although we have calculated $H_{\rm eff}$ here assuming repulsive boson-impurity interactions, it turns out to be unchanged for attractive interactions. Thus, the impurity always mediates attractive effective boson-boson interactions [57,58], and it is for this reason that the PT in the impurity model falls into the same universality class as the clumping PT for attractive bosons. We can visualize how this happens by considering the impurity localized in one well and having $|W| > W_c$, so the ground state will have a larger fraction of bosons in one well than in the other. For $W > 0$ the impurity expels bosons from the well it is in, and for $W < 0$ bosons are attracted to the impurity. In both cases there is a buildup of bosons in one well compared to the other, which is what happens when there are attractive boson-boson interactions.

An analytic calculation of the scaling exponents for the clumping transition for attractive bosons has been given in Ref. [44]. Their method for calculating the FS consists of approximating the ground-state wave function as a Gaussian in Fock space centered at $Z = 0$ for $W \ll W_c$ and a symmetric superposition of Gaussians for $W \gg W_c$. In our calculations we do not use a superposition of Gaussians for $W \gg W_c$ but, instead, choose to have a single Gaussian centered at one of the two mean-field solutions, shown in Eq. (A1), to represent the broken-symmetry phase. The difference in these two approaches results in terms proportional to $e^{-N|\Sigma-\Sigma_c|}$, so if we are sufficiently far from the critical region, then each approach is equivalent. Using a different form of the FS [44,59],

$$\chi_{\rm F}(\Sigma) = -\frac{1}{2}\frac{d^2}{d\delta\Sigma^2}\langle\psi_0(\Sigma)|\psi_0(\Sigma+\delta\Sigma)\rangle|_{\delta\Sigma=0}, \qquad (24)$$

they are able to calculate analytic expressions for the FS. Following their steps for Eq. (23), which we briefly outline in the Appendix, we obtain

$$\chi_{\rm F}(\Sigma) = \begin{cases} \frac{1}{64(\Sigma-2)^2}, & \Sigma \ll \Sigma_c; \\ \frac{N}{|\Sigma|^3\sqrt{2(\Sigma^2-4)}} + \frac{(\Sigma^2-2)^2}{4\Sigma^2(\Sigma^2-4)^2}, & \Sigma \gg \Sigma_c. \end{cases} \qquad (25)$$

We can see that the scaling exponents are $\alpha_- = 2$ and $\alpha_+ = 1/2$, agreeing with the numerical values calculated in the previous section. Equation (25) shows the leading-order behavior of the FS. Below Σ_c there is a single leading term because the Gaussian wave function is fixed at $Z = 0$, so changes in Σ can only affect its size. Above Σ_c changes in Σ affect both the size and the position of the wave function, giving two terms, where we see that in the thermodynamic limit the position-dependent term dominates.

VI. SUMMARY AND DISCUSSION

In this paper we have studied a symmetry-breaking bifurcation in a bosonic Josephson junction driven by the interaction with an impurity atom. The fact that the maximum value of the FS, which can be viewed as a generalized susceptibility, diverges in the thermodynamic limit confirms that the symmetry breaking is associated with a second-order PT (as expected from the continuous form of the bifurcation). By numerically calculating the critical scaling exponents of the FS and comparing them with those already known in the Dicke and Lipkin-Meshkov-Glick models, as well as for a system consisting of bosons in a double-well potential with attractive interactions, we conclude that the PT in the impurity model lies in the same universality class as these other models. For the two exponents $\alpha_\pm$ of the scaling of FS with W on either side of the transition, we also carried out an analytic calculation, and good agreement was found with the numerical result. We have also shown through extrapolation of $W_{\rm max}$ in the thermodynamic limit that the FS can be used to predict W_c numerically, and we find that it agrees with the analytic result calculated from the mean-field theory.

Interpreting the bosons as a meter measuring the position of the impurity, we have a particularly simple toy model for a binary quantum measurement in terms of a PT which occurs at a critical value of the system-meter interaction strength [20–24]. Quantum mechanically, the ground-state probability distribution goes from having Gaussian fluctuations around $\Delta N = 0$ to a superposition of two Gaussians, each centered at one of the two bifurcating mean-field solutions. The latter state becomes a Schrödinger Cat state if $N \gg 1$ and $W > W_c$. Cat states are notoriously sensitive to perturbations and can be expected to rapidly collapse into one of the two wells, thereby breaking the symmetry. This collapse is implicit in our model but it is interesting to ask whether a third agent beyond the impurity and the bosons is necessary to precipitate it. If the symmetry is broken by a classical field, then it can be simply included in the Hamiltonian as a tilt to the double-well potential [16,17,25], and as long as the perturbation is infinitesimal the PT is not affected. However, if the boson-impurity system is instead put into contact with a quantum mechanical environment, then the effects can be more marked. PTs in open quantum systems (systems coupled to an environment) are now the subject of intensive research [60,61], especially for the open Dicke model [62–65]. One conclusion of this body of work is that the critical exponents can be modified by the coupling to the environment and this effect has been seen experimentally [66].

Finally, we mention that the impurity localization described in this paper is somewhat different from that found in the classic problem of an impurity in a uniform superfluid [67] or its modern descendant, an impurity in an extended gaseous Bose-Einstein condensate (BEC) [68–72]. For example, the Bose-Hubbard Hamiltonian employed here is a tight-binding model where the single-particle wave functions (modes) are assumed to be unchanged by interactions, whereas the transition to a self-localized polaron state in an initially uniform BEC involves a change in the impurity wave function from delocalized to localized and the BEC develops a corresponding density dip. Furthermore, the type of symmetry that is broken in going from a uniform to a localized wave function is, in general, different from the binary choice underlying $\mathbb{Z}_2$ symmetry breaking (see Ref. [73] for the case of a particle living on 1D and 2D lattices with many lattice sites). However, in 1D extended systems the Josephson model underlying the physics studied here appears quite naturally as the impurity splits the BEC in two and we would expect there to be

connections [74,75]. We also point out that there are many aspects to the impurity model and its close relatives beyond those discussed here, including how the coherence of the bosons is affected by the impurity [17,76,77] and system-bath dynamics [78–81].

ACKNOWLEDGMENTS

We acknowledge insightful discussions with Jonas Larson and Sung-Sik Lee. This research was funded by the Natural Sciences and Engineering Research Council of Canada. J.M. also acknowledges funding from the government of Ontario.

APPENDIX: STEPS IN ANALYTIC CALCULATIONS

In this Appendix we briefly outline the steps used to derive Eq. (25) from Eq. (23). We start by expanding Eq. (23) around the minima above and below Σ_c,

$$Z_0 = \begin{cases} 0, & \Sigma \leqslant \Sigma_c, \\ \pm\sqrt{1-\left(\frac{2}{\Sigma}\right)^2}, & \Sigma > \Sigma_c, \end{cases} \tag{A1}$$

where $\Sigma_c = 2$. If we are sufficiently far away from Σ_c, then H_{eff} is parabolic in shape around the minima, so the leading-order term in the expansion will be the second, giving a Schrödinger equation

$$\left[-\frac{d^2}{du^2} + h(\Sigma)u^2\right]\Psi_\Sigma(Z) = E\Psi_\Sigma(Z), \tag{A2}$$

where $u = Z - Z_0$ and

$$h(\Sigma) = \begin{cases} \frac{N^2}{4}(-\Sigma+2), & \Sigma \ll \Sigma_c; \\ \frac{N^2}{32}\Sigma^2\left(\Sigma^2-4\right), & \Sigma \gg \Sigma_c. \end{cases} \tag{A3}$$

Equation (A2) describes a harmonic oscillator in Fock space, which means that the ground-state wave function will be a Gaussian of the form

$$\Psi_\Sigma(Z) = \frac{1}{\sqrt{\sigma_\Sigma\sqrt{2\pi}}} e^{-\frac{(Z-Z_0)^2}{4\sigma_\Sigma^2}}. \tag{A4}$$

The difference between the $\Sigma < \Sigma_c$ and the $\Sigma > \Sigma_c$ wave functions is due to Z_0 through Eq. (A1) and the relation $\sigma_\Sigma^2 = \frac{1}{2\sqrt{h(\Sigma)}}$. With these forms of the ground state we can use Eq. (24), giving

$$\chi_F(\Sigma) = -\frac{1}{2}\frac{d^2}{d\delta\Sigma^2}\int_{-\infty}^{\infty}\Psi_\Sigma(Z)\Psi_{\Sigma+\delta\Sigma}(Z)dZ|_{\delta\Sigma=0}, \tag{A5}$$

and from here we obtain the expressions given in Eq. (25).

[1] A. O. Caldeira and A. J. Leggett, Phys. Rev. Lett. **46**, 211 (1981); Ann. Phys. (NY) **149**, 374 (1983); **153**, 445(E) (1984).
[2] A. J. Leggett, S. Chakravarty, A. T. Dorsey, M. P. A. Fisher, A. Garg, and W. Zwerger, Rev. Mod. Phys. **59**, 1 (1987).
[3] Y. Shin, M. Saba, T. A. Pasquini, W. Ketterle, D. E. Pritchard, and A. E. Leanhardt, Phys. Rev. Lett. **92**, 050405 (2004); Y. Shin, C. Sanner, G.-B. Jo, T. A. Pasquini, M. Saba, W. Ketterle, D. E. Pritchard, M. Vengalattore, and M. Prentiss, Phys. Rev. A **72**, 021604(R) (2005); G.-B. Jo, J.-H. Choi, C. A. Christensen, T. A. Pasquini, Y.-R. Lee, W. Ketterle, and D. E. Pritchard, Phys. Rev. Lett. **98**, 180401 (2007); G.-B. Jo, J.-H. Choi, C. A. Christensen, Y.-R. Lee, T. A. Pasquini, W. Ketterle, and D. E. Pritchard, *ibid.* **99**, 240406 (2007).
[4] Y.-J. Wang, D. Z. Anderson, V. M. Bright, E. A. Cornell, Q. Diot, T. Kishimoto, M. Prentiss, R. A. Saravanan, S. R. Segal, and S. Wu, Phys. Rev. Lett. **94**, 090405 (2005).
[5] M. Albiez, R. Gati, J. Fölling, S. Hunsmann, M. Cristiani, and M. K. Oberthaler, Phys. Rev. Lett. **95**, 010402 (2005).
[6] R. Gati, B. Hemmerling, J. Fölling, M. Albiez, and M. K. Oberthaler, Phys. Rev. Lett. **96**, 130404 (2006); J. Estève, C. Gross, A. Weller, S. Giovanazzi, and M. K. Oberthaler, Nature (London) **455**, 1216 (2008).
[7] T. Schumm, S. Hofferberth, L. M. Andersson, S. Wildermuth, S. Groth, I. Bar-Joseph, J. Schmiedmayer, and P. Krüger, Nat. Phys. **1**, 57 (2005); S. Hofferberth, I. Lesanovsky, B. Fischer, T. Schumm, and J. Schmiedmayer, Nature (London) **449**, 324 (2007); T. Betz, S. Manz, R. Bücker, T. Berrada, Ch. Koller, G. Kazakov, I. E. Mazets, H.-P. Stimming, A. Perrin, T. Schumm, and J. Schmiedmayer, Phys. Rev. Lett. **106**, 020407 (2011).
[8] S. Levy, E. Lahoud, L. Shomroni, and J. Steinhauer, Nature **449**, 579 (2007).
[9] K. Maussang, G. E. Marti, T. Schneider, P. Treutlein, Y. Li, A. Sinatra, R. Long, J. Estève, and J. Reichel, Phys. Rev. Lett. **105**, 080403 (2010).
[10] F. Baumgärtner, R. J. Sewell, S. Eriksson, I. Llorente-Garcia, J. Dingjan, J. P. Cotter, and E. A. Hinds, Phys. Rev. Lett. **105**, 243003 (2010).
[11] L. J. LeBlanc, A. B. Bardon, J. McKeever, M. H. T. Extavour, D. Jervis, J. H. Thywissen, F. Piazza, and A. Smerzi, Phys. Rev. Lett. **106**, 025302 (2011).
[12] C. Gross, T. Zibold, E. Nicklas, J. Estève, and M. K. Oberthaler, Nature (London) **464**, 1165 (2010); E. Nicklas, H. Strobel, T. Zibold, C. Gross, B. A. Malomed, P. G. Kevrekidis, and M. K. Oberthaler, Phys. Rev. Lett. **107**, 193001 (2011).
[13] T. Zibold, E. Nicklas, C. Gross, and M. K. Oberthaler, Phys. Rev. Lett. **105**, 204101 (2010).
[14] S. Will, T. Best, S. Braun, U. Schneider, and I. Bloch, Phys. Rev. Lett. **106**, 115305 (2011).
[15] R. Scelle, T. Rentrop, A. Trautmann, T. Schuster, and M. K. Oberthaler, Phys. Rev. Lett. **111**, 070401 (2013).
[16] M. Rinck and C. Bruder, Phys. Rev. A **83**, 023608 (2011).
[17] F. Mulansky, J. Mumford, and D. H. J. O'Dell, Phys. Rev. A **84**, 063602 (2011).
[18] J. von Neumann, *Mathematische Grundlagen der Quantenmechanik* (Springer, Berlin, 1932) [English translation by R. T. Beyer, *Mathematical Foundations of Quantum Mechanics* (Princeton University Press, Princeton, NJ, 1955)].
[19] W. H. Zurek, Phys. Rev. D. **26**, 1862 (1982).
[20] M. Damnjanovic, Phys. Lett. A **134**, 77 (1988).
[21] S. N. Mayburov, in *Quantum Communications and Measurement*, edited by V. P. Belavkin, O. Hirota, and R. L. Hudson (Springer-Verlag, Berlin, 1995).

[22] A. E. Allahverdyan, R. Balian, and T. M. Nieuwenhuizen, arXiv:quant-ph/0508162.

[23] N. Bar-Gill, G. Kurizki, B. A. Malomed, and C. Sudheesh, Phys. Rev. A **82**, 013610 (2010).

[24] P. A. Ivanov and D. Porras, Phys. Rev. A **88**, 023803 (2013).

[25] J. Mumford, J. Larson, and D. H. J. O'Dell, Phys. Rev. A **89**, 023620 (2014).

[26] R. H. Dicke, Phys. Rev. **93**, 99 (1954).

[27] C. Emary and T. Brandes, Phys. Rev. E **67**, 066203 (2003).

[28] B. M. Garraway, Phil. Trans. R. Soc. A **369**, 1137 (2011).

[29] H. P. Breuer, D. Burgarth, and F. Petruccione, Phys. Rev. B **70**, 045323 (2004).

[30] K. A. Al-Hassanieh, V. V. Dobrovitski, E. Dagotto, and B. N. Harmon, Phys. Rev. Lett. **97**, 037204 (2006).

[31] S. S. Garmon, P. Ribeiro, and R. Mosseri, Phys. Rev. E **83**, 041128 (2011).

[32] K. Hepp and E. H. Lieb, Ann. Phys. **76**, 360 (1973).

[33] Y. K. Wang and F. Hioe, Phys. Rev. A **7**, 831 (1973).

[34] M. A. Nielsen and I. L. Chuang, *Quantum Computation and Quantum Information* (Cambridge University Press, Cambridge, UK, 2000).

[35] P. Zanardi and N. Paunkovic, Phys. Rev. E **74**, 031123 (2006).

[36] S. Chen, L. Wang, S. J. Gu, and Y. Wang, Phys. Rev. E **76**, 061108 (2007).

[37] P. Buonsante and A. Vezzani, Phys. Rev. Lett. **98**, 110601 (2007).

[38] H. T. Quan, Z. Song, X. F. Liu, P. Zanardi, and C. P. Sun, Phys. Rev. Lett. **96**, 140604 (2006).

[39] W. Q. Ning, S. J. Gu, Y. G. Chen, C. Q. Wu, and H. Q. Lin, J. Phys.: Condens. Matter **20**, 235236 (2008).

[40] W. L. You, Y. W. Li, and S. J. Gu, Phys. Rev. E **76**, 022101 (2007).

[41] M. F. Yang, Phys. Rev. B **76**, 180403(R) (2007).

[42] Z. Liu, H. Guo, S. Chen, and H. Feng, J. Phys. B: At. Mol. Opt. Phys. **45**, 055301 (2012).

[43] T. Sowinski, R. W. Chhajlany, O. Dutta, L. Tagliacozzo, and M. Lewenstein, arXiv:1304.4835 [cond-mat.quant-gas].

[44] P. Buonsante, R. Burioni, E. Vescovi, and A. Vezzani, Phys. Rev. A **85**, 043625 (2012).

[45] S.-J. Gu, H.-M. Kwok, W.-Q. Ning, and H.-Q. Lin, Phys. Rev. B **77**, 245109 (2008).

[46] H.-M. Kwok, W.-Q. Ning, S.-J. Gu, and H.-Q. Lin, Phys. Rev. E **78**, 032103 (2008).

[47] J. J. Sakurai, *Modern Quantum Mechanics* (Addison-Wesley, New York, 1994).

[48] G. J. Milburn, J. Corney, E. M. Wright, and D. F. Walls, Phys. Rev. A **55**, 4318 (1997).

[49] A. Smerzi, S. Fantoni, S. Giovanazzi, and S. R. Shenoy, Phys. Rev. Lett. **79**, 4950 (1997).

[50] N. T. Jacobson, S. Garnerone, S. Haas, and P. Zanardi, Phys. Rev. B **79**, 184427 (2009).

[51] L. Campos Venuti and P. Zanardi, Phys. Rev. Lett. **99**, 095701 (2007).

[52] In other words, when $1/(E_1 - E_0)$ is evaluated at $W = W_{\max}$ using the eigenvalues of Eq. (5) as it stands, it scales as $N^{1/3}$, as we have numerically verified.

[53] V. Privman and M. E. Fisher, Phys. Rev. B **30**, 322 (1984).

[54] R. K. Pathria and R. D. Beale, *Statistical Mechanics* (Elsevier, New York, 2011).

[55] S. Dusuel and J. Vidal, Phys. Rev. Lett. **93**, 237204 (2004); Phys. Rev. B **71**, 224420 (2005).

[56] T. Liu, Y. Y. Zhang, Q. H. Chen, and K. L. Wang, Phys. Rev. A **80**, 023810 (2009).

[57] H. Heiselberg, C. J. Pethick, H. Smith, and L. Viverit, Phys. Rev. Lett. **85**, 2418 (2000).

[58] D. H. Santamore and E. Timmermans, Phys. Rev. A **78**, 013619 (2008).

[59] M. Cozzini, R. Ionicioiu, and P. Zanardi, Phys. Rev. B **76**, 104420 (2007).

[60] S. Diehl, A. Micheli, A. Kantin, B. Kraus, H. P. Buechler, and P. Zoller, Nat. Phys. **4**, 878 (2008).

[61] S. Gopalakrishnan, B. L. Lev, and P. M. Goldbart, Nat. Phys. **5**, 845 (2009).

[62] D. Nagy, G. Konya, G. Szirmai, and P. Domokos, Phys. Rev. Lett. **104**, 130401 (2010); D. Nagy, G. Szirmai, and P. Domokos, Phys. Rev. A **84**, 043637 (2011).

[63] M. J. Bhaseen, J. Mayoh, B. D. Simons, and J. Keeling, Phys. Rev. A **85**, 013817 (2012).

[64] M. Öztop, M. Bordyuh, Ö. E. Müstecapliogu, and H. E. Türeci, New J. Phys. **14**, 085011 (2012).

[65] M. Buchhold, P. Strack, S. Sachdev, and S. Diehl, Phys. Rev. A **87**, 063622 (2013).

[66] F. Brennecke, R. Mottl, K. Baumann, R. Landig, T. Donner, and T. Esslinger, Proc. Natl. Acad. Sci. USA **110**, 11763 (2013).

[67] A. Miller, D. Pines, and P. Nozieres, Phys. Rev. **127**, 1452 (1962).

[68] R. M. Kalas and D. Blume, Phys. Rev. A **73**, 043608 (2006).

[69] F. M. Cucchietti and E. Timmermans, Phys. Rev. Lett. **96**, 210401 (2006).

[70] J. Tempere, W. Casteels, M. K. Oberthaler, S. Knoop, E. Timmermans, and J. T. Devreese, Phys. Rev. B **80**, 184504 (2009).

[71] M. A. Cirone, G. De Chiara, G. M. Palma, and A. Recati, New J. Phys. **11**, 103055 (2009).

[72] E. Compagno, G. De Chiara, D. G. Angelakis, and G. M. Palma, arXiv:1410.8833 [quant-ph].

[73] S. Dhar, S. Dasgupta, A. Dhar, and D. Sen, arXiv:1410.8701 [quant-ph].

[74] M. Schecter, D. M. Gangardt, and A. Kamenev, Ann. Phys. **327**, 639 (2012).

[75] M. Schecter, A. Kamenev, D. M. Gangardt, and A. Lamacraft, Phys. Rev. Lett. **108**, 207001 (2012).

[76] I. Bausmerth, U. R. Fischer, and A. Posazhennikova, Phys. Rev. A **75**, 053605 (2007); U. R. Fischer, C. Iniotakis, and A. Posazhennikova, *ibid.* **77**, 031602(R) (2008).

[77] P. Lu, Z.-H. Zhang, S. Feng, and S.-J. Yang, Phys. Rev. B **86**, 104504 (2012).

[78] D. Spehner and F. Haake, Phys. Rev. A **77**, 052114 (2008).

[79] G. Ferrini, D. Spehner, A. Minguzzi, and F. W. J. Hekking, Phys. Rev. A **82**, 033621 (2010).

[80] S. McEndoo, P. Haikka, G. De Chiara, G. M. Palma, and S. Maniscalco, Europhys. Lett. **101**, 60005 (2013).

[81] S. Krönke, J. Knörzer, and P. Schmelcher, arXiv:1410.8676 [cond-mat.quant-gas].

3.3 Paper III: Catastrophes in non-equilibrium many-particle wave functions: universality and critical scaling

Jesse Mumford, Wyatt Kirkby, and D. H. J. O'Dell
Catastrophes in non-equilibrium many-particle wave functions: universality and critical scaling
J. Phys. B: At. Mol. Opt. Phys. **50**, 044005 (2017);
DOI: https://doi.org/10.1088/1361-6455/aa56af

Summary: In this paper we analyze semiclassical dynamics of some many-body systems after a quench. The quench scheme consists starting the system in its ground state, then flashing on and off a single term in the semiclassical Hamiltonian at $t = 0$, then allowing the system to evolve normally. We show the dynamics of the wave function form a cusp catastrophe in continuous Fock space vs. time. When the system approaches a PT as $\lambda \to 0$, where λ is the reduced driving parameter, we show the intensity and fringe spacing of the wave function exhibit cusp catastrophe universal scaling. This paper marks the first use of catastrophe theory (CT) to analyze the effects of a PT on the quantum dynamics of a system.

Content: The majority of the article was written by the author with the exception of the introduction and conclusion which was written by Duncan O'Dell. All of the numerical and analytic calculations were done by the author with the help of Wyatt Kirkby.

IOP Publishing Journal of Physics B: Atomic, Molecular and Optical Physics
J. Phys. B: At. Mol. Opt. Phys. **50** (2017) 044005 (17pp) https://doi.org/10.1088/1361-6455/aa56af

Catastrophes in non-equilibrium many-particle wave functions: universality and critical scaling

J Mumford, W Kirkby and D H J O'Dell

Department of Physics and Astronomy, McMaster University, 1280 Main St. W., Hamilton, ON, L8S 4M1, Canada

E-mail: dodell@mcmaster.ca

Received 4 September 2016, revised 9 December 2016
Accepted for publication 4 January 2017
Published 31 January 2017

Abstract

As part of the quest to uncover universal features of quantum dynamics, we study catastrophes that form in simple many-particle wave functions following a quench, focusing on two-mode systems that include the two-site Bose–Hubbard model, and under some circumstances optomechanical systems and the Dicke model. When the wave function is plotted in Fock space certain characteristic shapes, that we identify as cusp catastrophes, appear under generic conditions. In the vicinity of a cusp the wave function takes on a universal structure described by the Pearcey function and obeys scaling relations which depend on the total number of particles N. In the thermodynamic limit ($N \to \infty$) the cusp becomes singular, but at finite N it is decorated by an interference pattern. This pattern contains an intricate network of vortex–antivortex pairs, initiating a theory of topological structures in Fock space. In the case where the quench is a δ-kick the problem can be solved analytically and we obtain scaling exponents for the size and position of the cusp, as well as those for the amplitude and characteristic length scales of its interference pattern. Finally, we use these scalings to describe the wave function in the critical regime of a $\mathbb{Z}_2$ symmetry-breaking dynamical phase transition.

Keywords: quantum dynamics, ultracold gases, catastrophe theory, phase transitions

(Some figures may appear in colour only in the online journal)

1. Introduction

Universality is one of the most cherished concepts in physics. Perhaps the best known example is near second-order (continuous) phase transitions where *equilibrium* properties such as correlation lengths and susceptibilities diverge according to power laws with universal exponents as a control parameter approaches its critical value. In fact, physical systems are partitioned into different universality classes, each characterized by a particular set of critical exponents. Members of the same class can be very different at the microscopic scale and yet they display the same asymptotic scale invariance in the critical regime.

Our goal in this paper is to study universality in non-equilibrium behavior. Current paradigms in this area include the Kibble–Zurek mechanism [1, 2] describing defect production upon ramping through a second order phase transition at a finite speed, and the eigenstate thermalization hypothesis describing thermalization of isolated quantum systems [3–5]. These problems have attracted the attention of the cold atom [6–17] and cold ion [18, 19] communities because such systems offer remarkable levels of coherence and control, making them useful for testing fundamental models of many-particle dynamics.

The universality we investigate here is somewhat different and occurs in the time-dependent many-particle wave function itself (rather than, say, correlation functions). In particular, we study striking geometric shapes that emerge in Fock space following a quench, identifying them as the catastrophes that are categorized by catastrophe theory (CT) [20–22]. They can occur far from any phase transition, although close to one they display familiar features such as

Table 1. Structurally stable catastrophes and their generating functions with co-dimension $K \leqslant 3$. Co-dimension is defined as the dimensionality of the control space minus the dimensionality of singularity. **R** represents the control parameters and **s** the state variables.

Name	K	Generating function $\Phi(\mathbf{s};\mathbf{R})$
Fold	1	$s^3 + Xs$
Cusp	2	$s^4 + Xs^2 + Ys$
Swallowtail	3	$s^5 + Xs^3 + Ys^2 + Zs$
Elliptic umbilic	3	$s_1^3 - 3s_1s_2^2 + Z(s_1^2 + s_2^2) + Ys_2 + Xs_1$
Hyperbolic umbilic	3	$s_1^3 + s_2^3 + Zs_1s_2 + Ys_2 + Zs_1$

critical slowing down. Catastrophes do in fact have a number of features that are reminiscent of phase transitions, including the occurrence of singularities, equivalence classes, and self-similar scaling relations [23, 24].

A list of the structurally stable catastrophes with co-dimension one, two and three is given in table 1. Each is defined via its normal form or generating function $\Phi(\mathbf{s};\mathbf{R})$; each generating function is a polynomial in the state variables $\mathbf{s} = \{s_1, s_2, s_3, \ldots\}$ but is linear in the control parameters $\mathbf{R} = \{X, Y, Z, \ldots\}$. *In this paper the physical role of the generating function is as the mechanical action*. In this way, each canonical generating function is associated with a canonical wave function via a Feynman path integral $\Psi(\mathbf{R}) \propto \int \exp[\mathrm{i}\Phi(\mathbf{s};\mathbf{R})/\hbar]\,\mathrm{d}\mathbf{s}$ [25, 26]. The state variables **s** specify the 'paths' or configurations and the control parameters **R** provide the coordinates. In the simplest case of the fold catastrophe this gives the Airy function [27], and in the case of the cusp, which will be the main subject of this paper, it gives the Pearcey function [28]. These functions, referred to variously as wave catastrophes or diffraction integrals [29, 30], have the status of special functions akin to, say, Bessel functions, and their mathematical properties are summarized in chapter 36 of reference [31]. In a typical physical problem the action does not automatically present itself in one of the normal forms listed in table 1, but the claim of CT is that close to a singularity it can always be mapped onto one of them. Finding the required transformation may not be easy, but in the present paper we shall consider simple situations where this can be done analytically.

It is important to point out that CT can be applied in a number of different ways to quantum mechanics. Our use of the catastrophe generating functions $\Phi(\mathbf{s};\mathbf{R})$ as actions is distinct from other applications, such as taking the generating functions as potentials to be used in the Schrödinger equation [32, 33], although in both cases universal structures are obtained which have a qualitative robustness. This important property, which is known as structural stability, means that catastrophes are qualitatively immune to perturbations and hence occur generically with no need for special symmetry. This is the reason behind their ubiquity.

Our application of CT in this paper is inspired by its use in the description of optical caustics [29, 30, 34]. Caustics are the result of natural focusing and occur widely in nature with examples including rainbows, bright lines on the bottom of swimming pools, twinkling of starlight [23], gravitational lensing, and freak waves [35]. Being a general wave phenomenon, caustics also appear in quantum waves such as those describing the motion of cold atoms. The experiment by Rooijakkers *et al* [36] observed caustics in the trajectories of cold atoms trapped in a magnetic waveguide, Huckans *et al* [37] observed them in the dynamics of a Bose–Einstein condensate (BEC) in an optical lattice, and in the experiment by Rosenblum *et al* [38] caustics appeared when a cold atomic cloud was reflected from an optical barrier in the presence of gravity. On the theoretical side, caustics have been predicted to occur in atomic diffraction from standing waves of light [39], in atom clouds in pulsed optical lattices [40, 41], in the dynamics of particles with long-range interactions [42], in the expansion dynamics of Bose gases released from one- and two-dimensional traps [43], and they can also produce characteristic features in the long-time (but non-thermal) probability distribution following quenches in optical lattices and Josephson junctions [44, 45]. Furthermore, although not identified as such by their authors, caustics can be seen in figures in papers on the dynamics of BECs encountering a supersonic obstacle [46], on the collapse and subsequent spreading of a BEC of polaritons pulsed by a laser [47] and in quantum random walks by interacting bosons in an optical lattice [48].

The properties of caustics depend on the scale at which they are viewed. At large scales they appear singular and the proper description is via geometric ray theory, equivalent to the classical ($\hbar \to 0$) limit of single-particle quantum mechanics. In this theory the intensity tends to infinity as the caustic is approached. At small scales, where the wavelength is finite, the singularity is removed by interference. Each class of caustic is dressed by a characteristic interference pattern (wave catastrophe). In the many-particle problem there are two new features: the first is a rather trivial replacement of $\hbar$ by $1/N$, where N is the total number of particles. The second, more fundamental difference, is an intrinsic granularity imposed on wave catastrophes by the discreteness of the number of particles [45]. This latter feature is particularly apparent in Fock space which is the natural arena for many-particle physics. In many-particle problems mean-field theory plays the role of geometric ray theory: it applies in the limit $N \to \infty$ and ignores the granularity of the particle number, providing an effective single-particle description which is usually nonlinear.

As an example, consider a BEC containing N ultracold atoms. In the mean-field theory for condensed bosons the condensate wave function $\psi(\mathbf{r}, t)$ obeys the Gross–Pitaevskii wave equation (GPE)

$$\mathrm{i}\hbar\frac{\partial\psi}{\partial t} = \left(-\frac{\hbar^2}{2m}\nabla^2 + V(\mathbf{r}) + g|\psi|^2\right)\psi, \qquad (1)$$

where $V(\mathbf{r})$ is the external potential and g characterizes the strength of the interactions. This 'first-quantization' in terms of a classical wave equation is sufficient to remove singularities in coordinate space. However, in Fock space mean-field theory predicts singular caustics that must be removed by

second-quantizing the field, i.e. by building in the discreteness of the number of field quanta (atoms) which is ignored by the GPE (see figure 2 below) [45]. In this paper we shall work in the semiclassical regime ($N \gg 1$) where a continuum approximation can be applied to Fock space although crucially we retain the non-commuting nature of quantum operators (such as the number and phase operators), in contrast to the mean-field approximation. Under this prescription standard continuous wave catastrophes are recovered [49].

A singularity in Fock space can be considered to be an example of a *quantum catastrophe*, i.e. a singularity in classical field theory that is removed by going over to quantum field theory where the field amplitudes are quantized (atoms in the case of BECs, photons in the case of electromagnetic fields [50, 51]). Hawking radiation, where pairs of photons are produced from the vacuum near a black hole, is an example of a quantum catastrophe as has been pointed out by Leonhardt [52] by considering the fate of a classical electromagnetic wave propagating over an event horizon. The wave suffers a phase singularity (it oscillates infinitely rapidly and hence takes all values) when seen by an observer at infinity. Indeed, there is no Hermitian operator for phase in quantum mechanics and the concept of phase only becomes well defined in the classical limit of a large number of quanta.

In this paper we study simple many-particle systems involving just two modes. This includes the two-site Bose–Hubbard model (a particular case of the Lipkin–Meshkov–Glick model [53]), the Dicke model, various optomechanical systems, and generally any collection of spins or pseudo-spins in the single mode approximation (including the Ising model with long-range interactions [54]). As we shall show in section 2, in the semiclassical regime these models can be mapped onto an effective Hamiltonian of the form

$$\frac{\hat{H}}{N} = \frac{\hat{p}^2}{2} + V(\hat{x}), \tag{2}$$

where $V(\hat{x})$ is an operator with a nonlinear (anharmonic) spectrum. Since this Hamiltonian has one degree of freedom, the space where dynamical catastrophes live is the two-dimensional (x, t)-plane known as the control space, and according to CT the structurally stable catastrophes in two dimensions are fold lines which can meet at cusp points (a general feature of CT is that the higher catastrophes contain the lower ones). We therefore expect from the very start that the structures we see will be comprised of Airy and Pearcey functions. Furthermore, all these models display second-order phase transitions as a parameter is varied and this fact will allow us to examine how catastrophes behave when the Hamiltonian is tuned close to the critical point.

The plan for the rest of this paper is as follows: after reviewing some examples of two-mode many-particle systems in section 2, we proceed in section 3 to study the classical (mean-field) dynamics of these systems following a quench, showing how catastrophes arise as the envelopes of families of classical trajectories compatible with the quantum conditions. Specializing to the δ-kicked case in section 4, we demonstrate the connection between the second-order phase transition in the instantaneous Hamiltonian and the appearance in the subsequent dynamics of different types of cusp catastrophe in Fock space + time. In section 5 we examine the quantum version of this behavior, showing how the wave function can be mapped onto the Pearcey function. This function obeys a set of scaling identities and we use these to understand the scaling properties of the many-particle wave function, including the size and position of the cusp, the oscillations in the interference pattern that decorates it, as well as topological features such as vortices. In section 6 we look beyond the δ-kicked case and discuss the features we expect when the system propagates under the full Hamiltonian. We give our conclusions in section 7.

The results presented in sections 2 and 3 are largely review, with the idea that granular catastrophes appear in the Fock space of many-particle systems being introduced previously by one of us (DO) in [45]. However, the mapping presented in sections 4–6 of δ-kicked two-mode many particle wave functions onto the Pearcey function is to the best of our knowledge new, including the connection to dynamical phase transitions and the concept of quantized vortices in Fock space.

2. Two-mode many-particle systems

In this section we show how various two-mode many-particle Hamiltonians can be written in the form given in equation (2). The Hilbert space of equation (2) is infinite, so it cannot properly model highly excited states that feel the finiteness of the original Hilbert space, however, when N is large and the highest states are not excited equation (2) can be used as a semiclassical approximation. Because $1/N$ plays the role of $\hbar$, the operators $\hat{x}$ and $\hat{p}$ satisfy the commutation relation $[\hat{x}, \hat{p}] = \mathrm{i}/N$, and the classical limit $\hbar \to 0$ is the same as the thermodynamic limit $N \to \infty$. Away from this limit, the finite value of the commutator must be preserved if singular caustics are to be avoided in Fock space.

2.1. Two-site Bose–Hubbard model

We begin with the Bose–Hubbard model with two sites and N particles. This can be used to describe a BEC in a double well potential which has been realized in a number of experiments [55–60]. In the single band regime the two modes can be taken to be the ground states on each site and the Hamiltonian is written [61]

$$\hat{H}_{\mathrm{BH}} = U\hat{n}^2 - J(\hat{a}_{\mathrm{R}}^{\dagger}\hat{a}_{\mathrm{L}} + \hat{a}_{\mathrm{L}}^{\dagger}\hat{a}_{\mathrm{R}}), \tag{3}$$

where $\hat{n} = (\hat{a}_{\mathrm{R}}^{\dagger}\hat{a}_{\mathrm{R}} - \hat{a}_{\mathrm{L}}^{\dagger}\hat{a}_{\mathrm{L}})/2$ is half the number-difference between the two sites labeled by L (left) and R (right). The annihilation and creation operators obey the usual bosonic commutation relations $[\hat{a}_{\mathrm{L/R}}, \hat{a}_{\mathrm{L/R}}^{\dagger}] = \delta_{\mathrm{L/R}}$. U is the on-site interaction energy between the bosons and can be positive or negative depending upon whether the interactions are repulsive or attractive, and $J > 0$ is the intersite hopping energy. The parameter $\Lambda_{\mathrm{BH}} = UN/2J$, which is the ratio of the interaction energy to the mode-coupling energy, determines the behavior of the system. For attractive enough interactions,

$\Lambda_{\rm BH} < -1$, the ground state suffers a $\mathbb{Z}_2$ symmetry-breaking phase transition where a majority of bosons clump on one site or the other, as seen in the recent experiment by Trenkwalder *et al* [60]. When $\Lambda_{\rm BH} > -1$ the ground state is symmetric but the dynamics can be divided into three regimes [61]: the Rabi regime ($-1 < \Lambda_{\rm BH} < 1$) where the interactions (which provide the nonlinearity) are weak enough that the system essentially behaves as N independent two-level oscillators (pseudo-spins); the Josephson regime ($1 < \Lambda_{\rm BH} \ll N^2$) where both the interactions and the single particle hopping are important; and the Fock regime ($\Lambda_{\rm BH} \gg N^2$) where interactions dominate.

The many-particle wave function can be expanded $|\Phi(t)\rangle = \sum c_n(t)|n\rangle$ in terms of the eigenstates $|n\rangle$ of $\hat{n}$, i.e. in terms of Fock states with well defined number differences. In general the system is in superposition of number difference states and the probabilities $|c_n(t)|^2 = |\langle n|\Phi(t)\rangle|^2$ define the probability distribution in Fock space. There is no explicit assumption of BEC although the bosons must be cold enough to only occupy the lowest state on each site. By contrast, in the Gross–Pitaevskii mean-field theory it is assumed that there is condensate on each site with a perfectly well-defined number difference $n(t)$ and phase difference $\phi(t) = \phi_{\rm R}(t) - \phi_{\rm L}(t)$ between the two sites at all times [62], in other words $\Delta n \Delta\phi = 0$. This implies a U(1) symmetry breaking in which the phase difference is selected. Furthermore, the number difference becomes a continuous variable rather than a discrete one. The mean-field Hamiltonian is [63]

$$\lim_{N\to\infty} \frac{\hat{H}_{\rm BH}}{NJ} = H_{\rm BH} = \Lambda_{\rm BH}\frac{z^2}{2} - \sqrt{1-z^2}\cos\phi. \qquad (4)$$

where it is customary to introduce $z = 2n/N$, where $-1 \leqslant z \leqslant 1$, as the number difference scaled by the total number of bosons. This Hamiltonian corresponds to that of a pendulum where the role of the angular momentum is played by the number difference and its angular position is given by the phase difference. However, the length of the pendulum depends on its angular momentum via the square root factor which gives rise to a type of classical motion, called π-oscillations, that is not present in the rigid pendulum [63]. In the Rabi regime there are two stable stationary points, one at $\phi = 0$ and the other at $\phi = \pi$, the latter corresponding to the pendulum standing upright. Small oscillations around $\phi = 0$ are called plasma oscillations (in analogy to similar excitations in Josephson junctions) and were observed using cold atoms in the pioneering experiments by Albiez *et al* [55] and Levy *et al* [57]. π-oscillations, on the other hand, correspond to small oscillations around $\phi = \pi$ and were seen in the experiment by Zibold *et al* [58]. Both plasma and π-oscillations have a time-averaged number difference of $\langle z\rangle = 0$ but are distinguished by having a time-averaged phase differences of $\langle\phi\rangle = 0$ and $\langle\phi\rangle = \pi$, respectively. However, upon entering the Josephson regime there is pitchfork bifurcation in which the stationary point at $\phi = \pi$ becomes unstable and is replaced by two new stable stationary points which have $\langle z\rangle \neq 0$. These excited yet stationary states are responsible for the phenomenon of macroscopic quantum self-trapping [64] where an initial imbalance of boson number between the two wells remains locked in place (rather than oscillating back and forth) and is related to the Josephson ac effect in Josephson junctions. The stationary point at $\phi = 0$ is unaffected by the bifurcation but is separated from the new stationary points by a separatrix. In the quantum theory the separatrix corresponds to a peak in the density of states [65] and can be interpreted as a dynamical phase transition in the thermodynamic limit [66]. The transition is of the $\mathbb{Z}_2$ symmetry breaking type corresponding to the choice of either $\langle z\rangle > 0$ or $\langle z\rangle < 0$.

The quantum dynamics is governed by the Schrödinger equation $\mathrm{i}\hbar\partial_t|\Phi\rangle = \hat{H}_{\rm BH}|\Phi\rangle$. Substituting in the expansion over Fock states one obtains a set of $N+1$ coupled differential-difference equations for the Fock space amplitudes $c_n(t)$. These can easily be solved numerically [65], and can also be tackled analytically in the semiclassical regime [39, 45] revealing cusp catastrophes in the wave function in Fock space plus time following a quench. The cusps have also been discussed in terms of quantum collapses and revivals of the initial state [67, 68].

For the purposes of this paper we seek a semiclassical Hamiltonian in the form of equation (2). The mean-field Hamiltonian given in equation (4) is close to the desired structure and can be re-quantized by promoting z and ϕ to operators. However, in contrast to the original problem, we now assume that $\hat{z}$ (and $\hat{\phi}$) has a continuous spectrum and obeys the commutation relation $[\hat{\phi}, \hat{z}] = 2\mathrm{i}/N$ [65]. We refer to this as the *continuum approximation*. There is still the matter of the square root factor involving $\hat{z}$ which means that this Hamiltonian is not quite separated into 'kinetic plus potential energy'. To remedy this we write the wave function (in the phase representation) as

$$\Psi(\phi) = \mathrm{e}^{\frac{N}{2\Lambda_{\rm BH}}\cos\phi} \sum_{n=-N/2}^{N/2} \frac{c_n}{\sqrt{\left(\frac{N}{2}+n\right)!\left(\frac{N}{2}-n\right)!}}\mathrm{e}^{\mathrm{i}n\phi}. \qquad (5)$$

Note that this wave function is not normalized.The time-independent Schrödinger equation then becomes (in the semiclassical regime $N \gg 1$) [69]

$$-\frac{2\Lambda_{\rm BH}}{N}\frac{\partial^2\Psi}{\partial\phi^2} - \frac{N}{2\Lambda_{\rm BH}}(\cos^2\phi + 2\Lambda_{\rm BH}\cos\phi - 1)\Psi = \frac{E}{J}\Psi, \qquad (6)$$

where $\hat{z} = -\frac{2\mathrm{i}}{N}\frac{\partial}{\partial\phi}$ in analogy to the standard relation $\hat{p} = -\mathrm{i}\hbar\partial/\partial x$. This suggests the effective Hamiltonian

$$\frac{\hat{H}'_{\rm BH}}{NJ} = \frac{\Lambda_{\rm BH}}{2}\hat{z}^2 - \frac{1}{2\Lambda_{\rm BH}}(\cos^2\hat{\phi} + 2\Lambda_{\rm BH}\cos\hat{\phi} - 1), \qquad (7)$$

where we use the prime to signify that equation (7) is the re-quantized version of equation (3). Equation (7) has the form of equation (2) where

$$V(\hat{\phi}) = -\frac{1}{2\Lambda_{\rm BH}}(\cos^2\hat{\phi} + 2\Lambda_{\rm BH}\cos\hat{\phi} - 1) \qquad (8)$$

plays the role of an effective potential for the position coordinate ϕ [64] which we plot in figure 1. When $\Lambda_{\rm BH} < 1$ we see two minima, one at $\phi = 0$ and the other at $\phi = \pm\pi$,

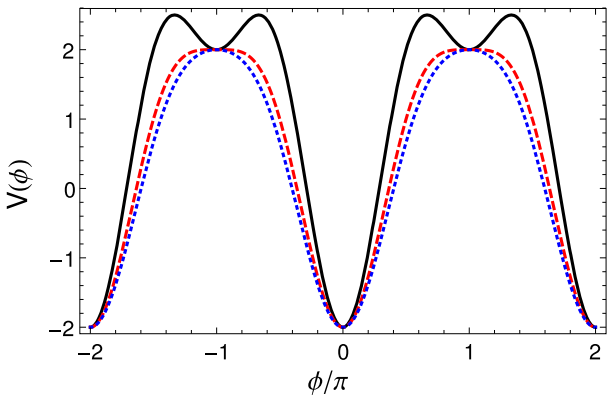

Figure 1. A plot of the effective potential $V(\phi)$ for the two-site Bose–Hubbard model as given in equation (8). Each curve is for a different value of $\Lambda_{\rm BH}$: 0.5 (solid black), 1.0 (dashed red), and 1.5 (dotted blue). When $\Lambda_{\rm BH} < 1$ there are two minima, one at $\phi = 0$ and the other at $\phi = \pm\pi$, and motion about these points gives rise to plasma- and π-oscillations, respectively. When $\Lambda_{\rm BH} > 1$ the potential features only a single minimum at $\phi = 0$. Two types of motion are possible in this latter regime: plasma oscillations around the minimum and macroscopic quantum self-trapping where the energy exceeds the barrier top at $\phi = \pm\pi$ and the phase grows continuously, either in the clockwise or anticlockwise direction. Note that $V(\phi)$ is periodic outside the fundamental domain $-\pi < \phi \leqslant \pi$, but we have plotted twice this range so that the properties of the potential near $\phi = \pm\pi$ are clear.

which are responsible for the plasma and π-oscillations, respectively. As expected, the minimum at $\phi = \pi$ disappears at $\Lambda_{\rm BH} = 1$ corresponding to the destruction of the π-oscillations. When $\Lambda_{\rm BH} > 1$ the potential has just a single well and two types of motion are possible: when the energy is below the separatrix given by the barrier tops at $E = NJ$ the motion is oscillatory with time average $\langle\phi\rangle = 0$ (plasma oscillations), but when the energy is above the separatrix the phase can continuously wind up in either the clockwise or anticlockwise directions. Because of the winding, the angular momentum also has a finite time-average implying that $\langle z\rangle \neq 0$ (macroscopic quantum self-trapping).

2.2. Optomechanics

The second system we consider is the 'membrane-in-the-middle' (MM) setup realized in optomechanics experiments [70, 71]. It consists of an optical cavity divided in two by a partially transmissive and elastic membrane. The cavity is pumped by laser light through the end mirrors and the membrane is deformed by the radiation pressure upon it. The membrane can be pushed to the left or the right: if it is pushed to the right, say, it reduces the length of the right hand cavity and increases the length of the left hand cavity. This changes the resonance frequency for each cavity resulting in a change in the number of photons which in turn changes the radiation pressure (this feedback is the origin of the nonlinearity in this system). The total Hamiltonian is [72]

$$\hat{H}_{\rm MM} = \hat{H}_{\rm m} + \hat{H}_{\rm l} + \hat{H}_{\rm int} + \hat{H}_{\rm p}, \tag{9}$$

where

$$\begin{aligned}\hat{H}_{\rm m} &= \frac{\hat{p}^2}{2m} + \frac{m\omega^2\hat{x}^2}{2}\\ \hat{H}_{\rm l} &= g(\hat{a}_{\rm R}^\dagger\hat{a}_{\rm L} + \hat{a}_{\rm L}^\dagger\hat{a}_{\rm R})\\ \hat{H}_{\rm int} &= \frac{2\gamma}{\sqrt{V}}\hat{x}\hat{n}\\ \hat{H}_{\rm p} &= \eta_{\rm R}\sqrt{V}(\hat{a}_{\rm R}^\dagger + \hat{a}_{\rm R}) + \eta_{\rm L}\sqrt{V}(\hat{a}_{\rm L}^\dagger + \hat{a}_{\rm L}),\end{aligned} \tag{10}$$

are the Hamiltonians for the membrane (mechanical harmonic oscillator), light hopping between cavities by transmission through the membrane, radiation pressure, and pump, respectively. Here, like in the previous example, the left- and right-hand cavity modes are labeled by L and R, respectively, however, now these modes are occupied by photons instead of massive particles. V is the cavity mode volume and is related to the number of photons in a cavity by $V = N/\rho$ where ρ is the number density of photons. The parameters ω and g are the natural oscillation frequencies of the membrane and light hopping, respectively, γ gives the interaction energy due to radiation pressure and $\eta_{\rm L}$ and $\eta_{\rm R}$ give the pumping strengths for the left and right cavities. The relevant parameter in this system is $\Lambda_{\rm MM} = (2g/m)(2\gamma\eta/[\omega(g^2+\kappa^2)])^2$ where for $\Lambda_{\rm MM} > 1$ the ground state of the system goes from being a centered membrane with an equal number of photons in each cavity to a shifted membrane with a buildup of light in one cavity over the other which is the result of breaking the $\mathbb{Z}_2$ symmetry of the system.

In experiments it is usually the case that the light field evolves much faster than the membrane, i.e. $g \gg \omega$ [73, 74], so that the light 'instantaneously' adjusts to the position of the membrane. The optical modes can then be adiabatically eliminated to give an effective potential for the membrane alone. To do this we assume the light satisfies the stationary solutions of the equations of motion, $\dot{\hat{a}}_{\rm R} = \dot{\hat{a}}_{\rm L} = 0$, giving

$$\begin{aligned}\hat{a}_{\rm R}^{\rm s} &= -\frac{{\rm i}\eta_{\rm R}\kappa\sqrt{V} + g\eta_{\rm L}\sqrt{V} + \hat{x}\eta_{\rm R}\gamma}{g^2+\kappa^2+\hat{x}^2\gamma^2/V}\\ \hat{a}_{\rm L}^{\rm s} &= -\frac{{\rm i}\eta_{\rm L}\kappa\sqrt{V} + g\eta_{\rm R}\sqrt{V} - \hat{x}\eta_{\rm L}\gamma}{g^2+\kappa^2+\hat{x}^2\gamma^2/V},\end{aligned} \tag{11}$$

where we have introduced a cavity decay rate κ. We obtain the effective potential by substituting equation (11) into

$$\dot{\hat{p}} = -m\omega^2\hat{x} - \frac{2\gamma}{\sqrt{V}}\hat{n} = -\frac{{\rm d}V(\hat{x})}{{\rm d}\hat{x}} \tag{12}$$

which upon integration gives the effective Hamiltonian for the membrane [75]

$$\frac{\hat{H}'_{\rm MM}}{V} = \frac{\hat{p}^2}{2m} + \frac{m\omega^2\hat{x}^2}{2} + \frac{4g\eta^2}{g^2+\kappa^2+\hat{x}^2\gamma^2}, \tag{13}$$

where the transformations $\hat{p} \to \hat{p}\sqrt{V}$ and $\hat{x} \to \hat{x}\sqrt{V}$ were made, so in $[\hat{x}, \hat{p}] = {\rm i}/V$ the limit $V \to \infty$ is again the same as $\hbar \to 0$. We have also assumed the ground state is being pumped, which for $g > 0$ means $\eta_{\rm R} = -\eta_{\rm L} = \eta$ [76]. This Hamiltonian is of the desired form given by equation (2). Near the critical value of $\Lambda_{\rm MM}$ it is sufficient to Taylor expand the effective potential up to quartic terms so that it can take on

a double-well shape. The transition from a single- to a double-well describes the $\mathbb{Z}_2$ symmetry breaking transition where the membrane spontaneously displaces to the left or right. Furthermore, this is a dynamical phase transition as the cavity is pumped by laser light and hence is not in its ground state.

2.3. Dicke model in the Holstein–Primakoff representation

Lastly, we look at the Dicke model (DM) which describes a collection of spin-1/2 particles coupled to a harmonic oscillator. In its original context this was used to model collective light emission (superradiance) by N two-level atoms coupled to a single mode of the electromagnetic field [77]. Unlike in the last example where we eliminated the degrees of freedom of one part of the system, we keep both here. In a cold atom context the DM has been realized using a BEC inside an optical cavity [78, 79], where the two 'spin' states refer to two different translational modes of the atoms. The DM Hamiltonian can be written

$$\hat{H}_{\rm DM} = \omega_0 \hat{S}_z + \omega \hat{b}^\dagger \hat{b} + \frac{\chi}{\sqrt{2S}}(\hat{b}^\dagger + \hat{b})(\hat{S}_+ + \hat{S}_-), \quad (14)$$

where the Schwinger representation has been used to describe the N two-level systems, each with excitation frequency ω_0, as a large pseudospin of length $S = N/2$. The electromagnetic field mode with frequency ω is acted on by the creation (annihilation) operator $\hat{b}^\dagger$ ($\hat{b}$) and the coupling with the spins is given by χ. For $\Lambda_{\rm DM} = 2\chi/\sqrt{\omega\omega_0} > 1$ the ground state suffers a parity breaking ($\mathbb{Z}_2$) phase transition resulting in a spontaneous excitation of the harmonic oscillator, i.e. the coherent emission of light by the atoms. The presence of external pumping of the cavity once again means that this is a dynamical rather than a ground state phase transition. To describe the phase transition Emary and Brandes [80] used the Holstein–Primakoff representation [81, 82] of spin operators to write them in terms of ordinary annihilation and creation operators

$$\hat{S}_+ = \hat{a}^\dagger\sqrt{2S - \hat{a}^\dagger\hat{a}}\,,\ \hat{S}_- = \sqrt{2S - \hat{a}^\dagger\hat{a}}\ \hat{a}$$
$$\hat{S}_z = \hat{a}^\dagger\hat{a} - S, \quad (15)$$

where $[\hat{a}, \hat{a}^\dagger] = 1$. The Holstein–Primakoff representation is useful when the spin is only weakly excited above its ground state which is the extremal spin projection state $|S, m = -S\rangle$, so that $\langle\hat{a}^\dagger\hat{a}\rangle/2S \ll 1$, and the square roots can be expanded in powers of $1/2S$. By converting the annihilation and creation operators into position and momentum operators using the standard definitions

$$\hat{b} \equiv \sqrt{\frac{\omega}{2}}\left(\hat{x} + \frac{\mathrm{i}}{\omega}\hat{p}_x\right), \quad \hat{b}^\dagger \equiv \sqrt{\frac{\omega}{2}}\left(\hat{x} - \frac{\mathrm{i}}{\omega}\hat{p}_x\right)$$
$$\hat{a} \equiv \sqrt{\frac{\omega_0}{2}}\left(\hat{y} + \frac{\mathrm{i}}{\omega_0}\hat{p}_y\right), \quad \hat{a}^\dagger \equiv \sqrt{\frac{\omega_0}{2}}\left(\hat{y} - \frac{\mathrm{i}}{\omega_0}\hat{p}_y\right), \quad (16)$$

they were able to show that equation (14) takes the form

$$\hat{H}_{\rm DM} = \frac{1}{2}(\hat{p}_x^2 + \omega^2\hat{x}^2 + \hat{p}_y^2 + \omega_0^2\hat{y}^2)$$
$$+ \chi\sqrt{\omega\omega_0}\hat{x}\left[\left(\hat{y} - \frac{\mathrm{i}}{\omega_0}\hat{p}_y\right)\sqrt{1-\hat{\eta}}\right.$$
$$\left. + \sqrt{1-\hat{\eta}}\left(\hat{y} + \frac{\mathrm{i}}{\omega_0}\hat{p}_y\right)\right], \quad (17)$$

where

$$\hat{\eta} = (\omega_0^2\hat{y}^2 + \hat{p}_y^2 - \omega_0)/(4S\omega_0). \quad (18)$$

Even though $\hat{H}_{\rm DM}$ has imaginary terms and a momentum dependent potential, $V(\hat{x}, \hat{y}, \hat{p}_y)$, for $S \gg 1$ we can approximate it by ignoring the commutation relation between the operators in the square brackets. With the transformations $\hat{x} \to \hat{x}\sqrt{S}$, $\hat{p}_x \to \hat{p}_x\sqrt{S}$, $\hat{y} \to \hat{y}\sqrt{S}$ and $\hat{p}_y \to \hat{p}_y\sqrt{S}$, equation (17) becomes

$$\frac{\hat{H}'_{\rm DM}}{S} = \frac{1}{2}(\hat{p}_x^2 + \omega^2\hat{x}^2 + \hat{p}_y^2 + \omega_0^2\hat{y}^2)$$
$$+ 2\chi\sqrt{\omega\omega_0}\hat{x}\hat{y}\sqrt{1 - \frac{\omega_0\hat{y}^2}{4}}. \quad (19)$$

together with the now familiar commutation relations $[\hat{x}, \hat{p}_x] = \mathrm{i}/S$, $[\hat{y}, \hat{p}_y] = \mathrm{i}/S$ ($[\hat{x}, \hat{p}_y] = 0$ and $[\hat{y}, \hat{p}_x] = 0$). We can see that since we kept both parts of the system the Hamiltonian is two-dimensional and so generalizes the form given in equation (2), but is nevertheless of the form of kinetic plus potential terms and so our proceeding analysis can be applied here as well.

In this section we have used various approximation methods to write the Hamiltonians of some simple many-particle systems in the form of a single effective quantum particle like in equation (2). The results represent a semi-classical approach to each system where we have assumed they are large enough to be approximated by continuous spectra, but we do not take the thermodynamic limit, so there are still canonical commutation relations to be obeyed. It is in this regime we will focus on investigating the quantum critical nature of catastrophes.

Once again, we emphasize that the catastrophes that exist in all three models described above properly live in Fock space. However, in the continuum approximation the fundamental discretization of Fock space vanishes, and hence the distinction between quantum catastrophes and the standard continuous wave catastrophes evaporates (for an analysis of a quantum catastrophe see [49]). For simplicity, in the remainder of this paper we will keep coming back to the example system of the two-site Bose–Hubbard model, although the basic results also apply to the optomechanical and Dicke models.

3. Catastrophes in classical dynamics

In the truncated Wigner approximation (TWA) one attempts to mimic quantum dynamics by an ensemble of classical trajectories [83, 84]. This method has been implemented for the two-mode Bose–Hubbard model in [85] where they also consider the effect of decoherence due to a continuous measurement of the number difference between the two sites, although we shall not include that additional feature here. The initial conditions for the classical trajectories are sampled from the initial quantum probability distribution, thus building in quantum fluctuations, but the subsequent time evolution of these trajectories is purely classical.

For an initial state let us consider the physically realistic situation where two independent condensates with an equal number of atoms are suddenly placed in contact through a tunneling barrier, i.e. a quench in the tunnelling rate from zero to a finite value specified by $\Lambda_{\rm BH}$. According to Heisenberg's uncertainty principle, if the number difference z is exactly known then its conjugate variable ϕ is completely unspecified and hence the classical trajectories sampling the initial state all have $z(0) = 0$ but differ in their initial value of the phase difference $\phi(0)$, being equally distributed over the range $(0, 2\pi]$. These trajectories are propagated in time by solving Hamilton's equations [63]

$$\dot{\phi} = \frac{\partial H_{\rm BH}}{\partial z} = \Lambda_{\rm BH} z + \frac{z}{\sqrt{1-z^2}}\cos\phi, \tag{20}$$

$$\dot{z} = -\frac{\partial H_{\rm BH}}{\partial \phi} = -\sqrt{1-z^2}\sin\phi \tag{21}$$

obtained from the mean-field Hamiltonian given in equation (4). The results are plotted in figure 2 for $\Lambda_{\rm BH} = 0.5$ where we see that a repeated series of cusp catastrophes are formed by the envelopes of the classical trajectories $z(t)$. To find the TWA (classical) prediction for the probability distribution in Fock space at time t one should average over the trajectories, i.e. break the z coordinate into little bins and count the number of trajectories that arrive in each bin. In this way one finds that the probability diverges on the cusps as the number of trajectories becomes large (see, e.g., figure 2 in [45]). It is worth pointing out that the cusps shown in figure 2 are not a special feature of the initial condition $z(0) = 0$. Although this initial condition does give cusps which are symmetric about $z = 0$, the structural stability of catastrophes ensures that they are robust to fluctuations in the initial conditions which can also be imbalanced (see figure 5 below).

The cusps arise from the focusing effect of the minima in the effective potential in the Hamiltonian. If the potential is replaced by its expansion up to second order around the origin, $V(\phi) \approx -1 + [(1+\Lambda_{\rm BH})/2\Lambda_{\rm BH}]\phi^2$, the focusing becomes perfect due to the isochronous nature of harmonic potentials: each cusp is reduced to a single focal point. However, this is a non-generic situation because perfect focal points are unstable to perturbations such as the inclusion of the non-harmonic part of $V(\phi)$ which smears them out into cusps. The cusps are, by contrast, structurally stable. The cusps in figure 2 are also stable against changes to the initial

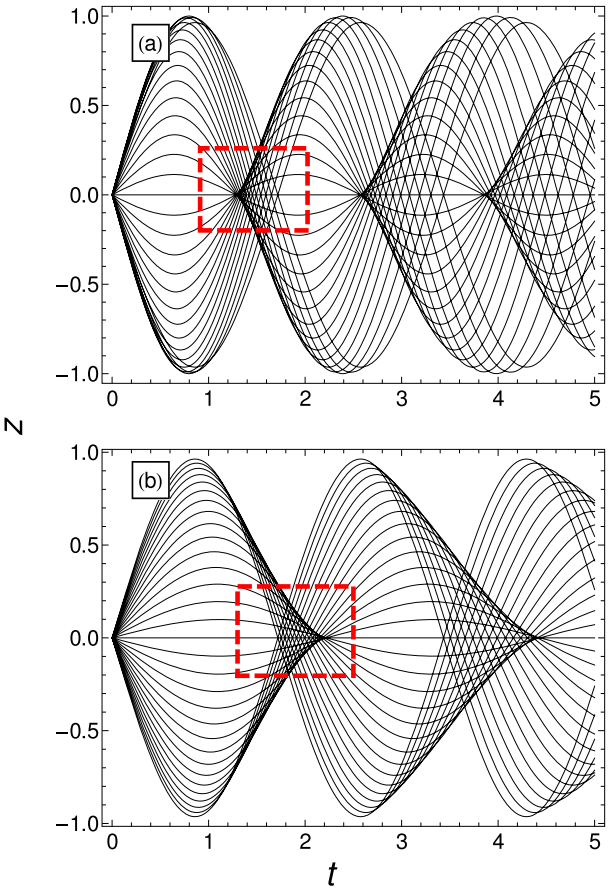

Figure 2. Cusps in the classical dynamics of the two-mode Bose–Hubbard model. Each curve is a solution of the mean-field equations of motion (Hamilton's equations) and gives the number difference $z(t)$ between the left and right sites for $\Lambda_{\rm BH} = 0.5$. The initial conditions are such that each trajectory starts with $z(0) = 0$ but has a different initial phase $\phi(0)$ sampled uniformly from $\phi(0) \in [0, 2\pi]$ in accordance with the truncated Wigner approximation. We have separated the trajectories into two groups: panel (a) shows those that oscillate around $\phi = 0$ (plasma oscillations) and panel (b) shows those that oscillate around $\phi = \pi$ (π-oscillations). Both groups are excited under these conditions and we plot them separately for clarity. Near $z = \pm 1$ the cusps reach the maximum excitation possible in this system and hence curve off. This is a non-generic feature specific to the bounded Fock space of our system. The red, dashed–boxed region indicates the approximate location of the generic or 'pure' cusp. Note that the quantum version of this figure is plotted in figure 8(a).

conditions. These can be varied to include imbalanced wells, or take $z(0) \neq 0$. Under these changes the cusp is modified quantitatively but not qualitatively. It is also interesting to note that in the Bogoliubov theory for the weakly interacting Bose gas the equations of motion are linearized [86], meaning that $V(\phi)$ is replaced by its harmonic approximation, and hence the Bogoliubov theory is unsuitable for describing catastrophes in the two-mode problem.

To understand why we specifically see cusps in the two-dimensional (z, t) control space, consider the generating function/action $\Phi = s^4 + Xs^2 + Ys$ for co-dimension 2 catastrophes in table 1. According to Hamilton's principle the

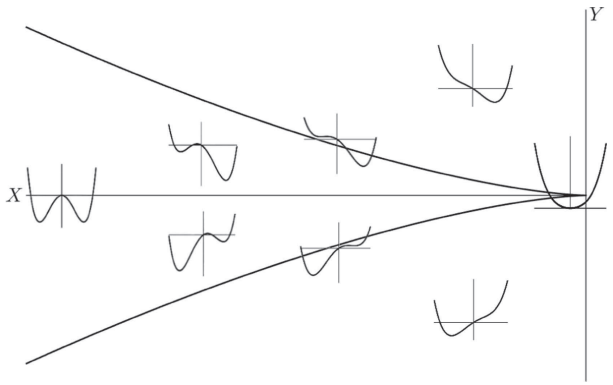

Figure 3. A plot of the canonical cusp as given by equation (22). It consists of two fold lines that meet at a cusp point. The insets at different points (X, Y) show the cusp generating function $\Phi(s; X, Y) = s^4 + Xs^2 + Ys$ plotted as a function of s. Each extremum of Φ corresponds to a classical trajectory; there are three at each point inside the cusp and one at each point outside. Note that equation (22) only has real solutions when X is negative. By changing the signs of the terms in $\Phi(s; X, Y)$ the cusp can instead be made to live in the positive-X half plane.

classical trajectories are those for which the action is stationary with respect to variations in the state variables which characterize them. This gives $\partial\Phi/\partial s = 4s^3 + 2Xs + Y = 0$. On a catastrophe the action is stationary to higher order $\partial^2\Phi/\partial s^2 = 12s^2 + 2X = 0$; physically this is the focusing condition. Eliminating s from these two equations gives the equation for a cusp

$$Y = \pm\sqrt{\frac{8}{27}}\,(-X)^{3/2} \tag{22}$$

and is plotted in figure 3. The insets at different points (X, Y) depict the action $\Phi(s; X, Y)$ as a function of s. Being a quartic function, Φ has at most three stationary points; each stationary point corresponds to a classical trajectory. We see that there are three classical trajectories reaching each point inside the cusp and just one reaching each point outside. As we cross one of the edges of the cusp (known as fold lines) two of the solutions coalesce and annihilate leading to a singularity. However, the most singular part is the point of the cusp where all three solutions coalesce at once. In a specific system the canonical coordinates $\{X, Y\}$ will not generally correspond to the actual physical coordinates, but transformations can (in principle) be found that relate the two. We will see an example of this in section 5.

Structural stability implies that we need not be concerned with the exact shape of the potential but rather with its general features such as the number of stationary points. Accordingly, in the rest of this paper we will confine our attention to a general quartic potential

$$V(x) = a_0 + a_2x^2 + a_3x^3 + a_4x^4. \tag{23}$$

In general the coefficients a_2 and a_4 depend on the parameters of the system. If we assume there is one such parameter Λ (like the ones identified in each example in section 2) which drives the system through a second order phase transition then we can take inspiration from the Landau theory of continuous phase transitions and approximate the coefficients near the critical point at Λ_c as $a_2(\Lambda) \approx \lambda/2$ and $a_4(\Lambda) \approx \pm 1$, where $\lambda = (\Lambda - \Lambda_c)/\Lambda_c$ is the reduced driving parameter. We have set $a_0 = 0$ without loss of generality because this just results in an overall shift of the energy. On the one hand, when $a_4 > 0$ (with $a_3 = 0$) we have either a single- or double-well potential depending upon whether λ is positive or negative. On the other hand, when $a_4 < 0$ (with $a_3 = 0$) for $\lambda > 0$ there is a local minimum at $x = 0$ sandwiched between two global maxima at $x_\pm = \pm\sqrt{\lambda}/2$, and for $\lambda < 0$ there is a global maximum at $x = 0$. This latter situation describes, for example, π-oscillations providing the quartic potential is understood as a Taylor series expansion about the point $\phi = \pi$. At the critical point $\lambda_c = 0$, dynamics near this region become unstable resulting in exponential divergence away from it. This is important for the fate of π-oscillation cusps because when the phase transition occurs the potential around $x = 0$ no longer focuses trajectories but instead becomes an unstable stationary point that defocuses and destroys the cusps.

4. δ-kicked Hamiltonians

A further simplification we shall make at this point is to consider δ-kicked Hamiltonians. δ-kicks play an important role in molecular physics where trains of short laser pulses are used to align molecules [87–89] and in experiments involving a small number of pulses molecules have been shown to exhibit 'classical alignment echoes' where the initial alignment is revived after initially collapsing [90]. We note that in the kicked rotor problem it is known that a cusp can form in the angular position distribution [41] and also in the angular momentum distribution [91]. In cold atom experiments one can exert real-time control over both the trapping potential and the interactions between the atoms which allows for a broad range of options for kicking the system into a non-equilibrium state. For example, the δ-kicked rotor can be realized in a cold atomic gas by flashing on and off an optical lattice [92], and in the case of a three-frequency periodic δ-kick the system displays a form of Anderson localization in time [93] at a critical kicking strength (equivalent to disorder strength). The Green's function for the probability distribution in this case happens to be an Airy function which gives it a scaling invariance characteristic of a second-order phase transition [94]. The critical behavior of the δ-kicked Lipkin–Meshkov–Glick model has been investigated in reference [95].

We shall consider the simplest case of a single δ-kick to one of the terms in the Hamiltonian while the rest is held constant. This type of time evolution facilitates analytical results and allows a very clean realization of the canonical wave catastrophes. In fact, one can kick either of the terms in the Hamiltonian (2) as what really counts is that we have two non-commuting pieces at some instant, one of which is also

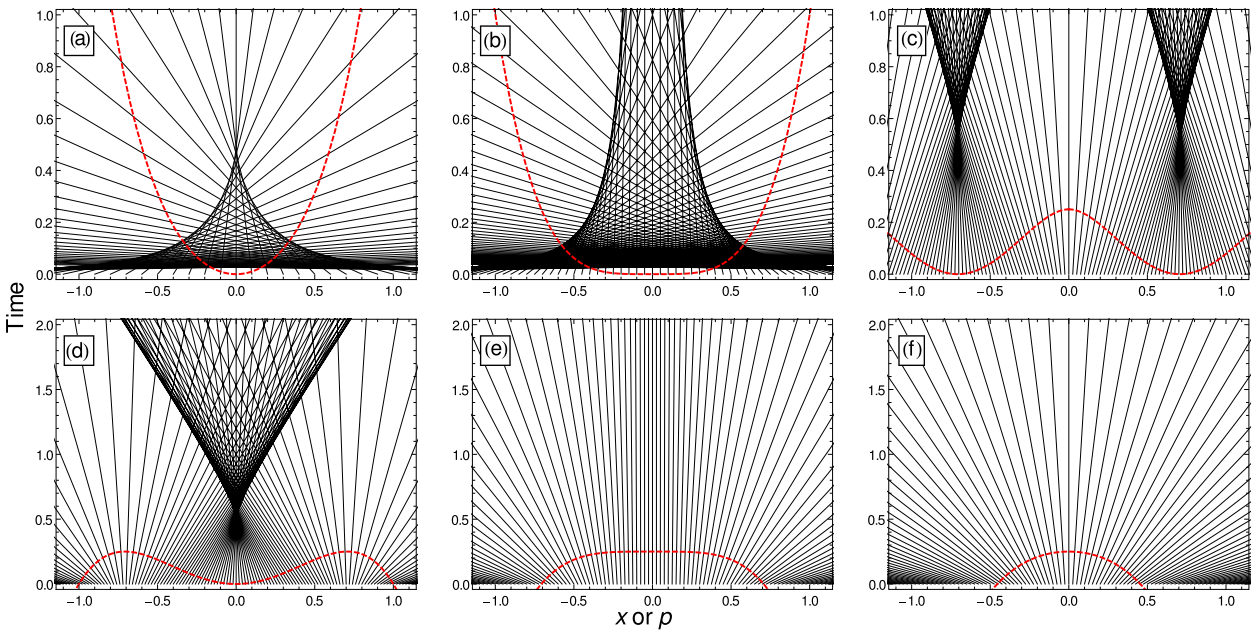

Figure 4. Classical dynamics for kicked Hamiltonians with a quartic potential whose shape is indicated by the red dashed curve in each panel. The top row has $a_4 > 0$ and the bottom row has $a_4 < 0$. The reduced parameter λ decreases from left to right so that $a_2 = 2$, $a_2 = 0$ and $a_2 = -2$ in the left hand, central and right hand columns, respectively. Each black solid line is a classical trajectory with a different initial $x \in [-3, 3]$. If the kinetic term is kicked then the dynamics take place in the (p, t)-plane, whereas if the potential term is kicked they take place in the (x, t)-plane. The images are similar to what one would find in the geometric theory of light where incoming parallel rays (not shown) reflect from a mirror with the same local curvature as the potential.

nonlinear. Thus, we consider two cases

$$\hat{H}_1 = \delta(t)\frac{\hat{p}^2}{2} + V(\hat{x}) \quad \text{Case 1}, \tag{24}$$

$$\hat{H}_2 = \frac{\hat{p}^2}{2} + \delta(t)V(\hat{x}) \quad \text{Case 2}, \tag{25}$$

where for now we have set N to unity. After the kick the system evolves due to only one term which makes an analytical description easier, especially in the classical case where Hamilton's equations $\dot{x} = \partial H/\partial p$, and $\dot{p} = -\partial H/\partial x$ can be solved trivially. For $\hat{H}_1$ one finds

$$x(t) = x(0) = p_0, \qquad p(t) = t\,F(x(0)) + p_0 \tag{26}$$

and for $\hat{H}_2$

$$x(t) = t\,p(0) + x_0, \qquad p(t) = p(0) = F(x(0)). \tag{27}$$

In both expressions $F(x) = -\partial V/\partial x$ is the force. We therefore see that the classical trajectories are straight lines in either the (p, t)- or (x, t)-plane with slopes determined by the initial force or momentum.

The classical trajectories following a kick for various incarnations of the quartic potential are plotted in figure 4. In the top row $a_4 > 0$, and as the potential turns from a single to a double well the dynamics evolve from featuring a single cusp to two cusps. Note that the new cusps open in the opposite direction to the original one. At the transition point at $\lambda = 0$ the cusp point is pushed off to $t = \infty$, a feature that may be viewed as an example of critical slowing down of the dynamics. Similarly, the two new cusps start at $t = \infty$ at the transition point and are brought down to finite times past the transition. In the bottom row $a_4 < 0$, and there is a single cusp generated by the central minimum of the potential when $\lambda > 0$, which becomes a maximum for $\lambda < 0$ leading to a divergence of the trajectories. The difference between positive and negative a_4 is also shown in figure 5, as well as including the effect of an asymmetric potential by having $a_3 \neq 0$. We see that the images still retain their qualitative cusp form, but are now skewed by the asymmetry.

5. Catastrophes in quantum dynamics

5.1. Mapping to the pearcey function

In the quantum description of the kicked system the evolution operator can be written as the product of two terms; one describing the kick at $t = 0$ and the other describing the subsequent evolution [96]. As for the classical problem, we will consider two cases; Case 1: Hamiltonians with a kicked kinetic term (H_1), and Case 2: Hamiltonians with a kicked potential term (H_2). The evolution operators in these two cases are $\hat{\mathcal{U}}_1 = \mathrm{e}^{-\mathrm{i}V(\hat{x})t}\mathrm{e}^{-\mathrm{i}\hat{p}^2/2}$ and $\hat{\mathcal{U}}_2 = \mathrm{e}^{-\mathrm{i}\hat{p}^2 t/2}\mathrm{e}^{-\mathrm{i}V(\hat{x})}$, respectively. The stability of the cusp to perturbations allows us to choose a wide range of initial states, however, with simplicity in mind we choose the ground state of the non-kicked term in the $\lambda > 0$ (symmetric) phase, so for case one $|\psi_0\rangle_1 = |x = 0\rangle = \int_{-\infty}^{\infty} |p_0\rangle\,\mathrm{d}p_0$ and for case two $|\psi_0\rangle_2 = |p = 0\rangle = \int_{-\infty}^{\infty} |x_0\rangle\,\mathrm{d}x_0$. Applying the evolution operators to these initial states gives the amplitude of being at any point in

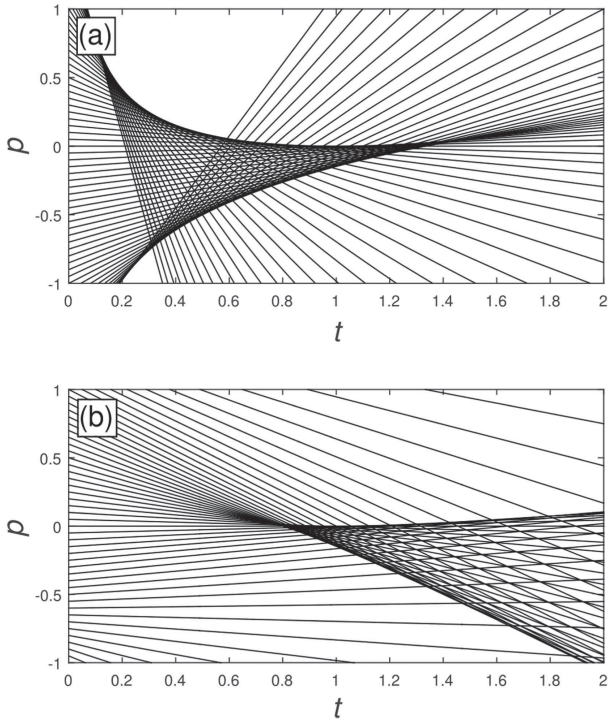

Figure 5. Trajectories for the case of a kicked kinetic term (H_1) with different initial $p \in [-2, 2]$ for different values of a_4: (a) $a_4 = 1$ and (b) $a_4 = -1$. For both images $a_2 = a_3 = 1$.

x or p at time t

$$\psi_1(p, t) = \int_{-\infty}^{\infty} \mathrm{d}p_0 \, \langle p|\hat{\mathcal{U}}_1|p_0\rangle = \frac{\mathrm{e}^{-\mathrm{i}\pi/4}}{\sqrt{2\pi}} \int_{-\infty}^{\infty} \mathrm{d}x_0 \, \mathrm{e}^{\mathrm{i}\left[\frac{x_0^2}{2} - px_0 - V(x_0)t\right]}, \tag{28}$$

$$\psi_2(x, t) = \int_{-\infty}^{\infty} \mathrm{d}x_0 \, \langle x|\hat{\mathcal{U}}_2|x_0\rangle = \frac{\mathrm{e}^{-\mathrm{i}\pi/4}}{\sqrt{2\pi t}} \int_{-\infty}^{\infty} \mathrm{d}x_0 \, \mathrm{e}^{\mathrm{i}\left[\frac{(x-x_0)^2}{2t} - V(x_0)\right]}. \tag{29}$$

To make the connection to CT we substitute the quartic potential defined in equation (23) into equations (28) and (29) giving

$$\psi_1(p, t) = \frac{\mathrm{e}^{\mathrm{i}\theta_1(p,t;\mathbf{a})}}{\sqrt{2\pi\sqrt{a_4 t}}} \mathrm{Pe}[X_1(t; \mathbf{a}), Y_1(p, t; \mathbf{a})], \tag{30}$$

$$\psi_2(x, t) = \frac{\mathrm{e}^{\mathrm{i}\theta_2(x,t;\mathbf{a})}}{\sqrt{2\pi t\sqrt{a_4}}} \mathrm{Pe}[X_2(t; \mathbf{a}), Y_2(x, t; \mathbf{a})], \tag{31}$$

where $\mathrm{Pe}[X, Y]$ is the Pearcey function [28]

$$\mathrm{Pe}[X, Y] = \int_{-\infty}^{\infty} \mathrm{d}s \, \mathrm{e}^{-\mathrm{i}(Ys + Xs^2 + s^4)}, \tag{32}$$

which is the wave catastrophe corresponding to the cusp [28, 31, 34, 97–100] and is plotted in figure 6. The phase factors multiplying the wave functions are

$$\theta_1(p, t; \mathbf{a}) = a_{0t} - \frac{a_3^2}{32a_4^2} - \frac{3a_3^4 t}{256a_4^3} + \frac{a_2 a_3^2 t}{16a_4^2} + px_m + \frac{x_m^2}{2}, \tag{33}$$

$$\theta_2(x, t; \mathbf{a}) = a_0 - \frac{a_3^2}{32a_4^2 t} - \frac{3a_3^4}{256a_4^3} + \frac{a_2 a_3^2}{16a_4^2} - \frac{a_3 x}{4a_4 t} - \frac{x^2}{2t} \tag{34}$$

where $\mathbf{a} = \{a_0, a_1, a_2, a_3\}$ are the four parameters specifying the quartic potential. The quantity x_m is required if the quartic potential $V(x)$ is a Taylor series expansion about the point $x_m \neq 0$ in which case all values of x are measured from x_m; otherwise $x_m = 0$. The transformation between the physical coordinates and parameters and the canonical state variables and control parameters is given, for Case 2, by

$$\begin{aligned} s_2 &= a_4^{1/4}\left(x_0 + \frac{a_3}{4a_4}\right) \\ X_2(t; \mathbf{a}) &= -\frac{(3a_3^2 t + a_4(4 - 8a_2 t))}{8a_4^{3/2} t} \\ Y_2(x, t; \mathbf{a}) &= \frac{(8a_4^2 x + a_3^3 t + a_3 a_4(2 - 4a_2 t))}{8a_4^{9/4} t}. \end{aligned} \tag{35}$$

We see that classical paths, as characterized by s_2, are specified by their initial x coordinate x_0. Also, the canonical control parameter Y mixes the physical coordinates (x, t) whereas X is a function purely of t. For Case 1 the transformations are closely related to those of Case 2

$$\begin{aligned} s_1 &= t^{1/4} s_2 \\ X_1(t; \mathbf{a}) &= \sqrt{t} X_2(t; \mathbf{a}) \\ Y_1(p, t; \mathbf{a}) &= t^{3/4} Y_2(p, t; \mathbf{a}). \end{aligned} \tag{36}$$

It is easier to see the fine details within a cusp opening in the positive t direction than the negative t direction, so we will assume $a_4 < 0$. With our definitions of a_2, a_3 and a_4 in the previous section, equation (35) becomes

$$\begin{aligned} s_2 &= x_0 \\ X_2(t; a) &= \frac{(1 - \lambda t)}{2t} \\ Y_2(x, t) &= \frac{x}{t}, \end{aligned} \tag{37}$$

where the relation of the variables between the two cases is the same as those given in equation (36).

5.2. Scaling exponents

The critical behavior of the ground states of the models studied in this paper have been investigated by a number of authors. For example, the critical exponents for the two-mode Bose–Hubbard model have been calculated in reference [101], and for the closely related Lipkin–Meshkov–Glick model in references [102, 103]. Similarly, the critical exponents of the Dicke model have been investigated in references [80, 104]. Part of the power of the methods developed in this paper is that they give us access to the scaling properties of non-equilibrium states. In particular, in the vicinity of a catastrophe the quantum wave function obeys a remarkable

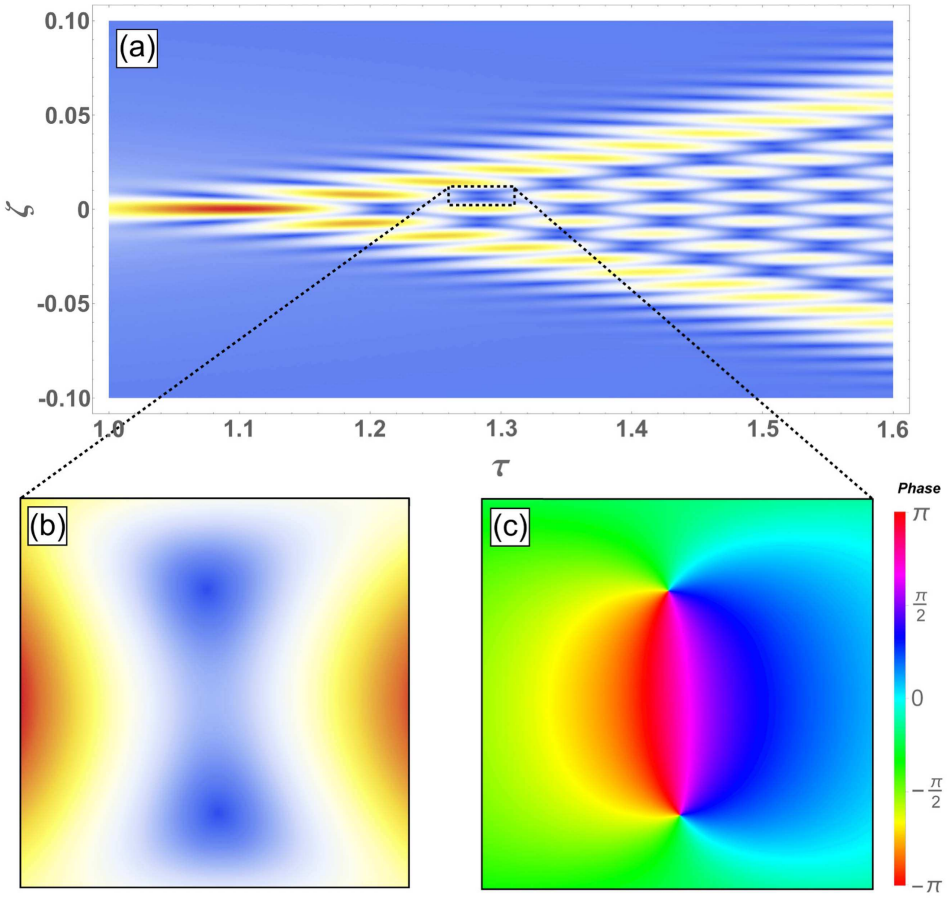

Figure 6. The wave function of a cusp catastrophe (the Pearcey function) for $N = 1$ plotted as a function of the scaled control parameters ζ and τ, i.e. Fock space and time. One sees that the underlying classical skeleton provided by the cusp is decorated by an intricate interference pattern with several levels of structure, and a slice at a fixed time through a fold line gives an Airy function provided one is not too close to the cusp point. In the (ζ, τ) coordinate system the classical cusp structure is held fixed, but the interference pattern evolves with $\lambda^{\alpha}N$. In the deep quantum regime where $\lambda^{\alpha}N \leqslant 1$ the 'fringes' are large. By contrast, in the opposite semiclassical regime $\lambda^{\alpha}N \gg 1$ the oscillations are very rapid and the fringe spacing is small. Inside the cusp there is a network of vortex–antivortex pairs. Panels: (a) $|\psi_2|^2$, (b) a closeup of a vortex-antivortex pair which together form a dipole, and (c) the phase of the same pair as (b). In (a) and (b) blue indicates a small amplitude and red a large amplitude.

self-similarity relation given in equation (38) below, with respect to the scale factor λ and this allows us to quantify the non-equlibrium critical behavior in terms of critical exponents. Consider first the classical scaling which governs both the position and size of the cusp. From figure 3 we see that the cusp point is located at ($X_{\rm cusp} = 0$, $Y_{\rm cusp} = 0$) in the canonical coordinates. Using equation (37) to convert to physical coordinates we find that the cusp point is shifted to finite times ($t_{\rm cusp} = \lambda^{-1}$, $x_{\rm cusp} = 0$). One can think of $t_{\rm cusp}$ as the time it takes the system to respond to the initial kick: the fact that $t_{\rm cusp} \to \infty$ as $\lambda \to 0$ can be viewed as critical slowing down. Using $t_{\rm cusp}$ as the natural time scale allows us to define a time coordinate $\tau = t/t_{\rm cusp} = \lambda t$ which is invariant with λ. The analogous coordinate for the transverse direction is obtained by substituting X and Y in the canonical cusp formula given in equation (22) by the relevant quantities according to the above transformations and then replacing the time coordinate by the scaled time $\tau = \lambda t$. One finds $p \propto \lambda^{1/2}$ and $x \propto \lambda^{1/2}$ for Case 1 and Case 2, respectively. Thus, as the critical point is approached the cusp not only starts at later times but also shrinks in its transverse extent. An invariant coordinate for the transverse direction can therefore be defined as $\zeta = x/\lambda^{1/2} = p/\lambda^{1/2}$.

The quantum case is richer than the classical one due to the interference pattern decorating the cusp, as shown in figure 6. To get at the purely quantum features we work in the (ζ, τ) coordinate system because these make Hamilton's equations invariant with λ so that the cusp remains fixed in the (ζ, τ)-plane even as λ is varied. Crucially, the action is not scale invariant and this is the source of the extra scaling properties of the quantum problem. Substituting in the new variables gives $\Phi_{\alpha} \to \lambda^{\alpha}\Phi_{\alpha}$, where $\alpha = 1, 2$ for Case 1 and Case 2, respectively. The index α has no physical significance and is only used for convenience in distinguishing the different scalings between the two cases. The factor of λ^{α} does not appear in the generating function for the canonical Pearcey function, but it can be absorbed into the control

Table 2. Critical scaling exponents of λ for the cusp catastrophe, where the critical point is at $\lambda = 0$. The first two columns refer to classical properties of the cusp: the exponent for the cusp size refers to the scaling in the transverse direction (p or x), and the exponent for the position refers to the location of the cusp point t_{cusp} in the time direction. The remaining three columns refer to quantum properties and assume that the classical properties of the cusp are held fixed by working in the (ζ, τ) coordinates. The exponent for the probability density at the cusp point $|\psi_\alpha(0, 1, \lambda)|^2$ is $2\alpha\beta$, where β is the Arnold index and $\alpha = 1, 2$ for Case 1, 2. The last two columns give the scaling of the interference fringes, where σ_X and σ_Y are the Berry indices. Thus, as $\lambda \to 0$ the fringe spacing diverges as $\lambda^{-\alpha\sigma_X}$ and $\lambda^{-\alpha\sigma_Y}$ in the X and Y directions, respectively.

	Classical		Quantum		
Kicked term	Size	Position	$\lvert\psi\rvert^2$	$\alpha\ \sigma_X$	$\alpha\ \sigma_Y$
Kinetic (Case 1)	1/2	−1	1/2	1/2	3/4
Potential (Case 2)	1/2	−1	1	1	3/2

parameters and state variable if they are rescaled in a particular way that depends on three indices: β, σ_X and σ_Y. The first index is known as the Arnold index, and the other two as Berry indices. The rescaling thus returns us to the Pearcey function but with new control parameters scaled by λ^α and forms the basis for identifying the scaling properties of the catastrophe as λ is varied. Following this procedure through, we find we can write the wave functions in equations (30) and (31) in the manifestly self-similar form

$$\psi_\alpha(\zeta, \tau; \lambda) \propto \left(\frac{\lambda}{\tau}\right)^{\alpha\beta} \mathrm{Pe}[\lambda^{\alpha\,\sigma_X} X_\alpha, \lambda^{\alpha\,\sigma_Y} Y_\alpha], \tag{38}$$

where the proportionality sign indicates that we have neglected overall phase and constant factors as they play no role in the following analysis. A derivation of equation (38) for Case 2 is given in the appendix. The Arnold index governs how the amplitude of the wave function depends on the scale factor λ. In the case of the cusp catastrophe it takes the value $\beta = 1/4$ [34]. The Berry indices dictate how rapidly the interference pattern varies in control space: in general the scaling in each direction is different and for the cusp they are $\sigma_X = 1/2$ and $\sigma_Y = 3/4$ [34].

With the wave function in the form of equation (38) it is easy to see that the probability density in Fock space at the cusp point scales as $|\psi_\alpha|^2 \propto \lambda^{2\alpha\beta}$, and so for the two cases we have $|\psi_1|^2 \propto \lambda^{1/2}$ and $|\psi_2|^2 \propto \lambda$. Thus, as $\lambda \to 0$ the cusp melts away, which is expected since the focusing region of the effective potential shrinks (when $a_4 < 0$) causing fewer Fock states to contribute to the cusp. The interference pattern, meanwhile, varies more slowly as $\lambda \to 0$ with the fringe spacing tending to infinity in this limit. The scaling properties of the cusp wave function are summarized in table 2.

So far we have set N to unity, but now we will take a look at the effects of its inclusion. In each example we gave in section 2 we saw that the transformations made to the original many-particle Hamiltonian converted it to an effective single particle Hamiltonian $\hat{H} \to N\hat{H}'$. The action undergoes the same transformation and this implies that the Pearcey function changes to $\int_{-\infty}^{\infty} \mathrm{d}s\, \mathrm{e}^{-\mathrm{i}N(Ys+Xs^2+s^4)}$, which means that $1/N$ plays the same role as $\hbar$ does in single particle path integrals. In particular, the thermodynamic limit, $N \to \infty$ is the same as the classical limit, $\hbar \to 0$. Furthermore, we see that N multiplies the action in the same way as λ^α did above, and thus λ^α is replaced by $\lambda^\alpha N$ in the full theory. This implies that there is a clash of limits between the thermodynamic limit $N \to \infty$ and the 'critical' point $\lambda \to 0$.

5.3. Vortices in fock space + time

Another remarkable feature of the interference pattern described by the Pearcey function is that it contains an intricate network of nodes [28, 98, 100]. This 'fine structure' can be seen by zooming in on the wave function as shown in panels (b) and (c) of figure 6. Examining the phase χ reveals that the nodes coincide with phase singularities where χ takes all possible values. Furthermore, χ circulates around the nodes in either a clockwise or anticlockwise sense such that in going around once it changes by $\pm 2\pi$

$$\oint \mathrm{d}\chi = \pm 2\pi. \tag{39}$$

This is a topological feature that does not depend on the path of integration providing it only encircles one node. All these properties are familiar from quantized vortices that occur in coordinate space in superfluids, type II superconductors and also optical fields (where they are referred to as dislocations [30, 34]). The difference is that here they occur in Fock space plus time. Note that the phase of the Fock space amplitudes should not be confused with, e.g. the relative phase in the two-mode Bose–Hubbard model, which is a different object.

Inside the cusp the vortices are arranged in vortex–antivortex pairs, whereas outside the cusp there is a line of single vortices along each fold line. The Berry indices govern the scaling of distances in the control plane and so can tell us how the separation between a vortex and its antivortex changes with λ. For a vortex–antivortex pair at positions $(X_\alpha^{\mathrm{v}}, Y_\alpha^{\mathrm{v}})$ and $(X_\alpha^{\mathrm{av}}, Y_\alpha^{\mathrm{av}})$, respectively, the physical distance between them, d_α, scales as

$$d_\alpha = \sqrt{\frac{(X_\alpha^{\mathrm{v}} - X_\alpha^{\mathrm{av}})^2}{\lambda^{2\alpha\sigma_X}} + \frac{(Y_\alpha^{\mathrm{v}} - Y_\alpha^{\mathrm{av}})^2}{\lambda^{2\alpha\sigma_Y}}} \tag{40}$$

and so increases as λ_{c} is approached. However, since $\sigma_X \neq \sigma_Y$ the two directions do not scale in the same way and the vortices become stretched out anisotropically. This effect persists in the (ζ, τ) coordinates as shown in figure 7.

The scaling of distances in the classically invariant (ζ, τ)-plane is less obvious because ζ and τ are functions of X and Y. However, we can get the leading order behavior as $\lambda \to 0$. First, we note a given vortex moves around within the cusp as λ is varied such that $\lambda^{\alpha\sigma_X} X_\alpha$ and $\lambda^{\alpha\sigma_Y} Y_\alpha$ remain constant. If we find a particular vortex for a given λ such that $\lambda^{\alpha\sigma_X} X_\alpha = A_\alpha$ and $\lambda^{\alpha\sigma_Y} Y_\alpha = B_\alpha$ where $A_\alpha < 0$ and B_α are constants, then we can find out how the vortices scale in ζ and τ. Using equation (36) together with equation (37) we find for

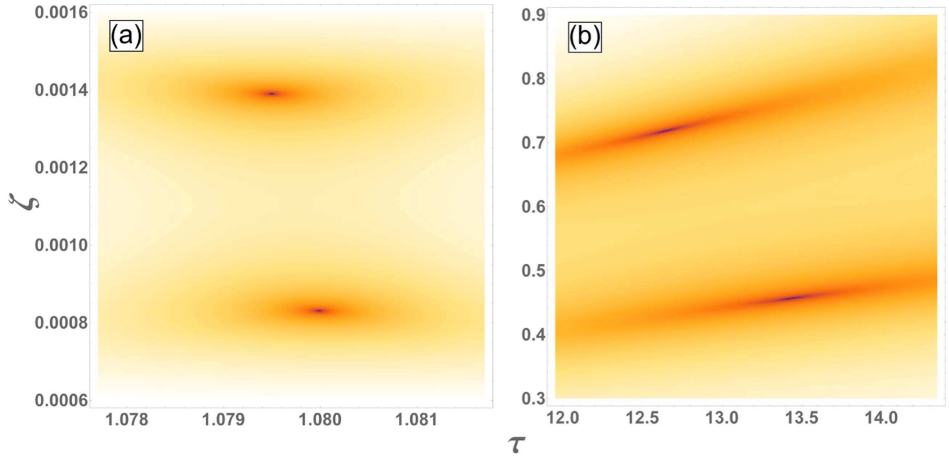

Figure 7. Evolution of a vortex–antivortex pair as λ is varied. Each panel shows $|\psi_2|$ plotted in Fock space plus time in the immediate vicinity of the same pair of vortices for: (a) $\lambda = 150$ (far from the phase transition), and (b) $\lambda = 12$ (approaching the phase transition). In order to demonstrate the apparent stretching of the vortices as they move apart, the aspect ratio $\Delta\tau/\Delta\zeta$ for the window remains unchanged.

Case 1

$$\tau - 1 = \frac{2A_1^2}{\lambda^{2\sigma_X}}\left(1 + \sqrt{1 + \frac{\lambda^{2\sigma_X}}{A_1^2}}\right), \tag{41}$$

so for $\lambda^{\sigma_X} \ll A_1$ we have $\tau \propto \lambda^{-2\sigma_X} = \lambda^{-1}$ and therefore $\zeta \propto \lambda^{-\sigma_Y - 1/4} = \lambda^{-1}$. For Case 2

$$\tau - 1 = \frac{1}{\frac{\lambda^{2\sigma_X}}{2\,|\,A_2\,|} - 1}, \tag{42}$$

so $\tau \to \infty$ as $\lambda \to 2|A_2|$ and since A_2 is different for each vortex the limit depends on which vortex we are looking at. Even though the quantitative features of the scalings are different between the (ζ, τ)- and (X, Y)-planes, qualitatively the fate of vortex pairs is the same in that the distance between the members of each pair diverges as $\lambda \to 0$. The increase in distance and smearing of a single vortex pair can be seen in figure 7 by comparing image (a) to image (b). The ratio between the ζ and τ axes for each image is kept constant, so the smearing of the region around the vortices is not affected by the change in scale.

Bringing back N, we saw above that the scaling factor λ^α is replaced by $\lambda^\alpha N$. The question then arises, at what value of this scaling factor is the separation between the vortices and the antivortices large enough so that they are visible? If we assume that in an experiment there is a value of the scaling total factor $\lambda^\alpha N = C$ below which they become distinguishable, then for a particular number of particles N the parameter λ must be tuned to values smaller than $(C/N)^{1/\alpha}$ for the individual vortices and antivortices to become visible.

5.4. Effect of kick strength

Here, we briefly show how the criticality of the cusp can be explored without approaching the critical point of $V(x)$ by changing the strength of the kick being applied. If the kick has strength Q, then $\delta(t) \to Q\delta(t)$ in our calculations. The result of this is that p and x are no longer treated on the same footing because applying a stronger kick increases the 'momentum' of the system which causes the cusp to appear at earlier times. Therefore, if we seek classically invariant coordinates where varying Q or λ only changes the quantum properties of the cusp, like equation (38), we must modify our previously defined classically invariant coordinates (ζ, τ). Suitable new coordinates are $\tau = Q\lambda t$, $\zeta_x = x/\sqrt{\lambda}$ and $\zeta_p = Qp/\sqrt{\lambda}$. These result in the transformation $\lambda^\alpha \to \lambda^\alpha Q^{2\alpha-3}$, so for Case 1 and Case 2 we have λQ^{-1} and $\lambda^2 Q$, respectively, and we can achieve the same critical behavior by varying Q while fixing λ. The inverse relation of Q between the two cases arises because when the kinetic term is kicked (Case 1) with greater strength only amplitudes with small initial p contribute to the cusp until in the limit $Q \to \infty$ only $p_0 = 0$ contributes and the cusp vanishes. The inverse limit for the kicked potential term (Case 2) accomplishes the same thing because as $Q \to 0$ the nonlinearity, which is responsible for the cusp, is removed. Thus, systems with no phase transition at all can show the same critical behavior as a system with a second order phase transition by applying weaker kicks.

6. Non-δ-kick quenches

The δ-kick quench allows for a simple analytic treatment and it also produces a single cusp, whereas for quenches where both terms in the Hamiltonian are present one typically gets oscillatory classical dynamics and hence multiple cusps, like in figure 2 and also in its quantum version figure 8. The interference between the different cusps makes the quantum wave function more complicated, although one cusp will dominate in the immediate vicinity of its cusp point. For these other types of quenches we do not expect the critical scaling to be the same as the kicked cases, but we do still expect there to be some form of scaling because this is a feature of the Pearcey function and the basic claim of CT is that any

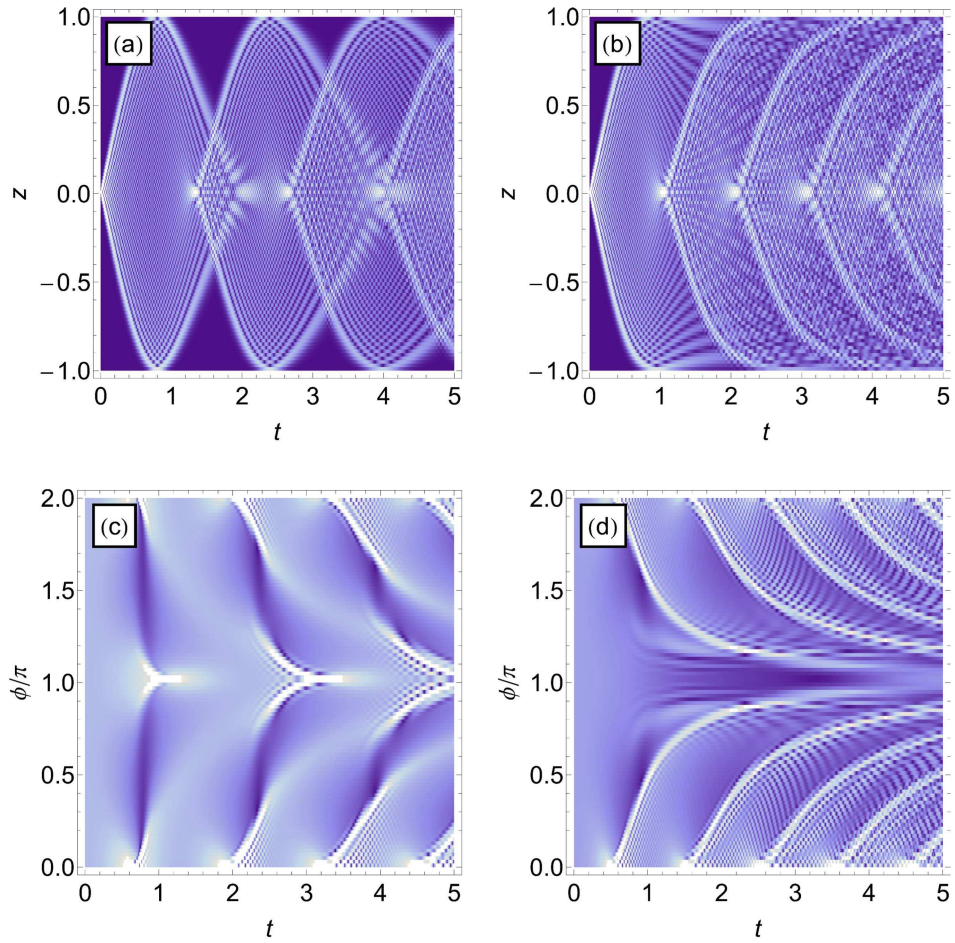

Figure 8. The amplitude of the wave function for the two-mode Bose–Hubbard model with 100 bosons following a quench at $t = 0$ where both terms in the Hamiltonian are present for the subsequent evolution. The initial state for all four panels is the Fock state with zero number difference, corresponding, for example, to a situation where two initially independent BECs are suddenly connected by a tunnelling barrier. The upper row gives the wave function in the number difference (z) basis and the lower row gives it in the phase difference (ϕ) basis. Each column is for a different value of $\Lambda_{\rm BH}$: the left column is for $\Lambda_{\rm BH} = 0.5$, so π-oscillations are possible and the right column is for $\Lambda_{\rm BH} = 1.5$ where π-oscillations are excluded. The cusps created by the π-oscillations open toward the negative t direction in both (a) and (c), the other cusps are due to plasma oscillations. Note that Panel (a) is the quantum version of figure 2 when both figures 2(a) and (b) are laid on top of each other.

structurally stable singularity must be mappable onto one of the canonical catastrophes.

In fact, we can still make some scaling arguments based on the results from the kicked cases. In deriving equation (38) we defined the new coordinates $\zeta = x/\sqrt{\lambda} = p/\sqrt{\lambda}$ and $\tau = \lambda t$ which were used to remove any classical scaling from the dynamics by making Hamilton's equations scale invariant in λ. The cusp generating function, which represents the action, was not scale invariant and the transformation resulted in $\Phi \to \lambda\Phi$ (Case 1) and $\Phi \to \lambda^2\Phi$ (Case 2). One can proceed in a similar vein in the case of the full Hamiltonian $H = p^2/2 + V(x)$, where the potential $V(x) = \lambda x^2 \pm x^4$, by looking for scalings of the classical coordinates that leave Hamilton's equations invariant. Hamilton's equations in this case are

$$\dot{x} = p, \tag{43}$$

$$\dot{p} = -2\lambda x \mp 4x^3 \tag{44}$$

and defining the new coordinates

$$\zeta_x = x/\sqrt{\lambda}, \tag{45}$$

$$\zeta_p = p/\lambda, \tag{46}$$

$$\tau = \sqrt{\lambda}t \tag{47}$$

transforms them to

$$\dot{\zeta}_x = \zeta_p, \tag{48}$$

$$\dot{\zeta}_p = -2\zeta_x \mp 4\zeta_x^3, \tag{49}$$

where the time derivative is now with respect to τ. Plugging the new coordinates into the action $S = \int [p^2/2 - V(x;\lambda)]{\rm d}t$ gives $S = \lambda^{3/2}\int [\zeta_p^2/2 - V(\zeta_x)]{\rm d}\tau$. Therefore, the action is transformed to $S \to \lambda^{3/2}S$. Interestingly, the exponent, $3/2$, is halfway between the exponents for the two kicked cases signaling each term in the Hamiltonian is playing an equal role in generating the dynamics.

Under these transformations the propagator is

$$K(\zeta, \tau; \zeta_0, \tau_0) = \int \mathcal{D}[\zeta(\tau)] e^{iN\lambda^{3/2} S[\zeta(\tau)]}. \quad (50)$$

We shall not analyze the quantum dynamics this generates here, but we note that an analytic treatment of the wave function that is valid away from the immediate region of the cusp points has been given by one of us (DO) in reference [45]. It uses a uniform approximation to extract the Airy function that decorates the fold lines that emanate from the cusp point.

Let us instead confine ourselves to a numerical solution obtained by an exact diagonalization of the full quantum Hamiltonian given in equation (3) for the two-mode Bose–Hubbard model and consider its qualitative features. The results are plotted in figure 8 which shows the dynamics of the modulus of the wave function where the initial state is the single number difference (Fock) state $|0\rangle$, so at $t = 0$ the system has exactly $N/2$ bosons on each site. The top row shows the wave function in the number difference (z) basis where panel (a) is for $\Lambda_{\rm BH} = 0.5$ and represents the quantum version of the combined panels of figure 2. Once again we can see the periodic cusps from plasma and π-oscillations opening in the postive and negative t directions, respectively. Their combined interference pattern forms a periodic diamond structure which grows in time. Panel (b) shows the same dynamics except $\Lambda_{\rm BH} = 1.5$, so the π-cusp vanishes. Panels (c) and (d) show the wave function in the phase difference (ϕ) basis for the same values of $\Lambda_{\rm BH}$ as in (a) and (b), respectively. The periodic π-cusp is clearly visible at the center of (c) bordered by half cusps from the plasma oscillations around zero phase difference. In (d) the plasma-cusps remain, but the π-cusps have vanished due to the excited state phase transition. The ϕ basis is useful because we can use the potential in equation (7) to give us the scaling of the size and position of the cusps as $\lambda \to 0$, namely, $t_{\rm cusp} \propto \lambda^{-1/2}$ and $\phi_{\rm cusp} \propto \lambda^{1/2}$. These scalings were already anticipated in equations (45) and (47).

The main difficulty in numerically determining the scaling of the vortices' separation comes from the interference with the plasma cusp, but the scalings above can help to design a better initial state which shows the cusps and their vortices more clearly. One might consider using a superposition of $\hat{\phi}$-states around π instead of the $|0\rangle$ $\hat{z}$-state which inconveniently gives a broad superposition over all $\hat{\phi}$-states. Finally, we note that in the exact solution plotted in figure 8, Fock space is discrete and this can smear out the vortex cores making their positions difficult to track. However, this discretization shrinks with increasing N, becoming invisible for a large enough system.

7. Discussion and conclusion

The main message of this paper is that close to a singularity the wave function takes on a universal form, namely one of the structures predicted by CT. These catastrophes obey scaling laws and also occur generically during dynamics without the need for fine tuning. This means we expect them to occur in a wide variety of situations, as is the case in optics, through analogues of the phenomenon of natural focusing. Of course, in high symmetry situations catastrophes can reduce to simpler structures (e.g. points rather than cusps) but these unfold to one of the canonical catastrophes when that symmetry is broken. We therefore come to the perhaps counter-intuitive conclusion that singularities represent islands of predictability in a sea of complexity, acting as organizing centers around which the wave function can only take on one of a limited number of forms and has well defined properties.

In previous work [45], we showed that in many-particle problems wave catastrophes occur in Fock space. They are naturally discretized by the granularity of the particles but become singular in the mean-field limit where the discretization is neglected. In this paper we worked within the continuum approximation where the granularity is neglected, but in contrast to the mean-field approximation the essential quantum nature of the number and phase operators is preserved as encapsulated by the commutation relation $[\hat{\phi}, \hat{z}] = 2i/N$. Furthermore, we specialized to the case of a δ-kick quench as this allows us to analytically solve for the Fock-space wave function of two-mode problems and represent it as a Pearcey function which is the universal wave function associated with cusp catastrophes. In particular, the centrepiece of our analysis is the result given in equation (38) which shows how the wave function scales with a parameter λ which controls a second-order dynamical phase transition: the scaling exponents for various properties of the wave function are summarized in table 2 and include both classical (mean-field) aspects such as the position and size of the cusp as well as quantum (many-particle) aspects such as the amplitude of the interference pattern and its fringe spacing in different directions.

A physical example where this general two-mode wave function applies is to the two-mode Bose–Hubbard model where there is a dynamical phase transition describing the appearance/disappearance of π-oscillations. Since our treatment is based on a general quartic potential (where λ controls the size of the quadratic term), it can be applied to other dynamical phase transitions too. The classical scaling of the cusp is independent of which term in the Hamiltonian is kicked, but when we go to the quantum theory kicking the potential term results in the cusp being more sensitive to changes in the control parameter λ as compared to when the kinetic term is kicked. As the phase transition is approached ($\lambda \to 0$) the cusp appears at later times and also shrinks, i.e. grows more slowly with time. The quantum aspects of the scaling mean that the interference peaks become fainter and farther apart as $\lambda \to 0$. When we explicitly include the number of particles N in the theory we find that the scaling parameter is transformed to $\lambda \to \lambda N$ and there is therefore a clash of limits between the phase transition as $\lambda \to 0$ and the thermodynamic limit $N \to \infty$.

Apart from its scaling properties, another important feature of the Pearcey function is a network of vortex–antivortex pairs inside the cusp. When applied to many-particle

dynamics this implies that there are vortex–antivortex pairs in the two-dimensional plane given by Fock space plus time. As far as we are aware the observation that there can be topological structures in such spaces, which are the Hilbert spaces describing many-particle quantum systems, is new and warrants further investigation. In the present context we find that as the phase transition is approached the vortex-antivortex pairs are pulled apart in an anisotropic manner described by the two Berry indices.

A key question is whether the present analysis can be applied to more complicated many-particle systems. In the three mode case (corresponding, e.g., to the three-site Bose–Hubbard model) the control space is three dimensional (two-dimensional Fock space plus time) and following a quench one indeed finds $K = 3$ catastrophes (swallowtail, elliptic umbilic, hyperbolic umbilic) [105]. In principle one can continue on to more modes and hence to higher catastrophes but the increasing complexity of the catastrophes as K becomes large would make this a challenging task for even a moderately sized lattice of sites as there is essentially too much information. A more promising approach in this case would be to switch to a statistical version of CT where the statistics of the fluctuations of the wave function are the central objects of interest [23].

Acknowledgments

We thank Maxim Olshanii for discussions and the Natural Sciences and Engineering Research Council of Canada for funding.

Appendix. Derivation of scaled wave function

Here, we explicitly go through the steps in deriving equation (38) for Case 2 (kicked potential) starting with equation (29) (the derivation for Case 1 is similar). To simplify the notation we will ignore all numerical factors and overall phases. We start by substituting equation (23) with $a_0 = 0$, $a_2 = \lambda/2$, $a_3 = 0$ and $a_4 = \pm 1$ into equation (29)

$$\psi_2(x,\, t;\, \lambda) \propto \frac{1}{\sqrt{t}} \int_{-\infty}^{\infty} \mathrm{d}x_0 \mathrm{e}^{\mathrm{i}\left[-\frac{xx_0}{t}+(1-\lambda t)\frac{x_0^2}{2t}\mp x_0^4\right]}. \qquad \text{(A.1)}$$

We then substitute in the rescaled position and time variables, $\tau = \lambda t$ and $\zeta = x/\sqrt{\lambda}$ so the cusp is stationary with respect to λ in the rescaled plane giving

$$\begin{aligned}\psi_2(\zeta,\, \tau;\, \lambda) &\propto \sqrt{\frac{\lambda}{\tau}} \int_{-\infty}^{\infty} \mathrm{d}x_0 \mathrm{e}^{\mp\mathrm{i}\left[\pm\lambda^{3/2}\frac{\zeta x_0}{\tau}\mp\lambda(1-\tau)\frac{x_0^2}{2\tau}+x_0^4\right]} \\ &= \sqrt{\frac{\lambda}{\tau}} \int_{-\infty}^{\infty} \mathrm{d}x_0 \mathrm{e}^{\mp\mathrm{i}[\pm\lambda^{3/2}Y_2(\zeta,\tau)x_0\mp\lambda X_2(\tau)x_0^2+x_0^4]} \\ &= \sqrt{\frac{\lambda}{\tau}}\, \mathrm{Pe}[\mp\lambda X_2(\tau),\, \lambda^{3/2}Y_2(\zeta,\, \tau)],\end{aligned} \qquad \text{(A.2)}$$

where we have used the fact that $\mathrm{Pe}[X, -Y] = \mathrm{Pe}[X, Y]$. We can see equation (A.2) matches equation (38) for the kicked potential case ($\alpha = 2$) given the Arnold index, $\beta = 1/4$, and Berry indices, $\sigma_X = 1/2$ and $\sigma_Y = 3/4$. The $\mp$ sign indicates whether the quartic term in the potential is positive or negative, respectively.

References

[1] Kibble T W B 1976 *J. Phys. A: Math. Nucl. Gen.* **9** 1387
[2] Zurek W H 1985 *Nature* **317** 505
[3] Deutsch J M 1991 *Phys. Rev.* A **43** 2046
[4] Srednicki M 1994 *Phys. Rev.* E **50** 888
[5] Rigol M, Dunjko V and Olshanii M 2008 *Nature* **452** 854
[6] Greiner M, Mandel O, Hänsch T W and Bloch I 2002 *Nature* **419** 51
[7] Lamacraft A 2007 *Phys. Rev. Lett.* **98** 160404
[8] Kollath C, Läuchli A and Altman E 2007 *Phys. Rev. Lett.* **98** 180601
[9] Rossini D, Silva A, Mussardo G and Santoro G E 2009 *Phys. Rev. Lett.* **102** 127204
[10] Trotzky S, Chen Y-A, Flesch A, McCulloch I P, Schollwöck U, Eisert J and Bloch I 2012 *Nat. Phys.* **8** 325
[11] Gerving C S, Hoang T M, Land B J, Anquez M, Hamley C D and Chapman M S 2012 *Nat. Commun.* **3** 1169
[12] Dalla Torre E G, Demler E and Polkovnikov A 2013 *Phys. Rev. Lett.* **110** 090404
[13] Braun S, Friesdorf M, Hodgman S S, Schreiber M, Ronzheimer J P, Riera A, del Reye M, Bloch I, Eisert J and Schneider U 2015 *Proc. Natl Acad. Sci. USA* **112** 3641
[14] Nicklas E, Karl M, Höfer M, Johnson A, Muessel W, Strobel H, Tomkovič J, Gasenzer T and Oberthaler M K 2015 *Phys. Rev. Lett.* **115** 245301
[15] Navon N, Gaunt A L, Smith R P and Hadzibabic Z 2015 *Science* **347** 167
[16] Eisert J, Friesdorf M and Gogolin C 2015 *Nat. Phys.* **11** 124
[17] Anquez M, Robbins B A, Bharath H M, Boguslawski M, Hoang T M and Chapman M S 2016 *Phys. Rev. Lett.* **116** 155301
[18] del Campo A, De Chiara G, Morigi G, Plenio M B and Retzker A 2010 *Phys. Rev. Lett.* **105** 075701
[19] Ejtemaee S and Haljan P C 2013 *Phys. Rev.* A **87** 051401
[20] Thom R 1975 *Structural Stability and Morphogenesis* (Reading, MA: Benjamin)
[21] Arnold V I 1975 *Russ. Math. Surys.* **30** 1
[22] Poston T and Stewart I 2012 *Catastrophe Theory and Its Applications* (Mineola, NY: Dover)
[23] Berry M V 1977 *J. Phys. A: Math. Gen.* **10** 2061
[24] Varčenko A N 1976 *Funkcional. Anal. Priložen.* **10** 13
[25] Duistermaat J J 1974 *Commun. Pure Appl. Math.* **27** 207
[26] Berry M V 1976 *Adv. Phys.* **25** 1
[27] Airy G B 1838 *Trans. Camb. Phil. Soc.* **6** 379
[28] Pearcey T 1946 *Phil. Mag.* **37** 311
[29] Berry M 1981 Singularities in waves and rays *Physics of Defects, Session 35th (Les Houches, 1980)* ed R Balian (Amsterdam: North Holland Publishing)
[30] Nye J F 1999 *Natural Focusing and the Fine Structure of Light* (Philadelphia: Institute of Physics)
[31] Olver F W J, Lozier D W, Boisvert R F and Clark C W (ed) 2010 *NIST Handbook of Mathematical Functions* (New York, NY: Cambridge University Press)
[32] Gilmore R, Kais S and Levine R D 1986 *Phys. Rev.* A **34** 2442
[33] Emary C, Lambert N and Brandes T 2005 *Phys. Rev.* A **71** 062302
[34] Berry M V and Upstill C 1980 *Prog. Opt.* **18** 257
[35] Höhmann R, Kuhl U, Stöckmann H-J, Kaplan L and Heller E J 2010 *Phys. Rev. Lett.* **104** 093901

[36] Rooijakkers W, Wu S, Striehl P, Vengalattore M and Prentiss M 2003 *Phys. Rev.* A **68** 063412
[37] Huckans J H, Spielman I B, Tolra B L, Phillips W D and Porto J V 2009 *Phys. Rev.* A **80** 043609
[38] Rosenblum S, Bechler O, Shomroni I, Kaner R, Arusi-Parpar T, Raz O and Dayan B 2014 *Phys. Rev. Lett.* **112** 120403
[39] O'Dell D H J 2001 *J. Phys. A: Math. Gen.* **34** 3897
[40] Averbukh I S and Arvieu R 2001 *Phys. Rev. Lett.* **87** 163601
[41] Leibscher M, Averbukh I S, Rozmej P and Arvieu R 2004 *Phys. Rev.* A **69** 032102
[42] Barré J, Bouchet F, Dauxois T and Ruffo S 2002 *Phys. Rev. Lett.* **89** 110601
[43] Chalker J T and Shapiro B 2009 *Phys. Rev.* A **80** 013603
[44] Berry M V and O'Dell D H J 1999 *J. Phys. A: Math. Gen.* **32** 3571
[45] O'Dell D H J 2012 *Phys. Rev. Lett.* **109** 150406
[46] Carusotto I, Hu S X, Collins L A and Smerzi A 2006 *Phys. Rev. Lett.* **97** 260403
[47] Dominici L *et al* 2015 *Nat. Commun.* **6** 8993
[48] Preiss P M, Ma R, Tai M E, Lukin A, Rispoli M, Zupancic P, Lahini Y, Islam R and Greiner M 2015 *Science* **347** 1229
[49] Mumford J, Turner E, Sprung D W L and O'Dell D H J 2016 (arXiv:1610.08031)
[50] Berry M V and Dennis M R 2004 *J. Opt.* A **6** S178
[51] Berry M V 2008 *Nonlinearity* **21** T19
[52] Leonhardt U 2002 *Nature* **415** 406
[53] Lipkin H J, Meshkov N and Glick A J 1965 *Nucl. Phys.* **62** 188
[54] Das A, Sengupta K, Sen D and Chakrabarti B K 2006 *Phys. Rev.* B **74** 144423
[55] Albiez M, Gati R, Fölling J, Hunsmann S, Cristiani M and Oberthaler M K 2005 *Phys. Rev. Lett.* **95** 010402
[56] Schumm T, Hofferberth S, Andersson L M, Wildermuth S, Groth S, Bar-Joseph I, Schmiedmayer J and Krüger P 2005 *Nat. Phys.* **1** 57
[57] Levy S, Lahoud E, Shomroni I and Steinhauer J 2007 *Nature* **449** 579
[58] Zibold T, Nicklas E, Gross C and Oberthaler M K 2010 *Phys. Rev. Lett.* **105** 204101
[59] LeBlanc L J, Bardon A, McKeever J, Extavour M, Jervis D, Thywissen J, Piazza F and Smerzi A 2011 *Phys. Rev. Lett.* **106** 025302
[60] Trenkwalder A *et al* 2016 *Nature Phys.* **12** 826–9
[61] Gati R and Oberthaler M K 2007 *J. Phys. B: At. Mol. Opt. Phys.* **40** R61
[62] Pitaevskii L and Stringari S 2001 *Phys. Rev. Lett.* **87** 180402
[63] Smerzi A, Fantoni S, Giovanazzi S and Shenoy S R 1997 *Phys. Rev. Lett.* **79** 4950
[64] Raghavan S, Smerzi A, Fantoni S and Shenoy S 1999 *Phys. Rev.* A **59** 620
[65] Krahn G J and O'Dell D H J 2009 *J. Phys. B: At. Mol. Opt. Phys.* **42** 205501
[66] Santos L F, Távora M and Pérez-Bernal F 2016 *Phys. Rev.* A **94** 012113
[67] Milburn G J, Corney J, Wright E M and Walls D F 1997 *Phys. Rev.* A **55** 4318
[68] Veksler H and Fishman S 2015 *New J. Phys.* **17** 053030
[69] Ulyanov V V and Zaslavskii O B 1992 *Phys. Rep.* **216** 179
[70] Thompson J D, Zwickl B M, Jayich A M, Marquardt F, Girvin S M and Harris J G E 2008 *Nature* **452** 72
[71] Jayich A M, Sankey J C, Zwickl B M, Yang C, Thompson J D, Girvin S M, Clerk A A, Marquardt F and Harris J G E 2008 *New J. Phys.* **10** 095008
[72] Heinrich G, Ludwig M, Wu H, Hammerer K and Marquardt F 2011 *C. R. Phys.* **12** 837
[73] Bhattacharya M, Uys H and Meystre P 2008 *Phys. Rev.* A **77** 033819
[74] Larson J and Horsdal M 2011 *Phys. Rev.* A **84** 021804(R)
[75] Mumford J, O'Dell D H J and Larson J 2015 *Ann. Phys.* **527** 115
[76] Miladinovic N, Hassan F, Chisholm N, Linnington I E, Hinds E A and O'Dell D H J 2011 *Phys. Rev.* A **84** 043822
[77] Dicke R H 1954 *Phys. Rev.* **93** 99
[78] Baumann K, Guerlin C, Brennecke F and Esslinger T 2010 *Nature* **464** 1301
[79] Nagy D, Kónya G, Szirmai G and Domokos P 2010 *Phys. Rev. Lett.* **104** 130401
[80] Emary C and Brandes T 2003 *Phys. Rev.* E **67** 066203
[81] Holstein T and Primakoff H 1949 *Phys. Rev.* **58** 1098
[82] Ressayre E and Tallet A 1975 *Phys. Rev.* A **11** 981
Persico F and Vetri G 1975 *Phys. Rev.* A **12** 2083
[83] Sinatra A, Lobo C and Castin Y 2002 *J. Phys. B: At. Mol. Opt. Phys.* **35** 3599
[84] Polkovnikov A 2003 *Phys. Rev.* A **68** 053604
[85] Javanainen J and Ruostekoski J 2013 *New J. Phys.* **15** 013005
[86] Pitaevskii L and Stringari S 2003 *Bose–Einstein Condensation* (New York: Oxford University Press)
[87] Leibscher M, Averbukh I S and Rabitz H 2003 *Phys. Rev. Lett.* **90** 213001
[88] Dion C M, Haj-Yedder A B, Cances E, Le Bris C, Keller A and Atabek O 2002 *Phys. Rev.* A **65** 063408
[89] Rosca-Pruna F and Vrakking M J J 2002 *Phys. Rev. Lett.* **87** 153902
[90] Karras G, Hertz E, Billard F, Lavorel B, Hartmann J-M, Faucher O, Gershnabel E, Prior Y and Averbukh I S 2015 *Phys. Rev. Lett* **114** 153601
[91] Floß J and Averbukh I S 2015 *Phys. Rev.* E **91** 052911
[92] Moore F L, Robinson J C, Bharucha C F, Sundaram B and Raizen M G 1995 *Phys. Rev. Lett.* **75** 4598
[93] Casati G, Guarneri I and Shepelyansky D L 1989 *Phys. Rev. Lett.* **62** 345
[94] Lemarié G, Lignier H, Delande D, Szriftgiser P and Garreau J C 2010 *Phys. Rev. Lett.* **105** 090601
[95] Bastidas V M, Prez-Fernndez P, Vogl M and Brandes T 2014 *Phys. Rev. Lett.* **112** 140408
[96] Haake F 2009 *Quantum Signatures of Chaos* 3rd edn (Berlin: Springer)
[97] Connor J N L 1973 *Mol. Phys.* **26** 1217
[98] Berry M V, Nye J F and Wright F J 1979 *Proc. R. Soc.* A **291** 453
[99] Stamnes J J and Spielkavik B 1983 *Opt. Acta* **30** 1331
[100] Kaminski D and Paris R B 1999 *J. Comput. Appl. Math.* **107** 31
[101] Buonsante P, Burioni R, Vescovi E and Vezzani A 2012 *Phys. Rev.* A **85** 043625
[102] Dusuel S and Vidal J 2004 *Phys. Rev. Lett.* **93** 237204
[103] Dusuel S and Vidal J 2005 *Phys. Rev.* B **71** 224420
[104] Vidal J and Dusuel S 2006 *Europhys. Lett.* **74** 817
[105] Yee Y and O'Dell D H J to be published
[106] Emary C and Brandes T 2003 *Phys. Rev.* E **67** 066203

3.4 Paper IV: Morphology of a quantum catastrophe

Jesse Mumford, Eric Turner, D. W. L. Sprung, and D. H. J. O'Dell
Morphology of a quantum catastrophe
Submitted to New Journal of Physics

Summary: In this paper we go beyond the semiclassical theory and look at the full many-body quantum dynamics of a BEC in a double well under the same quench scheme described in the previous paper (paper three). Due to the discrete nature of Fock space in the many-body theory a new length scale is introduced, $l_q \propto N^{-1}$, where N is the number of bosons in the BEC. We explore the effects of the competition between l_q and $l_v \propto N^{-3/4}$, the distance between vortex and anti-vortex pairs within the cusp catastrophe produced by the dynamics. What we find is that for system sizes where $l_v \gg l_q$ the vortices within the cusp resemble those of the Pearcey function (cusp catastrophe diffraction integral), but for system sizes where $l_v \leq l_q$ the vortices can vanish due to the inability to discern any details of the wave function beyond N^{-1}.

Content: The majority of the writing was done by the author with the exception of the introduction and conclusion which were written by Duncan O'Dell. All of the numerical and analytic work was done by the author with the exception of the code used to find the vortices which was written by Eric Turner. Donald Sprung provided guidance over the whole research project.

Morphology of a quantum catastrophe

J. Mumford, E. Turner, D. W. L. Sprung, and D. H. J. O'Dell
Department of Physics and Astronomy, McMaster University,
1280 Main St. W., Hamilton, ON, L8S 4M1, Canada
(Dated: December 24, 2016)

Catastrophe theory [1, 2] describes singularities that occur widely in the natural world in the form of caustics. Examples include rainbows [3], twinkling starlight [4], freak waves [5] and large scale structure in the universe [6]. Wave catastrophes have three levels of structure: at large scales the geometric ray caustic is singular, at the wavelength scale interference smooths the singularity and produces universal diffraction patterns [2, 7], and at sub-wavelength scales there are dislocations (nodes) around which the wave function circulates as a vortex [8, 9]. Here we study the morphology of cusp catastrophes which are fundamentally granular. They occur, for example, in the Fock space of quantum field theories and are well behaved as long as the field excitations are quantized [10]. However, quantum catastrophes become singular in the classical field limit where the number of excitations is continuous. Furthermore, their dislocations are nodeless and compete with a new length scale arising from the granularity, being created or annihilated in pairs as the number of quanta is varied.

A famous example of the necessity of quantizing excitations of fields (second-quantization) is Planck's spectrum which avoids the ultraviolet catastrophe by treating the electromagnetic field in terms of photons. The term 'quantum catastrophe' was used by Leonhardt [11] to describe the phase singularity suffered by a classical wave crossing an event horizon and is resolved in quantum field theory by the emission of pairs of photons as Hawking radiation. Related ideas have been discussed by Berry and Dennis [12, 13], also in the context of optical phase singularities. However, neither of these phenomena has an obvious connection to catastrophe theory [14] which describes structurally stable (and hence generic) singularities in theories obeying a variational principle. In this letter we examine catastrophes in a simple quantum field composed of just two modes. Physical examples include the two polarization states of photons in a laser beam [15, 16], the Lipkin-Meshkov-Glick model in nuclear physics [17], the Ising model with infinite range interactions [18], and two coupled Bose-Einstein condensates (BECs), or fermionic superfluids, forming a Josephson junction [19–22].

We use the term quantum catastrophe to describe situations where the action in the Feynman path integral representation of a quantum field takes on one of the canonical generating functions of catastrophe theory. The resulting complex wave catastrophe will be the object of central interest. This is distinct from other work where catastrophe generating functions are used as potentials in the Schrödinger equation [23, 24].

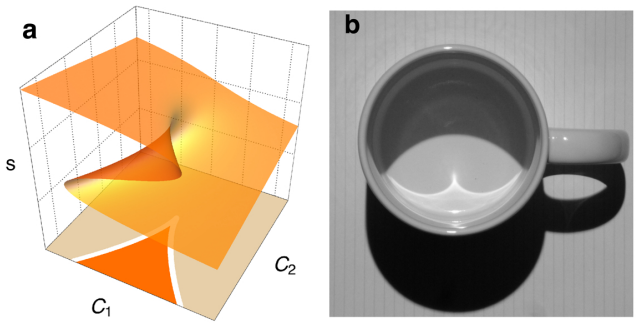

FIG. 1: Thom's elementary catastrophes are the only structurally stable singularities in up to four dimensions. Stability against perturbations removes any symmetry requirement which accounts for their widespread appearance in nature. The first catastrophe in the hierarchy is the fold and the second is the cusp which is shown above. The cusp is generated by a quartic action $I(C_1, C_2; s) = C_1 s + C_2 s^2 + s^4$, where (C_1, C_2) are control parameters, and s parameterizes paths. Classical paths satisfy the principle of stationary action $\partial I/\partial s = 0$, the solutions of which are plotted as the 3D surface in **(a)**. The folded portion has three solutions for every point (C_1, C_2) underneath it and the non-folded portion has one. The boundary between them forms a cusp $C_1 = \pm\sqrt{8/27}(-C_2)^{3/2}$ in the control plane: it is made of two fold lines where the action is stationary to higher order $\partial^2 I/\partial s^2 = 0$, giving the locus of points where two solutions coalesce. **(b)** Light reflects from the inside of a cup. Its circular (i.e. non-parabolic) shape focuses the light imperfectly forming a cusp at the bottom.

Consider a bosonic field with two modes and the associated annihilation operators $\hat{a}$ and $\hat{b}$. Using the Schwinger representation $\hat{S}_x \equiv (\hat{a}^\dagger\hat{b} + \hat{b}^\dagger\hat{a})/2$, $\hat{S}_y \equiv (\hat{a}^\dagger\hat{b} - \hat{b}^\dagger\hat{a})/2i$ and $\hat{S}_z \equiv (\hat{a}^\dagger\hat{a} - \hat{b}^\dagger\hat{b})/2$, the problem can be mapped onto a quantum spin of length $N/2$, where $N = N_a + N_b$ is the total number of excitations [25]. The quantum state of the field $|\Psi\rangle = \sum a_z|z\rangle$ is fully specified by the amplitudes a_z of the Fock states $|z\rangle$ which correspond to the discrete difference in the number of excitations between the two modes: $z \equiv 2S_z/N = (N_a - N_b)/N$, where z takes values between -1 and +1 in steps of $2/N$. Dynamics are obtained by evolving with a Hamiltonian which can always be written in terms of the three spin operators. Consider, for example, the two-site Bose-Hubbard model $\hat{H}_{\rm BH} = U\hat{S}_z^2 - \Omega\hat{S}_x$. This describes a bosonic Josephson junction where U is the on-site interaction energy and Ω governs the hopping between sites. In cold atom experiments U can be tuned by a Feshbach resonance and Ω

by laser or microwave intensity [26].

The structurally stable catastrophes which occur are determined by the dimension of control space. Here, Fock space is one dimensional with z acting as the coordinate. Time evolution adds a second coordinate giving a two dimensional control space. We therefore expect generic singularities to take the form of cusp catastrophes [1, 2] (see Fig. 1). Being two dimensional, the cusp is the simplest catastrophe exhibiting vortices in its diffraction pattern.

In the classical (mean-field) description the field excitation is continuous and a new quantity, phase, emerges. More precisely, the phase difference $\phi \equiv \phi_a - \phi_b$ between two condensates is the conjugate variable to z and can be directly measured in interference experiments [27, 28]. The Hamiltonian becomes $\lim_{N\to\infty} 2H_{\rm BH}/N\Omega \equiv H_{\rm class} = \Lambda z^2/2 - \sqrt{1-z^2}\cos\phi$ [30] and a single parameter $\Lambda = UN/\Omega$ fully determines the dynamics (for the quantum dynamics given below we also need to specify N). In the truncated Wigner approximation [29] the dynamics is treated by propagating classical solutions sampled from an initial quantum probability distribution as shown in Fig. 2. Each curve $z(t)$ is a solution of Hamilton's equations $\dot\phi = \partial H_{\rm class}/\partial z$ and $\dot z = -\partial H_{\rm class}/\partial\phi$ for a different value of the initial number difference z_0, and time is scaled as $t \to \Omega t/\hbar$. For the initial quantum state we choose a completely undefined number difference corresponding to a perfectly defined phase difference. Thus, the set of initial points $\{z_0\}$ is uniformly distributed over the range $-1 \le z_0 < 1$ and evolves into a repeated train of cusps as seen in Fig. 2(a). These correspond to the first, or geometric, level of a catastrophe and are singular. They are rendered finite by second quantization.

The precise form of the Hamiltonian will not affect the qualitative shape of any structurally stable singularities. Let us make the Hamiltonian simpler so we only have to deal with a single cusp by flashing the nonlinear term on and off instantaneously at $t = 0$ and also replace $\sqrt{1-z^2}$ by unity which is valid when $|z| \ll 1$. This gives the Hamiltonian for a δ-kicked rotor

$$\hat H_{\rm kick}/NJ = \Lambda\hat z^2\delta(t)/2 - \cos\hat\phi. \qquad (1)$$

The classical trajectories generated by $H_{\rm kick}$ are straight lines in the (z,t)-plane and form a single cusp as shown in Figure 2(b).

In quantum theory dynamics is generated by the application of the evolution operator to the initial state $|\Psi(t)\rangle = \hat{\mathcal{U}}(t,t_0)|\Psi_0\rangle$. For $\hat H_{\rm kick}$ we find $\hat{\mathcal{U}}(t,t_0) = \mathcal{T}\{\exp[-(\mathrm{i}/\hbar)\int_{t_0}^t \hat H(t')dt']\} = \exp[\mathrm{i}tN\cos\hat\phi]\,\exp[-\mathrm{i}\Lambda N\hat z^2/2]$, where $\mathcal{T}$ is the time ordering operator [31]. We take the initial state to be a discrete Gaussian normalized to N and with a width inversely proportional to Λ

$$|\Psi_0\rangle = \sqrt{\frac{4\Lambda}{\mathrm{erf}(2\Lambda/\pi)\,\pi^{3/2}}}\sum_{m=-N/2}^{N/2} \mathrm{e}^{-2(z_m\Lambda/\pi)^2}|z_m\rangle, \quad (2)$$

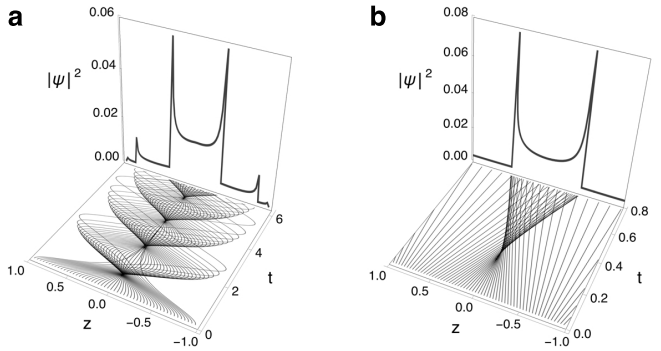

FIG. 2: Geometric cusps in Fock space as a function of time in a two mode field. The initial state has a well defined phase difference and Λ is quenched at $t = 0$. **(a)** The trajectories generated by the classical Bose-Hubbard Hamiltonian $H_{\rm class}$ form a train of cusps. **(b)** The kicked Hamiltonian $H_{\rm kick}$ generates a single cusp. The trajectories for the latter are straight lines: $z(t) = -2t\sin(2\Lambda z_0) + z_0$ (the phase trajectories are constants: $\phi(t) = \phi_0 = 2\Lambda z_0$). In both images $\Lambda = 2.1$ and the vertical back pane shows the probability density obtained by binning the trajectories arriving at the final time shown. The probability density diverges on the geometric cusp giving caustics.

where $z_m = 2m/N$ and $\mathrm{erf}(x)$ is the error function. This choice captures a significant range of classical trajectories and is more general than assuming a flat distribution. Under time evolution the Fock-space wave function becomes (see Methods)

$$\Psi(z_n,t) = \langle z_n|\hat{\mathcal{U}}(t)|\Psi_0\rangle = \sqrt{\frac{4\Lambda}{\mathrm{erf}(2\Lambda/\pi)\,\mathrm{N}^2\pi^{3/2}}}$$
$$\times \sum_{p,m=-N/2}^{N/2} \mathrm{e}^{-2\left(\frac{\Lambda z_m}{\pi}\right)^2}\mathrm{e}^{-\mathrm{i}N\left(\frac{\Lambda z_m^2}{2} - t\cos\phi_p - \frac{z_n - z_m}{2}\phi_p\right)} \quad (3)$$

where $\phi_p = \frac{2\pi p}{N+1}$ is a quantized phase [32], and we have neglected an unobservable overall phase factor.

It is useful to define a *continuum approximation*, applicable in the semiclassical regime $N \gg 1$, where ϕ and z are continuous and yet quantized via $[\hat\phi,\hat z] \approx 2\mathrm{i}/N$ [33]. In this approximation the wave function can be written as a Feynman path integral (see Methods)

$$\Psi(z,t) \propto \sqrt{N}\int_{-\infty}^{\infty}\mathrm{d}u\; e^{-\frac{u^2}{2\pi^2}}e^{\mathrm{i}N\left(\frac{u^2}{8\Lambda} + t\cos u + \frac{zu}{2}\right)} \quad (4)$$

and mapped onto the Pearcey function $\mathrm{Pe}(C_1,C_2) = \int_{-\infty}^{\infty}\mathrm{d}s\exp[\mathrm{i}(C_1 s + C_2 s^2 + s^4)]$, which is the universal diffraction integral for the cusp catastrophe [8]. Expanding the exponent of Eq. (4) around $u = 0$ gives

$$\Psi(z,t) \;\propto\; \left(\frac{N}{t}\right)^{1/4}\int_{-\infty}^{\infty}\mathrm{d}s\; e^{-\zeta(t)s^2/\sqrt{N}}$$
$$\times e^{\mathrm{i}\left(N^{3/4}Y(z,t)s + N^{1/2}X(t)s^2 + s^4\right)} \quad (5)$$

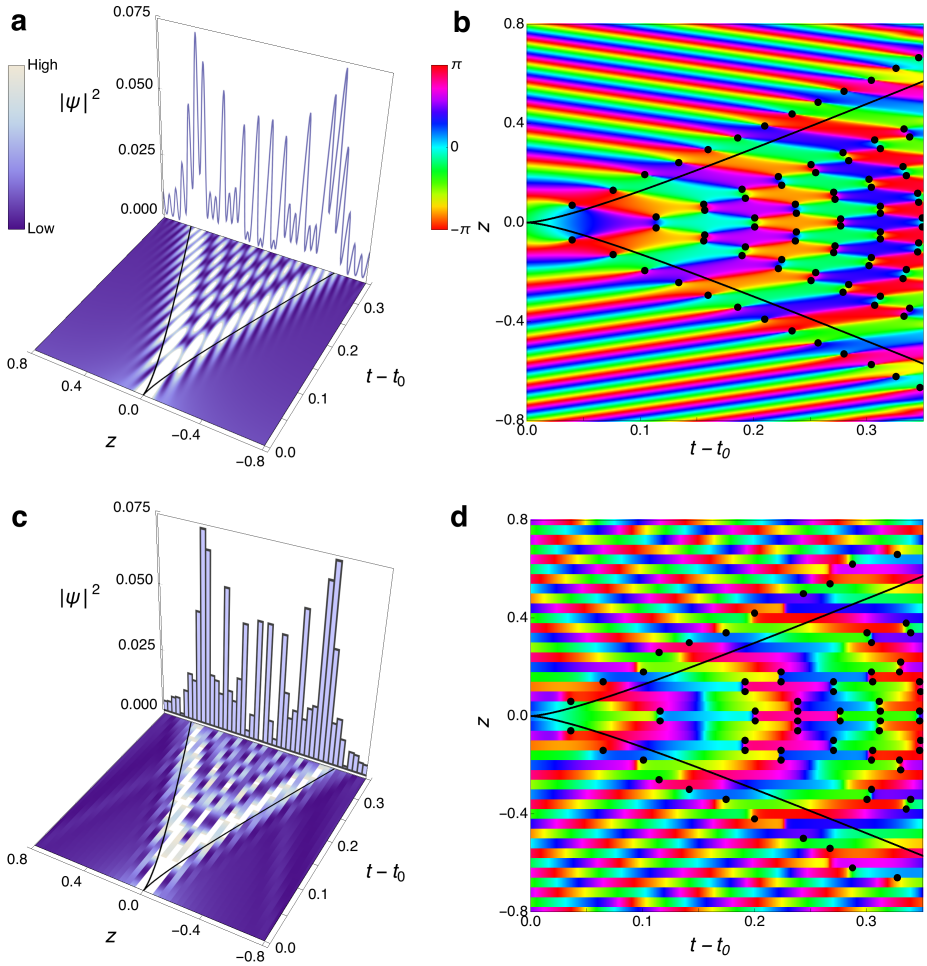

FIG. 3: A wave catastrophe (top row) versus a quantum catastrophe (bottom row). The latter is fundamentally granular but becomes a wave catastrophe in the continuum approximation. In both cases the divergences found in the geometric cusp (indicated by the black curves) are removed by interference. Panel **(a)** plots the probability density obtained from the continuum approximation given in Eq. (4). Panel **(b)** plots the phase of the same wave function. Black dots mark the positions of dislocations which lie at termination points of lines of constant phase: there is a single line of vortices on each side outside the cusp and a proliferating pattern of oppositely rotating vortex-antivortex pairs inside the cusp. Panels **(c)** and **(d)** are obtained from the second-quantized result given in Eq. (3). The probability amplitudes in this case exist on a discrete grid which we represent as ribbons of finite width $2/N$, which is the quantization length. The dislocation nodes therefore cease to exist unless by some chance they fall precisely on a grid line. Nevertheless, the quantized rotation around the dislocations is preserved. Comparing (b) and (d) we see that some vortex pairs are missing due to the granularity introduced by quantization. All images are generated with $N = 50$, $\Lambda = 2.1$, and $t_0 = 1/(4\Lambda)$ is the tip of the cusp.

where $s = (Nt/24)^{1/4}u$, $X(t) = (\frac{1}{4\Lambda} - t)\sqrt{6/t}$, $Y(z,t) = z(3/2t)^{1/4}$ and $\zeta(t) = \sqrt{\frac{6}{\pi^4 t}}$. The integrand is identical to that of $\mathrm{Pe}(N^{\sigma_1}Y, N^{\sigma_2}X)$ except for an additional real Gaussian envelope factor which, however, does not affect the properties of the interference pattern. The exponents $\sigma_1 = 3/4$ and $\sigma_2 = 1/2$ are Berry indices that govern the scaling of fringe spacings as a function of N in the (X, Y)-plane [4]. The wave function at two different values of N has the self-similar scaling property

$$\Psi\{Y, X; N_2\} = \left(\frac{N_2}{N_1}\right)^{\beta} \Psi\left\{\left(\frac{N_2}{N_1}\right)^{\sigma_1} Y, \left(\frac{N_2}{N_1}\right)^{\sigma_2} X; N_1\right\} \tag{6}$$

where $\beta = 1/4$ is the Arnold singularity index. Varying N is analogous to varying the wavenumber of diffracting waves and has no effect on the geometric caustic which is independent of N and fixed in the (z,t)-plane.

The continuum approximation and the exact second-quantized theory are compared in Fig. 3. The former corresponds to the standard wave catastrophe and has infinite resolution, allowing dislocations (vortices) to be perfectly resolved. Writing the wave function as $\Psi = \rho \exp[\mathrm{i}\theta]$, where θ should not be confused with ϕ, the total phase change around any circuit that contains a single dislocation yields $\oint \nabla\theta \cdot \mathrm{d}\mathbf{l} = \pm 2\pi$ corresponding to a quantized vortex or antivortex. Remarkably, performing the same integral in the discrete case (with a

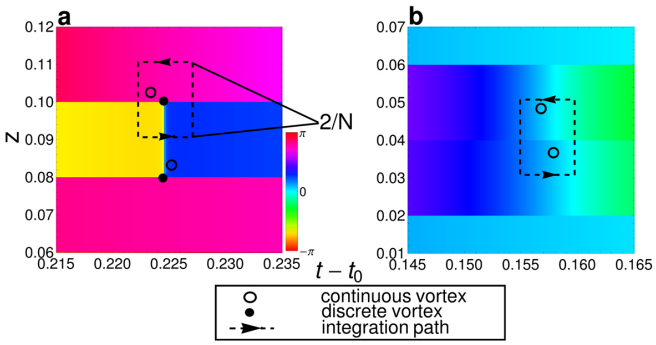

FIG. 4: Two magnified regions of the quantum catastrophe shown in Fig. 3(d). Panel **(a)** shows a region where a vortex-antivortex pair (filled circles) is detected and also indicates the location of the corresponding pair in the continuum approximation (unfilled circles) from Fig. 3(b). The dashed black box with arrows shows the integration path, exaggerated in the time (horizontal) direction to make it visible, but exact in the transverse direction due to the minimum length scale $2/N$. When just one continuum vortex is enclosed by the integration path it survives the discretization as does its partner. However, as seen in panel **(b)**, when both members of a continuum pair are enclosed they cannot be distinguished and annihilate each other.

suitable protocol for handling the discrete steps in the circuit–see Methods) also yields $\pm 2\pi$. This is despite the fact that the vortex cores themselves do not survive the quantization: in general granular vortices are not associated with nodes in the amplitudes $a_z(t)$. The black dots in Fig. 3(d) therefore indicate non-vanishing circuit integrals rather than nodes. Note that apart from the difference in positions of the dislocations in the z direction between Figs. 3(b) and 3(d), there are also discernible differences in their positions along the t direction (see also Fig. 4). This indicates that the second-quantized case is not merely a discrete sampling of the continuum case but has its own morphology.

A further consequence of granularity is that certain vortex pairs are missing altogether. Fig. 4 shows two magnified regions of Fig. 3(d) highlighting cases of both extant and missing pairs. A vortex annihilates with its antivortex partner when they both fall within the same discrete integration circuit. We can use the scaling properties of the continuum wave function to indicate the regime where vortices will be visible and hence when the quantum cusp will resemble the continuous Pearcey function. According to the discussion below Eq. (5), the wave catastrophe behaves as $\mathrm{Pe}(C_1, C_2) = \mathrm{Pe}(z[3N^3/2t]^{1/4}, (6N/t)^{1/2}[t_0 - t])$. Focusing on the dependence in the z direction, i.e. along C_1, we see that the distance between any two points, and in particular between the two members of a vortex-antivortex pair, scales as $d_\mathrm{v} \propto N^{-3/4}$. Forming the ratio with the quantization length $d_q = 2/N$ gives the resolution parameter

$$\mathcal{R} = d_\mathrm{v}/d_q \propto N^{1/4}\,. \tag{7}$$

The dependence on N is weak, but in principle all the vortices present in the Pearcey function should appear in the quantum cusp if there are a large enough number of excitations ($\mathcal{R} \gg 1$). However, the quantum catastrophe only becomes indistinguishable from the continuum wave catastrophe in the limit $N \to \infty$ at which point both are singular and correspond to the geometric cusp. In this sense the continuum approximation represents an idealization that can never quite be reached. According to the scaling relation Eq. (6), the probability density $|\Psi|^2$ on the cusp diverges as $N^{1/2}$. Granularity breaks this continuous classical scaling property, leading to the disappearance of vortex pairs, and can therefore be viewed as a type of quantum anomaly.

Quantum catastrophes can be observed in experiments with two coupled BECs by measuring the time-dependence of the probability distribution for either the number difference [19, 22, 26], or the phase difference [27, 28], as both of these variables will in general display cusps following a quench in Λ [34]. We have studied the quantum cusp for a specific Hamiltonian and initial conditions but the power of catastrophe theory is that the same results apply qualitatively to the dynamics of any two-mode quantum field, and higher catastrophes will be exhibited in higher mode fields. The significance of quantum catastrophes is that they extend the application of catastrophe theory beyond mean-field theory and so become particularly important near phase transitions [35].

METHODS

Number and Phase states

For pedagogical reasons, in this section we work with $\hat{S}_z$ rather than $\hat{z}$. The two are simply related via $\hat{S}_z = N\hat{z}/2$. The eigenstates of $\hat{S}_z$ are the spin states $\hat{S}_z|N/2, m\rangle = m|N/2, m\rangle$, where $\langle N/2, m|N/2, n\rangle = \delta_{mn}$. We suppress the "spin magnitude" label $N/2$ and write $|N/2, m\rangle$ simply as $|m\rangle$. The eigenvalues m are integers or half-integers depending upon whether N is even or odd. When N is even the $N+1$ eigenvalues are $m = \{-N/2, -N/2+1, \ldots, -1, 0, 1, \ldots, N/2-1, N/2\}$. The conjugate variable to S_z is the *discrete* phase difference $\phi_p = \phi_0 + 2\pi p/(N+1)$ [32] where ϕ_0 is an arbitrary constant which we set to zero, and p takes the same values as m. The discrete phase differences are $N+1$ equally spaced angles around a circle and are eigenvalues of the phase operator $\hat{\phi}|\phi_p\rangle = \phi_p|\phi_p\rangle$, where $\langle\phi_p|\phi_q\rangle = \delta_{pq}$. The number and phase states form discrete Fourier transform pairs: $|\phi_p\rangle = (N+1)^{-1/2}\sum_{m=-N/2}^{N/2}\exp[im\phi_p]|m\rangle$ and $|n\rangle = (N+1)^{-1/2}\sum_{p=-N/2}^{N/2}\exp[-im\phi_p]|\phi_p\rangle$.

Quantum state in Fock space

The evolution operator can be written in terms of $\hat{S}_z$ and $\hat{\phi}$ as $\hat{U}(t) = \exp[\mathrm{i}Nt\cos\hat{\phi}]\exp[-\mathrm{i}(2\Lambda/N)\hat{S}_z^2]$ [31]. Applying this to the initial Gaussian state $|\Psi_0\rangle$, the amplitude to be found in the $n^{\rm th}$ Fock state at time $t>0$ is

$$\Psi(n,t) = \langle n|\hat{U}(t)|\Psi_0\rangle = \sqrt{\frac{4\Lambda}{\mathrm{erf}(2\Lambda/\pi)\,\pi^{3/2}}} \times \sum_{m=-N/2}^{N/2} \mathrm{e}^{-2\left(\frac{2\Lambda m}{\pi N}\right)^2}\mathrm{e}^{-\mathrm{i}\frac{2\Lambda}{N}m^2}\langle n|\mathrm{e}^{\mathrm{i}Nt\cos\hat{\phi}}|m\rangle\,. \quad (8)$$

The matrix element on the right hand side can be evaluated by projecting over the phase basis: $\exp[\mathrm{i}Nt\cos\hat{\phi}] = \sum_{p=-N/2}^{N/2}\exp[\mathrm{i}Nt\cos\phi_p]|\phi_p\rangle\langle\phi_p|$, giving

$$\Psi(n,t) = \sqrt{\frac{4\Lambda}{\mathrm{erf}(2\Lambda/\pi)\,\pi^{3/2}}}\;\frac{1}{N+1} \times \sum_{m,p=-N/2}^{N/2} \mathrm{e}^{-2\left(\frac{2\Lambda m}{\pi N}\right)^2}\mathrm{e}^{\mathrm{i}\left(-\frac{2\Lambda}{N}m^2+(n-m)\phi_p+Nt\cos\phi_p\right)} \quad (9)$$

where we have used $\langle n|\phi_p\rangle = \frac{1}{\sqrt{N+1}}\mathrm{e}^{in\phi_p}$.

Continuum approximation

In the semiclassical regime $N\gg 1$ we can attempt to replace the discrete sums in Eq. (9) by continuous integrals. However, the Euler-Maclaurin formula [7]

$$\sum_{m=a}^{b} f(m) \;\sim\; \int_a^b f(m)\mathrm{d}m + \frac{f(a)+f(b)}{2} + \sum_{s=1}^{\infty}\frac{B_{2s}}{(2s)!}\left[f^{(2s-1)}(b) - f^{(2s-1)}(a)\right] \quad (10)$$

indicates that the direct replacement of a sum by an integral is only valid, even in this regime, if $f(m)$ is slowly varying [in this formula B_i denotes a Bernoulli number and $f^{(j)}(m)$ the $j^{\rm th}$ derivative of $f(m)$]. This condition is met for the exponent $n\phi_p$ because, by assumption, we are limiting ourselves to $|n|\ll N$, i.e. $|z|\ll 1$, and also holds for $Nt\cos\phi_p$. Thus, we put $\sum_{p=-N/2}^{N/2}\to N/(2\pi)\int_{-\pi}^{\pi}\mathrm{d}\phi$, and write the wave function as

$$\Psi(n,t) \sim \frac{1}{2\pi}\sqrt{\frac{4\Lambda}{\mathrm{erf}(2\Lambda/\pi)\,\pi^{3/2}}}\;\times \sum_{m=-\infty}^{\infty}\int_{-\pi}^{\pi}\underbrace{\mathrm{e}^{-2\left(\frac{2\Lambda m}{\pi N}\right)^2-\mathrm{i}\left(\frac{2\Lambda}{N}m^2+m\phi\right)}}_{g(m)}\mathrm{e}^{\mathrm{i}(Nt\cos\phi+n\phi)}\mathrm{d}\phi \quad (11)$$

where we have also extended the sum over m to $\pm\infty$. The remaining factors, denoted by $g(m)$ in Eq. (11), are highly oscillatory and cannot be replaced by an integral. However, they can be handled using the Poisson summation formula [36]

$$\sum_{m=-\infty}^{\infty} g(m) = \sum_{k=-\infty}^{\infty}\int_{-\infty}^{\infty} g(m)\;\mathrm{e}^{-2\pi\mathrm{i}mk}\;\mathrm{d}m \quad (12)$$

which is exact. The Fourier transform of $g(m)$ is

$$\begin{aligned}&\int_{-\infty}^{\infty} g(m)\;\mathrm{e}^{-2\pi\mathrm{i}mk}\;\mathrm{d}m\\ &= \sqrt{\frac{\pi^3N^2}{2\Lambda(\mathrm{i}N\pi^2+4\Lambda)}}\mathrm{e}^{-\frac{\pi^2N^2(\phi-2\pi k)^2}{2(\pi^4N^2+16\Lambda^2)}}\mathrm{e}^{\mathrm{i}\frac{\pi^4N^3(\phi-2\pi k)^2}{8\Lambda(\pi^4N^2+16\Lambda^2)}}\\ &\approx \sqrt{\frac{\pi N}{2\Lambda\mathrm{i}}}\mathrm{e}^{-\frac{(\phi-2\pi k)^2}{2\pi^2}}\mathrm{e}^{\mathrm{i}\frac{N(\phi-2\pi k)^2}{8\Lambda}} \end{aligned} \quad (13)$$

where in the last step we assumed $N\gg\Lambda$. Substituting into Eq. (11), we obtain the asymptotic continuum approximation to the Fock-space wave function as quoted in Eq. (4) in the main text

$$\Psi(z,t) \sim \frac{\mathrm{e}^{-\mathrm{i}\pi/4}\sqrt{N}}{\sqrt{2\pi^{5/2}\mathrm{erf}(2\Lambda/\pi)}}\int_{-\infty}^{\infty}\mathrm{e}^{-\frac{u^2}{2\pi^2}}\mathrm{e}^{\mathrm{i}N\left(\frac{u^2}{8\Lambda}+t\cos u+\frac{zu}{2}\right)}\mathrm{d}u \quad (14)$$

where we have substituted in $u=\phi-2\pi k$ and $n=Nz/2$, and used the fact that $\sum_{k=-\infty}^{\infty}\int_{-\pi(1+2k)}^{\pi(1-2k)}\mathrm{d}u = \int_{-\infty}^{\infty}\mathrm{d}u$.

Numerical location of vortices

To find the locations of vortices in Figs. 3 and 4 we divided the (z,t)-plane into a grid of cells and calculated the total phase change around the perimeter of each cell. If a cell contains a single vortex the phase change is $\pm 2\pi$. The grid spacing should be small enough to resolve individual vortices: In the continuum case we used $\Delta z = 0.1/N$ and $\Delta t = 0.001$. In the granular case the z direction is of course already discretized at $\Delta z = 2/N$, and for the time direction we again used $\Delta t = 0.001$. There is ambiguity in assigning a phase difference between two discrete points as it is impossible to tell whether the phase difference is $\theta_2-\theta_1$ (the "short way" around the phase circle) or $\theta_2-\theta_1-2\pi$ (the "long way" around the phase circle). This problem does not arise in continuum systems where one can always make the numerical grid smaller until the phase difference becomes vanishingly small, but in a fundamentally discrete system this is not possible. We adopted the convention of always choosing the smallest phase difference between the two points, i.e. we mapped the phase difference into the range $-\pi<\theta<\pi$. There is also some arbitrariness in the placement of the black dots marking the dislocations in the discrete cases shown in Figs. 3 and 4. As the circuits cannot be shrunk to a size of less than $2/N$ in the z direction, we opted for the most democratic placement of the dots which is between two "ribbons" of width $2/N$ (each ribbon represents a single Fock space amplitude).

Number of excitations required to resolve vortices

An estimate for the minimum value of N required to preserve any particular vortex pair can be obtained by considering the positions of vortices in the Pearcey function, which are tabulated in reference [7], and comparing their separation with the discretization length $2/N$. This approach treats the quantum catastrophe as simply a discretely sampled version of the Pearcey function, when in fact it is not, but is nevertheless a useful starting point. According to the discussion below Eq. (5), the canonical coordinates (C_1, C_2) are related to the physical coordinates as $C_1 = (3N^3/2t)^{1/4}z$ and $C_2 = (6N/t)^{1/2}(t_0 - t)$, where $t_0 = 1/(4\Lambda)$. Denoting the distance between two vortices, labelled by a and b, in the C_1 direction as ΔC_1 we have $\Delta C_1 = (3N^3/2)^{1/4}[z_a/t_a^{1/4} - z_b/t_b^{1/4}]$. The vortices in a pair occur at almost the same time so we shall put $t_a \approx t_b = t$. In order to be preserved under quantization we require $|z_a - z_b| \gtrsim 2/N$. Thus, we find

$$N_{\min} \approx \frac{24}{t}\frac{1}{(\Delta C_1)^4}. \tag{15}$$

Solving the relation $(C_2)^2 t/6N = (t_0 - t)^2$ for t we obtain

$$\frac{1}{t} = \frac{1}{t_0}\left(1 + \frac{\alpha}{2N} - \frac{1}{2}\sqrt{\frac{\alpha^2}{N^2} + 4\frac{\alpha}{N}}\right) \tag{16}$$

where $\alpha = (C_2)^2/(6t_0)$. Combining Eqns. (15) and (16) yields

$$N_{\min} = \frac{8\Lambda}{(\Delta C_1)^2}\left[\frac{12}{(\Delta C_1)^2} - |C_2|\right]. \tag{17}$$

The vortices shown in Fig. 4(b) occur at $(C_1^a = 1.41101, C_2^a = -5.55470)$ and $(C_1^b = 2.36094, C_2^b = -5.52321)$ in the Pearcey function [7]. For the purposes of evaluating Eq. (17), we take C_2 to be the average of C_2^a and C_2^b. This gives $N_{\min} \approx 69\,\Lambda$ and provides an upper bound as the actual value depends upon precisely where the pair fall: as long as they straddle a circuit boundary they can in fact have a very small separation and yet survive because they will be counted as separate objects. Calculating the quantum case exactly for $\Lambda = 2.1$ we find that upon increasing N gradually from small values this vortex pair pop in and out of existence but finally become a permanent feature at $N \approx 60$ (we checked up to $N = 300$). This is safely within the upper bound $N_{\min} = 144$ set by Eq. (17).

[1] Thom, R. *Structural Stability and Morphogenesis* (Benjamin, Reading MA, 1975).

[2] Arnol'd, V. I. Critical points of smooth functions and their normal forms. *Russ. Math. Survs.* **30**, 1 (1975).

[3] Nye, J. F. *Natural focusing and the fine structure of light* (Institute of Physics, Philadelphia, 1999).

[4] Berry, M. V. Focusing and twinkling: critical exponents from catastrophes in non-Gaussian random short waves. *J. Phys. A: Math. Gen.* **10**, 2061 (1977).

[5] Höhmann, R., Kuhl, U., Stöckmann, H.-J., Kaplan, L. and Heller, E. J. Freak waves in the linear regime: a microwave study. *Phys. Rev. Lett.* **104**, 093901 (2010).

[6] Arnold, V. I., Shandarin, S. F and Zeldovich, Ya. B. The Large Scale Structure of the Universe I. General Properties. One- and Two-Dimensional Models. *Geophys. Astrophys. Fluid Dynamics* **20**, 111 (1982).

[7] *NIST Handbook of Mathematical Functions*, edited by Olver et al. (Cambridge University, New York, 2010), chapter 36.

[8] Pearcey, T. The structure of an electromagnetic field in the neighborhood of a caustic. *Phil. Mag.* **37**, 311 (1946).

[9] Nye, J. F. and Berry, M. V. Dislocations in wave trains. *Proc. R. Soc. Lond. A* **336**, 165 (1974).

[10] O'Dell, D. H. J. Quantum catastrophes and ergodicity in the dynamics of bosonic Josephson junctions. *Phys. Rev. Lett.* **109**, 150406 (2012).

[11] Leonhardt, U. A laboratory analogue of the event horizon using slow light in an atomic medium. *Nature* **415**, 406 (2002).

[12] Berry, M. V. and Dennis, M. R. Quantum cores of optical phase singularities. *J. Opt. A: Pure Appl. Opt.* **6**, S178 (2004).

[13] Berry, M. V. Three quantum obsessions. *Nonlinearity* **21**, T19 (2008).

[14] Kiss, T. and Leonhardt, U. Towards a classification of wave catastrophes. *J. Opt. A: Pure Appl. Opt.* **6**, S246 (2004).

[15] Luis, A. Degree of polarization in quantum optics. *Phys. Rev. A* **66**, 013806 (2002).

[16] Korolkova, N. and Loudon, R. Nonseparability and squeezing of continuous polarization variables. *Phys. Rev. A* **71**, 032343 (2005).

[17] Lipkin, H. J., Meshkov, N. and Glick, A. J. Validity of many-body approximation methods for a solvable model: (I). Exact solutions and perturbation theory. *Nuclear Phys.* **62**, 188 (1965).

[18] Das, A., Sengupta, K., Sen, D. and Chakrabarti, B. K. Infinite-range Ising ferromagnet in a time-dependent transverse magnetic field: quench and ac dynamics near the quantum critical point. *Phys. Rev. B* **74**, 144423 (2006).

[19] Albiez, M., Gati, R., Fölling, J., Hunsmann, S., Cristiani, M. and Oberthaler, M. K. Direct observation of tunneling and nonlinear self-trapping in a single bosonic Josephson junction. *Phys. Rev. Lett.* **95**, 010402 (2005).

[20] Levy, S., Lahoud, E., Shomroni, I. and Steinhauer, J. The a.c. and d.c. Josephson effects in a Bose-Einstein condensate. *Nature* **449**, 579 (2007).

[21] Valtolina, G., Burchianti, A., Amico, A., Neri, E., Xhani, K., Seman, J. A., Trombettoni, A., Smerzi, A., Zac-

canti, M., Inguscio, M. and Roati, G. Josephson effect in fermionic superfluids across the BEC-BCS crossover. *Science* **350**, 1505 (2015).

[22] Trenkwalder, A., Spagnolli, G., Semeghini, G., Coop, S., Landini, M., Castilho, P., Pezzè, L., Modugno, G., Inguscio, M., Smerzi, A. and Fattori, M. Quantum phase transitions with parity-symmetry breaking and hysteresis. *Nat. Phys.* **12**, 826 (2016).

[23] Gilmore, R., Kais, S. and Levine, R. D. Quantum cusp. *Phys. Rev. A* **34**, 2442 (1986).

[24] Emary, C., Lambert, N. and Brandes, T. Entanglement in quantum catastrophes. *Phys. Rev. A* **71**, 062302 (2005).

[25] Milburn, G. J., Corney, J., Wright, E. M. and Walls, D. F. Quantum dynamics of an atomic Bose-Einstein condensate in a double-well potential. *Phys. Rev. A* **55**, 4318 (1997).

[26] Zibold, T., Nicklas, E., Gross, C. and Oberthaler, M. K. Classicial bifurcation at the Transition from Rabi to Josephson dynamics. *Phys. Rev. Lett.* **105**, 204101 (2010).

[27] Schumm, T., Hofferberth, S., Andersson, L. M., Wildermuth, S., Groth, S., Bar-Joseph, I., Schmiedmayer, J. and Krüger, P. Matter-wave interferometry in a double well on an atom chip. *Nature Phys.* **1**, 57 (2005).

[28] Saba, M., Pasquini, T. A., Sanner, C., Shin, Y., Ketterle, W. and Pritchard, D. E. Light scattering to determine the relative phase of two Bose-Einstein condensates. *Science* **307**, 1945 (2005).

[29] Javanainen, J. and Ruostekoski, Emergent classicality in continuous quantum measurements. *New J. Phys.* **15**, 013005 (2013).

[30] Smerzi, A., Fantoni, S., Giovanazzi, S. and Shenoy, S. R. Quantum coherent atomic tunneling between two trapped Bose-Einstein condensates. *Phys. Rev. Lett.* **79**, 4950 (1997).

[31] Haake, F. *Quantum Signatures of Chaos*, 3rd edition (Springer, Berlin, 2009).

[32] Pegg, D. T. and Barnett, S. M. Phase properties of the quantized single-mode electromagnetic field. *Phys. Rev. A* **39**, 1665 (1989).

[33] Leggett, A. J. *Chance and Matter* (Les Houches 1986, Session XLVI) ed J Souletie et al (North-Holland, Amsterdam, 1987).

[34] Berry, M. V. and O'Dell, D. H. J. Ergodicity in wave-wave diffraction. *J. Phys. A: Math. Gen.* **32**, 3571 (1999).

[35] Mumford, J., Kirkby, W. and O'Dell, D. H. J. Catastrophes in many-body wave functions: universality and critical scaling. arXiv:1609.04502.

[36] Berry, M. V. and Bodenschatz, E. Caustics, multiply reconstructed by Talbot interference. *J. Mod. Opt.* **46**, 2 (1999).

Chapter 4

Conclusions

This thesis explored the effects singularities have on the steady-state and dynamical properties of many-body quantum systems, emphasizing the BJJ. For the steady-state effects it was shown that N bosons forming a Bose-Einstein condensate (BEC) in a double well is extremely sensitive to the inclusion of a single impurity. In the mean-field theory the Landau theory of phase transitions (PTs) showed there existed a spontaneous PT breaking $\mathbb{Z}_2$ symmetry at a critical value of the BEC-impurity interaction energy, Λ_c. The PT separates two phases where the symmetric phase consists of an equal amount of the BEC in each well and the symmetry broken phase consists of a buildup of the BEC in one well over the other. In the mean-field dynamics the system went from having regular motion in the symmetric phase to having chaotic motion in the symmetry broken phase where it was also shown the system was ergodic. To see if the PT persisted through to the quantum theory, fidelity susceptibility (FS), χ_F, was used to determine the susceptibility of the ground state to changes in Λ. The FS exhibited singular behaviour at Λ_c in the thermodynamic limit, $N \to \infty$, by diverging, thus confirming the existence of the PT. To characterize the divergence, scaling exponents were calculated for the FS where it was found that the divergence was asymmetric with $\chi_F \sim |\lambda|^{-2}$ as $\lambda \to 0^-$ and $\chi_F \sim |\lambda|^{-1/2}$ as $\lambda \to 0^+$ where $\lambda = (\Lambda - \Lambda_c)/\Lambda_c$ is the reduced BEC-impurity interaction energy. The source of the asymmetry was found to be the difference in the dependence on N of the energy level spacing on either side of the PT. The correlation length in Fock space was also found to diverge like $\xi \sim |\lambda|^{-3/2}$ as $\lambda \to 0$. These exponents were used to determine that the BEC-impurity system belonged in the same universality class as the Lipkin-Meshkov-Glick and Dicke models which are also systems of N bosons.

The second half of this thesis focused on mean-field and semiclassical dynamics of a BEC in a double well (without an impurity) after a quench which involved flashing on, then off, a term in the Hamiltonian at $t = 0$, then allowing the system to evolve. The dynamics occurred in the Fock-space plus time plane displaying a cusp shape from oscillations around zero number and phase difference (plasma oscillations) between

the two wells for all repulsive boson-boson interactions and from oscillations around zero number difference and π phase difference (π oscillations) for interactions less than some critical value, U_c. Thus, the transition from a cusp to no cusp at U_c can be considered as a *dynamical* PT.

Within the cusps were networks of vortex-antivortex pairs which are points of zero amplitude and undefined phase (not to be confused with the phase difference between the two wells). To analyze the cusps and vortices we were able map the action to the cusp generating function given by catastrophe theory (CT). We then were able to map the wave function around the cusp to the Pearcey function which is the diffraction integral form of the cusp. The Pearcey function comes with scaling exponents describing how distances between the vortices scale with wavenumber. Our main result was to show a relation between the boson-boson interaction energy and the wavenumber, so the critical exponents were used to describe the singular behaviour of the divergence of the distance between vortices as U_c was approached.

Finally, we went beyond the semiclassical theory to the full many-body quantum theory to describe how second quantization affects cusps. The cusp we analyzed was formed by the plasma oscillations after the boson-boson interactions were flashed on, then off at $t = 0$. Due to second quantization, a minimum length scale, $l_q = N^{-1}$, was introduced which resulted in the destruction of the vortices because their locations could no longer be discerned since they are points. However, remnants of them remained as there were still circuits in the Fock space plus time plane producing phase changes (again, not the phase difference between the two wells) of $\pm 2\pi$. We found these remnants persisted so long as $l_v \gg l_q$ where $l_v \propto N^{-3/4}$ is the distance between vortices in Fock space. When $l_v \approx l_q$ the remnants were also destroyed in pairs.

Overview and outlook

The work presented in this thesis on the BEC-impurity system represents the characterization of its critical behaviour. The next step will be to see if what we have found has any use. A promising topic to pursue is measurement theory. The fact that quantum fluctuations depend on the number of bosons, N, in a BJJ means it can potentially fulfill many different roles in the context of measurement theory when coupled to an impurity (qubit). If the BJJ plays the role of the measurement device it can be tuned from classical (large N) to quantum (small N) which can help elucidate the issues dealing with the interactions between measurement devices and quantum systems. When N is very large the BJJ can be considered as the environment of the qubit. Environment induced decoherence is an intensely studied topic these days [84] which may help explain the cause of wavefunction collapse upon measurement. The ramping on and off of qubit-environment interactions has been studied with interac-

tions between the transverse field Ising model (environment) and a spin-1/2 particle (qubit) [85]. It was shown that the decoherence of the qubit was sensitive to the PT in the Ising model opening up the possibility of using PTs in the environment to control the coherence of qubits. This system is especially relevant because it has been shown that the transverse field Ising model with infinite interaction distance can be mapped to the BJJ [86]. The BJJ has a second order PT for attractive boson-boson interactions and although attractive interactions makes the BEC unstable to collapse the PT has been recently confirmed experimentally [72]. Another approach to take would be to make the BJJ the quantum system and make the impurity the measurement device. It has been shown that impurities make good nondestructive probes of excitations within a BEC in a linear trap [87].

It is difficult to determine how CT might be used to study dynamical PTs in the future because this approach is still in its early stages. The first step should be to study the catastrophes that appear in the dynamics we see now before turning to PTs. Currently, there are papers showing the emergence of caustics in the dynamics of a cold atoms in an optical lattice [88] and in a magnetic trap [89]after a quench. However, there is no discussion about the catastrophes formed by the caustics nor their universal properties. Similar experimental results come from recent papers showing, but not identifying, catastrophes in the dynamics of single particles 'walking' around on lattices [90, 91]. The fact that catastrophes are appearing in the dynamics of such different systems provides evidence of their universality and stability as well as provides motivation for their study.

A major hurdle in the study of catastrophes in many-body quantum systems is establishing exactly how their diffraction integral forms emerge from quantum fluctuations. Statistical methods have been used by Berry [53] to describe the twinkling of starlight and although the work was done at the mean-field level, this suggests it could be extended to include quantum fluctuations near PTs. In the BJJ we have only considered a quantum field with a small number of modes (two), so the viability of this approach for a larger number of modes remains to be demonstrated. The possible exception to this is the transverse field Ising model discussed in Appendix A because it has as many modes as it has sites. Thus, this latter work has potential for considerable significance.

Appendix A

Catastrophes in the transverse field Ising model

In this section we derive the ground state for the transverse field Ising model (TFIM) and show cusp-like structures form in the dynamics of single particle excitations. We start with the TFIM Hamiltonian

$$H = -J \sum_j S_j^x S_{j+1}^x - h \sum_j S_j^z \tag{A.1}$$

where J is the hopping energy between adjacent sites and h is some applied field in the z direction.

Jordan-Wigner Transformation

The Jordan-Wigner transformation changes the TFIM from a chain of 1/2-spins to free fermions with the following transformations [92]

$$\begin{aligned} S_j^z &= f_j^\dagger f_j - 1/2 \\ S_j^+ &= f_j^\dagger \mathrm{e}^{i\pi \sum_{l<j} n_l} \\ S_j^- &= f_j \mathrm{e}^{-i\pi \sum_{l<j} n_l} . \end{aligned} \tag{A.2}$$

Substituting these into Eq. (A.1) gives

$$
\begin{aligned}
H &= -\frac{J}{4}\sum_j \Big(f_j^\dagger f_{j+1}^\dagger \mathrm{e}^{i2\pi\sum_{l<j} n_l}\mathrm{e}^{i\pi n_j} + f_j^\dagger f_{j+1}\mathrm{e}^{-i\pi n_j} + f_j f_{j+1}^\dagger \mathrm{e}^{i\pi n_j} \\
&\quad + f_j f_{j+1}\mathrm{e}^{-i2\pi\sum_{l<j} n_l}\mathrm{e}^{-i\pi n_j}\Big) - h\sum_j f_j^\dagger f_j \\
H &= -\frac{J}{4}\sum_j \Big(f_j^\dagger f_{j+1}^\dagger + f_j^\dagger f_{j+1} - f_j f_{j+1}^\dagger - f_j f_{j+1}\Big) - h\sum_j f_j^\dagger f_j \qquad \text{(A.3)}
\end{aligned}
$$

where we have removed the constant term $hN/2$. We have also used the fact that $\mathrm{e}^{i2\pi\sum_{l<j} n_l} = 1$ and

$$
\begin{aligned}
&f_j^\dagger \mathrm{e}^{\pm i\pi n_j}|...1_j...\rangle = 0 \qquad f_j^\dagger \mathrm{e}^{\pm i\pi n_j}|...0_j...\rangle = |...1_j...\rangle \\
&f_j \mathrm{e}^{\pm i\pi n_j}|...1_j...\rangle = -|...0_j...\rangle \qquad f_j \mathrm{e}^{\pm i\pi n_j}|...0_j...\rangle = 0\,.
\end{aligned}
$$

Fourier Transform

Here, we transform Eq. (A.3) from spatial operators to momentum operators with the Fourier transformation

$$
f_j = \frac{1}{\sqrt{N_s}}\sum_k d_k \mathrm{e}^{-ikR_j}; \quad R_j = ja, \quad k \equiv k_n = \frac{2\pi n}{L} \qquad \text{(A.4)}
$$

giving

$$
\begin{aligned}
H &= -\frac{J}{4N_s}\sum_j\sum_{k,k'} d_k^\dagger d_{k'}^\dagger \mathrm{e}^{i(k+k')R_j}\mathrm{e}^{ik'a} + d_k^\dagger d_{k'}\mathrm{e}^{i(k-k')R_j}\mathrm{e}^{-ik'a} - d_k d_{k'}^\dagger \mathrm{e}^{-i(k-k')R_j}\mathrm{e}^{ik'a} \\
&- d_k d_{k'}\mathrm{e}^{-i(k+k')R_j}\mathrm{e}^{-ik'a} - \frac{h}{N_s}\sum_j\sum_{k,k'} d_k^\dagger d_{k'}\mathrm{e}^{i(k-k')R_j} \\
H &= \sum_k \frac{J}{4}\Big(-d_k^\dagger d_{-k}^\dagger \mathrm{e}^{-ika} - d_k^\dagger d_k \mathrm{e}^{-ika} + d_k d_k^\dagger \mathrm{e}^{ika} + d_k d_{-k}\mathrm{e}^{ika}\Big) - h d_k^\dagger d_k \qquad \text{(A.5)}
\end{aligned}
$$

where we have used the fact that $\sum_j \mathrm{e}^{i(k\pm k')R_j} = N_s\delta_{k,\mp k'}$. In Eq. (A.5) the range of the sum is $k \in [-\pi/a, \pi/a]$, however if we have the range over positive k the Hamiltonian becomes

$$
H = \sum_{k\geq 0} \epsilon_k \Big(d_k^\dagger d_k - d_{-k} d_{-k}^\dagger\Big) + i\Delta_k\Big(d_k^\dagger d_{-k}^\dagger - d_{-k} d_k\Big) \qquad \text{(A.6)}
$$

where $\epsilon_k = -\frac{J}{2}\cos ka - h$, $\Delta_k = \frac{J}{2}\sin ka$ and we have neglected the constant ground energy term $E_0 = \frac{J}{2}\sum_{k\geq 0}\cos ka$. The Hamiltonian can be written in a simpler form

$$H = \sum_{k\geq 0} \begin{pmatrix} d_k^\dagger & d_{-k} \end{pmatrix} h_k \begin{pmatrix} d_k \\ d_{-k}^\dagger \end{pmatrix} \tag{A.7}$$

where

$$h_k = \begin{pmatrix} \epsilon_k & i\Delta_k \\ -i\Delta_k & -\epsilon_k \end{pmatrix} \tag{A.8}$$

and its eigenvalues give the energies of the system

$$\omega_k = \pm\sqrt{\epsilon_k^2 + \Delta_k^2}\,. \tag{A.9}$$

Bogoliubov Transformation

To diagonalize Eq. (A.6) we make the canonical transformation from the d_k, $d_k^\dagger$ operators to the Bogoliubov operators, γ_k, $\gamma_k^\dagger$

$$\begin{pmatrix} \gamma_k \\ \gamma_{-k}^\dagger \end{pmatrix} = B_k \begin{pmatrix} d_k \\ d_{-k}^\dagger \end{pmatrix} \tag{A.10}$$

where

$$B_k = \begin{pmatrix} u_k & iv_k \\ iv_k & u_k \end{pmatrix} \tag{A.11}$$

and the anticommutation relations $\left\{\gamma_k, \gamma_{k'}^\dagger\right\} = \delta_{k,k'}$ leads to the constraint $u_k^2 + v_k^2 = 1$. Thus, to find the values of u_k and v_k we need

$$B_k h_k B_k^\dagger = \begin{pmatrix} \omega_k & 0 \\ 0 & -\omega_k \end{pmatrix} \tag{A.12}$$

which gives

$$u_k = \sqrt{\frac{\omega_k + \epsilon_k}{2\omega_k}}\,, \qquad v_k = \sqrt{\frac{\omega_k - \epsilon_k}{2\omega_k}}\,. \tag{A.13}$$

Now the Hamiltonian can be written in diagonal form

$$H = \sum_{k\geq 0} \omega_k \left(\gamma_k^\dagger \gamma_k + \gamma_{-k}^\dagger \gamma_{-k} - 1\right) \tag{A.14}$$

where we see the ground state is the Bogoliubov vacuum state defined as $\gamma_k|\tilde{0}\rangle$ (the tilde is to distinguish from the d_k operator vacuum) with energy $E_0 = -\sum_{k\geq 0}\omega_k$. We can find the Bogoliubov vacuum in terms of the d_k vacuum with the ansatz

$$|\tilde{0}\rangle = G(d_k^\dagger d_{-k}^\dagger)|0\rangle \tag{A.15}$$

where $G(x)$ is some yet to be determined function of x. This ansatz is motivated by conservation of momentum. Taylor expanding $G(x)$ gives

$$\left[G(0) + G'(0)d_k^\dagger d_{-k}^\dagger\right]|0\rangle \tag{A.16}$$

where we have neglected all terms beyond quadratic in the creation operator because they give zero when acting on the vacuum. Combining this with the fact that $\gamma_k = u_k d_k + iv_k d_{-k}^\dagger$ and $\gamma_k|\tilde{0}\rangle = 0$ we get the condition

$$u_k G'(0) = -iv_k G(0) \implies G(d_k^\dagger d_{-k}^\dagger) = C_k \mathrm{e}^{-i\frac{v_k}{u_k}d_k^\dagger d_{-k}^\dagger} \tag{A.17}$$

for a particular k where C_k is some constant. The normalization condition $\langle\tilde{0}|\tilde{0}\rangle = 1$ gives $C_k = u_k$, so the normalized ground state for all k as

$$|\tilde{0}\rangle = \prod_{k\geq 0} u_k \mathrm{e}^{-i\frac{v_k}{u_k}d_k^\dagger d_{-k}^\dagger}|0\rangle = \prod_{k\geq 0}\left[u_k - iv_k d_k^\dagger d_{-k}^\dagger\right]|0\rangle \tag{A.18}$$

Dynamics of single particle excitations from the ground state

We can ask how the system evolves when a single particle is added to the ground state, whether it is a Bogoliubov quasi-particle or a regular fermion. The dynamics of a general state in the quasi-particle basis is given by $|\psi(t)\rangle = \sum_k c_k(t)|\tilde{k}\rangle$ where the amplitudes are $c_k(t) = \langle\tilde{k}|\psi_0\rangle \mathrm{e}^{-i\omega_k t}$. For a single quasi-particle placed at position R_j in the vacuum the resulting dynamics is

$$\begin{aligned} |\psi(t)\rangle = \mathrm{e}^{-iHt}\gamma_j^\dagger|\tilde{0}\rangle &= \frac{1}{\sqrt{N_s}}\sum_k \mathrm{e}^{-ikR_j}\mathrm{e}^{-iHt}\gamma_k^\dagger|\tilde{0}\rangle \\ &= \frac{\mathrm{e}^{iE_0 t}}{\sqrt{N_s}}\sum_k \mathrm{e}^{-ikR_j}\mathrm{e}^{-i\omega_k t}|\tilde{k}\rangle \end{aligned} \tag{A.19}$$

where the amplitudes are $c_k(t) = \frac{\mathrm{e}^{iE_0 t}}{\sqrt{N_s}}\mathrm{e}^{-ikR_j}\mathrm{e}^{-i\omega_k t}$. If we want to find the amplitudes of the position of the quasi-particle we have

$$\langle\tilde{R}_i|\psi(t)\rangle = \frac{1}{\sqrt{N_s}}\sum_k \mathrm{e}^{iR_i k}c_k(t) = \frac{\mathrm{e}^{iE_0 t}}{N_s}\sum_k \mathrm{e}^{i(R_i - R_j)k}\mathrm{e}^{-i\omega_k t}\,. \tag{A.20}$$

If $a \ll 1$, $N_s \gg 1$, but $N_s a = L \gg 1$, then we can change the sum into an integral, $\frac{2\pi}{L}\sum_{k=-\pi/a}^{\pi/a} \to \int_{-\infty}^{\infty}\mathrm{d}k$. We are interested in the dynamics caused by the oscillations about $k = 0$, so we expand the energy around this point

$$\begin{aligned}\frac{\omega_k}{J/2} &= \sqrt{1+g^2+2g\cos ka} \\ &\approx |1+g| - \frac{g}{2|1+g|}k^2 + \frac{g(1-g+g^2)}{24|1+g|^3}k^4 \end{aligned} \tag{A.21}$$

where we have defined a new parameter $g = 2h/J$ and we see we get divergences at $g = g_c = -1$ signaling a phase transition (PT). We can see the effect the PT has on the energy in Fig. A.1 where around the minimum at $k = 0$ the spectrum becomes linear in k. For small momenta and for $g < 0$, but away from g_c we can substitute Eq. (A.21) into Eq. (A.20) giving

$$\langle \tilde{R}|\psi(t)\rangle = \frac{\mathrm{e}^{i(E_0-1-g)t}}{2\pi}\int_{-\pi}^{\pi} \mathrm{e}^{i\left[(R-R')k - \frac{|g|t}{2|1+g|}k^2 + \frac{|g|(1-g+g^2)t}{24|1+g|^3}k^4\right]}\mathrm{d}k \tag{A.22}$$

where we have set $a = 1$ for simplification. Making the substitution $u = \left(\frac{|g|(1-g+g^2)t}{24|1+g|^3}\right)^{1/4} k$ transforms Eq. (A.22) into

$$\begin{aligned}\langle \tilde{R}|\psi(t)\rangle &= A(t)\int_{-\pi}^{\pi} \mathrm{e}^{i\left[Y(R,t)u + X(t)u^2 + u^4\right]}\mathrm{d}u \\ &= A(t)\,\mathrm{Pe}^*\left[X(t), Y(R,t)\right] \end{aligned} \tag{A.23}$$

where $\mathrm{Pe}^*\left[X,Y\right]$ is a truncated Pearcey function $\mathrm{Pe}\left[X,Y\right] = \int_{-\infty}^{\infty} \mathrm{e}^{i\left[Yu+Xu^2+u^4\right]}\mathrm{d}u$ and

$$\begin{aligned} X(t) &= -\sqrt{\frac{6t|g||1+g|}{1-g+g^2}} \\ Y(R,t) &= (R-R')\left(\frac{24|1+g|^3}{t|g|(1-g+g^2)}\right)^{1/4} \\ A(t) &= \frac{e^{i(E_0-1-g)t}}{2\pi}\left(\frac{24|1+g|^3}{t|g|(1-g+g^2)}\right)^{1/4}. \end{aligned} \tag{A.24}$$

The analysis done so far has been fine away from g_c, but what happens at the critical point? We see from Eq. (A.9) the energy around $k = 0$ becomes

$$\begin{aligned}\frac{\omega_k}{J/2} &= 2|\sin ka/2| \\ &\approx |k| + \frac{|k|^3}{24}, \end{aligned} \tag{A.25}$$

so adding a quasi-particle at position R at the critical point gives

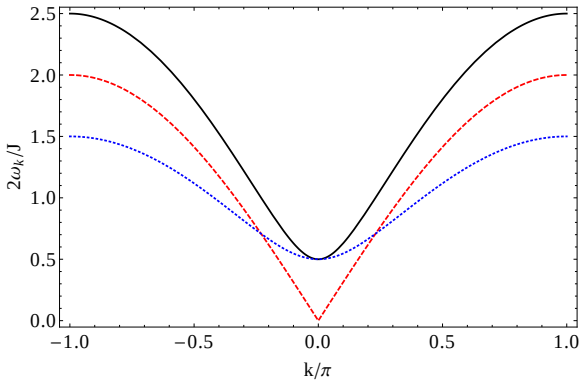

Figure A.1: ω_k as a function of k for different values of g: $g = -1.5$ (solid, black), $g = g_c = -1.0$ (dashed, red) and $g = -0.5$ (dotted, blue). One can see on either side of g_c $k = 0$ is a global minimum, so it is different from a second order PT where a global minimum becomes a local maximum.

$$\begin{aligned}
\langle \tilde{R}|\psi(t)\rangle &= \frac{e^{iE_0 t}}{2\pi}\int_{-\pi}^{\pi} e^{i\left[(R-R')k - t|k| - \frac{t|k|^3}{24}\right]}\mathrm{d}k \\
&= \frac{e^{iE_0 t}}{\pi}\int_{0}^{\pi} \cos\left[(R-R')k\right] e^{-i\left[tk+\frac{tk^3}{24}\right]}\mathrm{d}k \\
&= \frac{e^{iE_0 t}}{\pi}\left(\frac{24}{t}\right)^{1/3}\int_{0}^{\pi} \cos\left[B(R-R',t)s\right] e^{-i\left[C(t)s+s^3\right]}\mathrm{d}s \qquad \text{(A.26)}
\end{aligned}$$

where in the last line we made the substitution $k = (24/t)^{1/3}s$, so

$$B(R-R',t) = \left(\frac{24}{t}\right)^{1/3}(R-R') \qquad \text{(A.27)}$$

$$C(t) = (24\,t^2)^{1/3}\,. \qquad \text{(A.28)}$$

We can see at $g = g_c$ the amplitude turns into half an Airy function in a sinusoidal envelope determined by the distance $R - R'$.

Instead of looking at the dynamics produced by the placement of quasiparticle in the ground state at position R', let us look at the dynamics after a $f_k, f_k^\dagger$ particle is placed in the ground state at position R'. We start by finding the $d_k^\dagger$ operator in terms of the quasiparticle operators using Eq. (A.10) which gives

$$d_k^\dagger = u_k\gamma_k^\dagger + iv_k\gamma_{-k}\,. \qquad \text{(A.29)}$$

We know that $f_j^\dagger = \frac{1}{\sqrt{N_s}}\sum_k d_k^\dagger e^{ikR_j}$, so the dynamics produced by the addition of a particle is

$$|\psi(t)\rangle = \mathrm{e}^{-iHt} f_j^\dagger |\tilde{0}\rangle = \frac{1}{\sqrt{N_s}} \sum_k \mathrm{e}^{ikR_j} \mathrm{e}^{-iHt} \left(u_k \gamma_k^\dagger + i v_k \gamma_{-k} \right) |\tilde{0}\rangle$$
$$= \frac{\mathrm{e}^{iE_0 t}}{\sqrt{N_s}} \sum_k \mathrm{e}^{ikR_j} \mathrm{e}^{-i\omega_k t} u_k |\tilde{k}\rangle \,. \tag{A.30}$$

The amplitude to be at position R_i is

$$\langle \tilde{R}_i | \psi(t) \rangle = \frac{\mathrm{e}^{iE_0 t}}{N_s} \sum_k \mathrm{e}^{i(R_j - R_i)k} \mathrm{e}^{-i\omega_k t} u_k \tag{A.31}$$

where we can see the difference between this equation and Eq. (A.20) is the factor of u_k.

Figure A.2 shows the dynamics resulting from the two different initial states of placing a single particle in the ground state at site zero. We can see in the first column where $g = -1.5$ the dynamics is qualitatively the same where we see a cusp with the usual pattern of dark and bright spots within it. In the middle column where $g = g_c = -1.0$ again both are the same and they become blurrier than the first column which is expected as the wave function for both no longer takes the form of a truncated Pearcey function, but of a truncated Airy function. In the final column on the right where $g = -0.5$ we do see a different from placing a Bogoliubov particle (top) and a regular fermion (bottom). The fermion dynamics is blurrier than the Bogoliubov dynamics. The reason for this is because the major contributor to the form of the wave function for $t > 0$ is the state $k = 0$ and $u_0 = 0$.

The black curves represent the cusp which is calculated from the cusp equation

$$Y = \pm \sqrt{\frac{8}{27}} (-X)^{3/2} \tag{A.32}$$

and the parameters in the Eq. (A.24) giving

$$R = \pm \frac{4t|g|}{3\sqrt{1 - g + g^2}} \,. \tag{A.33}$$

Interestingly enough in the plane of the physical coordinates (t, R) the cusp is not a cusp at all due to t being linear. Nevertheless, the fact that wave function can be transformed into the canonical form with coordinates (X, Y) means it retains features of the cusp such as the interference pattern within it.

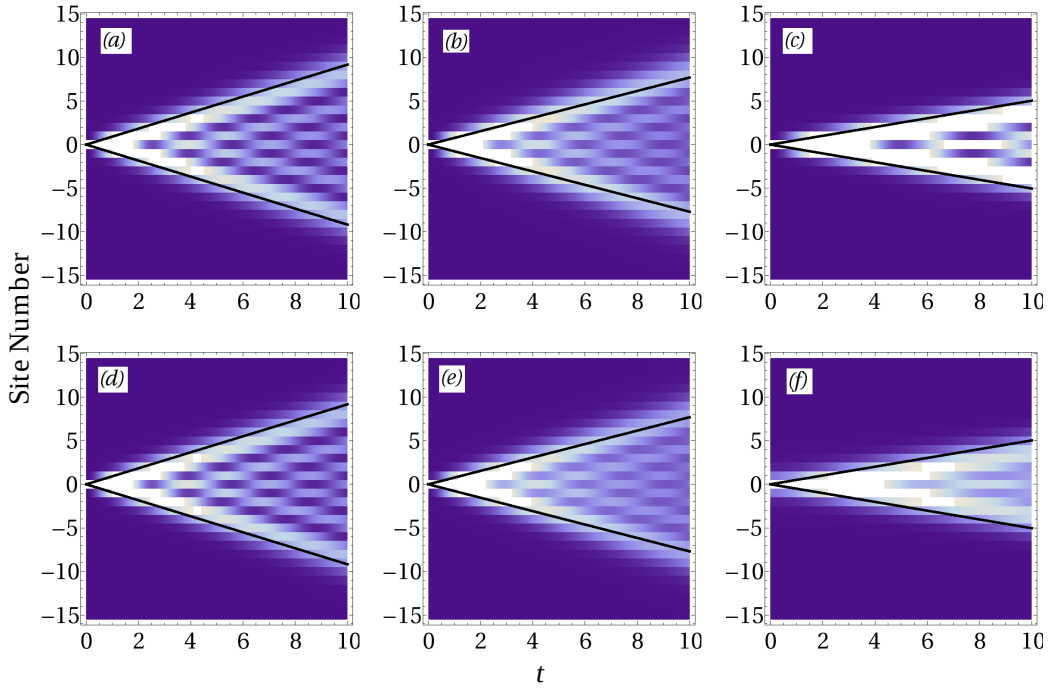

Figure A.2: Dynamics of the intensity of the wave function with initial condition of a Bogoliubov particle placed in the ground state at site zero (top row, $(a)-(c)$) from Eq. (A.20) and a fermion from the Jordan-Wigner transformation placed into the ground state at site zero (bottom row, $(d)-(f)$) from Eq. (A.31). Each column is for a different values of g and are the same as in Fig. A.1: $g=-1.5$ (left column), $g=-1.0$ (middle column) and $g=-0.5$ (right column). One can see the dynamics are pretty similar until $g>g_c$ where the fermion placed dynamics is blurry compared to the bogoliubov placed dynamics. In both cases the cusp from the dynamics is blurry at $g=g_c$ which is what is expected as the corresponding semiclassical wave function no longer takes the form of the Pearcey function. The black curves form the cusp from the equation $Y=\pm\sqrt{\frac{8}{27}}(-X)^{3/2}$.

Bibliography

[1] L. de Broglie, "Recherches sur la theorie des quanta", Thesis (1924).

[2] A. Einstein, Sitzungsber. Preuss. Akad. Wiss., page 262, (1924).

[3] S. N. Bose, Z. Phys. **26**, 178 (1924).

[4] M. Anderson, J. Ensher, M. Matthews, C. Wieman and E. Cornell, Science **269**, 198 (1995).

[5] K. Davis, M.-O. Mewes, M. Andrews, N. van Druten, D. Kurn and W. Ketterle, Phys. Rev. Lett. **75**, 3969 (1995).

[6] C. C. Bradley, C. A. Sackett, J. J. Tollet and R. G. Hulet, Phys. Rev. Lett. **75**, 1687 (1995).

[7] M. R. Andrews, C. G. Townsend, H.-J. Miesner, D. S. Durfee, D. M. Kurn and W. Ketterle, Science **275**, 637 (1997).

[8] J. E. Simsarian, J. Denschlag, M. Edwards, C. W. Clark, L. Deng, E. W. Hagley, K. Helmerson, S. L. Rolston and W. D. Phillips, Phys. Rev. Lett. **85**, 2040 (2000).

[9] T. Schumm, S. Hofferberth, L. M. Andersson, S. Wildermuth, S. Groth, I. Bar-Joseph, J. Schmiedmayer and P. Krüger, Nat. Phys. **1**, 57 (2005).

[10] B. D. Josephson, Phys. Rev. Lett. **1**, 251 (1962).

[11] C. Chin, R. Grimm, P. Julienne and E. Tiesinga, Rev. Mod. Phys. **82**, 1225 (2010).

[12] R. W. Spekkens and J. E. Sipe, Phys. Rev. A **59**, 3868 (1999).

[13] E. J. Mueller, T.-L. Ho, M. Ueda and G. Baym, Phys. Rev. A **74**, 033612 (2006).

[14] L. Pitaevskii and S. Stringari, Phys. Rev. Lett. **87**, 180402 (2001).

[15] G. Mazzarella, L. Salasnich and F. Toigo, J. Phys. B: At. Mol. Opt. Phys. **45**, 185301 (2012).

[16] Gh.-S. Paraoanu, S. Kohler, F. Sols and A. J. Leggett, J. Phys. B: At. Mol. Opt. Phys. **34**, 4689 (2001).

[17] J. Javanainen and M Wilkens, Phys. Rev. Lett. **78**, 4675 (1997).

[18] G.-B. Jo, Y. Shin, S. Will, T. A. Pasquini, M. Saba, W. Ketterle, M. Vengalattore, M. Prentiss and D. E. Pritchard, Phys. Rev. Lett. **98**, 030407 (2007).

[19] K. Maussang, G. E. Marti, T. Schneider, P. Treutlein, Y. Li, A. Sinatra, R. Long, J. Estéve and J. Reichel, Phys. Rev. Lett. **105**, 080403 (2010).

[20] WD. Li and J. Liu, Phys. Rev. A **74**, 063613 (2006).

[21] R. Gati, J. Estéve, B. Hemmerling, T. B. Ottenstein, J. Appmeier, A. Weller and M. K. Oberthaler, New J. Phys. **8**, 189 (2006).

[22] S. Chu, L. Hollberg, J. E. Bjorkholm, A. Cable and A. Ashkin, Phys. Rev. Lett. **55**, 48 (1985).

[23] P. D. Lett, R. N. Watts, C. I. Westbrook, W. D. Phillips, P. L. Gould and H. J. Metcalf, Phys. Rev. Lett. **61**, 169 (1988).

[24] A. Aspect, E. Arimondo, R. Kaiser, N. Vansteenkiste and C. Cohen-Tannoudji, Phys. Rev. Lett. **61**, 826 (1988).

[25] H. J. Metcalf and P. van der Straten, *Laser Cooling and Trapping*, (Springer, New York 1999).

[26] I. Bloch, J. Dalibard and W. Zwerger, Rev. Mod. Phys. **80**, 885 (2008).

[27] H. Qiu, J. Tian and L.-B. Fu, Phys. Rev. A **81**, 043613 (2010).

[28] I. Bausmerth, U. R. Fischer and A Posazhennikova, Phys. Rev. A **75**, 053605 (2007); U. R. Fischer, C. Iniotakis and A. Posazhennikova, Phys. Rev. A **77**, 031602(R) (2008).

[29] M. Rinck and C. Bruder, Phys. Rev. A **83**, 023608 (2011).

[30] H. J. Lipkin, N. Meshkov and A. J. Glick, Nucl. Phys. **62**, 188 (1965).

[31] R. H. Dicke, Phys. Rev. **93**, 99 (1954).

[32] K. Baumann, C. Guerlin, F. Brennecke and T Esslinger, Nature **464**, 1301 (2010).

[33] M. Greiner, O. Mandel, T. W. Hänsch and I. Bloch, Nature **419** (2002), 51 (2002).

[34] T. Volz, N. Syassen, D. M. Bauer, E. Hansis, S. Dürr and G. Rempe, Nat. Phys. **2**, 692 (2006).

[35] P. Barmettler, M. Punk, V. Gritsev, E. Demler and E. Altman, Phys. Rev. Lett. **102**, 130603 (2009).

[36] M. Eckstein, M. Kollar and P. Werner, Phys. Rev. Lett. **103**, 056403 (2009).

[37] R. P. Feynman, Rev. Mod. Phys. **20**, 367 (1948).

[38] C. M. Bender and S. A. Orszag, *Advanced Mathematical Methods for Scientists and Engineers: Asymptotic Methods and Perturbation Theory*, (Springer-Verlag, New York, 1999).

[39] R. Thom, *Structural Stability and Morphogenesis*, (Benjamin, Reading, MA, 1975).

[40] R. Gilmore, S. Kais and R. D. Levine, Phys. Rev. A **34**, 2442 (1986).

[41] R. P. Saxena, P. K. Srivastava and V. S. Varma, J. Phys. A: Math. Gen. **21**, L389 (1988).

[42] J. A. Gaite, Phys. Rev. A **41**, 5320 (1990).

[43] T. V. Bogdan and D. J. Wales, J. Chem. Phys. **120**, 11090 (2004).

[44] C. Emary, N. Lambert and T. Brandes, Phys. Rev. A **71**, 062302 (2005).

[45] T. Poston and I. Stewart, *Catastrophe Theory and its Applications*, (Dover, Mineola, NY, 2012).

[46] M. Leibscher, I. Sh. Averbukh, P. Rozmej and R. Arvieu, Phys. Rev. A **69**, 032102 (2004).

[47] D. H. J. O'Dell, Phys. Rev. Lett. **109**, 150406 (2012).

[48] M. V. Berry, Singularities in Waves in Les Houches Lecture Series Session XXXV, eds. R Balian, M Klman and J-P Poirier, North-Holland: Amsterdam, 453-543 (1981).

[49] J. F. Nye, *Natural Focusing and Fine Structure of Light: Caustics and Wave Dislocations*, (IOP Publishing, Bristol, 1999).

[50] V. I. Arnol'd, V. S. Afrajmovich, Y. S. Il'yashenko and Y. S. Shil'nikov, *Dynamical Systems V:Bifurcation Theory and Catastrophe Theory*, (Springs-Verlag, Berlin, (1994).

[51] T. Pearcey, Phil. Mag. **37**, 311 (1946).

[52] V. I. Arnol'd, Russ. Math. Survs. **30**, (5) (1975).

[53] M. V. Berry, J. Phys. A **10**, 2061 (1977).

[54] M. V. Berry and M. R. Dennis, J. Opt. A: Pure Appl. Opt. **6**, S178 (2004).

[55] M. Kardar, *Statistical Physics of Fields*, (Cambridge University Press, Cambridge, 2013).

[56] R. K. Pathria and P. D. Beale, *Statistical Mechanics*, (Elsevier Ltd., Oxford, 2011).

[57] L. D. Landau, Phys. Z. Sowjetunion **11**, 26 (1937).

[58] J. Rudnick, H. Guo, and D. Jasnow, J. Stat. Phys. **41**, 3 (1985).

[59] A. F. Albuquerque, F. Alet, C. Sire and S. Capponi, Phys. Rev. B **81**, 064418 (2010).

[60] V. Gritsev and A. Polkovnikov, in *Understanding in Quantum Phase Transitions* edited by L. Carr, (Taylor and Francis, Boca Raton, 2010).

[61] R. Gati, M. K. Oberthaler, J. Phys. B: At., Mol. Opt. Phys. **40**, R61 (2007).

[62] I. Bloch, Nat. Phys. **1**, 23-30 (2005).

[63] L. Pitaevskii and S. Stringari, *Bose-Einstein Condensation*, (Clarendon Press, Oxford, 2003).

[64] G. J. Milburn, J. Corney, E. M. Wright and D. F. Walls, Phys. Rev. A **55**, 4318 (1997).

[65] S. Raghavan, A. Smerzi, S. Fantoni and S. R. Shenoy, Phys. Rev. A **59**, 620 (1999).

[66] A. J. Leggett, Rev. Mod. Phys. **73**, 307 (2001).

[67] J. J. Sakurai, *Modern Quantum Mechanics*, (Addison-Wesley, Boston, 1993).

[68] W. M. Zhang, D. H. Feng and R. Gilmore, Rev. Mod. Phys. **62**, 867 (1990).

[69] N. S. Tonchev, J. G. Brankov and V. A. Zagrebnov, J. Optoelectron. Adv. M. **11**, 1142-1149 (2009).

[70] Y. K. Wang and F. T. Hioe, Phys. Rev. A **8**, 2517 (1973).

[71] E. H. Lockwood, Ch. 8 in *A Book of Curves*, (Cambridge University Press, Cambridge, 1967).

[72] A. Trenkwalder, G. Spagnolli, G. Semeghini, S. Coop, M. Landini, P. Castilho, L. Pezzë, G. Modugno, M. Inguscio, A. Smerzi and M. Fattori, Nat. Phys. **12**, 826-829 (2016).

[73] E. P. Wigner, Phys. Rev. **40**, 749 (1932).

[74] A. Polkovnikov, Ann. Phys. (N.Y.) **325**, 1790 (2010).

[75] D. H. J. O'Dell, to be published.

[76] Y. Yee, J. Mumford and D. H. J. O'Dell, to be published.

[77] G. Wentzel, Zeitschrift für Physik **38**, 518-529 (1926); H. A. Kramers, Zeitschrift für Physik **39**, 828-840 (1926); L. Brillouin, Comptes Rendus de l'Academie des Sciences **183**, 24-26 (1926).

[78] M. V. Berry, Adv. Phys. **25**, 1 (1976).

[79] J. J. Duistermaat, Commun. Pure App. Math. **27**, 207 (1974).

[80] V. Guillemin and S. Sternberg, *Geometric Asymptotics*, Am. Math. Soc. Surv. **14**, (Providence, USA, 1977).

[81] G. B. Airy, Trans. Camb. Phil. Soc. **6**, 379 (1838).

[82] J. F. Nye and M. V. Berry, Proc. R. Soc. Lond. **A336**, 165 (1974).

[83] J. M. Kosterlitz and D. J. Thouless, J. Phys. C: Solid State Phys. **6**, 1181 (1973).

[84] W. H. Zurek, Rev. Mod. Phys. **75**, 715 (2003).

[85] B. Damski, H. T. Quan and W. H. Zurek, Phys. Rev. A **83**, 062104 (2011).

[86] A. Das, K. Sengupta, D. Sen and B. K. Chakrabarti, Phys. Rev. B **74**, 144423 (2006).

[87] D. Hangleiter, M. T. Mitchison, T. H. Johnson, M. Bruderer, M. B. Plenio and D. Jaksch, Phy. Rev. A **91**, 013661 (2015).

[88] W. Rooijakkers, S. Wu, P. Striehl, M. Vengalattore and M. Prentiss, Phys. Rev. A **68**, 063412 (2003).

[89] J. H. Huckans, I. B. Spielman, B. L. Tolra, W. D. Phillips abd J. V. Porto, Phys. Rev. A **80**, 043609 (2009).

[90] P. M. Preiss, R. Ma, M. E. Tai, A. Lukin, M. Rispoli, P. Zupancic, Y. Lahini, R. Islam and M. Greiner, Science **347**, 6227 pp. 1229-1233 (2015).

[91] A.-M. Visuri, J. J. Kinnunen, J. E. Baarsma and P. Törmä, Phys. Rev. A **94**, 013619 (2016).

[92] P. Coleman, *Introduction to Many-Body Physics*, (Cambridge University Press, Cambridge, 2015).